Investigation of localized fatigue properties in unalloyed steels by infrared thermography

Untersuchung von lokalen Ermüdungsvorgängen in unlegiertem Stahl mit Hilfe der Infrarot-Thermografie

Von der
Fakultät Architektur, Bauingenieurwesen und Umweltwissenschaften
der Technischen Universität Carolo-Wilhelmina
zu Braunschweig

zur Erlangung des Grades eines
Doktor-Ingenieurs (Dr.-Ing.)
genehmigte

Dissertation

von
Dipl.-Ing. Justus Medgenberg
aus Annweiler am Trifels

Eingereicht am	26. Juni 2007
Mündliche Prüfung am	30. November 2007

Berichterstatter	Prof. Dr.-Ing. Thomas Ummenhofer
	Prof. Dr.-Ing. Udo Peil
	Prof. Dr.-Ing. Martin Mensinger

Braunschweig 2008

Vorwort

Die vorliegende Arbeit entstand während meiner Tätigkeit am Institut für Bauwerkserhaltung und Tragwerk der Technischen Universität Carolo-Wilhelmina zu Braunschweig im Rahmen meiner Forschungstätigkeit im Sonderforschungsbereich 477 „Sicherstellung der Nutzungsfähigkeit von Bauwerken mit Hilfe innovativer Bauwerksüberwachung“. Die Arbeit ist als Beitrag zur internationalen Forschungsaktivität in diesem Bereich in englischer Sprache verfasst. Zum Gelingen dieser Arbeit haben zahlreiche Personen beigetragen, die ich an dieser Stelle erwähnen und denen ich meinen Dank aussprechen möchte.

Besonderer Dank gebührt meinem Doktorvater, Prof. Dr.-Ing. Thomas Ummenhofer, dessen Unterstützung und Anregungen massgeblich zu dieser Arbeit beigetragen haben. Die motivierende, vertrauensvolle, spannende und herausfordernde Tätigkeit an seinem Institut während der letzten Jahre hat mich fachlich und persönlich geprägt. Nicht zuletzt der von ihm gewährte Freiraum hat mir die Bearbeitung dieses interdisziplinären Themas überhaupt erst ermöglicht. Meine Zeit am Institut für Bauwerkserhaltung und Tragwerk wird mir wohl immer in guter Erinnerung bleiben.

Herrn Prof. Dr.-Ing. Udo Peil danke ich für die freundliche Übernahme des Korreferats, die Bereitstellung der hervorragenden und motivierenden Arbeitsmöglichkeiten im Rahmen des Sonderforschungsbereichs 477, sowie für die Möglichkeit, die Forschungs- und Laboreinrichtungen des Instituts für Stahlbau wie selbstverständlich nutzen zu können.

Meinen herzlichen Dank möchte ich auch Herrn Prof. Dr.-Ing. Martin Mensinger aussprechen, der sich zur Übernahme des zweiten Korreferats bereit erklärt hat.

Bei Herrn Prof. Dr.-Ing. Harald Budelmann und Herrn Prof. Dr.-Ing. Martin Empelmann bedanke ich mich für die freundliche Übernahme der Aufgaben in der Prüfungskommission zu dieser Promotion.

Herrn Dipl.-Ing. Robin Plum möchte ich für die kritischen und gewissenhaften Korrekturen danken. Ich würde mich freuen, wenn er an der im Rahmen dieser Arbeit begonnenen Forschung auch zukünftig Freude und Interesse finden könnte und hoffe, ihn dabei weiterhin unterstützen zu können.

Allen Kollegen am Institut für Bauwerkserhaltung und Tragwerk sei auch noch einmal für das angenehme Arbeitsklima und die zahlreichen Diskussionen, Anregungen und Unterstützungen gedankt. Darüber hinaus möchte ich besonders Herrn Dr.-Ing. Matthias Reininghaus am Institut für Stahlbau für die anregenden fachlichen Diskussionen und die unkomplizierte kollegiale Zusammenarbeit danken. Herrn Dipl.-Ing. Björn Brodersen danke ich für die Durchsicht der Herleitungen in Kapitel 4.

Many thanks also to US Airways Captain Ron Wiens, Scottsdale Arizona, for the prompt support with linguistic corrections and his valuable suggestions. I hope that we can preserve and intensify the friendship of our families for the future.

Danken möchte ich auch der Laborleitung des Instituts für Stahlbau, Herrn Dipl.-Ing. Olaf Einsiedler und besonders Herrn Stefan Amelung für die kollegiale und lösungsorientierte Zusammenarbeit und vielfältige Unterstützung. Hervorheben möchte ich die hervorragende Arbeit aller technischen Mitarbeiter des Instituts für Stahlbau, die in zahllosen Arbeitsstunden die teils schwierigen technischen Problemstellungen umgesetzt haben.

Schließlich gebührt mein Dank meiner Freundin Franziska Nagel für ihre Nachsicht, Geduld und moralische Unterstützung in der heißen Phase der Promotion. Besonders möchte ich mich auch bei meinen Eltern Gabriele und Karl-Walter Medgenberg für die jahrelange treue Unterstützung bedanken, die mir diesen Weg überhaupt erst eröffnet hat. Ihnen sei diese Arbeit deshalb gewidmet.

Abschließend gilt mein Dank der Deutschen Forschungsgemeinschaft (DFG) für die großzügige finanzielle Unterstützung meiner Forschungstätigkeit.

Braunschweig, im Dezember 2007 Justus Medgenberg

Zusammenfassung

Ein interessantes Anwendungsgebiet der Infrarot-Technologie als zerstörungsfreies Prüfverfahren stellt die berührungslose und zeitaufgelöste Erfassung von thermomechanischen Kopplungsvorgängen bei ermüdungsbeanspruchten Bauteilen dar. Ziel ist es, anhand der Temperaturveränderungen unter mechanischer Beanspruchung Rückschlüsse auf das Werkstoffverhalten zu ziehen. In der Vergangenheit sind hierzu zahlreiche Untersuchungen mit verschiedenen Messtechniken erfolgt, die überwiegend makroskopische Vorgänge unter Zugrundelegung homogenen Werkstoffverhaltens analysieren. Ziel der vorliegenden Arbeit ist hingegen die thermografische Untersuchung von lokalisierten mikroskopischen Schädigungsvorgängen bei der Werkstoffermüdung von unlegiertem Stahl S355 im High-Cycle-Fatigue-Bereich.

Zunächst erfolgt eine Zusammenstellung des State-of-the-art bei der experimentellen Erfassung thermomechanischer Kopplungsvorgänge und bisheriger Erkenntnisse zum zyklischen Werkstoffverhalten unlegierter Kohlenstoffstähle unter kraftgeregelter Beanspruchung. Danach wird auf Grundlage der Wärmeleitungsgleichung unter Berücksichtigung thermoelastischer Kopplung und plastischer Dissipation ein numerisches Modell vorgestellt, dass die Simulation thermomechanischer Kopplungsvorgänge durch deren Integration in bestehende FE-Programme erlaubt. Nach Anpassung der Werkstoffparameter zeigt das FE-Modell eine sehr gute Übereinstimmung mit experimentellen Ergebnissen und wird im Folgenden zur Untersuchung zahlreicher Einflussparameter, insbesondere auch dem Einfluss von Wärmeausbreitung und verschiedener Nichtlinearitäten auf das thermische Kopplungsverhalten eingesetzt.

Auf Basis der numerischen Erkenntnisse wird ein Auswerteverfahren zur Detektion von Nichtlinearitäten im Temperatur-Zeitverlauf mit einer Auflösung bis zu einem mK für experimentelle Untersuchungen entwickelt. Die erstmalig durchgeführte versuchstechnische Erfassung lokaler Nichtlinearitäten im Temperatur-Zeitverlauf in Folge Werkstoff-Entfestigung erlaubt die Auflösung und Beobachtung stark lokalisierter Vorgänge wie die Entstehung von Lüdersbändern und die Untersuchung von Schädigungsvorgängen im Kerbgrund geometrischer Kerben.

Die thermischen Untersuchungen zeigen eine direkte Korrelation mit Daten aus Dehnungsmessungen und Ergebnissen mikroskopischer Untersuchungen von Oberflächenveränderungen wie der Entwicklung von persistenten Gleitbändern. Zudem können der Zeitpunkt und der Ort der Rissentstehung thermografisch direkt ermittelt werden. Weitere Versuche an geschweißten Probekörpern verdeutlichen die große Bedeutung des Risswachstums im Schweißnahtübergangsbereich für das gesamte Ermüdungsverhalten. Anzeichen für zyklisch-plastische Verformungen im Schweißnahtübergangsbereich vor der Rissinitierung konnten nicht nachgewiesen werden.

Insgesamt zeigen die Untersuchungen das weitgehend unerschlossene Potential thermografischer Untersuchungen des lokalen thermomechanischen Kopplungsverhaltens bei Ermüdungsversuchen. Zukünftige Entwicklungen sollten insbesondere stärker auf die Quantifizierung der Ergebnisse und auf die Einbindung der Ergebnisse in rechnerische Methoden zur Lebensdauervorhersage abzielen.

Contents

List of Figures

List of Tables

Notations

Abbreviations

A/D	analog/digital
DFT	Discrete Fourier Transform
FE(M)	finite element (method)
FFT	Fast Fourier Transform
HCF	high cycle fatigue
InSb	indium-antimony
IR	infrared
LCF	low cycle fatigue
MTC	mechanical-thermal coupling
NETD	noise equivalent temperature difference
PtSi	platinum silicide
TMC	thermal-mechanical coupling
TSA	thermoelastic stress analysis
1-D	one-dimensional
2-D	two-dimensional
3-D	three-dimensional

Units

m	meter
cm	centimeter
mm	millimeter
μm	micrometer
min	minute
s	second
Hz	Hertz
GV	grey values
lc	load cycle
MPa	Megapascal (N/mm^2)
N	Newton
W	Watt
K	Kelvin
mK	Milli-Kelvin
°C	degree Celsius
k...	kilo...

Indices

$(...)_0$	reference value
$(...)_m$	mean value
$(...)_a$	amplitude
$(...)^e$	elastic
$(...)^p$	plastic
$(...)^{tot}$	total value
$(...)_L$	load
$(...)^{lin}$	linear
$(...)^{nlin}$	nonlinear

Operators

y, Y	scalar
$\vec{y}$	vector (first order tensor)
$\boldsymbol{Y}$	second order tensor
$\mathfrak{Y}$	virtual quantity
$max(y)$	maximum of y
$min(y)$	minimum of y
$abs(y)$	absolute value of y
Δy	difference or peak to peak variation of y
$\boldsymbol{Y} : \boldsymbol{Z}$	double contracted product of Y and Z
$\mathbf{Y}_I$	first invariant of Y
$\mathbf{Y}_{II}$	second invariant of Y
$\mathbf{Y}_{III}$	third invariant of Y
∂	partial derivative operator
d	absolute derivative operator
δ	Kronecker delta

Symbols

α	coefficient of thermal expansion
A	area
C	specific heat capacity
ϵ	emissivity
ε	strain
ε^e	elastic strain
ε^p	plastic strain
E_{tot}	total energy

E_{kin}	kinetic energy
E_u	internal energy
E	Young's modulus of elasticity
$\boldsymbol{E}$	elasticity tensor
g, h	undefined pseudo functions
f	frequency
H	height
k	coefficient of thermal conductivity
L	length
μ, λ	Lamé constants
λ_T	thermal diffusivity
λ_Φ	wavelength
M	mass
$\vec{n}$	normal unit vector
ν	Poisson's ratio
N, N_f	number of load cycles, failure load cycles
p	momentum
P_k	particle
$\vec{q}$	heat flux vector
ρ	mass density
r	specific heat generation
R	load ratio $R = \frac{min(\sigma)}{max(\sigma)}$
σ	stress
$\boldsymbol{\sigma}$	Cauchy stress tensor
σ_y	yield stress (general)
σ_{y0}	initial yield stress
σ_{yN}	load-history dependent yield stress
$\sigma_{y,u}$	monotonic 1-D upper yield stress
$\sigma_{y,l}$	monotonic 1-D lower yield stress
σ_u	monotonic 1-D ultimate stress
S	entropy
s	specific entropy
T	absolute temperature
T_0	reference temperature
t	time
u	specific internal energy
$\vec{v}$	velocity vector
V	volume
V_k	undefined state variables
$\vec{w}$	deformation vector

$\vec{x}$	position vector
ϕ	phase shift
Φ	spectral radiant excitance
Ψ	Helmholtz free energy

1 Introduction

Metal fatigue is generally strongly governed by localized damage phenomena which - in the early stages of fatigue - cannot be assessed by conventional testing methods. The lack of reliable tools for the experimental assessment of localized damage phenomena contributes to the poor verification of advanced damage models. Recent theoretical attempts aim to incorporate energy based approaches in the description of material fatigue. Here infrared thermography can make a powerful contribution to experimental mechanics. The basis for the application of thermography for material characterization is laid by the laws of thermodynamics. They state that mechanical loading of a solid is coupled to a change of its thermal state. Thus temperature measurements can be used to evaluate the local thermomechanical coupling of components and provide insight in the local material behavior and damage progress. The application of infrared thermography for the full-field investigation of thermomechanical coupling becomes especially promising for the study of metal fatigue which generally involves a high level of uncertainty with respect to the underlying damage processes. The rapid technical progress of starring-array infrared cameras bears a high potential that this technique can become a standard tool during experimental fatigues studies in the future. During the last 15 years revolutionary developments have been achieved in infrared technology, data processing and computational abilities. Now further development of the experimental techniques is needed with the objective to unify experimental, numerical and analytical approaches for fatigue damage assessment.

The application of thermal measurements for the investigation of thermomechanical coupling phenomena is a well established experimental technique. Along with the improvement of technical equipment many attempts have been made in the past to use temperature information to characterize the material behavior during fatigue and monotonic loading. The early investigations relied exclusively on contacting measurement techniques such as electrical resistance measurements, thermocouples, thermometers or calorimetric measurements. During the last three decades infrared technology based on radiometry has gained more and more attention as a fast, full-field non-contacting temperature measurement technique. However so far only a few attempts have been made to apply thermal measurements to the characterization of strongly localized phenomena. One major obstacle for a broader application of thermal methods is the current focus on global temperature values (e.g. the mean temperature of the tested specimens). These approaches suffer from a strong dependence of the results on the specific testing and environmental conditions, so that the quantification and transferability of the results is rather poor. Generalization of the methodology to localized properties can only be achieved if local temperature values are used instead, which are directly related to the local thermomechanical coupling. Additionally the effects of internal heat diffusion or heat exchange with the surroundings need to be considered, especially if highly heat conductive materials such as metals are investigated.

Encouraged by the recent technical progress the purpose of this thesis is to investigate the potential of infrared thermography for the assessment of local damage phenomena during fatigue loading of mild low-carbon steel. In contrast to earlier studies special attention has been given to the pre-crack phase where typical damage phenomena are hard to assess by conventional experimental techniques. The studies start with a compromising review of thermal investigations in experimental mechanics. The purpose of this review is to provide a conceive state of the art and highlights the strong correlation between mechanical and thermal behavior. Then the general cyclic material behavior of low-carbon steels under load-controlled testing in the high cycle fatigue regime is discussed. It has been concluded that in the absence of significant flaws cyclic plasticity constitutes the dominating mechanism for fatigue damage evolution. Based on an outline of the thermomechanical background a numerical solution procedure for the simulation of thermomechanical coupling phenomena is introduced. The solution procedure is purposely based on a commercial finite element code which facilitates its integration in an industrial environment. The finite element studies are used to investigate potential linear and nonlinear coupling phenomena during fatigue loading. The results serve to develop a new, specialized data processing methodology for infrared sequences recorded during experimental fatigue studies. The new technique allows for the analysis of minor nonlinearities in the spatial-temporal temperature evolution. Finally local thermomechanical coupling and damage phenomena during fatigue loading of low carbon steel are investigated experimentally using high resolution infrared thermography. The experiments compromise investigations on unnotched, geometrically notched and welded specimens. The thermal results are compared with strain gauge measurements and microscopic investigations of the damage processes on the surface of the specimens. They reveal various potential starting points for further investigations and verify a high potential for thermographic investigations of local damage phenomena.

2 Applications of thermal measurements in experimental mechanics

In the past various efforts have been made to relate specific mechanical properties to the measured temperature changes during mechanical loading or to the intrinsic heat generation deduced from the temperature evolution. This chapter is a brief summary of the reported methods and results with an emphasis on recent findings. Due to the amount of published material only a few historical remarks are given here where it may help for better understanding. A rough characterization of the reported applications of thermal measurements for material characterization allows to identify the following categories:

- thermoelastic stress analysis
- notch and crack tip investigations in fracture mechanics
- dissipation measurements and damage assessment during monotonic and cyclic loading

2.1 Thermoelastic stress analysis

It is well known that a volume change of contained gases causes a specific temperature change. A similar effect occurring for solids is widely ignored. For elastic loading the rate of elastic volume work exerted upon a solid body equals an equivalent heat generation within the body. Under adiabatic conditions the resulting thermoelastic temperature variations are proportional to the sum of the principal stresses or strains. Accordingly pure shear strains do not contribute to the thermoelastic temperature changes. The so-called thermoelastic effect is a long-known phenomenon and dates back to theoretical conclusions of Lord Kelvin (William Thomson) [Tho53] and experimental findings of Joule [Jou59]. The temperature changes in solids caused by thermoelasticity are rather small. For steel a change of the principal stress sum of 1 Mpa causes a temperature change of only about 1 mK if heat transfer is negligible, i.e. under adiabatic conditions. Technically this effect can be used for full-field strain analysis by measuring the small temperature changes occurring on the surface of solids during mechanical loading. For thermally well conducting materials such as metals, typically high mechanical work rates are needed in order to minimize the effects of heat conduction and to assure quasi-adiabatic conditions. In the past various contacting or non-contacting measurement techniques have been used to determine the temperature variations due to thermoelasticity. The most elegant way now commonly used is based on radiometric full field measurements by means of an infrared camera. This technique has been primarily developed in the 1980s and 1990s and has been termed Thermoelastic Stress Analysis (TSA). A good summary of the early development of the TSA technique can be found in [HC91].

Belgen can be considered as one of the first pioneers of TSA. He performed experimental studies on thermoelastic coupling using non-contact single-point radiometric measurements [Bel68]. The experimental findings were accompanied by comprehensive theoretical studies concerning the effects of the loading frequency, surface coatings and other factors as well as by a discussion of the achievable space and stress resolution. The introduction of the SPATE systems (Stress Pattern Analysis by measurement of Thermal Emissions) in the early 1980s (see [HC91] and [SC85]) made it possible to perform full-field measurements of the thermoelastic temperature variations in a relatively short time (figure 1(a)). The scanning infrared camera used for SPATE 4000 consisted of a single cadmium-mercury-telluride (CMT) detector. A set of digitally controlled two-axes scanning mirrors provided a picture up to 256 x 256 pixels. In order to reduce the influence of the detector noise, cyclic loads were applied. Noise reduction was done by means of an incorporated hardware lockin-amplifier. The lockin-amplifier was fed with a reference signal provided by the testing machine, strain gauges, etc. and filtered out any signal contributions which were not directly correlated to the reference signal. Typical acquisition times for full field measurements were in the range of hours. This prevented the application of the system to investigations with temporarily changing conditions (e.g. fatigue studies). The Deltatherm system introduced in 1991 (figure 1(b)) replaced the mechanical scanner by a 128 x 128 pixel focal plane infrared camera with an indium-antimony (InSb) detector operating in the wavelengths range 2 - 5 μm [LB95]. Frame rates as high as 434 frames per second could be achieved, which reduced the time needed for thermoelastic testing from hours to seconds [DBQ98]. The FAST system introduced in 1993 used a 512 x 512 pixel platinum silicide (PtSi) detector array which overcame the problem of the low spatial discretization of the Deltatherm system [RW93]. The disadvantages of the system were a relatively poor thermal sensitivity of the PtSi detector and low frame rates of 25 Hz at full resolution which limited the range of applications [WR95]. Current (commercially available) infrared cameras provide detector sizes up to 640 x 512 pixels at full frame rates above 100 Hz and a thermal resolution in the mK range. Rapid advances in camera technology are to be expected for the future.

Since the introduction of these first and second generation single-purpose systems, infrared camera technology, computer technology and data processing methods have been extensively developed. Modern systems are based on a modular design and data processing is performed by specialized software solutions. The built-in hardware lock-in amplifiers of the first generation systems have been completely replaced by online digital data processing methods or specialized post-processing. In order to extend

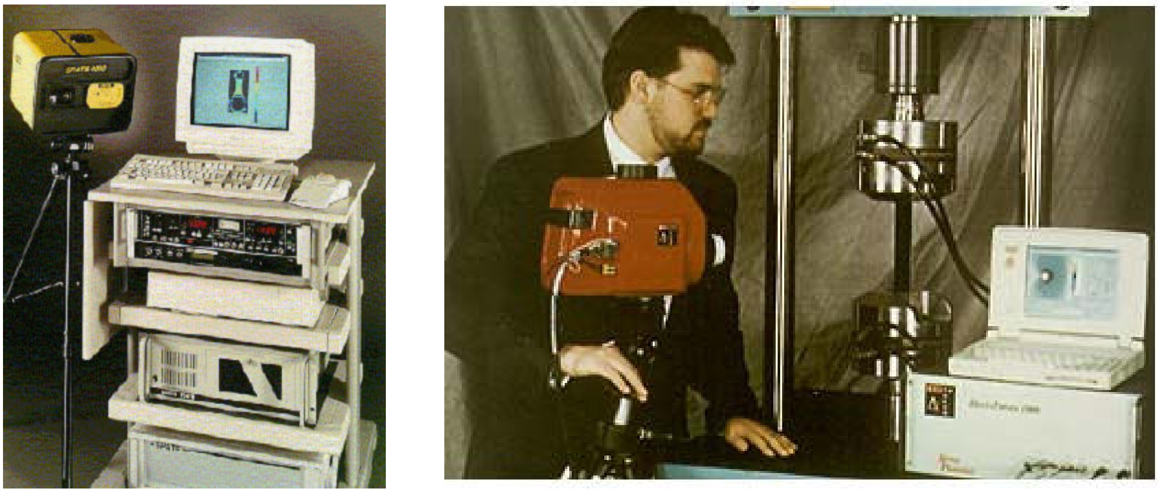

(a) SPATE 4000 [Spa08]

(b) Deltatherm 1000 [Del07]

Figure 1: Early commercial systems for thermoelastic stress analysis

the range of possible applications more advanced data processing techniques were developed for non-harmonic loading ([HC87], [MS93], [LMR97], [LBH98], [GMS05]). [DBEQC06] proposed a correction methodology which corrects the TSA results for influences from the mean temperature.

The advances in infrared technology motivated worldwide research activities since the 1980s which give a profound understanding of underlying thermomechanical coupling phenomena and the potential for TSA applications. [DBQ98] and [PP03] give a comprehensive state of the art of the thermoelastic stress analysis technique and the underlying theory at the end of the 20th century. Since the beginning of TSA investigations the extraction of the full stress or strain tensor of the thermal data has attracted special research attention. Various attempts have been undertaken to separate individual stress components or to obtain the full stress or strain tensor ([HAR90], [FZRS92], [RR93], [Fei94], [BP96], [SDS96], [KISS97], [Ino04]) from the scalar temperature field. Despite all efforts this problem remains mostly unsolved and the methods reported so far are limited to special applications and testing conditions or require additional measurement techniques.

For quantitative measurements adiabatic conditions need to be achieved which poses limitations on the loading frequency. In general the direct proportionality between the change of the first stress invariant and the temperature changes is not given anymore if heat conduction within the tested component becomes significant. The problem of non-adiabatic conditions has been addressed by several researchers ([Dun93], [OBBF97], [Dun93], [QDB02]). For harmonic loading it has been shown that regions strongly influenced by heat diffusion can be identified by a phase shift of the temperature signal ([OBBF97], [QDB02]) with respect to the loading. So far only a few attempts have been made to compensate for the heat diffusion ([SD04], [GS05] and [Yan03a] for a 2-D case). The existing correction schemes can be considered to be insufficient for complex (but realistic) loading scenarios with 3-D stress gradients. As a result often only general recommendations regarding the loading frequency or the load rate are given and the effects of geometry and non-homogeneous stress distribution on the internal heat transfer are neglected, even in case of complex geometries.

In extent to the classical theory [MSS87b] and [MSS87a] reported a dependence of the thermoelastic temperature signal on the mean stress, which [WJS87] and [WSD88] attributed to the temperature dependence of the Young's modulus. The dependence causes additional coupling terms which - for harmonic loading - become dependent on the stress amplitude and the mean load. This opens the opportunity to quantify residual stresses and/or mean stresses from thermoelastic temperature records. Further investigations and applications have been reported by [DLS89], [GB99], [GB01] and [QDBL04]. Besides some studies under laboratory conditions no practical investigations have been reported which can be explained by the difficulties to properly quantify the mean load effect under realistic conditions.

Often TSA has to be applied under conditions where the natural emissivity of the component surfaces to be investigated is too low. This becomes especially important for the investigation of metallic components. In this case an emissivity coating needs to be applied to the investigated surface which avoids reflectance and increases thermal emission. Unfortunately the coating itself has a thermoelastic response and additionally alters the measured surface temperatures due to its thermal conductivity. The influence of the coating on the recorded TSA signal has been investigated by [Bel68], [McK87], [Mac89] and [WZ93]. Depending on the loading frequency, the coating thickness and the properties of the substrate and the coating

- the IR transparency,
- the heat transfer from the substrate to the surface of the coating,
- the thermoelastic answer of the coating itself,
- a combination of the effects cited above,

can alter the inquired thermoelastic temperature signal of the tested component. The coating effects provoke a time lag and alter the magnitude of the measured surface signal with respect to the temperature changes at the direct surface of the tested component.

With the spread of numerical methods as the finite element method (FEM), TSA results have been more and more used to verify numerical models of the tested components. Two general approaches can be distinguished. For the first approach followed by [GP03] adiabatic conditions are assumed a priori. Possible effects of heat diffusion are not taken into account. Therefore the temperature changes induced during mechanical loading can be directly calibrated into an equivalent change of the first invariant of the strain tensor. Then TSA results can be compared to the principal stress sum obtained from a numerical solution of the mechanical problem. By contrast the second approach considers the effects of heat diffusion. For this purpose the temperature variations of the fully transient coupled mechanical-thermal problem are calculated numerically and compared to the temperature measurements obtained during mechanical loading ([OBBF97], [UM06]). A similar approach is followed by [BR01] and [BZH03] in order to calculate the transient temperature fields in front of growing cracks. The advantage of this methodology is the correct consideration of heat diffusion, which becomes especially important for complex geometries. The approach requires the correct evaluation of all material constants so that the adjustment of the numerical model becomes more demanding.

2.2 Application of thermal methods to crack detection and crack tip investigations

The detection of fatigue cracks in metal structures is one of the most prominent tasks of non-destructive testing. The application of thermography during mechanical loading offers various opportunities for crack detection and studies in fracture mechanics. It has been recognized that localized phenomena as the fatigue crack initiation and growth lead to strong inhomogeneities in the measured temperature distribution. The strong plastic dissipation at the crack tip causes a local increase of the stabilized mean temperature ([CAF75], [Yan03a]). This effect can be used to estimate the moment of crack initiation during fatigue tests. [BP01] gave results of fatigue tests on different components from the automotive industry and localizes small cracks. Data processing is performed by a specific 'D-mode' available as a commercial software module by Cedip/France. To the author's knowledge no detailed publications concerning the theoretical background of the 'D-Mode' are available, so that the underlying approach cannot be verified. According to the manufacturer the methodology allows one to quantify the dissipated energy on a local or a global scale but presumably does not take into account the effects of heat diffusion. To detect cracks [Hus94] concentrated on the detection of non-linearities in the thermomechanical temperature signal which arise from crack-closure and plastic deformation. He compared the TSA measurements with extensive numerical studies of the first and second harmonic of the first invariant of the stress tensor. The results show that higher harmonics of the fundamental frequency can be used for the detection of cracks. The studies reveal that the nonlinearities in the temperature signal caused by crack closure exceed greatly the nonlinearities due to crack tip plasticity. The work was further developed by [Sch98]. [SGOC00] evaluated the applicability of the SPATE system for the detection of hidden internal cracks in aeronautical structures. For this approach the disturbance of the surface principal stress sum due to a hidden crack has been investigated experimentally and numerically. [ACI03] demonstrated that infrared measurements can be applied to the detection of strain localization and crack initiation during monotonic punch tests. [GZRR01] presented temperature measurements of a growing crack under impact loading in specimens made of an ultrahigh strength steel (C300) and a ductile medium strength steel (HY100). For their investigations they used a custom-built ultra-high-speed thermal imaging system with a spatial resolution of only 8 x 8 pixels.

Another field of investigation is the quantitative relation of thermoelastic and thermoplastic measurements to classical approaches in fracture mechanics. [Pip82] investigated the temperature field in front of growing fatigue cracks in construction steels St 37 (S235) and St 70 using liquid crystals. [DYP04b] and [DYP04a] used TSA measurements to estimate experimentally the effective stress intensity factor and compare the TSA measurements to classical compliance methods. [DYP04b] introduced a new technique for the estimation of the crack tip position from TSA data. In general good agreement in the estimation of the crack tip location could be achieved in comparison to other techniques as microscopic investigation. For welded specimens [DYP04a] noticed a substantial difference in the mode I stress intensity factor which he attributed to the residual stress field in the vicinity of the weld seam. The investigations concentrated on the cross-section of the weld detail so that an overall 2-D problem was given. [BR01] conducted numerical and experimental investigations using thermocouples and reported a significant drop of the temperature in front of growing fatigue cracks in brittle materials, attributed to thermoelasticity. [BZH03] studied the slow stable crack growth on specimens of 302 stainless steel under monotonic loading. They compare numerically calculated temperature distributions obtained from a coupled mechanical-thermal model with temperature variations obtained from infrared thermography.

2.3 Plastic dissipation and damage assessment

In contrast to the thermoelastic temperature variations thermoplastic dissipation causes a net heat generation and leads to a local or global temperature rise during repeated fatigue loading (figure 2(a)). Different attempts have been made to retrieve the energy dissipation from temperature measurements, e.g by calorimetric techniques, electrical resistance methods, thermocouples, liquid crystals, single point non-contacting infrared radiometry or full field infrared cameras. An all-encompassing review of early applications of thermometric measurements during monotonic or fatigue testing can be found in [Har75] and is not repeated here. Numerous investigators related the observed mean temperature rise or derived parameters to specific fatigue properties ([LWJ$^+$00], [JWL$^+$01], [Yan03b]) or mechanical damping [ACZ03] of the tested specimens. Mostly the results have been reported for unnotched specimens with a homogenous distribution of plastic strains. The investigations differ primarily in the tested material and the applied measurement techniques. The main parameter of interest for these investigations is the evolution of the mean temperature which can be used to estimate the bulk dissipation due to plasticity. It has been shown by a remarkable number of researchers that the fatigue limit of metals can be estimated from temperature measurements. For this purpose fatigue tests with stepwise increasing load amplitudes are performed and the stabilized mean temperature of the specimen at each load step is evaluated (figure 2(a)). A sharp increase of the mean temperature has been observed at load amplitudes close to the fatigue limit. Therefore the fatigue limit of the tested material can be estimated from a plot of the stabilized mean temperature over the applied load amplitude ([Har75], [Esc80], [LRR00]). The strong increase of the stabilized temperature close to the fatigue limit indicates the sudden massive onset of plastic deformations (figure 2(b)).

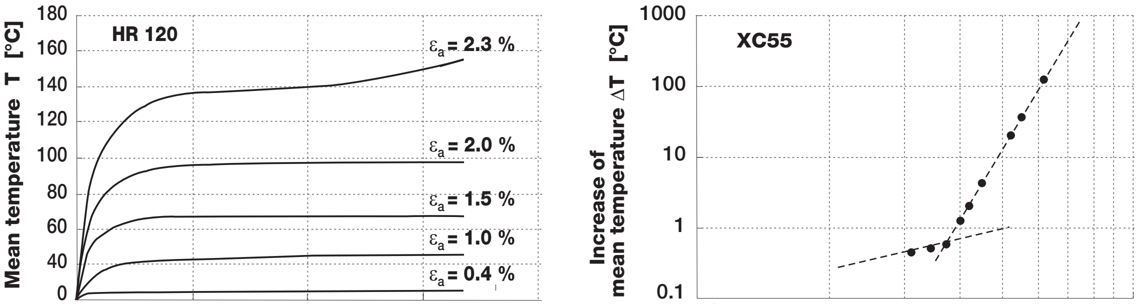

(a) stabilization of the mean temperature

(b) increase of mean temperature vs. applied stress amplitude

Figure 2: Influence of plastic dissipation on the mean temperature evolution [CC04] based on experimental results of [JWL$^+$04] and [Luo98]

[Stä80] reported similar results for tests on austenitic steel and gray iron cast (GG-20). The procedure has also been transferred to the fatigue testing of entire components [Luo98]. [Esc80] conducted fatigue tests on specimens made out of unalloyed steel Ck 15 and Ck 30 and observed a small rise of the mean temperature, even for specimens which did not fail before termination of the tests. He explained this observation with the occurrence of plastic strains even at stress levels below the fatigue limit. [Web83] investigated the evolution of the mean temperature during fatigue testing on specimens of different steels. The results demonstrated that typical hardening and softening phenomena can be assessed by a corresponding change of the mean temperature. In addition to standard testing procedures the mean temperature has been used as control variable for some of the fatigue tests. The evolution of the mean specimen temperature during cyclic testing has been proven to correspond to the evolution of plastic strains [PE95]. [KPB99] and [KP02] showed that the fatigue limit cannot only be determined by the mean temperature rise but also by a change in the first and second natural frequency of the harmonic thermoelastic/thermoplastic temperature signal (figure 3). However these investigations have not been developed further with respect to the investigations of localized phenomena.

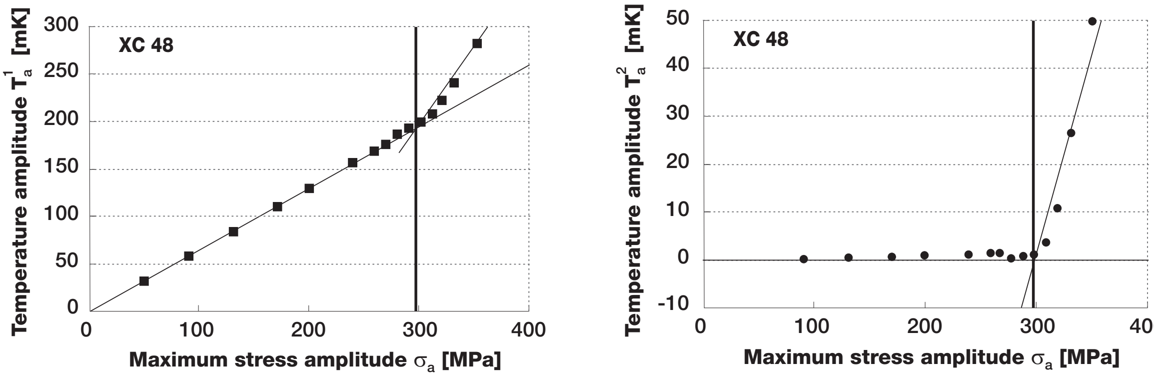

(a) first harmonic temperature amplitude

(b) second harmonic temperature amplitude

Figure 3: Estimation of the fatigue limit by analysis of the first and second harmonic of the temperature evolution [KP02]

To extend the rather empirical approaches based entirely on temperature data, different researchers focus on the deduction of the heat source distribution ([Stä80], [BCMG04]). The heat source distribution is estimated from the temperature records by inversion of the heat conduction equation which generally requires the simplification to a 1-D or 2-D case. The approaches are accompanied by theoretical and conceptional efforts to reconsider fatigue in terms of dissipated energy [CC04]. [Yan03a] conducted thermographically supervised fatigue experiments in the low-cycle-fatigue

(LCF) and high-cycle fatigue (HCF) regime on specimens of steel SA533B1 and of ULTIMET superalloy. From the measured mean temperature rise and the superimposed thermoelastic temperature oscillations he calculated the dissipated mechanical work within the specimens. The calculation is based on the 2-D heat conduction equation with thermoelastic and thermoplastic coupling terms. Very good correlation to the macroscopically observed stress-strain hysteresis loops has been achieved if the heat losses at the boundaries are taken into consideration. From the results the lifetime of the specimens could be predicted based on the total plastic strain energy density [JWL$^+$04]. [YLW$^+$01] reported an initial hump in the mean temperature distribution before a quasi-constant temperature plateau was reached during fatigue tests on reactor pressure vessel steel. By comparing the macroscopic stress-strain hysteresis loop with the temperature evolution the hump was attributed to a yielding phenomenon [1]

Fatigue experiments performed on titanium by [Rös03] showed that, in contrast to the observations made for steels, the mean temperature did not stabilize during testing but constantly increased during the entire fatigue test. After a short interruption of the loading during which the specimens cooled down, the mean temperature reached the pre-interruption level after a short period of strong initial heating. [Rös03] concluded that the accumulated fatigue damage could to some extent be quantified by measuring the temperature evolution during a short time 'testing' excitation. Both short time low frequency high amplitude and high frequency low amplitude mechanical excitation applied by a testing machine or an ultrasonic device, respectively have been successfully used for the characterization of the bulk fatigue damage [MRKS02].

For monotonic loading [LC01] studied thermographically the development and the propagation of Lüders bands during tensile tests on S355. From the measured spatio-temporal temperature evolution they calculated the heat source distribution and showed that the dissipation distribution takes the form of propagating waves with constant velocity. [Pas03] conducted uniaxial tension tests on different materials with the purpose to quantitatively relate the thermoelastic and thermoplastic temperature changes to the local strain field. A similar idea is followed by [RWL93] who proposed a method for the assessment of residual stresses based on thermal measurements during monotonic loading.

Only few attempts have been made so far to apply thermal measurements for the detection of localized damage phenomena in the pre-crack phase. An early approach on steel and fiberglass-epoxy is presented by [CAF75]. They measured the evolution of the mean temperature in the vicinity of strong stress concentrators (saw cuts) and

---

[1] According to the opinion of the author the presented trend in the stress strain hysteresis loops seems to clearly indicate a ratchetting phenomenon (compare [Kuc95]). A similar phenomenon found by the same group for Ultimet superalloy was also interpreted as ratchetting [JWL$^+$01].

concluded that thermal studies allowed the prediction of the likely position of crack initiation and the investigation of fatigue crack growth. [Mül89] investigated the fatigue behavior of geometric notches by small thermoelements which had been welded to the specimen surface within the notch. The investigations focused on the measurement of the thermoelastic temperature variations. Upon a certain load amplitude a loss of linearity between the applied load amplitudes and the measured temperature amplitudes was denoted. The observed decrease of the temperature amplitudes has been attributed to load redistributions due to cyclic plasticity. During single-step tests the load redistributions could be identified by corresponding changes of the temperature amplitudes at different measuring points. [PPLS$^+$05] focused on the detection of fatigue cracks in unnotched specimens made of 35CrMo4 with an unknown location of crack initiation. The proposed data processing for crack detection is based on the calculation of the spatial standard deviation from the recorded infrared pictures. The methodology allows to study localization phenomena including crack initiation, crack propagation and crack jumping. The experiments reported by [Ask91] focused on the assessment of welding seams with the purpose to retrieve the local 'hot spots' from TSA measurements. The results suffered from the insufficient resolution of the available experimental techniques and unspecific data processing. The application has therefore not been developed further.

2.4 Chapter summary and conclusion

Extensive theoretical, numerical and experimental work has been published on TSA and related thermal techniques for the assessment of thermomechanical coupling phenomena during static testing and fatigue loading. The results reported so far demonstrate the strong interdependence of mechanical exposure, local material behavior and thermal answer of solids under mechanical loading and thus proof the high potential of thermal methods in experimental mechanics. Mechanical phenomena such as thermoelasticity, plasticity, cracks, localization phenomena etc. have been assessed so far in different materials. Additionally various special topics of the measuring and data processing technique have been addressed.

A characteristics of the reported applications in the field of damage assessment and assessment of plastic dissipation is that these methods mostly rely on global temperature measurements based on the assumption of homogeneous processes. Few attempts have been made to investigate localized damage phenomena. As an example investigation on fatigue crack tips have been reported which verify the enormous potential of infrared measurements in the field of fracture mechanics. Further approaches become especially interesting in the context of recent advances in material and damage modeling, e.g. for finite element (FE) analysis. This requires closing the gap between experimental, theoretical and numerical approaches in thermomechanics. In this context a few urgent and so far mostly unsolved problems can be identified:

- further experimental verification of the applicability of thermal measurements to assess localized damage phenomena and development of techniques for the improved detection of localized effects
- improved quantification of the results, which becomes independent of the specific setup and boundary conditions
- correction for the effects of heat diffusion during static, harmonic and random loading
- transfer and mapping of the results to numerical simulations and methodical incorporation into thermomechanical motivated damage models

3 Mechanical behavior of unalloyed carbon steels

3.1 Monotonic loading

In the following section the material behavior of low carbon steel (also called mild steel) during monotonic and load-controlled cyclic loading is reviewed and various influences on the material behavior are discussed. The purpose is to provide the relevant background for an understanding of local fatigue properties rather than an all-encompassing state of research.

Depending on the carbon content the typical microstructure of mild steels is either ferritic-pearlitic, pearlitic or pearlitic with fall-outs of cementite. During strain or displacement-controlled tension tests the steel behaves nearly linear-elastic on a macroscopic scale until the upper yield limit $\sigma_{y,u}$ is reached. Then the stress falls back to a lower yield limit $\sigma_{y,l}$ and subsequent plastic flow occurs without any significant rise of the applied stress. [2]

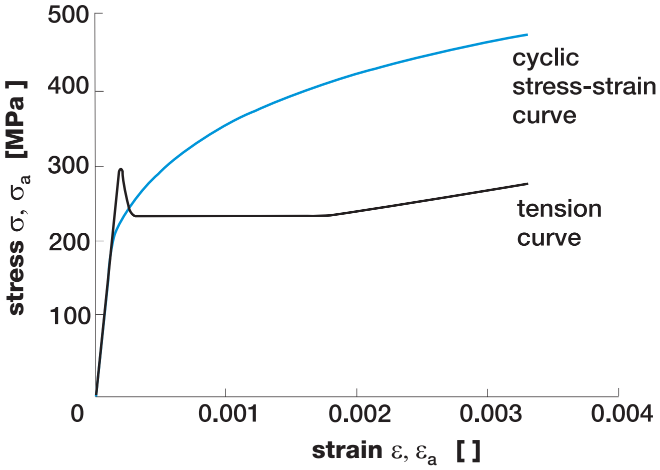

Figure 4: General behavior of low carbon steel under monotonic and cyclic loading

The plastic deformations are concentrated to the softer ferrite whereas the harder pearlite blocks the dislocation movement and limits the spatial extension of the dislocations. The upper yield limit is attributed to interstitial dissolved carbon or nitrogen impurity atoms in the ferrite lattice. In the normalized state they cause a concentration of edge dislocations which remain bound to the impurity atoms during macroscopic elastic loading. At the upper yield limit the macroscopic stress is high enough to cause a massive separation of dislocation clouds from the interstitial atoms. The

---

[2] Since the occurrence of the upper yield limit is not mandatory for low carbon steels the monotonic yield limit refers to the lower yield limit $\sigma_{y,l}$ throughout this thesis.

avalanche-like growth of plastically deformed sections leads to a drop of stresses on a macroscopic scale. The process starts at exposed spots of the specimen as shoulders, notches etc. and then spreads out as so-called Lüders bands [Chr91]. The extent of the upper yield limit differs strongly and depends on the composition of the steel, the heat treatment of the specimens etc. The subsequent yield plateau is characterized by ongoing multiplication and movement of dislocations until the increasing dislocation density starts to impede further slip. Macroscopically hardening sets on at this point. The ultimate strength of the steel is reached if the ongoing hardening of the material cannot compensate for the stress rise caused by the reduction of cross-section of the the specimen.

The grain boundaries act as barriers and reduce the mobility of the dislocations. Therefore the yield stress and the extension of the yield plateau depend strongly on the grain size [Bil93]. The plastic deformations of unalloyed steels during monotonic loading are found to be particularly sensitive towards the strain rate. Higher strain rates cause both an increase of the upper and lower yield limit. The rate dependence is more pronounced for the upper yield limit. [Böt02] shows that with decreasing deformation rate the lower yield limit tends towards a static yield limit, which would have been obtained at zero strain rate.[3]

3.2 Cyclic loading

3.2.1 Definitions and general concepts

The well-developed monotonic (lower) yield limit $\sigma_{y,l}$ represents a particularity in the material behavior of unalloyed low-carbon steels. During monotonic loading the yield limit allows for the easy differentiation between elastic and plastic deformations. At stress levels below the yield limit purely elastic deformations can be assumed, whereas plastic deformations set in if the monotonic yield limit is exceeded at least locally. For cyclic loading this understanding of plasticity loses its validity. The ongoing loading and unloading of metals alters the microstructure of the steels and finally allows for dislocation generation and movement at load levels below the monotonic yield limit. Eventually the repeated loading and unloading might lead to fatigue-failure at load levels far below the monotonic ultimate strength.

Any fatigue relevant loading will be referred to as ’cyclic’ loading throughout this thesis without restrictions on the shape function of the imposed loading. A complete loading

---

[3] Obviously a strain rate of zero cannot be realized experimentally. [Böt02] conducts tension tests at different strain rates, which are subsequently interrupted at different strain levels if the level of the lower yield limit is reached. The observed relaxation for all strain rates stabilizes at a pronounced level which has been related to the yield limit at zero strain rate.

and unloading sequence will referred to as load cycle. The actual number of applied load cycles is denoted with N. If the loading is harmonic a load cycle corresponds to the completion of sinusoidal load variation.

For cyclic loading plastic deformations can set on at load levels below the monotonic yield limit $\sigma_{y,l}$. This effect is called cyclic softening. The associated yield limit will be denoted with σ_{y0} which is generally significantly smaller than $\sigma_{y,l}$. It refers to the stress (amplitude) below which only elastic strains occur even after an infinite number of applied load cycles. In the absence of significant defects cyclic plastic strains are widely accepted to be the decisive factor in the process of fatigue damage accumulation and constitute the driving mechanism behind the fatigue process. Especially it has been shown that without defects the first microcracks originate at slip band intrusions and extrusions at the free surface. Cyclic plastic deformations might or might not appear homogeneously distributed on a macroscopic scale or can even be confined to individual grains. This phenomena will be referred to as cyclic plasticity throughout this thesis as opposed to the monotonic plasticity discussed in the prior section. The onset of cyclic plastic deformations is marked by a nonlinear relationship between stresses and strains. For the one-dimensional case the stress-strain curve of a complete load cycle defines a stress-strain hysteresis curve (figure 5). The cyclic material behavior is described by the quantities stress σ, total strain ε^{tot}, elastic strain ε^{e} and plastic strain ε^{p}. The elastic strains define the reversible material deformations, whereas plastic strains correspond to the remaining non-reversible deformations after removal of all applied loads. An additive composition of the total strain is generally assumed so that:

$$\varepsilon^{tot} = \varepsilon^{e} + \varepsilon^{p} \tag{1}$$

Therefore only two of the strains are mutually independent whereas the third strain value is given through equation (1).

The cyclic material properties are obtained from cyclic tests during which one of these three parameters (i.e. total stress, total strain or plastic strain) is chosen as independent control variable. The values of the other parameters are dependent and adjust during the test according to the specific cyclic material behavior and the damage state of the material. The evolution of the independent variable under repeated loading is associated with cyclic softening and cyclic hardening. Table 1 summarizes how the choice of the control variable affects the evolution of the dependent variables.

Cyclic softening or hardening implies that the cyclic stress-strain curve lies below or above the corresponding monotonic stress-strain curve (figure 4). However this definition is not unique since softening and hardening can occur at different stages during fatigue testing. In this case the actual material response might e.g. be 'softer' with respect to the monotonic behavior even though the material is actually subject to a hardening stage. Therefore softening and hardening are always understood here

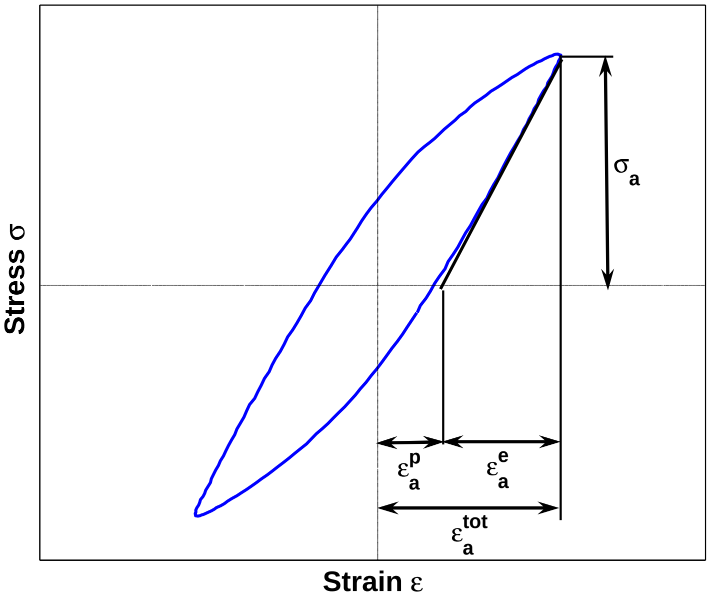

Figure 5: Stress-strain hysteresis loop and parameter definition

Table 1: Variation of the measured material properties as a function of the chosen control variable

control variable	**stress/load**	**total strain**	**plastic strain**
cyclic softening	σ_a → ε_a^{tot} ↑ ε_a^p ↑	σ_a ↓ ε_a^{tot} → ε_a^p ↑	σ_a ↓ ε_a^{tot} ↓ ε_a^p →
cyclic hardening	σ_a → ε_a^{tot} ↓ ε_a^p ↓	σ_a ↑ ε_a^{tot} → ε_a^p ↓	σ_a ↑ ε_a^{tot} ↑ ε_a^p →

as damage-dependent processes and refer to the change of the actual state rather than to the material behavior with respect to monotonic loading.

The evolution of the cyclic stress-strain hysteresis behavior during an entire fatigue test is commonly represented in cyclic hardening/softening curves (figure 6). In these graphs the dependent variables (i.e. the total strain, the plastic strain or the stress) are plotted against the number of applied load cycles, normally given on a logarithmic scale. Unalloyed steels typically show a quasi-saturation behavior after an initial phase, so that constant values are reached for the dependent variables after a certain number of load cycles. In order to compare the results obtained at different load levels it is suitable to represent the material behavior by the saturated stress or strain values.

Similar to the monotonic stress-strain curve the so-called cyclic stress-strain curve is constructed from the saturated values of the stress amplitudes and either the total strain or the plastic strain amplitudes. The saturated stress or strain values might be replaced by the instantaneous values at a certain number of load cycles, commonly at $0.5 \cdot N_f$, where N_f is the number of applied load cycles until failure. For unalloyed steels the cyclic stress-strain hysteresis loops obtained at different load levels are not necessarily geometrical similar to each other. This is referred to as Non-Masing behavior.

3.2.2 Cyclic behavior of unalloyed low-carbon steels

Cyclic plasticity is often regarded as an exclusive phenomenon in the range of low cycle fatigue (LCF) which is defined here by failure load cycles $N_f < 10^4$. In this range typically the static yield limit is exceeded during the first load cycle and high plastic strains are involved. For high cycle fatigue (HCF) with $N_f >> 10^4$ the occurring plastic strains are very small and might be limited to small regions. In this range measurable plastic strain evolve only after hundreds or thousands of load cycles, assuming constant amplitude loading. The assessment of small, localized strains poses significant experimental difficulties, since strain gauge measurements or other techniques can only partially be applied.

Even though plasticity evolves below the monotonic yield limit during cyclic loading the pronounced yield limit of low carbon steels represents a discontinuity in their material behavior. It provokes experimental difficulties and justifies a distinction of the cyclic material behavior for $\sigma_a > \sigma_{y,l}$ and $\sigma_a < \sigma_{y,l}$. The well developed yield plateau requires strain or displacement control in order to avoid undefined control states if the yield limit is exceeded during the first load cycle. For $\sigma_a < \sigma_{y,l}$ load control can be used without any difficulties.

For $\sigma_a > \sigma_{y,l}$ generally either cyclic hardening or cyclic softening predominates the material behavior from the first load cycle until crack initiation [Sch90]. By contrast for $\sigma_a < \sigma_{y,l}$ both softening and hardening can occur during the same test, so that the cyclic material behavior becomes more complex [Web83]. Very detailed investigations of the cyclic material behavior of unalloyed steel St52 (S355) under uniaxial and two-axial loading can be found in [Sch90], [Rei94], [Dan99] and [Kuc95]. These results have been obtained at relatively high strain amplitudes with $\sigma_a > \sigma_{y,l}$ during the first quarter-load-cycle. These investigations focus on experimental, theoretical and numerical modeling of the cyclic material behavior of S355 in the context of the elastic-plastic design of steel structures introduced by DIN-18800 and EUROCODE 3. The results cannot be generalized to the investigations throughout this thesis for which the focus has been put onto the technically interesting mid to high cycle fatigue regime. In this case N_f is in the range from 10^4 to 10^7 load cycles and $\sigma_a < \sigma_{y,l}$. For the case of load-controlled testing with $\sigma_a < \sigma_{y,l}$ a compromising review of the cyclic material and fatigue behavior of the unalloyed steel Ck 45 can be found in [Rei78]. [Gon79] extended these investigations on Ck 01, Ck 10, Ck 22, Ck 70, Ck 80 and Ck 100. Figure 6 shows exemplarily the evolution of the dependent plastic strain amplitude of Ck 10 under harmonic stress-controlled testing obtained for two different load amplitudes. Based on this general evolution [Gon79] distinguished five principal stages in the typical cyclic hardening/softening curves prior to the initiation of a macroscopic fatigue crack.

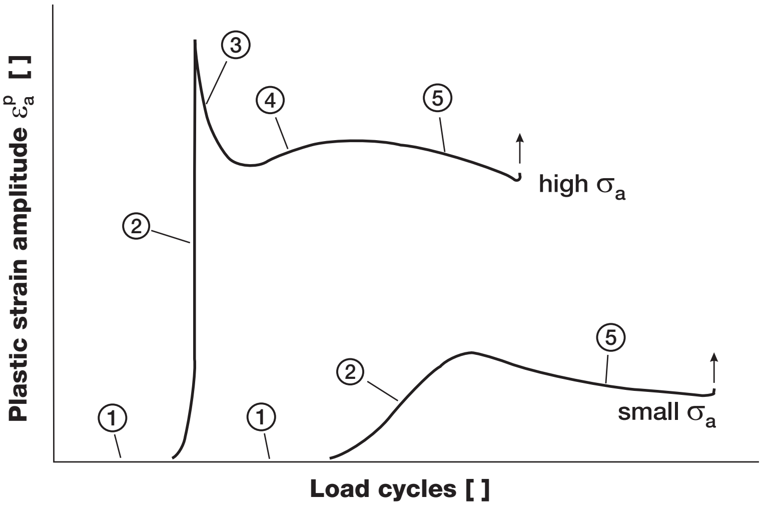

Figure 6: Softening/hardening curves of Ck 10 and distinction of the principal stages in the cyclic deformation behavior [Gon79]

1. **Incubation interval**
   The incubation interval is given as the number of load cycles after which the plastic strain amplitude reaches a certain level. [Gon79] proposes to use $\varepsilon_a^p = 10^{-4}$ as criteria. During the incubation interval the material behaves (almost) completely linear-elastic. For unalloyed steels the incubation interval compromises the first 0.1 % to 0.2 % of the fatigue lifetime N_f.

2. **Primary softening**
   The softening phase is marked by a strong increase of the total strains and the plastic strains. It compromises only a few load cycles with a total duration of typically below 0.01 % of N_f. According to [Chr91] the material state in this stage is characterized by the coexistence of plastically deformed grains and grains which still behave linear-elastic. The macroscopically observable softening behavior is associated with the increasing number of plastically deformed grains and zones with mobile dislocations.

3. **Primary hardening**
   For high stress amplitudes and low carbon content a phase of primary hardening can follow onto primary softening which [Gon79] attributes to reduced slip

caused by the increasing dislocation density. According to [Chr91] local hardening sets on already during the phase of primary softening, due to reduction of the dislocation mobility in some of the grains. The endpoint of the macroscopically observable softening phase is reached if the blocking cannot be compensated by the generation of new mobile dislocations. The overall dislocation density still increases and leads to a further reduction of the dislocation mobility. This process manifests itself macroscopically as hardening.

4. **Secondary softening**
   Onto primary hardening a secondary phase of softening can occur for low-carbon steels which is attributed to a partial remobilization due to the redistribution of primary dislocations.

5. **Secondary hardening**
   Secondary hardening can to some extent be found in all unalloyed steels and takes place between 80 % and 90 % of N_f. The stage of secondary hardening is marked by a decrease of dislocation mobility and dislocation number due to the development of three-dimensional dislocation clusters.

For low carbon steels with carbon contents below 0.45 % the plastic deformations are almost completely limited to the softer ferrite grains [Chr91].

3.2.3 Influence of the load amplitude

The stress amplitude has a major influence on the fatigue life as well as on the extent and the magnitude of plastic deformations. With increasing stress amplitudes the onset of primary softening is shifted to smaller load cycle numbers and higher plastic strains are reached. The lifetime of the specimens until crack initiation is reduced. For very high load amplitudes [Gon79] found a distinct and sharp maximum in the primary softening behavior which strongly resembled the upper yield limit observed during monotonic testing of unalloyed steels. This peak value could not be observed for smaller stress amplitudes. At smaller stress amplitudes the primary hardening came to saturation whereas for higher load amplitudes the material often hardened until crack initiation.

In order to clarify the discrepancies in the cyclic hardening/softening curves for high and small stress amplitudes [Rei78], [PRMM77] and [Gon79] determined the spatial distribution of plastic deformations by stress-optical measurements during stress-controlled fatigue tests on unnotched specimens. Similar investigations can also be found in [Eif81]. Figure 7 shows two examples obtained for 'high' and 'low' stress amplitudes. For high amplitude loading a germ of a Lüders band develops with the onset of primary softening in the shoulder region of the specimen, where stresses are

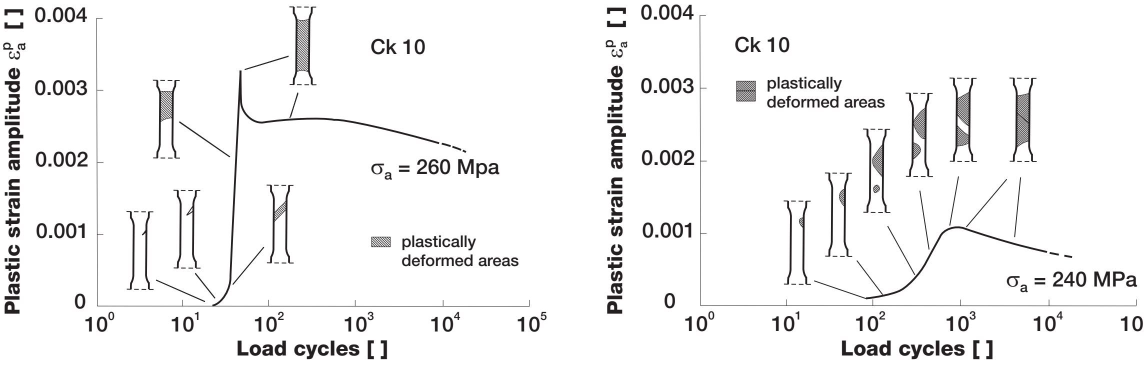

(a) high stress amplitude (b) small stress amplitude

Figure 7: Evolution of plastic deformations for different load amplitudes [Gon79]

slightly increased due to the notch effect. From this initiation point a complete Lüders band develops during the next few load cycles and progresses until the entire mid section of the specimen becomes plasticized. A completely homogeneous elastic-plastic strain state is reached 10 to 50 load cycles after the first initiation. For smaller amplitude loading multiple initiation areas have been found where plastic deformations subsequently set on. Plastic strains may remain inhomogeneous until failure of the specimen. The front lines of these distinct initiation points grow even beyond the phase of global softening. The results demonstrate that even for unnotched specimens cyclic plasticity is governed by localization effects which have to be taken into account for the interpretation of experimental results. [PRMM77] stated that macroscopic strain measurements can only give an insufficient picture of the inhomogeneous plastic deformations. Local plastic strains might become much higher than indicated by the integral values obtained from macroscopic deformation measurements.

3.2.4 Influence of mean stresses

If harmonic testing is performed with a superimposed constant load i.e. with a load ratio $R = \frac{min(\sigma)}{max(\sigma)} \neq -1$ typically both the strain or stress amplitude and the mean stress or mean strain vary during testing. Unalloyed steels exhibit significant cyclic creep (ratchetting) under the influence of mean stresses. The mean strains change strongly with or close to the end of the incubation period and often do not saturate until failure. The strongest permanent changes of the mean strains occur during primary softening [PRMM78]. Therefore the rate of the mean strain increase shows a maximum during the period of primary softening [Gon79]. Positive mean stresses lead to elongation, and negative mean stresses lead to shortening of the specimens. Under the same positive and negative mean stress levels elongation is more pronounced than shortening.

With increasing positive mean stresses it has been found that [Gon79]:

- primary softening sets on earlier
- the plastic strain amplitudes reach higher values
- the lifetime is reduced

[Rei78] conducted stress-controlled cyclic tests on Ck 45 with variable stress amplitudes and superimposed mean stresses. For all tests the maximum applied stress stayed below the static yield limit. Even for relatively small mean stresses a significant rise of the mean strains could be observed for both low and high load amplitudes (figure 8(a)).

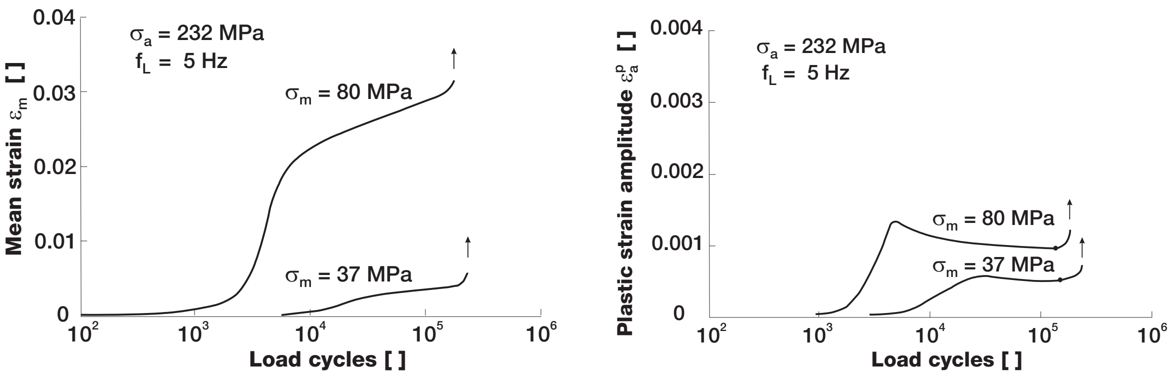

(a) mean strains (b) plastic strain amplitudes

Figure 8: Evolution of the mean strains and plastic strain amplitudes on Ck 45 for constant amplitude loading and varying mean loads [Rei78]

For high load amplitudes ($\sigma_a \approx 0.8 \cdot \sigma_{y,l}$) with low mean stresses ($\sigma_m \leq 0.075 \cdot \sigma_{y,l}$) the superimposed mean stress showed a significant influence on the mean strain evolution during the tests but had only a minor influence on the hardening/softening curve. For higher mean stress levels the influence on the cyclic softening/hardening curve was more pronounced (figure 8(b)). It has been supposed that a critical value of the mean stress level exists, beyond which the superimposed mean stress significantly influences the hardening/softening curve.

3.2.5 Influence of the testing frequency

The influence of the testing frequency on the cyclic material behavior and the fatigue properties is discussed controversially in the literature. [Ste58] gave an early review on the effect of the testing frequency on the fatigue and cyclic properties of different metals and stated an overall weak influence. By contrast [Rei78] and [Eif81] reported a significant influence of the testing frequency during stress-controlled fatigue tests on the cyclic deformation behavior (figure 9(a)) and the specimen fatigue lifetime (figure 9(b)).

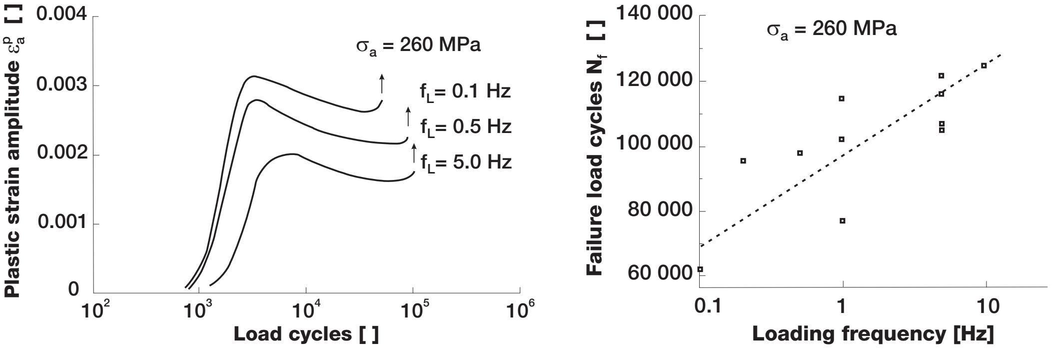

(a) cyclic softening/hardening curves for three different testing frequencies

(b) failure load cycles for different testing frequencies

Figure 9: Influence of the testing frequency on the cyclic deformation behavior of Ck 45 [Rei78]

Two different effects of the testing frequency need to be distinguished. First the plastic deformation of unalloyed steels has been found to be a rate dependent process. For monotonic loading this has been investigated by [Böt02]. A similar rate dependency can also be presumed for cyclic loading. In the frequency range between 0.1 Hz and 10 Hz, [Rei78] and [Eif81] observed that the lifetime of the specimens increased by a factor of about two (figure 9(b)). Compared to higher testing frequencies lower testing frequencies caused

- an earlier onset of primary softening
- an increase of the stabilized level of the plastic strain amplitude
- a reduction of the fatigue lifetime

The effect of different testing frequencies also manifested in the cyclic stress-strain curves obtained at $0.5 \cdot N_f$. In contrast to the findings cited above, [Bil93] concluded based on a series of strain-controlled tests on a low-carbon steel that in the technically interesting range between 1 and 10 Hz no significant influence of the frequency on the cyclic stress-strain-curve could be observed.

The second aspect of the testing frequency, which is often ignored, consists of the temperature rise of the specimens due to dissipative effects. The temperature increase becomes stronger at higher testing frequencies due to the limitations of the heat exchange with the surroundings. The mean temperature eventually reaches values where its effect on the material behavior needs to be taken into account. [Web83] compared the fatigue lifetimes of oil-cooled and uncooled specimens. For uncooled specimens a significant rise of the temperature was reported at the same testing frequency of

37 Hz. Compared to the cooled specimens the lifetime of the uncooled specimens was reduced by a factor of two. Thus temperature can be regarded as an essential influence parameter on the fatigue and cyclic behavior of unalloyed steels which has to be taken into account if results obtained at different loading frequencies are to be compared. However this is widely ignored and rarely any information of the specimen temperature during testing is given in the literature.

[Gon79] showed for stress controlled tests that the testing frequency had significant influence on the evolution of the mean stresses. He explained his finding by the influence of the testing frequency on the plastic strain amplitude. This assumption has been supported by results obtained under plastic strain control. In this case the evolution of the mean strains became independent of the testing frequency.

3.2.6 Influence of the control mode

As outlined before either stress, total strain or plastic strain can be used as a control variable during cyclic testing. In order to investigate the influence of the different control modes [Rei78] compared Wöhler curves obtained for normalized Ck 45 under stress, total strain and plastic strain control. The different Wöhler diagrams were transformed into one single Wöhler diagram where all test results fell close together. [Rei78] proposed to use the total strain amplitude at $0.5 \cdot N_f$ to compare the individual test results and concluded that the test results obtained with the different control modes can be regarded as equivalent. However this equivalence can only be assumed for the saturation behavior whereas for the initial softening phase significant discrepancies are to be expected. [Eif81] conducted cyclic tests under total strain and stress control on normalized 42CrMo4 which reconfirmed the findings of [Rei78]. In the quasi-saturated regime at $0.5 \cdot N_f$ the Wöhler curves constructed for testing under total strain control and under total stress control can be converted into each other so that the results of both control modes fall close together.

3.2.7 Influence of load changes

The characteristics of the cyclic material behavior given above are strictly valid only for single step testing for which the controlled parameter, i.e. the stress or strain amplitude, is kept constant during the entire test. Realistic loading conditions are often more complex and typically show strong variations in maximum load, mean load and frequency.

[Rei78] conducted stress controlled cyclic testing with a change of the stress amplitude at constant mean stress level. He found that after changing the stress amplitudes the plastic strain amplitudes quasi instantaneously saturated at levels corresponding to those obtained for a single step test (figure 10(a)). An additional change of the imposed mean stress had no influence on the further evolution of the cyclic hardening/softening curve. By contrast the change of the stress amplitude strongly influenced the mean strain evolution. A change of the stress amplitude from low to high levels caused a strong increase of the mean strain whereas a change from high to low levels had no influence.

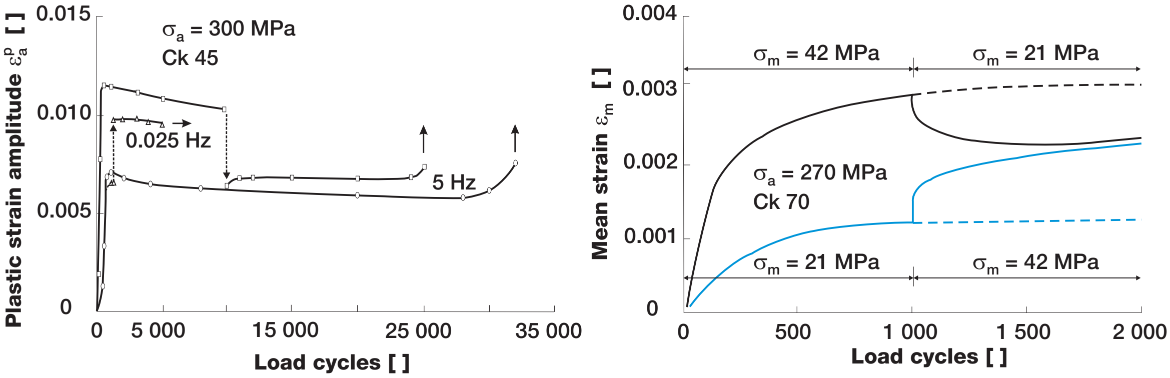

(a) change of the load amplitude [Rei78]

(b) change of the mean stress [Gon79]

Figure 10: Influence of load changes on the cyclic softening/hardening behavior

The increase or decrease of the mean stress level for constant stress amplitudes caused a corresponding elongation or shortening of the specimens, even if the mean stresses were only changed within tensional or compressional mean loading. [Gon79] noticed that the mean strain levels obtained during testing with variation in the applied mean stress level did not match the results of a single-step test with a constant mean stress level 10(b). The results of [Rei78] show that the differences in the saturated mean strains become more pronounced the later the mean stress level is changed.

Comparing testing frequencies of 0.025 Hz and 5 Hz [Rei78] noticed for both frequencies a characteristic saturation level of the plastic strain amplitude. For a frequency change during the tests from 0.025 Hz to 5 Hz and vice versa the plastic strain amplitudes quickly adjusted to the corresponding saturation level.

Specimens which had been subjected to a preceding monotonic tension test above the monotonic yield limit $\sigma_{y,l}$ showed a pronounced back-deformation i.e. a reduction of the mean strain during subsequent cyclic loading with $\sigma_a < \sigma_{y,l}$. An applied plastic strain below 2% during monotonic loading had only minor influence on the subsequent saturation of the cyclic hardening/softening curve, but cyclic softening occurred more homogeneously after a monotonic plastic deformation ([Rei78]).

3.2.8 Influence of the carbon content and heat treatment

[Gon79] tested different unalloyed steels under normalized conditions with varying carbon contents ranging from 0.01 % to 1.0 % i.e. from hypoeutectoid ferritic to hypereutectoid pearlitic steels. The contiguity of the cyclic material behavior and the carbon content was not unique so that further influences, particularly from the microstructure were assumed. Some general trends can be inferred from the test results. They indicate that the carbon content influences:

- the duration of the incubation interval
- the shape of the hardening/softening curve
- the cyclic stress strain curve at $0.5 \cdot N_f$
- the fatigue lifetime upon initiation of a macrocrack

Pearlitic steels require higher stress amplitudes for the initiation of the primary softening and tend to deform more homogeneously than prevailing ferritic steels. For both types of steels plastic deformations are primarily bound to the softer ferrite. Based on the assumption that dislocation behavior in bound ferrite (pearlite) and in pure ferrite are similar [Gon79] concluded that the cementite lamellae must have significant influence on the average run length and the length of the dislocations within the ferrite lamellae. Consequently higher stress amplitudes are needed for the initiation of plastic deformations in pearlitic steels.

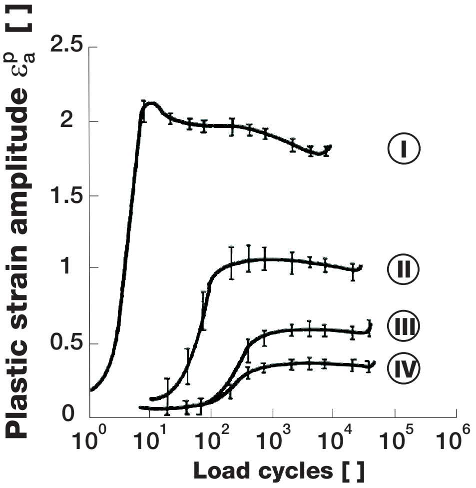

Ck 70
σ_a =340 MPa

	I	II	III	IV
cooling rate @700°C [K/s]	0.015	0.28	0.52	1.05
$\sigma_{P0,2}$ [MPa]	326	420	465	465
σ_u [MPa]	685	805	865	870
lamella spacing [μm]	61	44	39	27

Figure 11: Influence of the cementite lamella spacing on the cyclic deformation behavior of Ck 70 [Gon79]

To clarify the influence of the cementite lamellae on the cyclic behavior, normalized steels with different cooling rates were compared (figure 11). The influence of the cooling rate increased with increasing carbon content which has been attributed to the overall influence of the cooling rate on the development of the ferrite-cementite microstructure. The spacing between the cementite lamellae has been found to have an especially strong influence on the cyclic behavior. Softening becomes more pronounced for steels with coarse cementite lamellae. For low carbon steels the influence of the cooling rate arises mostly from its influence on the average grain size. Steels with larger grain sizes show an earlier and more pronounced softening behavior. [Böh85] compared the cyclic deformation behavior of normalized Ck 45 at different tempered states obtained by hardening in a salt melt. For the tempered specimens a completely different macroscopic cyclic deformation behavior was found (figure 11) which was characterized by successive cyclic softening until crack initiation. From the findings [Böh85] concluded that in the tempered state plasticity must be heterogeneously distributed with very high local plastic strains and large areas of exclusively elastic behavior.

3.2.9 Influence of stress concentrations

The fatigue behavior of complex components with stress concentration is strongly governed by the processes within the geometric notches. For strong geometric notches plastic deformations remain concentrated to the regions with the highest stresses. For HCF the location of later crack initiation is generally predetermined by the notch. With increasing notch sharpness the ratio between the number of load cycles at the first crack initiation and the total fatigue lifetime N_f becomes smaller. This means that crack initiation sets on earlier and crack growth and propagation become more important for the fatigue behavior of sharper notched components.

Even within the geometric notches plastic deformations might be strongly inhomogeneous and localized [Böh85]. Additionally the characteristic dislocation structure found during fatigue experiments on unnotched specimens is less pronounced or completely absent even in the close vicinity of the notch so that plasticity becomes more irregular [Böh85]. The elastic-plastic deformations around the stress concentrations are more complex than those of unnotched specimens. First the stress field in the vicinity of the notch is multiaxial which complicates the direct comparison of the local material behavior to the results obtained from uniaxial tests. Second - once plastic deformations set on in the notch - stresses are more and more transferred to the inner parts of the specimen, where the material still behaves linear-elastic. This relieves stresses from the notch and causes a residual stress field within the specimen. Accordingly the linear-elastic shape factor which gives the ratio between the maximum principal stress within the notch and the nominal stress loses its validity. [TK83] showed on specimens loaded in bending that the reduction of the effective stress amplitudes due to stress redistributions resulted in an increase of the fatigue lifetime compared to uniaxial tested specimens tested with the same nominal stress amplitudes. [Böh85] showed by strain gauge measurements in geometric notches on specimens of Ck 45 with different shape factors, that the softening behavior is slower than for unnotched specimens. For the investigated shape factors the entire cyclic material behavior was dominated by cyclic softening. The occurrence of cyclic hardening of the material within the notch could not be verified. By measurements with multiple strain gauges it was found that softening occurs heterogeneously within the notch.

3.2.10 Chapter summary and conclusion

In the preceding chapter a summary of the cyclic material behavior of low carbon steels under load-controlled testing in the high cycle fatigue regime has been given and the influence of various factors has been discussed. The results show that the cyclic behavior and the onset of plastic strains are closely linked to the fatigue behavior but are strongly influenced by the specific loading conditions. For low carbon steels plastic deformations are concentrated to the ferrite grains or ferrite phases. Accordingly heat treatment and microstructure strongly influence the softening and hardening behavior. Besides the microstructure the load amplitude, the load rate, the testing frequency and the mean load can be identified as the most important influence factors. By contrast the control mode during testing has been found to be of minor importance as long as the saturation values are compared.

The cyclic behavior of mild steels under stress-controlled loading is characterized by cyclic softening and hardening which occur in different stages of the fatigue process. With increasing fatigue lifetime and decreasing load levels plastic strains become strongly heterogenous. Under non-zero mean stresses mild steels show a strong tendency to cyclic creep (ratchetting) so that significant mean strains evolve. The magnitude of the mean strains can exceed significantly those of the plastic strain amplitudes. Changes of the loading conditions during testing leads to a corresponding change of the associated material response without that the values obtained in a single-step test are generally achieved. Within geometric notches the onset of plastic deformations causes changes of the local stress exposure which depend on the softening behavior itself and thus become rather complex. The transfer of the cyclic material behavior determined at unnotched specimens to the specific situation at the notch bottom is therefore rather questionable.

4 Review of the governing equations and derivation of the heat equation

4.1 Definitions

4.1.1 Reference frame and material derivative

The intention of the following chapter is to present an outline of the theoretical background of thermomechanical phenomena as basis for the following numerical and experimental investigations. The focus is laid rather on a brief but complete overview than on a strict mathematical derivation. All derivations presented here are based on [LC90], [KH95], [Par03] and [MF05].

Consider a reference body $\mathfrak{B}$ of arbitrary size and shape with a finite volume V of a deformable solid whose specific material properties are defined later on. $\mathfrak{B}$ is surrounded by an exterior universe $\mathfrak{U}$ from which different mechanical, chemical, thermal etc. influences act on it. The boundary of $\mathfrak{B}$ is the surface membrane $\mathfrak{A}$ which allows for specific exchange phenomena between $\mathfrak{B}$ and $\mathfrak{U}$ to be defined later. $\mathfrak{B}$ is assumed to be composed of individual discrete particles P_k. The original position of each particle P_k at the reference time t_0 is given by its unique position vector $\vec{X}_k$. Unless noted otherwise a single global cartesian coordinate system with a fixed origin O is assumed.

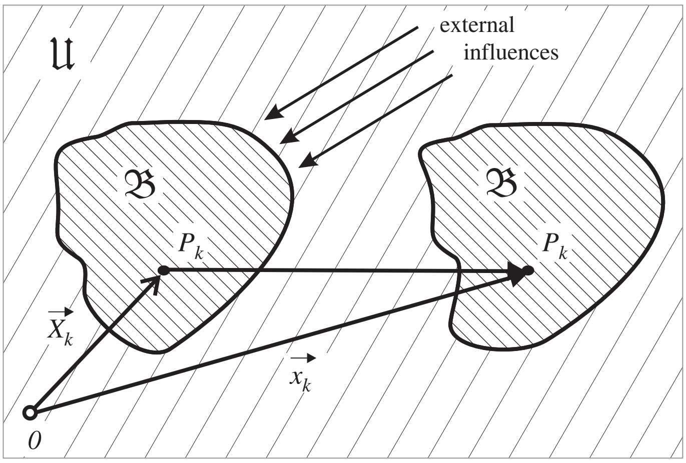

Figure 12: Reference body

At an instance $t \neq t_0$ the body has moved through the universe $\mathfrak{U}$ and has been deformed with respect to its original state. The location of a particle P_k is now given by the current position vector $\vec{x}_k$. The velocity of the material particles P_k is given as the derivative of their current position with respect to time:

$$\vec{v}_k = \frac{d\vec{x}_k}{dt} \tag{2}$$

For a representation in Lagrangian coordinates the original position $\vec{X}_k$ of a specific particle P_k and the time are chosen as independent variables. Therefore the velocity vector is given as:

$$\vec{v}_k = \vec{v}_k(\vec{X}_k, t) = \frac{\partial \vec{x}_k}{\partial t} \tag{3}$$

which defines the current velocity of each individual particle identified by its reference position vector $\vec{X}_k$. For the alternative Eulerian representation the time dependent position of a material point $\vec{x}_k(t)$ and the time are chosen as variables. In this case the velocity vector is given as:

$$\vec{v}_k = \vec{v}_k(\vec{x}_k, t) \tag{4}$$

Equation (4) defines the velocity of a particle which is currently passing through a fixed point in space. Both coordinate representations are equivalent, but the choice of the representation has influence on the formulation of the constitutive laws.

The total derivative or material derivative will be assigned to the operator $\frac{d}{dt}$ which indicates that the calculations are performed for an individual particle. For the Lagrangian representation the material derivative is identical to the partial derivative with respect to time, whereas for the Eulerian representation the time dependency of the current position $\vec{x}_k$ needs to be considered. For the Eulerian representation the material derivative is defined for any arbitrary scalar or tensor-valued function $f(\vec{x}_k, t)$ through:

$$\frac{df(\vec{x}_k, t)}{dt} = \frac{\partial f(\vec{x}_k, t)}{\partial t} + \frac{\partial f(\vec{x}_k, t)}{\partial \vec{x}_k}\vec{v} \tag{5}$$

As an example the derivative of the velocity vector with respect to time gives the acceleration of the material points. The Lagrangian definition of the acceleration is given through:

$$\vec{a}_k = \frac{d\vec{v}_k(\vec{X}_k, t)}{dt} = \frac{\partial \vec{v}_k}{\partial t} \tag{6}$$

since the reference position $\vec{X}_k$ of the material particles is independent of time. By contrast the time dependency of the current position $\vec{x}_k$ needs to be taken into account if the Eulerian representation is adopted so that the acceleration is given by:

$$\vec{a}_k = \frac{d\vec{v}_k(\vec{x}_k, t)}{dt} = \frac{\partial \vec{v}_k}{\partial t} + \frac{\partial \vec{v}_k}{\partial \vec{x}_k}\frac{\partial \vec{x}_k}{\partial t} \tag{7}$$

The particle subscripts '$_k$' will be omitted from now on.

4.1.2 Einstein' summation convention

For the sake of simplicity and clarity the Einstein' summation notation is used as an alternative to the tensor or vector representation. For the original form of the summation convention subscript and superscripts are used to distinguish between co- and contravariant tensor representation. Here this difference is neglected for simplicity and only subscripts are used. Accordingly expressions with two equal indices are generally to be summed and are consumed during the summation. Expression with more than two equal indices are not allowed for the Einstein' summation notation and are therefore expressed by a summation sign. Unless noted otherwise all indices run from 1 to 3 which will not be repeated for every equation. For matrices and tensors the first and the second index symbolize the row and the column, respectively. With these definitions one has:

$$\sum_{i=1}^{n} c_i x_i = c_i x_i \qquad i = 1, 2, 3 \tag{8}$$

and

$$b_i = \sum_{i=1}^{n} c_{ij} x_j = c_{ij} x_j \qquad i = 1, 2, 3 \tag{9}$$

4.1.3 Transport and divergence theorem

During the following derivations frequent use is made of basic principles which are repeated for convenience and completeness. It is assumed that the finite volume V of $\mathfrak{B}$ varies with respect to time, so that $V = V(t)$. Reynold's transport theorem states that for any steady function $f(\vec{x}, t)$ defined inside $\mathfrak{B}$ the following expression holds:

$$\frac{d}{dt}\int_V f(\vec{x}, t)dV = \int_V \frac{\partial f(\vec{x}, t)}{\partial t} dV + \oint_{\partial V} f(\vec{x}, t) v_j n_j dA \tag{10}$$

Equation (10) describes the variation of $f(\vec{x}, t)$ due to the change in volume and transport across the boundaries of $\mathfrak{B}$. In equation (10) $\vec{n}$ is an outward pointing normal unit vector and $\vec{v}$ is the velocity in the direction of $\vec{n}$. $\oint$ represents a surface integral which has to be evaluated over the surface ∂V of the varying body volume. The application of Gauss' divergence theorem allows to convert the surface integral on the right hand side of (10) into a volume integral:

$$\int_V \frac{\partial f(\vec{x}, t)}{\partial t} dV + \oint_{\partial V} f(\vec{x}, t) v_j n_j dA = \int_V \left[\frac{\partial f(\vec{x}, t)}{\partial t} + \frac{\partial \left(f(\vec{x}, t) v_j\right)}{\partial x_j}\right] dV \tag{11}$$

4.2 Balance principles

4.2.1 Conservation of mass

It is assumed that the mass of $\mathfrak{B}$ at a given time t is continuously distributed over V with a specific density function $\rho(\vec{x}, t)$. The entire mass of $\mathfrak{B}$ is given as:

$$M = \int_V \rho dV \tag{12}$$

The conservation of mass demands that no mass is destroyed or created within V. Therefore the material derivative of the mass must be equal to zero:

$$\frac{dM}{dt} = \frac{d}{dt} \int_V \rho dV = 0 \tag{13}$$

Using (10) and (11) the conservation of mass results in:

$$\int_V \left[\frac{\partial \rho}{\partial t} + \frac{\partial(\rho v_j)}{\partial x_j} \right] dV \tag{14}$$

Alternatively (14) can be rewritten in local form as:

$$\frac{\partial \rho}{\partial t} + \frac{\partial(\rho v_j)}{\partial x_j} = 0 \tag{15}$$

4.2.2 Conservation of momentum

Through the interaction with its surroundings the body $\mathfrak{B}$ is subject to various mechanical forces. It is distinguished between volume forces $\vec{f}$ given per unit mass and surface forces $\vec{t}$. The track forces are given per unit area as the projection of the Cauchy stress tensor $\boldsymbol{\sigma}$ with a unit normal vector $\vec{n}$. According to Newton the rate of change of the total momentum of all mass particles contained in $\mathfrak{B}$ is equal to the vectorial sum of all external forces. Additionally the shape of the deformable body $\mathfrak{B}$ will be altered by the presence of the track forces. The conservation of total momentum p_i for a deformable body is given as:

$$\frac{dp_i}{dt} = \frac{d}{dt} \int_V \rho v_i dV = \int_V \rho f_i dV + \oint_{\partial V} \sigma_{ij} n_j dA \tag{16}$$

Reynold's transport theorem (10) is used to rewrite the left hand side of (16) as:

$$\frac{d}{dt} \int_V \rho v_i dV = \int_V \frac{\partial(\rho v_i)}{\partial t} dV + \oint_{\partial V} (\rho v_i) v_j n_j dA \tag{17}$$

Now (11) is applied to rewrite the surface integrals in equations (16) and (17) which yields the global representation of the conservation of momentum:

$$\int_V \left[\frac{\partial(\rho v_i)}{\partial t} + \frac{\partial(\rho v_i v_j)}{\partial x_j} - \rho f_i - \frac{\partial \sigma_{ij}}{\partial x_j} \right] dV = 0 \tag{18}$$

or in local form as:

$$\frac{\partial(\rho v_i)}{\partial t} + \frac{\partial(\rho v_i v_j)}{\partial x_j} = \rho f_i + \frac{\partial \sigma_{ij}}{\partial x_j} \tag{19}$$

A similar conservation law needs to be satisfied for the moment of momentum. It can be shown that the conservation of the moment of momentum requires a symmetric stress tensor $\boldsymbol{\sigma}$ which will be presumed from now on without limiting the validity of the following derivations.

4.2.3 Balance of kinetic energy

The balance of kinetic energy of a deformable body evolves as a consequence of the conservation of momentum. In analogy to the kinetic energy of a rigid body $E_{kin} = \frac{1}{2}M\vec{v}^2$ the balance of kinetic energy of a deformable body is given in terms of $\frac{1}{2}\rho\vec{v}^2$. For the derivation the local form of the conservation of momentum (19) is multiplied with the velocity vector $\vec{v}$:

$$v_i \frac{\partial(\rho v_i)}{\partial t} + v_i \frac{\partial(\rho v_i v_j)}{\partial x_j} = v_i \rho f_i + v_i \frac{\partial(\sigma_{ij})}{\partial x_j} \tag{20}$$

The product rule is used to express the two terms on the left hand hand side:

$$\begin{aligned} v_i \frac{\partial(\rho v_i)}{\partial t} + v_i \frac{\partial(\rho v_i v_j)}{\partial x_j} &= v_i^2 \left(\frac{\partial \rho}{\partial t} + \frac{\partial(\rho v_j)}{\partial x_j} \right) + \rho v_i \left(\frac{\partial v_i}{\partial t} + v_j \frac{\partial v_i}{\partial x_j} \right) \\ &= \frac{1}{2}\frac{\partial}{\partial t}(\rho v_i^2) + \frac{1}{2}\frac{\partial}{\partial x_j}(\rho v_i^2 v_j) - \frac{1}{2}v_i^2 \frac{\partial \rho}{\partial t} - \frac{1}{2}v_i^2 \frac{\partial(\rho v_j)}{\partial x_j} \\ &= \frac{\partial}{\partial t}(\frac{\rho}{2}v_i^2) + \frac{\partial}{\partial x_j}(\frac{\rho}{2}v_i^2 v_j) \end{aligned} \tag{21}$$

where the conservation of mass (15) has been used. Next the left hand side of (20) is replaced by expression (21).

The global balance of the kinetic energy is obtained by integrating (20) over the entire volume of $\mathfrak{B}$ which yields:

$$\begin{aligned} \frac{d}{dt}\int_V (\frac{\rho {v_i}^2}{2}) dV &= \int_V \left[\frac{\partial (v_i \sigma_{ij})}{\partial x_j} - \sigma_{ij}\frac{\partial v_i}{\partial x_j} + v_i \rho f_i \right] dV \\ &= \oint_{\partial V} v_i \sigma_{ij} n_j dA - \int_V \sigma_{ij}\frac{\partial v_i}{\partial x_j} dV + \int_V v_i \rho f_i dV \end{aligned} \tag{22}$$

For the formulation of the kinetic energy (22) use has been made of:

$$v_i \frac{\partial}{\partial x_j}(\sigma_{ij}) = \frac{\partial}{\partial x_j}(v_i \sigma_{ij}) - \sigma_{ij}\frac{\partial v_i}{\partial x_j} \tag{23}$$

and

$$\begin{aligned} \frac{d}{dt}\int_V \frac{\rho}{2}{v_i}^2 dV &= \int_V \frac{\partial}{\partial t}(\frac{\rho}{2}{v_i}^2) dV + \oint_{\partial V} \frac{\rho}{2}{v_i}^2 v_j n_j \, dA \\ &= \int_V \left[\frac{\partial}{\partial t}(\frac{\rho}{2}{v_i}^2) + \frac{\partial}{\partial x_j}(\frac{\rho}{2}{v_i}^2 v_j) \right] dV \end{aligned} \tag{24}$$

4.2.4 Conservation of energy and first principle of thermodynamics

One of the most fundamental physical principles is the conservation of energy. It is based on extensive experimental observations and states that energy can never be destroyed but can only be transferred from one form into another. Depending on the form of energy involved in a given problem the conservation of energy can involve mechanical, thermal, magnetic, electrical, chemical and other types of energy. Without going into further detail a pure thermomechanical problem is considered here. It is assumed that the total energy of $\mathfrak{B}$ can solely be changed by heat flow through the boundaries of $\mathfrak{B}$, by volume and surface forces acting on $\mathfrak{B}$ from its surrounding $\mathfrak{U}$ and by internal heat conversion due to radiation, chemical reactions etc. The total energy E_{tot} of $\mathfrak{B}$ is given as the sum of the internal energy E_u and kinetic energy E_{kin}:

$$E_{tot} = E_{kin} + E_u \tag{25}$$

The expression for the kinetic energy E_{kin} was derived in the prior section. The internal energy E_u is formally represented by the specific internal energy $u = u(\vec{x}, t)$ so that equation (25) can be written as:

$$E_{tot} = \int_V \frac{\rho {v_i}^2}{2} dV + \int_V \rho u dV \tag{26}$$

If the heat flow $\vec{q}$ through the boundaries of $\mathfrak{B}$ and the specific internal heat generation r e.g. due to chemical processes are considered the rate of the total energy E_{tot} can be expressed as:

$$\frac{d}{dt}\int_V \rho(\frac{{v_i}^2}{2}+u)dV = -\oint_{\partial V} q_j n_j dA + \oint_{\partial V} v_i\sigma_{ij}n_j dA + \int_V v_i\rho f_i dV + \int_V \rho r dV \quad (27)$$

The balance of the internal energy (the first law of thermodynamics) is obtained if the expression for the kinetic energy (22) is subtracted from (27):

$$\frac{d}{dt}\int_V \rho u dV = -\oint_{\partial V} q_j n_j dA + \int_V \sigma_{ij}\frac{\partial v_i}{\partial x_j}dV + \int_V \rho r dV \quad (28)$$

Using (10), (11) and the conservation of mass (15), equation (28) is rewritten as:

$$\int_V \rho\left[\frac{\partial u}{\partial t}+\frac{\partial(uv_j)}{\partial x_j}\right]dV = -\oint_{\partial V} q_j n_j dA + \int_V \sigma_{ij}\frac{\partial v_i}{\partial x_j}dV + \int_V \rho r dV \quad (29)$$

which represents the integral form of the first law of thermodynamics. In contrast to the total energy neither the kinetic nor the internal energy are conserved quantities. The application of the product rule, the conservation of mass (15) and the definition of the material derivative (5) allows to rewrite equation (28) as:

$$\int_V \rho\frac{du}{dt}dV = -\oint_{\partial V} q_j n_j dA + \int_V \sigma_{ij}\frac{\partial v_i}{\partial x_j}dV + \int_V \rho r dV \quad (30)$$

or in local form as:

$$\rho\frac{du}{dt} = -\frac{\partial q_j}{\partial x_j} + \sigma_{ij}\frac{\partial v_i}{\partial x_j} + \rho r \quad (31)$$

4.2.5 Second principle of thermodynamics

The second principle of thermodynamics takes into account the direction of energy transformation, which cannot be described solely by the conservation of energy. The second principle of thermodynamics introduces the absolute temperature T and the entropy S as additional field variables. The entropy S of $\mathfrak{B}$ is defined through the specific entropy s per unit mass as:

$$S = \int_V \rho s dV \quad (32)$$

The entropy can be physically interpreted as the disorder of the thermodynamic system under consideration. The second principle of thermodynamics states that the rate of entropy production must always be greater than or equal to the entropy production due to pure heating:

$$\frac{dS}{dt} = \frac{d}{dt}\int_V \rho s dV \geq \int_V \frac{\rho r}{T} dV - \oint_{\partial V} \frac{q_j n_j}{T} dA \tag{33}$$

For the hypothetical case of reversible processes the inequality simplifies to an equality. Using (10), (11), the conservation of mass (15) and the definition of the material derivative (5) allows to reexpress the left hand side of equation (33) as:

$$\int_V \left[\rho \frac{ds}{dt} + \frac{\partial}{\partial x_j}\left(\frac{q_j}{T}\right) - \frac{\rho r}{T}\right] dV \geq 0 \tag{34}$$

or in local form

$$\rho \frac{ds}{dt} + \frac{\partial}{\partial x_j}\left(\frac{q_j}{T}\right) - \frac{\rho r}{T} \geq 0 \tag{35}$$

4.3 Concept of internal state variables

The formulation of practicable equations of the general thermodynamic concepts introduced in the preceding sections requires us to give up generality to some extent. The concept of state variables allows to introduce more meaningful formulations for the entropy and the internal energy. The concept of state variables postulates that any thermodynamic state of a given system at a given instance and at a given point is completely defined by a finite number of thermodynamic state variables. The current values of the state variables are solely dependent on the momentary state and independent of the way the state has been reached.

The choice of the state variables to be used depends on the nature of the given problem. Once the state variables have been defined, the concept allows to formulate thermodynamically consistent equations for the entire problem. The particular richness and the major weakness of this concept lies in the rather subjective choice of the state variables. In some ways this approach resembles that of a practical engineer who, examining the particular circumstances, needs to make a 'good guess' for loads, simplifications of the mechanical system etc. wherever reliable information is not available. The choice of the state variables allows for a detailed consideration of particular mechanisms of interest for which meaningful and experimentally assessable state variables are defined. By contrast less important phenomena are hidden behind unspecific internal variables.

The state variables define the equilibrium state only and do not take into account dynamic processes. An extension to dynamic processes can be made with the assumption of minor variations around the thermodynamic equilibrium. In this case dynamic processes can be described by a set of successive equilibrium states. Without going too far into the details this assumption is justified for the processes considered here.

Two types of state variables can be distinguished: observable variables which can be directly measured experimentally (e.g. temperature or strain) and internal variables which cannot be assessed in the context of the problem (e.g. the damage state). Generally the state variables are not independent of each other. The functional relationships between the different state variables are the state laws which are obtained by choosing one of the state variables as an independent state function. The constitutive relationship between the individual state variables is then obtained by applying the general laws of thermodynamics.

4.4 Heat equation

4.4.1 Derivation of the general heat equation

The aim is to keep any further representations as general as possible. Therefore only the temperature T is chosen as state variable but all other state variables V_k are still unspecified. In order to derive the specific state laws a thermodynamic potential needs to be defined which describes the energetic state of the thermodynamic system given by $\mathfrak{B}$. For the energetic representation the Helmholtz' free energy Ψ is chosen which is defined through:

$$\Psi = u - Ts \quad or \quad u = \Psi + Ts \tag{36}$$

Based on the choice of the state variables the free energy is solely dependent on the temperature T and further state variables V_k:

$$\Psi = \Psi(T, V_k) \tag{37}$$

Based on (36) the material derivative of the internal energy u is given as:

$$\frac{du}{dt} = \frac{d\Psi}{dt} + \frac{dT}{dt}s + T\frac{ds}{dt} \tag{38}$$

which is inserted into the conservation of energy, equation (30):

$$\int_V \rho \left(\frac{d\Psi}{dt} + \frac{dT}{dt}s + T\frac{ds}{dt} \right) dV = -\oint_{\partial V} q_j n_j dA + \int_V \sigma_{ij} \frac{\partial v_i}{\partial x_j} dV + \int_V \rho r dV \tag{39}$$

Now the internal state variables are used to express the material derivative of Ψ in terms of a variation of the state variables which gives:

$$\frac{d\Psi}{dt} = \frac{\partial\Psi}{\partial T}\frac{dT}{dt} + \frac{\partial\Psi}{\partial V_k}\frac{dV_k}{dt} \tag{40}$$

It is a general finding from thermostatics that:

$$s = -\frac{\partial\Psi}{\partial T}. \tag{41}$$

For the thermodynamic case this formulation can be derived from the Clausius-Duhem inequality. Using (41) the derivative of the specific entropy is given by:

$$\begin{aligned} \frac{ds}{dt} = -\frac{d}{dt}\left(\frac{\partial\Psi}{\partial T}\right) &= -\frac{\partial^2\Psi}{\partial T^2}\frac{dT}{dt} - \frac{\partial^2\Psi}{\partial T\partial V_k}\frac{dV_k}{dt} \\ &= \frac{\partial s}{\partial T}\frac{dT}{dt} - \frac{\partial^2\Psi}{\partial T\partial V_k}\frac{dV_k}{dt} \end{aligned} \tag{42}$$

Inserting (40), (42) and (41) into (39) gives:

$$\begin{aligned} \int_V \rho\left[\frac{\partial\Psi}{\partial T}\frac{dT}{dt} + \frac{\partial\Psi}{\partial V_k}\frac{dV_k}{dt} - \frac{dT}{dt}\frac{\partial\Psi}{\partial T} + T\left(\frac{\partial s}{\partial T}\frac{dT}{dt} - \frac{\partial^2\Psi}{\partial T\partial V_k}\frac{dV_k}{dt}\right)\right] dV = \\ -\oint_{\partial V} q_j n_j dA + \int_V \sigma_{ij}\frac{\partial v_i}{\partial x_j} dV + \int_V \rho r dV \end{aligned} \tag{43}$$

which is the general heat equation with coupling terms depending on V_k. Next the specific heat capacity C is introduced by:

$$C = T\frac{\partial s}{\partial T} \tag{44}$$

The general form of the heat equation (43) is then rewritten as:

$$\int_V \rho C\frac{dT}{dt} dV + \oint_{\partial V} q_j n_j dA = \int_V \left[\sigma_{ij}\frac{\partial v_i}{\partial x_j} + \rho r + \rho T\frac{\partial^2\Psi}{\partial T\partial V_k}\frac{dV_k}{dt} - \rho\frac{\partial\Psi}{\partial V_k}\frac{dV_k}{dt}\right] dV \tag{45}$$

From Fouriers' law of heat conduction one has:

$$q_j = -\boldsymbol{k}\frac{\partial T}{\partial x_j} \tag{46}$$

where $\boldsymbol{k}$ is the heat conductivity tensor. Therefore

$$\frac{\partial q_j}{\partial x_j} = -\frac{\partial}{\partial x_j}(\boldsymbol{k}\frac{\partial T}{\partial x_j}) \tag{47}$$

As mentioned before the stress tensor is symmetric and the overall deformations are considered to be sufficiently small. In this case the deformation term appearing on the right hand side of equation (45) can be rewritten as:

$$\begin{aligned}\sigma_{ij}\frac{\partial v_i}{\partial x_j} &= \sigma_{ij}\frac{1}{2}\left(\frac{\partial v_i}{\partial x_j}+\frac{\partial v_j}{\partial x_i}\right)\\ &= \sigma_{ij}\frac{1}{2}\left[\frac{\partial}{\partial x_j}\left(\frac{\partial w_i}{\partial t}\right)+\frac{\partial}{\partial x_i}\left(\frac{\partial w_j}{\partial t}\right)\right]\\ &= \frac{1}{2}\sigma_{ij}\frac{\partial}{\partial t}\left(\frac{\partial w_i}{\partial x_j}+\frac{\partial w_j}{\partial x_i}\right)=\sigma_{ij}\frac{\partial \varepsilon_{ij}}{\partial t} \qquad (48)\end{aligned}$$

where the strain tensor $\boldsymbol{\varepsilon}$ has been introduced and $\vec{w}$ represents the deformation vector. Now equations (46) through (48) and the divergence theorem (11) are used in equation (45) which is then rewritten in local form as:

$$\rho C\frac{dT}{dt}-\frac{\partial}{\partial x_j}(\boldsymbol{k}\frac{\partial T}{\partial x_j})=\rho r+\sigma_{ij}\frac{\partial \varepsilon_{ij}}{\partial t}-\rho\frac{\partial \Psi}{\partial V_k}\frac{dV_k}{dt}+\rho T\frac{\partial^2\Psi}{\partial T\partial V_k}\frac{dV_k}{dt} \qquad (49)$$

Equation (49) represents the general form of the heat equation, which is still independent of a particular choice of the state variables. The term $\sigma_{ij}\frac{\partial \varepsilon_{ij}}{\partial t}-\rho\frac{\partial\Psi}{\partial V_k}\frac{dV_k}{dt}$ is called the intrinsic dissipation which is associated with the mechanical dissipation plus the evolution of the internal state variables V_k. The term $\rho T\frac{\partial^2\Psi}{\partial T\partial V_k}\frac{dV_k}{dt}$ represents the internal coupling between the temperature field and the state variables V_k.

4.4.2 Heat equation with thermoelastic coupling and plastic dissipation

Up to this point no further assumptions on the nature of the strain tensor $\boldsymbol{\varepsilon}$ have been made. According to the review given in chapter 3 the rate-sensitivity of the cyclic material behavior of low alloy steels is relatively weak in the frequency range between 1 and 20 Hz. For the sake of simplicity rate-independent elastic and plastic deformations are therefore assumed. An additive decomposition of the strain tensor $\boldsymbol{\varepsilon}$ into elastic strains $\boldsymbol{\varepsilon}^e$ and plastic strains $\boldsymbol{\varepsilon}^p$ is assumed. The plastic strains are given as the non-reversible strains which characterize the remaining irreversible deformation after complete loading and unloading of the material.

Plasticity is incorporated by two additional internal variables. Following [LC90] the current state of the material is represented by the internal variable p which is often chosen as the accumulated plastic strain or the dissipated plastic work. Kinematic hardening is associated with the tensor variable $\boldsymbol{\alpha}$. If decoupling between the elastic behavior and the hardening state is assumed, the free energy can be split into:

$$\Psi=\Psi(T,\boldsymbol{\varepsilon}^e,p,\boldsymbol{\alpha})=\Psi^e(T,\boldsymbol{\varepsilon}^e)+\Psi^p(T,p,\boldsymbol{\alpha}) \qquad (50)$$

As an additional restriction only thermoelastic coupling will be considered here, so that all coupling terms associated with Ψ^p can be neglected. This involves the following assumption: the thermoplastic coupling terms associated with the coupling term $\rho T \frac{\partial^2 \Psi}{\partial T \partial V_k} \frac{dV_k}{dt}$ consider the temperature dependency of the hardening variables themselves. For the purpose of all further investigations only small variations of the temperature around the thermal equilibrium will be regarded. The thermoelastic and plasticity-induced temperature variations during one load cycle are assumed to be sufficiently small to neglect higher order plastic coupling effects. The terms associated with the evolution of the internal state variables in the intrinsic dissipation $\rho \frac{\partial \Psi}{\partial V_k} \frac{dV_k}{dt}$ are typically small compared to the plastic work dissipation.

Commonly it is assumed that the ratio between plastic work dissipation and the total intrinsic dissipation β is between 0.8 and 1.0 for metals but might depend on the current hardening state [HRRR00]. During the following investigations the evolution of the hardening parameters will not be regarded, although for future approaches it might be promising to take them into account for damage assessment. However this is beyond the scope of this thesis and will not be discussed further.

With the restrictions made above the Clausius-Duhem inequality is obtained by eliminating the internal heat sources r from the first and second principle of thermodynamics, equations (31) and (35) which yields:

$$\rho T \frac{ds}{dt} - \rho \frac{du}{dt} - \frac{q_j}{T} \frac{\partial T}{\partial x_j} + \sigma_{ij} \frac{\partial v_i}{\partial x_j} dV \geq 0 \tag{51}$$

Based on the specific Helmholtz' free energy Ψ introduced by (36) one gets:

$$\frac{d\Psi}{dt} = \frac{du}{dt} - s\frac{dT}{dt} - T\frac{ds}{dt} \quad or \quad T\frac{ds}{dt} - \frac{du}{dt} = -s\frac{dT}{dt} - \frac{d\Psi}{dt} \tag{52}$$

Reinserting (52) into (51) and using (48) yields the Clausius-Duhem inequality:

$$\sigma_{ij} \frac{\partial \varepsilon_{ij}}{\partial t} - \rho \left(s\frac{dT}{dt} + \frac{d\Psi}{dt} \right) - \frac{q_j}{T} \frac{\partial T}{\partial x_j} \geq 0 \tag{53}$$

With the particular choice of the state variables made earlier one gets:

$$\left(\sigma_{ij} - \rho \frac{\partial \Psi}{\partial \varepsilon^e} \right) \frac{\partial \varepsilon^e_{ij}}{\partial t} + \sigma_{ij} \frac{\partial \varepsilon^p_{ij}}{\partial t} - \rho \frac{dT}{dt} \left(s + \frac{\partial \Psi}{\partial T} \right) - \frac{q_j}{T} \frac{\partial T}{\partial x_j} \geq 0 \tag{54}$$

Now a classical approach allows the derivation of the state laws for thermoelastic coupling. Equation (54) must hold for any specific process. First a process is assumed for which purely elastic deformations ($\varepsilon^p = 0$) take place at a constant and uniform temperature ($\frac{dT}{dt} = 0$ and $\frac{q_j}{T} \frac{\partial T}{\partial x_j} = 0$). This invokes some assumptions about the time scale within which this process takes place which are discussed in [Mau99].

Presuming the general validity of (54) it follows that:

$$\left(\sigma_{ij} - \rho \frac{\partial \Psi}{\partial \varepsilon^e}\right) = 0 \tag{55}$$

Assuming equality (55) to hold, a second deformation process is assumed for which the heat exchange with the surroundings $\frac{q_j}{T}\frac{\partial T}{\partial x_j}$ equals zero and vanishing plastic strains $\varepsilon^p = 0$. Therefore it can be concluded from (54) that:

$$\left(s + \frac{\partial \Psi}{\partial T}\right) = 0 \tag{56}$$

Using the strain decomposition (1), (55) and (56) in the general heat equation (49) gives:

$$\rho C \frac{dT}{dt} - \frac{\partial}{\partial x_j}(\boldsymbol{k}\frac{\partial T}{\partial x_j}) = T\frac{\partial \sigma_{ij}}{\partial T}\frac{d\varepsilon^e_{ij}}{dt} + \sigma_{ij}\frac{\varepsilon^p_{ij}}{\partial t} + \rho r \tag{57}$$

Equation (57) represents the heat equation with thermoelastic coupling terms and mechanical dissipation due to plasticity. It constitutes the basis for the numerical and experimental investigations presented throughout chapters 5 and 6. Note that the elastic coupling term on the right hand side of equation (57) depends on the temperature T and thus poses a nonlinear coupling problem.

4.5 Material models

4.5.1 General requirements

For further analysis and application of equation (57) material models for the elastic-plastic deformation behavior need to be implemented. As described in chapter 3 the cyclic material behavior is rather complex and some restrictions have to be made regarding the phenomena to be included within the material models. The intent of all following investigations is to study how elasticity and plasticity affect the temperature evolution during fatigue loading and to investigate the potential to extract fatigue-related phenomena from infrared measurements. Within this context a rather simple approach is sufficient which models the principal behavior of mild steel under cyclic loading. The following features should be covered by an adequate material model:

1. linear-elastic behavior below the yield limit
2. rate-independent plasticity with kinematic hardening during cyclic plastic deformation

3. an adequate representation of measured stress-strain-hysteresis loops within the stabilized regime
4. easy application in a commercial finite-element-program (ANSYS 10.0) without the need for specific programming

The derivation of the elastic material model is completely reviewed here. By contrast the formulation of a special plasticity model is not within the scope of this thesis, since only the effects of plastic dissipation on the temperature evolution are of interest here. Therefore a rather simple plasticity model has been chosen which is then adjusted to the cyclic saturation behavior measured experimentally.

4.5.2 Elasticity

For the elastic regime homogenous, isotropic material behavior is assumed. In this case the relation between stresses and strains under the influence of temperature changes is described by the general Hooke's law:

$$\varepsilon_{ij}^{e} = \frac{1+\nu}{E}\sigma_{ij} - \left(\frac{\nu}{E}\sigma_{kk} - \alpha\Delta T\right)\delta_{ij} \tag{58}$$

In (58) ν is the Poisson's ratio, α is the coefficient of thermal expansion, δ_{ij} is the Kronecker's delta and σ_{kk} represents the first invariant $\boldsymbol{\sigma}_I = \sigma_{11} + \sigma_{22} + \sigma_{33}$ of the stress tensor. Hooke's law allows one to rewrite the thermoelastic coupling term in (57) in terms of elastic strains or stresses. Here a representation in terms of strains is preferred. Therefore expression (58) needs to be solved for σ_{ij}. Using $\sigma_{kk} = \boldsymbol{\sigma}_I$ and respectively $\varepsilon_{kk} = \boldsymbol{\varepsilon}_I$ yields (compare to [Hus94] for the derivation of the inverse):

$$\sigma_{ij} = \frac{E}{1+\nu}\varepsilon_{ij}^{e} + \left[\frac{E\nu}{(1+\nu)(1-2\nu)}\boldsymbol{\varepsilon}_I^{e} - \frac{E}{1-2\nu}\alpha\Delta T\right]\delta_{ij} \tag{59}$$

The introduction of the Lamé constants

$$\mu = \frac{E}{2(1+\nu)} = G \quad ; \quad \lambda = \frac{E\nu}{(1+\nu)(1-2\nu)} \tag{60}$$

and

$$\beta = \frac{E\alpha}{1-2\nu} \tag{61}$$

allows one to rewrite equation (59) as:

$$\sigma_{ij} = 2\mu\varepsilon_{ij}^{e} + \left(\lambda\varepsilon_{kk}^{e} - \beta\Delta T\right)\delta_{ij} \tag{62}$$

The derivative of (62) with respect to temperature is given as:

$$\frac{\partial \sigma_{ij}}{\partial T} = 2\frac{\partial \mu}{\partial T}\varepsilon^e_{ij} + \left(\frac{\partial \lambda}{\partial T}\varepsilon^e_{kk} - \frac{\partial \beta}{\partial T}\Delta T - \beta\right)\delta_{ij} \tag{63}$$

where the temperature dependence of the material parameters has been taken into account. $\frac{\partial \beta}{\partial T}\Delta T$ becomes negligible which can be verified by a simple order of magnitude check based on the material constants given in appendix I. Using the definition of the Lamé constants (60) the temperature derivatives in expression (63) are rewritten as:

$$\frac{\partial \mu}{\partial T} = \frac{1}{2(1+\nu)}\frac{\partial E}{\partial T} - \frac{E}{2(1+\nu)^2}\frac{\partial \nu}{\partial T} \tag{64}$$

$$\frac{\partial \lambda}{\partial T} = \frac{\nu}{(1+\nu)(1-2\nu)}\frac{\partial E}{\partial T} + \frac{E(2\nu^2+1)}{(1+\nu)^2(1-2\nu)^2}\frac{\partial \nu}{\partial T} \tag{65}$$

Inserting equations (64) and (65) into equation (63) yields:

$$\begin{aligned}\frac{\partial \sigma_{ij}}{\partial T} &= \left[\frac{1}{(1+\nu)}\frac{\partial E}{\partial T} - \frac{E}{(1+\nu)^2}\frac{\partial \nu}{\partial T}\right]\varepsilon^e_{ij} \\ &+ \left[\left(\frac{\nu}{(1+\nu)(1-2\nu)}\frac{\partial E}{\partial T} + \frac{E(2\nu^2+1)}{(1+\nu)^2(1-2\nu)^2}\frac{\partial \nu}{\partial T}\right)\varepsilon^e_{kk} - \frac{E\alpha}{1-2\nu}\right]\delta_{ij}\end{aligned} \tag{66}$$

Note that equation (66) can be directly used in the elastic coupling term of (57) which requires summation over the indices i and j.

4.5.3 Plasticity

The incorporation of plasticity leads to path-dependent non-linear mechanical problems for which the relation between stresses and strains is no longer unique. [LC90] defines plasticity as the mathematical theory of time-independent irreversible deformations. In the context of the classical approach an additive strain decomposition (1) is assumed. The constitutive representation of plasticity requires the definition of:

- a yield criterion
- a hardening law
- a flow rule

The *yield criterion* $f(\sigma, V_k)$ defines the limit function between elastic and plastic deformations. It is generally dependent on the stress tensor and an additional set of scalar or tensor hardening parameters V_k. The yield criterion can be represented by a convex closed yield surface in the six-dimensional stress space, where all stress variations enclosed by the yield surface generate only elastic deformations. All states on the surface represent plastic flow. In classical plasticity theory stress states outside the yield criterion are not permitted.

The *hardening law* describes the evolution of the yield surface $f(\sigma, V_k)$ during plastic flow. The common types are isotropic, kinematic and geometric hardening. Isotropic hardening is modeled by a dilatation of the yield criterion without altering its original shape. Kinematic hardening (e.g. the Bauschinger effect) is modeled by a translation of the yield criterion within the stress space without altering its dimensions or shape. Geometric hardening corresponds to a modification of the shape of the yield surface.

The *flow rule* gives the direction and the magnitude of plastic deformations. It is derived from a plastic potential which in case of associated flow is set to the yield surface itself. In this case plastic deformations are described by an outward pointing normal vector to the yield surface. Within this general framework plastic flow for work hardening materials only occurs if [LC90]:

1. The considered point in the stress state lies on the yield surface, i.e.

$$f(\sigma, V_k) = 0 \tag{67}$$

2. The consistency equation is satisfied during continuous plastic flow

$$df = \frac{\partial f}{\partial \sigma} : d\sigma + \frac{\partial f}{\partial V_k} dV_k = 0 \tag{68}$$

   since states with $f(\sigma, V_k) > 0$ are not permitted in the framework of the classical theory.

Elastic behavior is given for $f < 0$, plastic flow is given for $f = 0$ and $df(\sigma) = 0$ and elastic unloading is given for $f = 0$ and $df(\sigma) < 0$.

The mechanical description of plasticity becomes rather complex in detail and a large number of different models have been proposed in the past. It is not within the scope of this thesis to review or modify any of the different concepts. By contrast the focus here is to apply an existing plasticity model for the simulation of plastic dissipation. For this purpose a rather simplistic plasticity model has been chosen which includes multilinear kinematic hardening. The model is based on a sublayer representation proposed by [Bes58] and is readily implemented in the FE program ANSYS 10.0. The complex elastic-plastic material behavior is modeled by a set of individual sub-portions of a volume element, which are subjected to the same strain but exhibit different elasticity limits. The yield limit of each sub-layer is represented by the van Mises yield criterion which gives a good representation of metal plasticity. Plastic flow occurs if the yield limit of the first sub-layer is reached. The Besseling model allows to give a piecewise continuous representation of any stabilized stress-strain-hysteresis loop which makes it suitable for the simulation of the saturated cyclic elastic-plastic material behavior during fatigue loading of mild steels. The model is adjusted by defining a set of stress-strain points which represent the cyclic elastic-plastic material behavior obtained by 1-D cyclic experiments. A close description of the model can be found in [Bes58]. The adjustment of the model will be described in more detail in chapter 5.

4.6 Chapter summary

The preceding chapter constitutes a brief review of the underlying principles of thermodynamics. For the sake of simplicity a schematic representation of all derivations has been used with the aim to bring the following investigations in a broader theoretical context. The derivation of the principal equations started off with basic principles as the conservation of mass, conservation of momentum and the first and second laws of thermodynamics. It ends with the formulation of the heat equation with thermoelastic coupling and plastic work dissipation which will be treated extensively throughout the next sections. For convenience the main assumptions and restrictions o the derivations are repeated here:

- additive decomposition of the strain tensor
- symmetric stress tensor
- small deformations
- no coupling between elasticity and the hardening state
- independence of all material parameters of the hardening state
- negligible contribution of the evolution of the internal hardening variables to the intrinsic dissipation e.g. full conversion of plastic work into heat

The heat equation can be used to study the general influence of localized plastic flow on the thermal response of a solid body subjected to mechanical loading. Based on the presented review possible starting points for further investigations and for the incorporation of damage models into thermomechanical studies can be identified. In the future the extension of the classical heat equation can eventually be used to e.g. incorporate damage modeling which bears potential for advanced damage assessment by thermographic means.

5 Numerical analysis

5.1 Discussion of the problem

The heat equation (57) with thermoelastic coupling terms and plastic dissipation allows to study thermomechanical coupling phenomena during arbitrary mechanical loading of solids. In the case of complex geometries and/or elastic-plastic material behavior numerical solution procedures are required. The goal of the following investigations is to study a priori how different linear and nonlinear phenomena affect the temperature evolution during harmonic fatigue loading. Since all temperature variations due to thermomechanical coupling are rather small, only the knowledge of the expected coupling phenomena allows to develop specific data processing algorithms for experimental studies.

The numerical investigation of thermomechanical coupling phenomena by standard FE-programs - which is highly recommended for engineering applications - involves some specific problems. Whereas the consideration of unidirectional thermal-mechanical coupling (TMC) can be regarded as standard procedure for engineering applications by now and suitable formulations are available in most commercially available FE-programs, mechanical-thermal coupling (MTC) is still rarely considered due to its overall minor importance for most engineering problems. Therefore the numerical investigation of MTC requires a specialized solution procedure if commercial FE-programs are to be used. The following investigations are based on numerical calculations with the general purpose FE-Program ANSYS 10.0, Multiphysics [ANS05].

Even though thermomechanical coupling is considered here through the rather simple heat equation (57) it involves potential nonlinearities which eventually need to be taken into account:

- the material parameters might depend on the applied stresses and/or the temperature
- the thermoelastic coupling term on the right hand side of equation (57) includes the temperature T so that the magnitude of the coupling term becomes dependent on the temperature variations itself
- the temperature perturbations induced by MTC affect the strain and stress state and thus cause a complex bidirectional coupled problem
- potential nonlinearities arise due to geometric or material nonlinearities of the mechanical problem and the transient effects of heat diffusion

The purpose of the following investigations is to clarify the significance of the different nonlinearities above and whether they need to be taken into account during experimental investigations. The investigations start with the assumption that all nonlinearities have only secondary effects on the temperature variations due to MTC. Then the influence of different nonlinearities on the temperature evolution is studied and discussed.

5.2 Numerical modeling and solution procedure

Initially it will be presumed that at conditions near thermal equilibrium all nonlinear temperature perturbations become small. Consequently the temperature T which appears in the thermoelastic coupling term of equation (57) is replaced by the stabilized temperature T_0. For the linear solution all material properties are treated as constants and set to the values corresponding to the stabilized mean temperature T_0. The justification of this approach will be discussed later.

The numerical approach developed for the studies throughout this thesis is based on a step-by-step procedure based on a mechanical and a thermal model. The solution of the heat equation (57) with thermomechanical coupling includes the following steps:

1. the temporal load variation is subdivided into a number of discrete time steps. For each time step the linear or nonlinear mechanical problem is solved numerically by a standard nonlinear mechanical FE-simulation
2. the local values of the thermoelastic coupling term $T\frac{\partial \sigma_{ij}}{\partial T}\frac{d\varepsilon_{ij}^{e}}{dt}$ and - in case of plastic flow - the plastic work rate are calculated as numerical approximations of the mechanical results
3. the values calculated for the coupling terms are transferred as equivalent heat sources onto a transient thermal model
4. the local temperature evolution for each time step is obtained by solving the transient heat conduction problem based on the thermal model

The implementation of this procedure in any existing FE-program is straightforward without the need for modifications of the existing FE-code. The mechanical and the thermal models are based on available mechanical and thermal element types and share coincident nodes and elements. This allows for direct mapping of the mechanical results onto the corresponding nodes of the thermal model and avoids additional interpolation procedures. Since the overall deformations are small, the thermal problem is solved for the undeformed model i.e. possible effects of the shape variation due to the mechanical loading are neglected. If large deformations are to be expected a geometry update should be implemented for the thermal model.

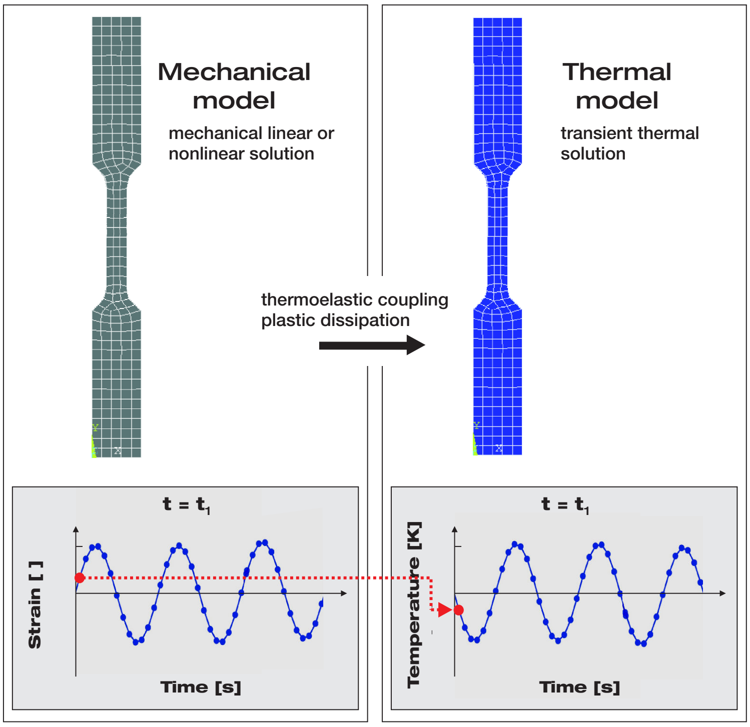

Figure 13: Working principle of the numerical solution procedure

Two different test cases are considered for the present numerical investigations (figure 14). The first test case represents a simple cylindrical specimen referred to as specimen type I (compare figure 75(a) in appendix I). For this specimen geometry loading in the longitudinal direction of the specimen causes a pure 1-D stress state in the center part. The second test case is a mildly notched version of the cylindrical specimen which will be referred to as specimen type II (compare figure 75(b) in appendix I). The notch causes a local stress rise and a 3-D stress state in the center section of the specimen. Making use of symmetry aspects allows to reduce the computation time by using quarter models of the geometries. The mechanical model is based on 10-Node tetrahedral structural solid elements (SOLID92) which are suitable for irregular shaped geometries. The thermal model consists of comparable thermal solid elements (SOLID87).

The numerical solution of equation (57) based on the material models presented in chapter 4 requires the identification of the following thermal and mechanical material parameters:

- the input parameters for the *elastic model* are the isotropic Young's modulus E, the Poisson's ratio ν and - in case of nonlinear behavior with respect to temperature - the temperature dependency $\frac{\partial E}{\partial T}$ and $\frac{\partial \nu}{\partial T}$ of the Young's modulus and the Poisson's ratio
- the adjustment of the *plasticity model* requires the definition of the initial yield

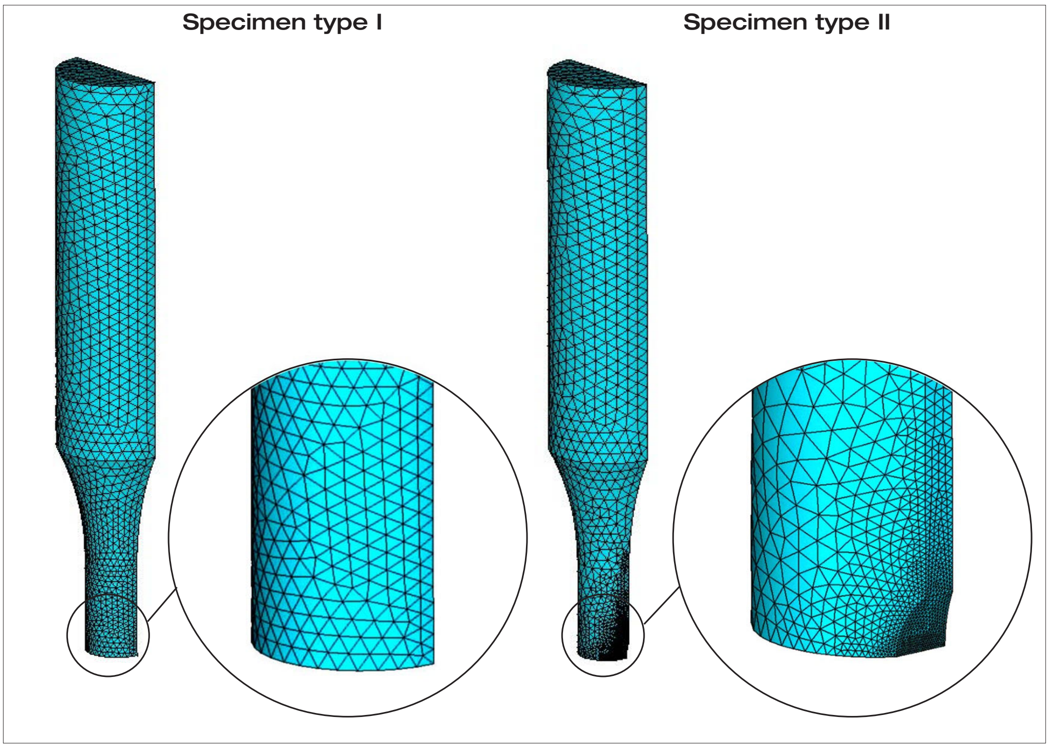

Figure 14: Element meshes for finite element analysis of specimens I and II

limit σ_{y0} and multiple stress-strain points of the stabilized stress-strain hysteresis loops of the 1-D stabilized state

- the *thermal properties* needed are the specific heat capacity C, the thermal conductivity k and the coefficient of thermal expansion α. Additionally the mass density ρ needs to be specified

The values of these parameters have been determined experimentally for the used mild steel S355J2G3. The parameter identification is described in detail in appendix I. For all numerical calculations the material is assumed to be isotropic and homogenous with respect to the relevant material parameters E, ν, k, ρ, C_ε and α.

The boundary conditions for the mechanical and the thermal model have been chosen to match as closely as possible the situation during mechanical testing of the specimens. The circumferential clamping of the specimen due to the hydraulic grips of the testing machine is taken into account by suppressing radial and circumferential displacements of the surface nodes within the clamped section. Prestresses induced by the hydraulic gripping - which act mainly as radial stresses within the clamped section of the specimen - are neglected. They can be regarded as invariant during testing so that their effect on the stabilized thermomechanical coupling becomes negligible. This assumption holds only for the varying part of the temperature evolution which is the primary focus of the following investigations. By contrast the stabilized temperature level itself might depend significantly on the heat exchange.

As an initial condition for the thermal model a uniform temperature of 290 K is assigned to all nodes during the first load step. The nodes associated with the gripped section of the specimen are held at a constant temperature of 290 K during the entire simulation. This accounts for the fact that these parts of the specimen are in direct (metallic) contact to the temperature-controlled hydraulic grips during physical testing. Since only short term low-amplitude variations of the temperature around thermal equilibrium are considered here, any additional heat transfer at the surface of the specimen due to convection and radiation is considered to be negligible.

Mechanical loading is assigned as temporarily varying pressure acting on the upper front surface of the specimen in longitudinal direction. Unless stated otherwise loading is sinusoidal with variable mean stresses, load amplitudes and frequencies. Except for some convergence studies the loading is subdivided into discrete time steps of 1/40 of a complete load cycle. This temporal discretization has been found to be a good trade-off between numerical accuracy and computational costs. The sub-time-steps width for nonlinear or transient calculations is chosen automatically during the iterative solution of each load step.

5.3 Linear thermoelastic coupling

5.3.1 Cylindrical specimen type

First linear thermoelastic coupling under adiabatic conditions, the simplest case, will be briefly investigated. In this case only the linear thermoelastic coupling term and heat conduction within the specimen are included. The applied loading is harmonic and acts in the longitudinal direction of specimen I. This simulates fatigue loading below the elasticity limit of the material. As mentioned before, the stress state is 1-D in the center section of specimen type I and stresses are uniformly distributed. Accordingly thermomechanical coupling causes a uniform harmonic temperature variation within the center section of the specimen. This allows to represent all temperature variations by the values of a single surface point of the specimen. As an introduction to the general coupling behavior figure 15 shows the applied sinusoidal mechanical loading (load ratio $R = -1$) with an amplitude F_a=15 kN and a frequency of f_L=15 Hz, the resulting evolution of the thermoelastic coupling term (also referred to as elastic work rate in the following) and the corresponding temperature variation at a surface point in the central section of specimen type I.

The variation of the thermoelastic coupling term and of the temperature follow the applied harmonic loading. In the adiabatic case, i.e. for negligible heat exchange between the specimen and the surroundings, the thermoelastic coupling term and the

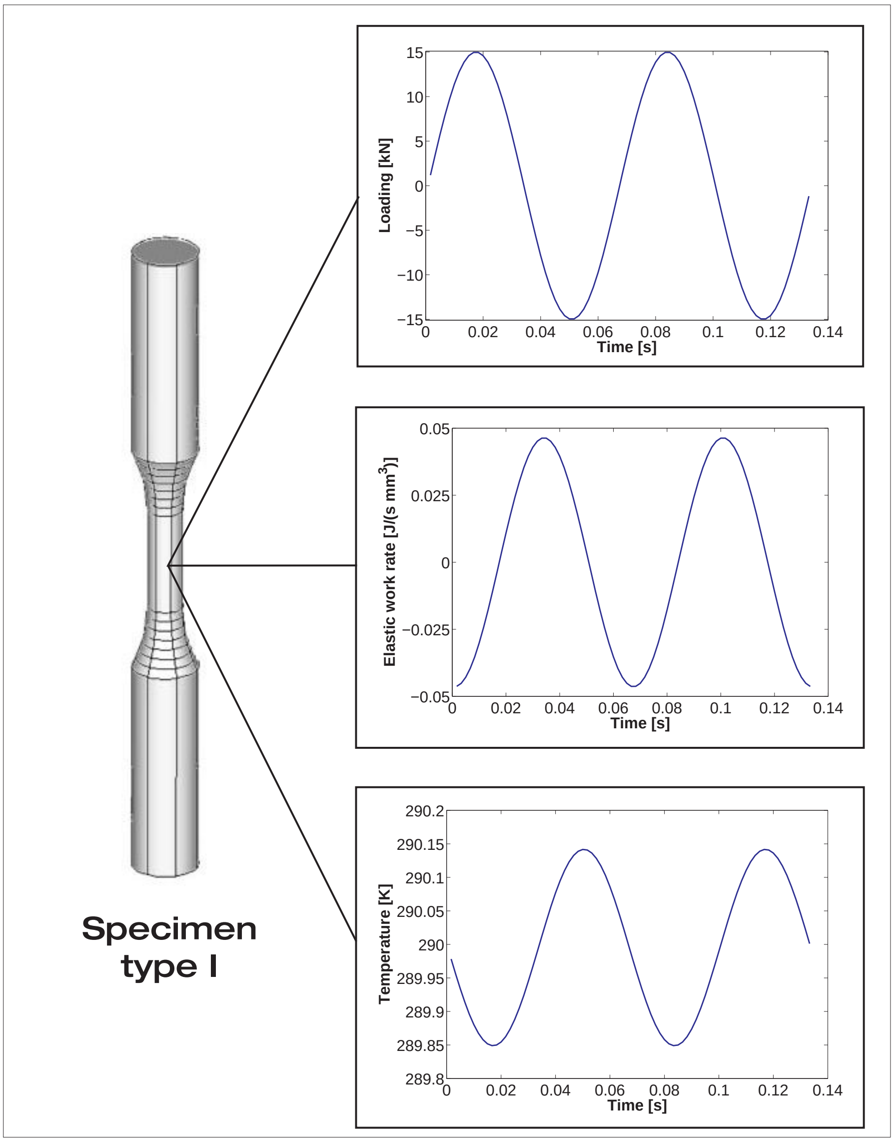

Figure 15: Temporal variation of the mechanical loading, the thermoelastic coupling term and of the temperature at a single surface point in the mid-section of specimen type I, F_a=15 kN, f_L=15 Hz

temperature evolution are shifted by $\pi/2$ and π, respectively to the mechanical loading. Accordingly the temperature drops during tension and rises during compression.

Figure 16(a) gives the calculated thermoelastic temperature amplitudes at a surface point around the equilibrium temperature of 290 K with respect to changes of the load amplitude. The mechanical load is applied at a constant loading frequency of 15 Hz. The diagram shows that the temperature amplitude varies linearly with the load amplitude. Figure 16(b) gives the temperature amplitude at different frequencies f_L but at a constant load amplitude F_a of 15 kN. Obviously the loading frequency has no effect on the temperature amplitude in the investigated frequency range and thus

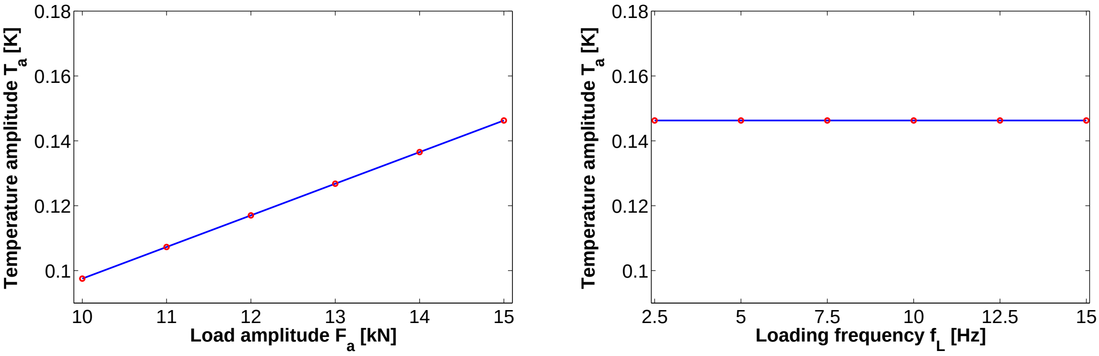

(a) temperature amplitudes vs. loading amplitudes; F_a=15 kN

(b) temperature amplitudes vs. loading frequencies; f_L=15 Hz

Figure 16: Linearity of the thermoelastic temperature variation with respect to loading; specimen type I, F_a= var., f_L= var.

confirms adiabatic conditions within the central part of the specimen. The results demonstrate a direct proportionality of the temperature variations with respect to the applied loading of linear MTC under adiabatic conditions. This proportionality is always implied for quantitative thermoelastic stress analysis and allows to assess the local stresses by measuring the temperature changes during mechanical loading.

5.3.2 Notched specimen type

Within the central section of specimen type I the assumption of adiabatic conditions is fully justified. By contrast stresses are more concentrated for the notched specimen type II (for the specimen geometry refer to figure 75(b) in appendix I) and the stress state becomes 3-D which leads to an overall more complex situation.

Figures 17(a) and 17(b) show the amplitude distribution of the thermoelastic coupling term on the surface of the notched specimen type II subjected to harmonic loading with F_a=15 kN and f_L=15 Hz. The coordinate system chosen for the diagrams is centered in the middle of the notch bottom with the x-axis and y-axis pointing in the longitudinal and transverse direction of the specimen, respectively. According to the stress distribution thermoelastic coupling reaches the highest values in the close vicinity of the notch bottom, whereas at the unloaded etches of the notch the values of the thermoelastic coupling term drop almost to zero. In the nominal cross-section of the specimen the thermoelastic coupling is uniform.

Figures 18(a) and 18(b) show the corresponding spatial distribution of the simulated temperature amplitudes. Under adiabatic conditions the temperature changes would be directly proportional to the thermoelastic coupling term given in figures 17(a) and 17(b). Clearly this is not the case here. Obviously the distribution of the temperature

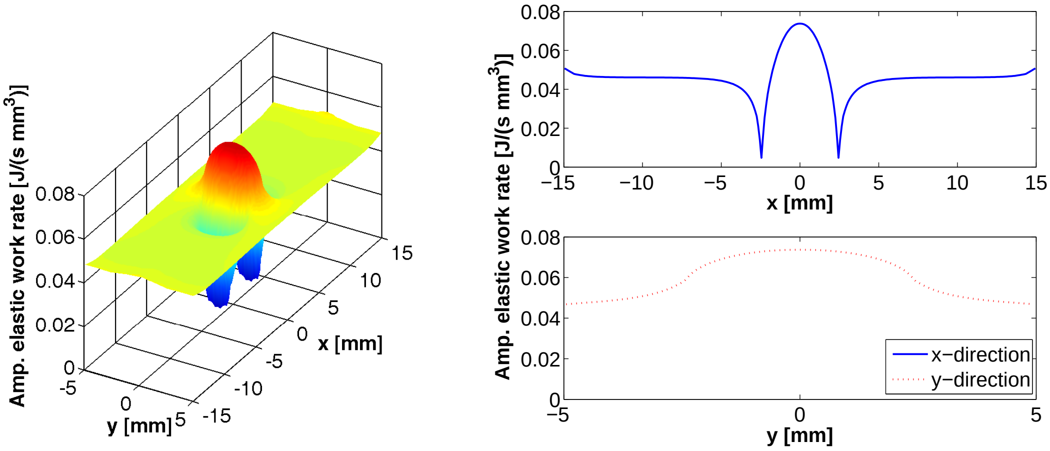

(a) spatial distribution (b) distribution along y=0 and x=0

Figure 17: Distribution of the amplitude of the elastic work rate on the surface of specimen type II, F_a=15 kN, f_L=15 Hz

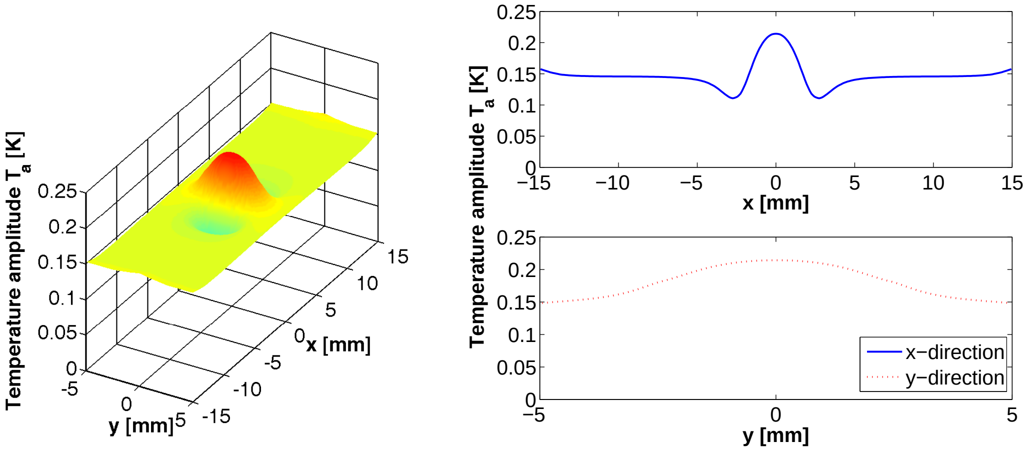

(a) spatial distribution (b) distribution along y=0 and x=0

Figure 18: Distribution of the surface temperature amplitude for specimen type II, F_a=15 kN, f_L=15 Hz

amplitudes appears much more blurred compared to the distribution of the local thermoelastic coupling term. The blurring is caused by the effects of heat diffusion within the specimen. Within the notch heat diffusion leads to a reduction of the temperature amplitudes with respect to the adiabatic (directly proportional) temperature amplitudes. Respectively at the edges of the notch it causes temperature amplitudes which are higher than under adiabatic conditions. The numerical calculations confirm that even for a loading frequency of 15 Hz the temperature variations at the surface of the specimen are still significantly affected by the heat flow within the specimen. Thus the situation at the notch is far from adiabatic conditions. With decreasing loading frequency (load rate) diffusion gains importance so that the temperature distribution becomes more and more blurred. This fact is demonstrated by figures 19(a) and 19(b). Figure 19(a) gives the temperature amplitudes at the central point within the notch of the specimen, obtained for different load amplitudes at a constant load frequency of 15 Hz. Figure 19(b) shows the temperature amplitudes for different frequencies but at constant load amplitude of 15 kN .

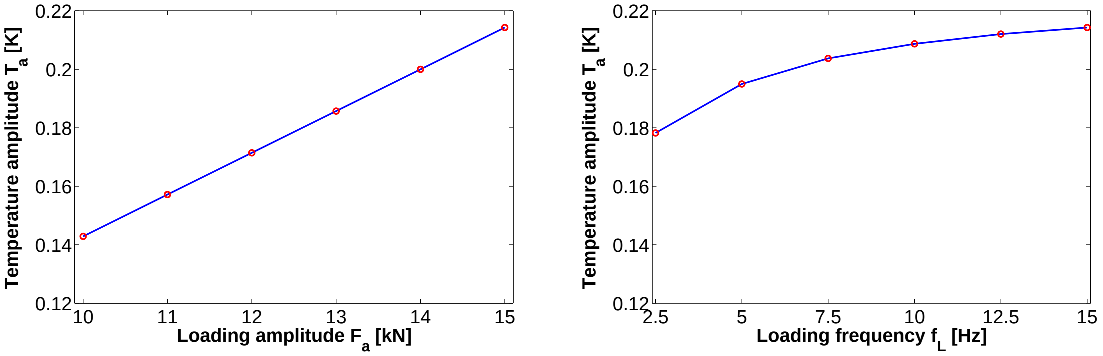

(a) constant frequency f_L=15 Hz, varying loading amplitudes (b) constant load amplitude F_a=15 kN, varying loading frequencies

Figure 19: Temperature amplitude at the central point (x=0, y=0) on the surface of specimen type II, F_a= var., f_L= var.

Under non-adiabatic conditions linearity of the temperature changes is maintained between different load levels as long as the loading frequency is kept constant. By contrast the thermoelastic temperature variations are strongly nonlinear with respect to variations in the loading frequency.

5.3.3 Identification of non-adiabatic conditions

Obviously the direct proportionality of the temperature changes and the local elastic stresses or strains is not preserved for the notched specimen type and the temperature changes become dependent of the applied load rate. Under these conditions heat diffusion must be taken into account for quantitative TSA. Therefore it becomes essential to know where direct proportionality between stress variations and temperature variations can be assumed. Even though until now no reliable method has been found to compensate the surface temperature changes for the effects from heat diffusion the incorporation of further information on the temperature evolution can be used to identify the local loss of adiabatic conditions under complex loading situation and to prevent misleading interpretation of TSA results. It has been reported by [OBBF97] that areas which are strongly affected by heat conduction and loss of adiabatic conditions can be identified by a phase shift of the temperature signal with respect to the (harmonic) mechanical loading. As mentioned earlier the temperature changes under harmonic loading are shifted by π against the mechanical excitation for adiabatic conditions. For the identification of non-adiabatic conditions a relative phase shift $\phi^* = \phi - \pi$ is defined. Assuming a harmonic oscillation of the temperature at a point x, y one has:

$$T(x,y) = T_a(x,y) * sin(2\pi \cdot f_L \cdot t + \phi^*(x,y)) \tag{69}$$

For $\phi^*(x,y) > 0$ and $\phi^*(x,y) < 0$ the harmonic function is shifted to the left or right on the time axis, respectively.

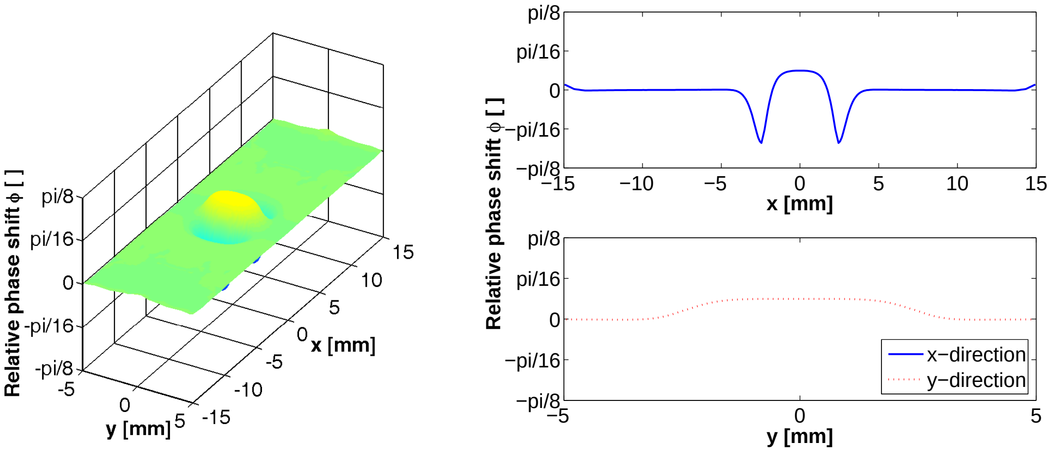

(a) spatial distribution (b) distribution along y=0 and x=0

Figure 20: Distribution of the relative phase shift of the temperature evolution on the surface of specimen type II, F_a=15 kN, f_L=15 Hz

Figures 20(a) and 20(b) show the spatial distribution of the relative phase shift of the temperature evolution and the distribution along the symmetry surface lines x=0 and y=0 for F_a=15 kN and f_L=15 Hz. Areas with lower stresses are marked by a negative relative phase shift. At these points the temperature evolution is shifted to the right on the time axis and stays behind the adiabatic solution. Accordingly the heat flow vector points inwards. Locations of stress concentrations (and loss of adiabatic conditions) are marked by a positive relative phase shift using the given definition. The temperature evolution is shifted to the left on the time axis. Accordingly the temperature evolution is ahead of the adiabatic solution and the corresponding heat flow vector points outwards. To clarify the effect figure 21 compares the temporal temperature evolution for three surface points of specimen II. The diagram validates that temperature evolution at the notch bottom and the edge of the notch are ahead or behind the (adiabatic) solution in the nominal cross-section.

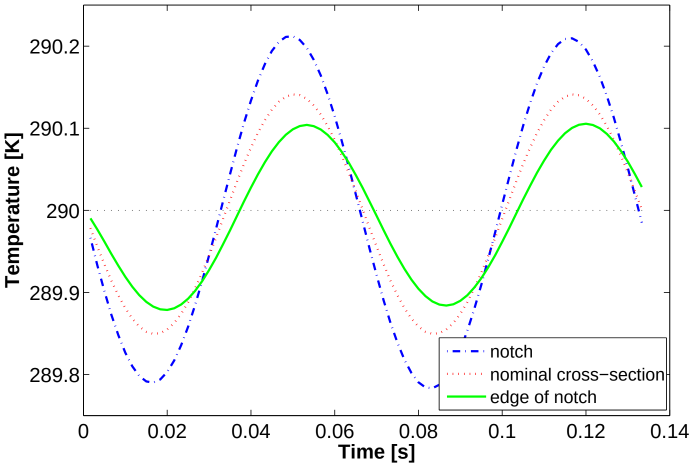

Figure 21: Temperature evolution at different surface points; specimen type II, F_a=15 kN, f_L=15 Hz

5.4 Higher order thermoelastic coupling and nonlinear effects

5.4.1 Discussion of temperature and stress dependency of the material parameters

The most obvious nonlinearity of thermoelastic coupling arises if the material parameters are not constant but depend on the stress state and/or the temperature. Potentially all mechanical and thermal material constants of equation (57) can be altered by mechanical loading and the associated temperature changes. The following consideration refers to thermoelastic coupling with small temperature perturbations in the order of ±0.3 K:

- The variability of the thermal conductivity k is of minor importance since it does not influence thermomechanical coupling itself but only the way the heat is dispersed within the structure.

- The temperature dependency of the bulk density ρ can be easily estimated by an order of magnitude consideration. The density change is directly associated with a volume change, since the contained mass is constant. We assume a temperature variation of 0.3 K around the stabilized temperature T_0 due to thermoelastic coupling. This causes a volume change of $\Delta V/V_0 = 3\alpha\Delta T = 7.9 \cdot 10^{-6}$ which can be neglected. Experimental results concerning the temperature dependency of the density can also be found in [PW05].

- It can be assumed that in the investigated temperature range possible variations of C_ε or C_p mostly result from volume changes due to thermal dilatation which according to the prior explanations become negligible. The minor dependency of the heat capacity on small temperature changes is also demonstrated by the experimental results of [PW05].

- The temperature dependency of the elastic parameters E and ν has been found to be significant for thermoelastic coupling. The experimental determination for the used steel S355J2G3 is discussed in appendix I. The results demonstrate that the temperature dependency of the Poisson's ratio $\frac{\partial \nu}{\partial T}$ is negligible in the range of the room temperature, whereas $\frac{\partial E}{\partial T}$ is pronounced enough to cause a measurable variation of the Young's Modulus even for the small temperature changes considered here.

- Similar to the consideration above the dependency of the density and the heat capacity on the applied stresses can be estimated. The application of mechanical stresses of 300 Mpa causes a volume change of $\Delta V/V_0 = \frac{\sigma}{E}(1-2\nu) = 0.00064$ with the given material parameters. This minor variation of the density and heat capacity due to mechanical loading is considered to be negligible. For the stress dependency of the heat capacity [Dun97] mentions that it is typically two or three orders of magnitude smaller than the stress dependency of the coefficient of thermal expansion α.

- For the present calculations a linear coefficient of thermal expansion α has been assumed. This means that any possible temperature dependency of α has been neglected for the given steel assuming overall small temperature changes. This assumption seems to be justified based on a review of the experimental findings of [PW04] for a comparable steel.
- Based on theoretical considerations [Dun97] mentions that the temperature dependency of the Young's modulus is equivalent to the stress dependency of the coefficient of thermal expansion α. For the nonlinear problem it is therefore sufficient to consider only one of the two effects.

It can be concluded that the only relevant influence on the material properties within the elastic range is to be expected from the temperature dependency of the Young's modulus. Note that for more pronounced changes of the mean temperature e.g. due to plastic dissipation it might indeed be necessary to consider further temperature dependencies and to adjust the values of the material properties according to the actual mean temperature.

5.4.2 Temperature dependency of the Young's modulus

The derivation of the thermoelastic coupling term (66) shows that the temperature dependencies of the elastic parameters E and ν cause a higher order dependency of thermoelastic coupling on the stress state. The occurrence of a higher order dependency was first observed experimentally by [Bel68] and later confirmed by [MSS87b]. The observed nonlinearities have been explained theoretically by [WJS87] and [WSD88]. For some metals as e.g. titanium alloys the higher order dependency is quite pronounced and its evaluation has been proposed for the measurement of residual stresses ([GB99], [GB01]).

The additional terms in equation (66) cause a dependency of the thermoelastic coupling term on the entire elastic strain tensor ε^e_{ij} as well as on the first invariant of the strain tensor $\varepsilon^e_{kk} = \varepsilon^e_I$. The experimental investigations reported in appendix I show that the temperature dependency of the Poisson's ratio $\frac{\partial \nu}{\partial T}$ is negligible around room temperature. By contrast the temperature dependency of the Young's modulus has been found to be significant at approximately $\frac{\partial E}{\partial T} = -76.6\ \mathrm{MPa}/\mathrm{K}$. If $\frac{\partial \nu}{\partial T}$ is set to zero, the thermoelastic coupling term (66) simplifies to

$$\frac{\partial \sigma_{ij}}{\partial T} = \left[\frac{1}{(1+\nu)}\frac{\partial E}{\partial T}\right]\varepsilon^e_{ij} + \left[\left(\frac{\nu}{(1+\nu)(1-2\nu)}\frac{\partial E}{\partial T}\right)\varepsilon^e_{kk} - \frac{E\alpha}{1-2\nu}\right]\delta_{ij} \tag{70}$$

Since the coordinate system for the strains is arbitrary, the axes can be set to the direction of principal strains without losing generality. In this case the strain tensor ε^e_{ij} becomes zero for $i \neq j$. Plugging (70) into the right hand side of equation (57) leaves three distinct thermoelastic coupling terms:

$$\begin{aligned} Term\ \ I \ &: \ T\left(-\frac{E\alpha}{1-2\nu}\right)\dot{\varepsilon}^e_I \\ Term\ \ II \ &: \ T\left(\frac{1}{1+\nu}\frac{\partial E}{\partial T}\right)\varepsilon^e_{kk}\dot{\varepsilon}^e_{kk} = T\left(\frac{1}{1+\nu}\frac{\partial E}{\partial T}\right)\left(\varepsilon^e_{11}\dot{\varepsilon}^e_{11}+\varepsilon^e_{22}\dot{\varepsilon}^e_{22}+\varepsilon^e_{33}\dot{\varepsilon}^e_{33}\right) \\ Term\ \ III \ &: \ T\left(\frac{\nu}{(1+\nu)(1-2\nu)}\frac{\partial E}{\partial T}\right)\varepsilon^e_I\dot{\varepsilon}^e_I \end{aligned} \tag{71}$$

Term I represents the linear thermoelastic coupling used earlier. Terms II and III cause a dependency of thermoelastic coupling on the absolute value of the strain tensor and therefore on the level of mean strains.

The incorporation of the additional terms into the numerical solution procedure requires further consideration. For each time step terms I through III need to be calculated based on the solution of the preceding mechanical solution and provide the heat source terms for the subsequent thermal calculation. The numerical approximation of $\dot{\varepsilon}^e$ is given by the differentiation coefficient $\frac{\varepsilon^i-\varepsilon^{i-1}}{\Delta t}$ which corresponds to a linearized strain rate at time $t_{i-1}+\Delta t/2$, e.g. half way in between time steps i and $i-1$. Terms II and III need to be evaluated based on temporally consistent values. This can be guaranteed if the mean value $\frac{\varepsilon^i+\varepsilon^{i-1}}{2}$ is used for the evaluation of ε^e_I. In order to avoid long transient stabilization phases the mean loading is applied in a preceding mechanical calculation for which the thermal response is not calculated. Otherwise the terms depending on $\dot{\varepsilon}^e$ become unrealistically high at the first time step and provoke a transient behavior.

Figures 22(a) through 22(d) show the variation of the individual thermoelastic coupling terms I through III and the temperature difference between the solution obtained for higher order thermoelastic coupling (terms I through III) with respect to the linear solution (term I only) for a single surface point of specimen I. The specimen is sinusoidally loaded with a load amplitude of 7.5 kN, a loading frequency of 15 Hz and mean loads of -7.5 kN, 0 kN and 7.5 kN. Pretests show that time steps of 1/40 of a load cycle are sufficiently small to provide a converged solution. Note that the magnitudes of coupling terms II and III are three and two orders of magnitude smaller than that of coupling term I, respectively.

As expected term I is not influenced by the variation of the mean load and is equal for all three calculations. For $\sigma_m = 0$ the work rate terms II and III provide additional thermoelastic coupling with a natural frequency of $2 \cdot f_L$ (figure 22(d)). According to [PP03] the thermoelastic coupling at $2 \cdot f_L$ depends solely on the square of the load

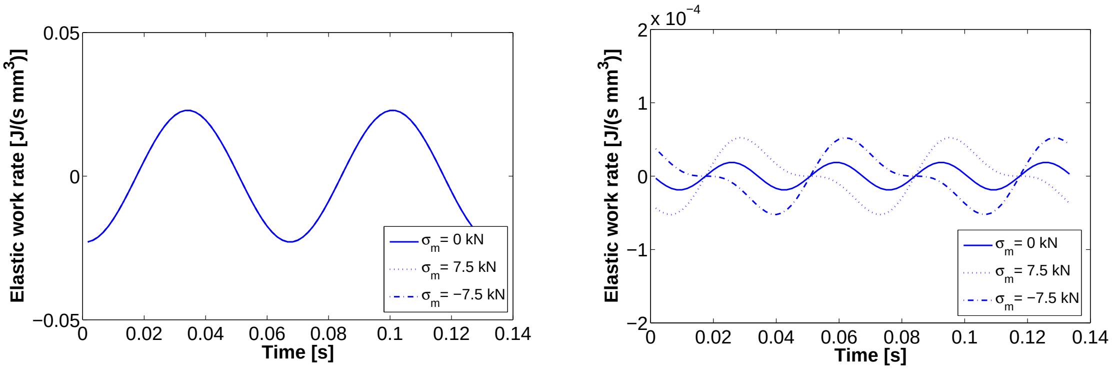

(a) term I (b) term II

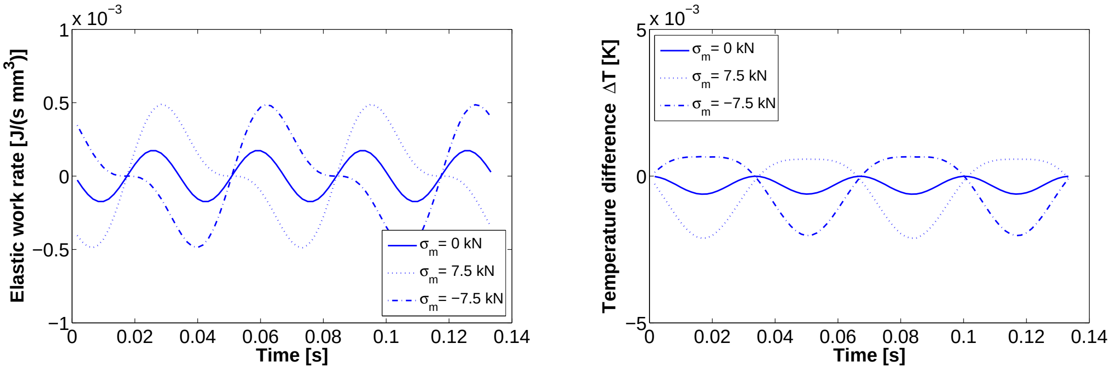

(c) term III (d) temperature difference

Figure 22: Temporal variation of the thermoelastic coupling terms I through III and influence on the temperature signal; specimen type I, F_a=7.5 kN, f_L=15 Hz, F_m=var.

amplitude for the 1-D case and is independent of the applied mean load levels. For $\sigma_m \neq 0$ the coupling terms II and III constitute a superposition of two harmonic oscillations at f_L and $2 \cdot f_L$ (figures 22(b) and 22(c)). The thermoelastic coupling at f_L is dependent on the mean load and the applied load amplitude.

The additional coupling terms alter the temperature variations with respect to the simple linear solution. For $\sigma_m = 0$ terms II and III cause a harmonic temperature variation at $2 \cdot f_L$ which is in the range of 10^{-4} K for the given steel. It is therefore considered to be negligible for the present investigations. For $\sigma_m < 0$ and $\sigma_m > 0$ the consideration of the higher order coupling terms causes a reduction or an increase of the temperature variations at f_L with respect to the temperature evolution at $\sigma_m = 0$.

The dependence of terms II and III on the load amplitude causes a more complex coupling behavior for $\sigma_m \neq 0$ which is still linear with respect to load or mean load changes. By contrast the dependence on the square of the load amplitude leads to nonlinear behavior. Note that in the case $\sigma_m \neq 0$ both, the variation of the load amplitude and the variation of the mean load cause a change of the thermoelastic coupling behavior. Figures 23(a) through 23(d) provide a comparison of the total temperature amplitudes obtained for linear (term I only) and higher order (terms I through III) coupling and the corresponding difference of the temperature amplitudes at f_L and $2 \cdot f_L$ with respect to the linear solution. The results are calculated for a constant mean load of 5.0 kN and sinusoidal loading with different load amplitudes.

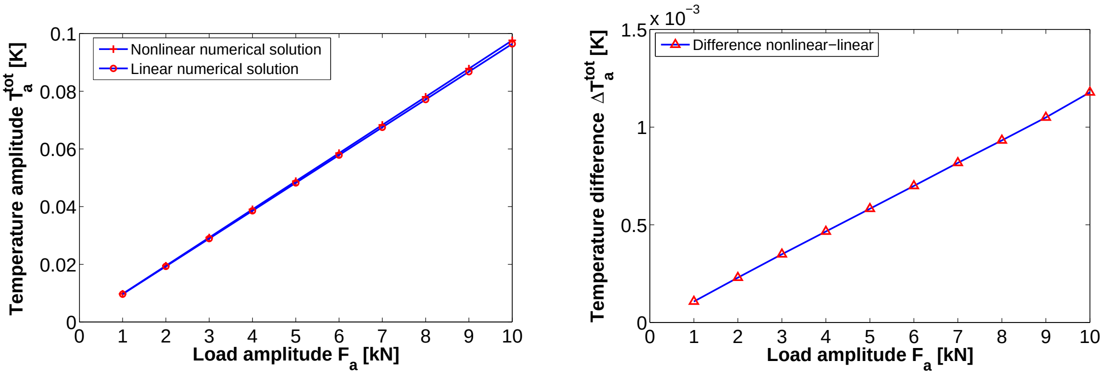

(a) total temperature amplitudes

(b) difference of total amplitudes

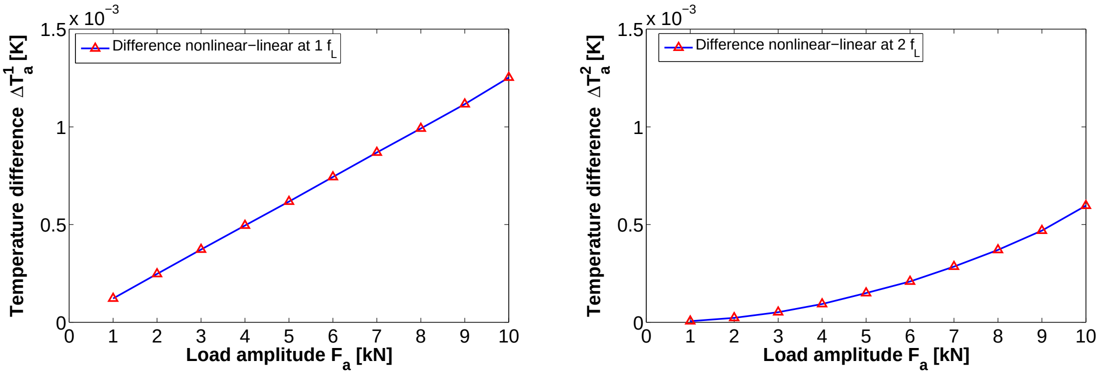

(c) difference of amplitudes at $1 \cdot f_L$

(d) difference of amplitudes at $2 \cdot f_L$

Figure 23: Total and differential temperature amplitudes at f_L and $2 \cdot f_L$; specimen type I, F_a=var., F_m=5 kN, f_L=15 Hz

The difference of the solution with higher order coupling with respect to the linear solution increases with increasing load amplitude. The differences at $2 \cdot f_L$ grow quadratically with the load amplitude (figure 23(d)), whereas the differences at f_L depend linearly on the load amplitude. The comparison of figures 23(b) and 23(c) demonstrates that the additional oscillation at $2 \cdot f_L$ has only minor influence on the total temperature amplitudes. This shows that the contribution of terms II and III at $2 \cdot f_L$ is mainly confined to the appearance of higher harmonics (or nonlinearities for more general loading) whereas the total amplitude of the thermoelastic temperature variations is only slightly influenced.

The results presented above for the center section of the cylindrical specimen type I correspond to the classical extended theory of thermoelasticity introduced by [MSS87b], [WJS87] and [WSD88] and compare well with the analytical solution given for the 1-D stress state by [WJS87]. It can be concluded that for a correct numerical modeling of thermoelastic coupling the temperature dependency of the Young's modulus needs to be taken into account. The results show that for the given steel the quantitative assessment of residual or mean loads and the load amplitude at the same time based on an investigation of thermoelastic coupling becomes difficult. The temperature oscillations at $2 \cdot f_L$ which would allow for a proper quantification of the load amplitude are very small and therefore very difficult to separate experimentally. By contrast the effect of coupling terms II and III on the temperature evolution at f_L is in a measurable range. However here it is not possible to distinguish properly between the effects of the load amplitude and of the mean load at the same time. It can be concluded that higher order coupling due to the temperature dependency of the Young's modulus is significant but the different effects cannot be separated properly during experimental studies.

5.4.3 Temperature dependency of thermoelastic coupling

A further nonlinear effect arises if the dependency of the thermoelastic coupling term on the actual temperature T is taken into account in equation (57). The influence of these nonlinearity can be checked by a simple order of magnitude estimation. As seen before temperature variations around equilibrium due to thermomechanical coupling are typically less than 0.3 K. If one assumes a stabilized mean temperature of 290 K a temperature variation of 0.3 K causes an increase of the thermoelastic coupling term $T \frac{\partial \sigma_{ij}}{\partial T} \frac{d\varepsilon^e_{ij}}{dt}$ by approximately 0.1 %. At maximum load the variation of the coupling term corresponds to an additional temperature change of the order of 10^{-4} K. This is well below the noise limit (currently $\sim$ 20 mK NETD) of commercially available focal plane array (FPA) infrared cameras. Nevertheless one can assume that the signal to noise ratio might be improved substantially by specialized data processing. In this case the quantization of the camera could become the limiting factor. For a 14 bit grey value resolution one has $2^{14} = 16384$ grey values (GV). If it is now assumed that the integration time of the camera and all parameters could be adjusted to allow for an quantization of 10^{-4} K/GV the operating range of the camera would be approximately 10^{-4} K/GV $\cdot$ 16384 GV $=$ 1.6 K. This is impractical for typical testing situations and not realistic for most TSA applications. The outcome of the temperature variation on the thermoelastic coupling term can therefore be neglected without losing much information. Accordingly the stabilized mean value T_0 can be used in the thermoelastic coupling term for numerical analysis and processing of experimental results. However the mean value T_0 can vary considerably experimental investigation due to the variability of the mean temperature or strong thermal gradients within one scene. Based on the estimation above the thermoelastic temperature variations T_a measured or simulated at a temperature T_0 can be scaled to a reference temperature T_0^* by

$$T_a^* = \frac{T_0^*}{T_0} T_a \tag{72}$$

5.4.4 Bidirectional coupling

So far the influences of the thermomechanically induced temperature changes on the stress or strain field have not been taken into account. A short example for the 1-D case allows to check the order of magnitude of possible influences from bidirectional coupling. According to equation (84) given in appendix I the thermoelastic temperature changes in the 1-D stress state under adiabatic conditions are given through

$$\rho C_p \frac{dT}{dt} = -T_0 \alpha \frac{d\boldsymbol{\sigma}_I}{dt} \tag{73}$$

with $\boldsymbol{\sigma}_I = \sigma_{11}$ based on a coordinate system in the direction of the principal stresses. With the material parameters for the given steel a change of the stress state of 300 MPa provokes a temperature drop ΔT of approximately -0.23 K. If in a first step the influence of the temperature on the strains is neglected (e.g. using the decoupled approach as before), the strains due to mechanical loading with $\sigma = 300$ Mpa are directly obtained by Hooke's law (58) as

$$\boldsymbol{\varepsilon}^{\boldsymbol{e}} = \begin{pmatrix} \frac{\sigma}{E} & 0 & 0 \\ 0 & -\frac{\sigma\nu}{E} & 0 \\ 0 & 0 & -\frac{\sigma\nu}{E} \end{pmatrix} \tag{74}$$

and therefore $\boldsymbol{\varepsilon}_I^{\boldsymbol{e}} = 0.00064$ using the material values given in appendix I. Next it is assumed that thermal dilatation can occur without affecting the stress state so that the temperature change of $\Delta T =$ -0.23 K causes a change of the first invariant of the strain tensor of $\Delta \boldsymbol{\varepsilon}_I^{\boldsymbol{e}} = 3\alpha\Delta T = -6.1 \cdot 10^{-6}$. The change of the strain invariant due to thermal strains is therefore about 1 % of the original mechanical strain invariant. Based on this simple example one can expect that decoupling leads to an error in the range of a few mK with respect to the fully coupled problem. This means that the expected influence on the temperature evolution is one order of magnitude higher than that of the temperature dependency of the thermoelastic coupling term discussed earlier.

Since the effect of bidirectional coupling seems to be relatively large compared to other nonlinear effects, bidirectional coupling is numerically studied in more detail here. For this purpose the temperature changes obtained from thermomechanical coupling are transferred back as temperature loads onto the mechanical model during the numerical

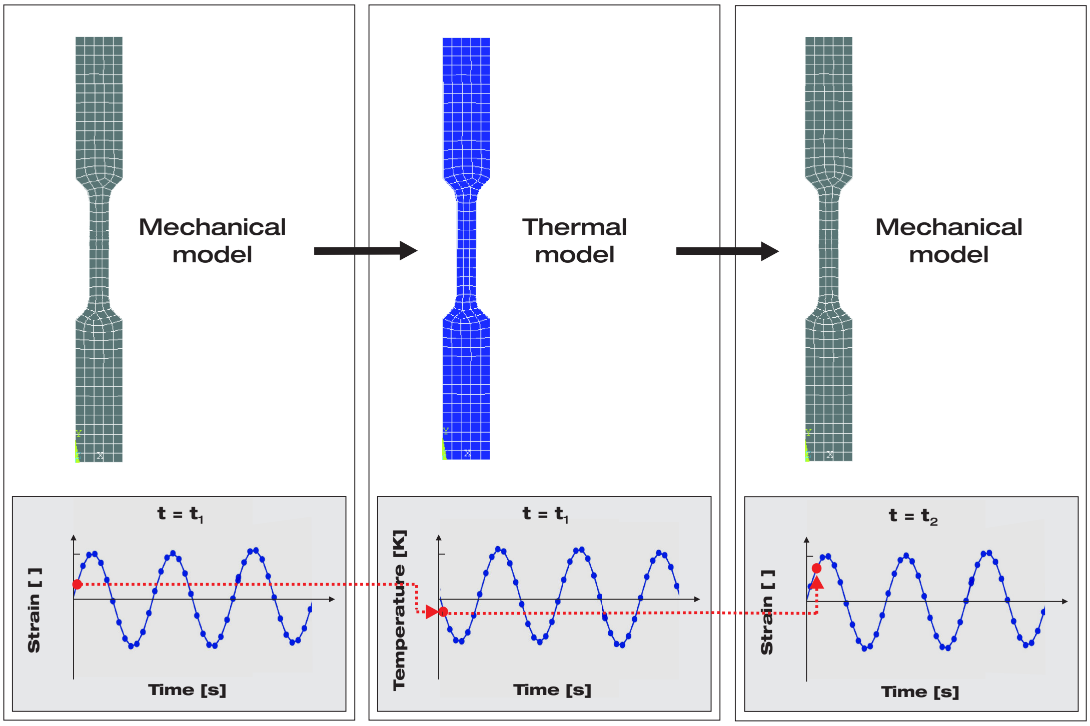

Figure 24: Numerical simulation procedure for bidirectional coupling

simulation (figure 24). Since the bidirectional coupling effects are rather weak, it is assumed that the utilization of the temperature values obtained at the last time step provides an accurate approximation of the coupled solution using sufficiently small time step sizes.

Figure 25 gives the temperature difference between the bidirectional coupled and the unidirectional coupled (decoupled) linear problem obtained for different time step sizes. As before these values represent a surface point of specimen type I under reversed loading with a load amplitude of 15 kN at a loading frequency f_L=15 Hz. The nonlinear solution can be regarded as converged for time steps smaller than 1/80 of an entire load cycle. Under adiabatic conditions the difference signal (which represents the effects of bidirectional coupling on the thermoelastic temperature variations with respect to the linear solution) has the same natural frequency and phase as the applied mechanical loading. The temperature variations caused by thermoelastic coupling cause a strain or stress field which acts against the applied mechanical loading. The result is an apparent stiffening of the specimen.

Figure 26(a) shows the temperature amplitudes obtained for the coupled and the decoupled model for different load amplitudes at a constant loading frequency of 15 Hz where the same material parameters have been used for both models. Figure 26(b) gives the temperature amplitudes for a variation of the loading frequency at a constant load amplitude. Figures 26(c) and 26(d) show the corresponding differences between

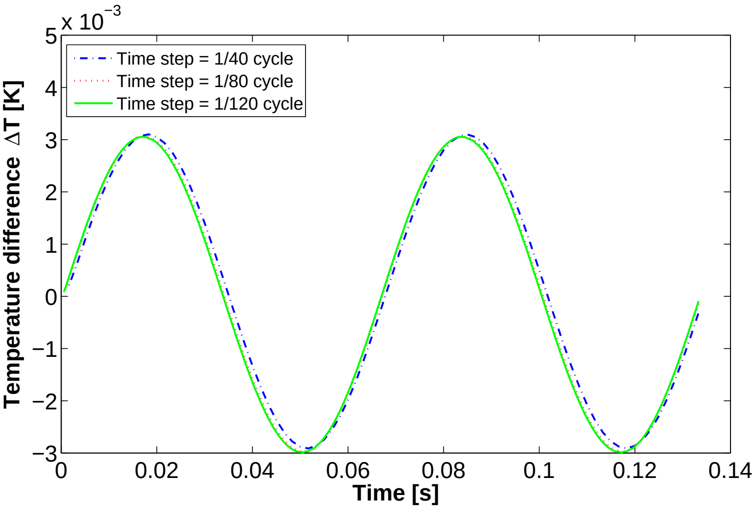

Figure 25: Temperature difference between the thermoelastic temperature variations of a linear decoupled model and coupled model; specimen type I, F_a=15 Hz, f_L=15 Hz

both models. All solutions have been obtained for load stepping with $1/80$ of a load cycle which assures convergence of the solution. The results demonstrate that with the same material parameters the coupled model results in temperature amplitudes which are about 1.8 % smaller than those obtained for the decoupled model. Figures 26(c) and 26(d) show that under adiabatic conditions the differences of the temperature amplitudes vary linearly with respect to changes in the load amplitude and are not influenced by changes of the load frequency. This demonstrates that the consideration of bidirectional coupling results in a linear reduction of the thermoelastic coupling term with respect to the decoupled problem if the material parameters for both approaches are taken as their quasi-static values. By contrast the results obtained from the decoupled and the coupled problem become equivalent if either the coefficient of thermal expansion is reduced for the decoupled approach or alternatively if the Young's modulus is increased for the coupled approach. As a consequence bidirectional coupling would explain differences in the values of the Young's modulus and the coefficient of thermal expansion obtained for quasi-static and dynamic experiments.

For the present studies the coefficient of thermal expansion has been determined by examination of the temperature changes under dynamic loading (compare appendix I). The evaluation of the coefficient of thermal expansion is based on a linear decoupled theory. Therefore the resulting coefficient of thermal expansion already takes into account the effect of bidirectional coupling and needs no further modification in order to give quantitatively correct results if the decoupled numerical approach is applied.

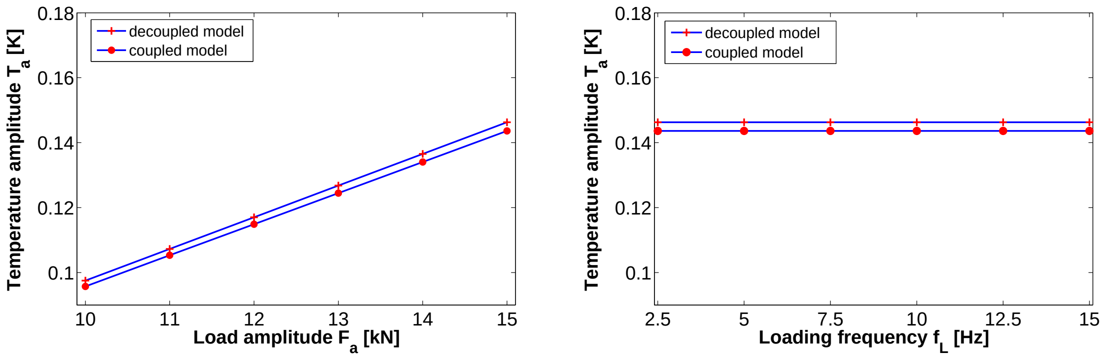

(a) temperature amplitudes vs. load amplitude; f_L=15 Hz

(b) temperature amplitudes vs. load frequency; F_a=15 kN

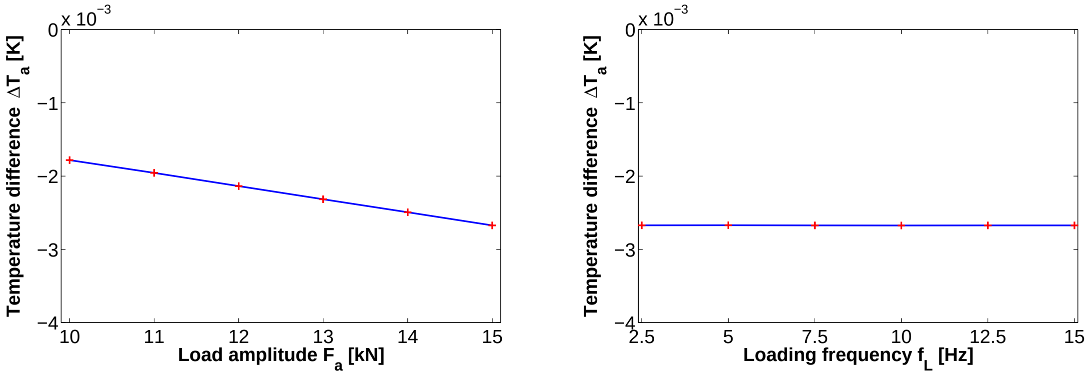

(c) difference of temperature amplitudes vs. load amplitude (coupled-decoupled); f_L=15 Hz

(d) difference of temperature amplitudes vs. load frequency (coupled-decoupled); F_a=15 kN

Figure 26: Temperature amplitudes of the bidirectional and the unidirectional coupled model with respect to the linear variation in load amplitude and load frequency (a, b). Differential temperature amplitudes between the coupled and decoupled model (c, d); specimen type I, F_a=var., f_L=var.

5.5 Plasticity

5.5.1 General remarks

In the past the effect of cyclic plasticity onto the temperature evolution during mechanical loading has been primarily investigated under the aspect of the mean temperature rise due to plastic dissipation. Evidence has been found [Yan03b] that the rise of the surface temperature during fatigue testing allows to quantify the dissipated mechanical energy, if the heat exchange of the test specimen with its surrounding is properly taken into account. By contrast almost no investigations have been made with respect to the local changes in the thermomechanical temperature evolution due to the (local) onset of plasticity. Numerical simulations provide a suitable tool to study the effects of plasticity on the temperature evolution in detail and thus help to understand the underlying mechanisms. The focus of the following investigations has been put on a phenomenological representation of plasticity and on a study of the effects of plasticity on the local temperature evolution. Additional finesses as a thermodynamical motivated representation of damage processes etc. are considered to be beyond the scope of this thesis and might be motivation for further research.

5.5.2 Experimental determination of the cyclic stress-strain behavior

The purpose of the elastic-plastic material model used for the following numerical investigations is to provide an adequate representation of the saturated cyclic stress-strain behavior during load controlled fatigue testing of mild steels at zero mean stress. The adjustment of the model is based on experimental results of the cyclic material behavior obtained during fatigue tests on the cylindrical specimen type I. The preparation of the specimens for cyclic testing is described in appendix I. Testing was performed in the setup described in appendix II with sinusoidal fully reversed single-step loading (load ratio $R = -1$). The tests were terminated by the failure of the specimens. In order to prevent excessive self-heating during testing, the loading frequency was set to 2.5 Hz. This relatively low frequency guaranteed that the temperature increase at all tested load amplitudes was less than 10 K with respect to the initial temperature $T_0 \approx 290$ K. During testing the grips of the testing machine were temperature stabilized by a constant water flow at $T_{in} \approx 290$ K. The load amplitudes varied between ≈ 220 Mpa and ≈ 275 Mpa so that only elastic strains occurred during the first load cycles before the onset of primary softening. The strains in the nominal section of the specimen were integrally measured by a strain gauge with a grid length of 20 mm. An additional unloaded strain gauge applied to a piece of the same steel has been used to compensate the Wheatstone bridge for temperature influence. The reference gauge has been attached to the middle section of the specimens by a heat conductive paste (compare figure 27). During the tests the load signal and the corresponding strains have been recorded by a National Instruments 1520-SCXI data acquisition card. In order to reduce the amount of data, interrupted sampling was used so that only two hysteresis loops were acquired every 100 load cycles.

Figure 28(a) summarizes the hysteresis loops obtained at $0.5 \cdot N_f$ for the individual specimens which are assumed to represent the saturated behavior of the steel. For further evaluation of the cyclic behavior, elastic and plastic strains need to be separated. If an additive strain decomposition is used one has:

$$\varepsilon^p = \varepsilon^{tot} - \sigma/E; \tag{75}$$

The plastic strain amplitude ε^p_a is then obtained as one half of the variability of plastic strains between the turning points of the hysteresis loop given by σ_{max} and σ_{min} (see

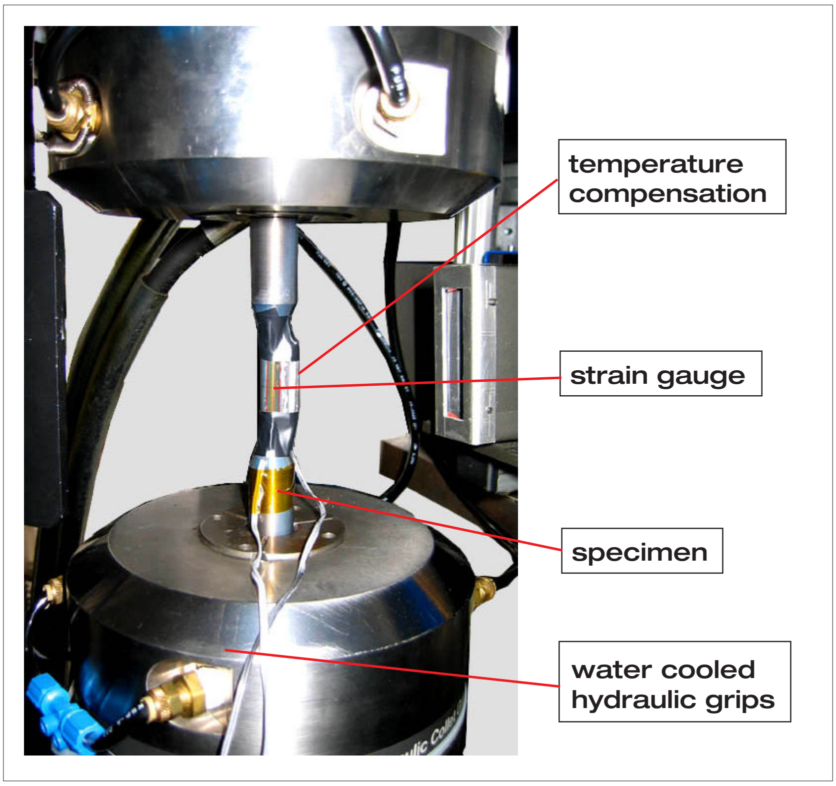

Figure 27: Experimental setup for determination of cyclic material behavior

figure 5). The elastic strain amplitude is given by $\varepsilon_a^e = \sigma_a/E$. Different possible choices for the value of the Young's modulus arise in equation (75):

1. the Young's modulus is assumed to remain constant during the entire test and can thus be set to the original value obtained during the first (elastic) load cycle. In this case the plastic strains obtained from the individual hysteresis loops remain independent of the Young's modulus but might not correspond exactly to the true plastic strains observed during the individual load cycles

2. alternatively the Young's modulus can be reevaluated for each hysteresis loop. In this case the plastic strains are determined correctly but the evolution of plastic strains becomes dependent on the changes of the Young's modulus

3. since often slightly different Young's modula are observed during tension and compression, an additional choice has to be made whether the correct direction dependent Young's modulus or a mean value of the compressional and tensional modulus is to be used

At a first glance the evaluation of the plastic strains based on an updated Young's modulus seems to be the most accurate approach. However this choice invokes some problems concerning the adjustment of the material model. The updated Young's modulus depends on the hardening state and consequently cannot be treated as a constant value. Therefore its variability on the plastic strains needs to be taken into account during modeling. For complex geometries with localized plasticity this leads to a non-uniform distribution of the Young's modulus. In order to avoid this problem during numerical modeling, the original Young's modulus obtained during the first (elastic) load cycle is used to calculate the strain decomposition (75).

The evaluation of the experimental results shows that the mean Young's modulus calculated from the cyclic tests corresponds well to the Young's modulus of 214300 Mpa which has been obtained from tension tests reported in appendix I. Therefore the elastic strains in equation (75) are calculated based on the mean Young's modulus of 214300 Mpa for all specimens. Figure 28(b) shows the cyclic stress-strain curve which is constructed from the stabilized plastic strain amplitudes ε_a^p obtained for the individual specimens at different stress amplitudes σ_a. Based on the results a cyclic yield limit of approximately 210 Mpa can be estimated below which no plastic deformations are to be expected at a continuum scale. Therefore σ_{y0} corresponds to the stress limit below which the material remains elastic even after an infinite number of load cycles. If stress amplitudes are above σ_{y0}, softening occurs during the course of applied loading.

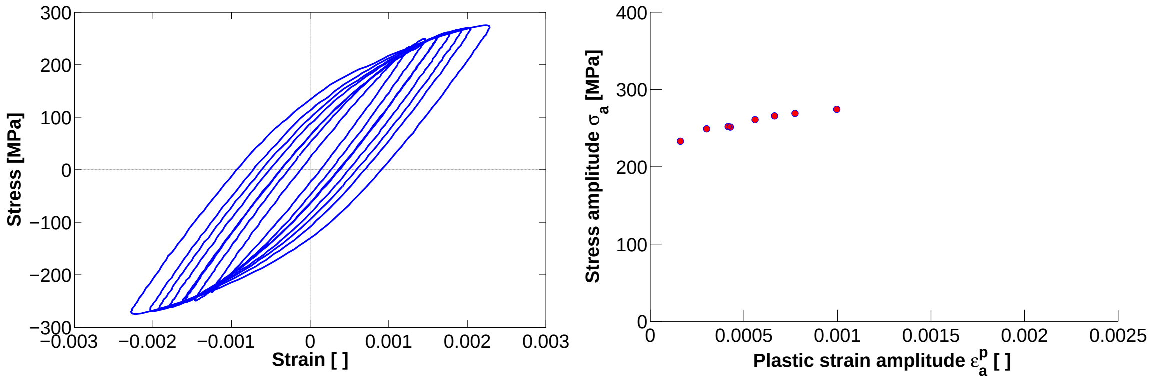

(a) stabilized hysteresis loops of the individual specimens

(b) cyclic stress strain curve

Figure 28: Stabilized stress-strain hysteresis loops at $0.5 \cdot N_f$ and cyclic stress strain curve in terms of plastic strains

5.5.3 Modeling of cyclic softening

The multi-linear kinematic hardening model used throughout these studies can be easily adapted to represent the stabilized stress-strain hysteresis loops given above. The adjustment requires the definition of multiple total strain/stress points as corner points of the multi-linear representation of the cyclic behavior. In order to simplify the numerical representation and to reduce the number of the experiments the cyclic material behavior has been assumed to be independent of the strain rate. In the 1-D case (specimen type I) the adjustment of the plasticity model is straightforward. In this case the initial yield limit can be set to the elastic range obtained after saturation of the cyclic behavior.

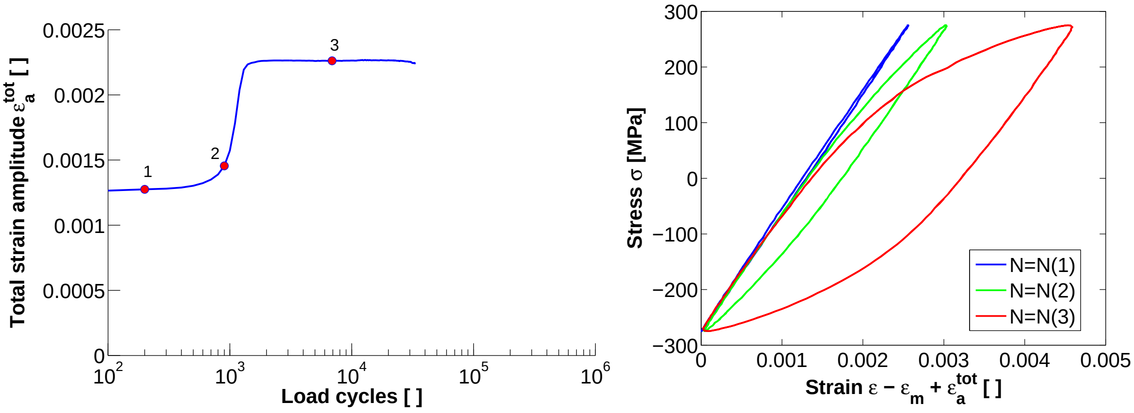

(a) evolution of the total strain amplitude

(b) hysteresis loops at different load cycle numbers

Figure 29: Reduction of the elasticity limit with ongoing softening

For a more general case which involves stress concentrations, a special problem arises due to the softening behavior of the mild steel. The experimental results show that the range of the elastic domain contracts during load-controlled cyclic loading. The reduction of the elastic domain becomes more pronounced with increasing stress amplitudes and higher plastic strains, respectively. As an example figure 29(a) shows the evolution of the total strain amplitudes with ongoing cyclic loading. In figure 29(b) three hysteresis loops are given which represent different hardening states of the same specimen. For the diagram the hysteresis loops have been relocated so that $min(\varepsilon)$ falls together for all hysteresis loops.

The hysteresis loops show that during softening the elastic domain is reduced to an elasticity limit σ_{yN} which becomes significantly lower than σ_{y0}. Accordingly plastic deformations set on at stress levels which are smaller than at the beginning of the cyclic loading. The evolution of the elasticity limit σ_{yN} is in general a rather complex function of the applied load history. Additionally the correct representation of the cyclic softening behavior would require the calculation of numerous time steps which would become impossible for the following investigations. Therefore the complex behavior needs to be considered in a simplified manner.

For elastic-plastic numerical investigations in the vicinity of stress concentrations the reduction of the yield limit leads to a dilemma: If the initial yield limit of the plasticity

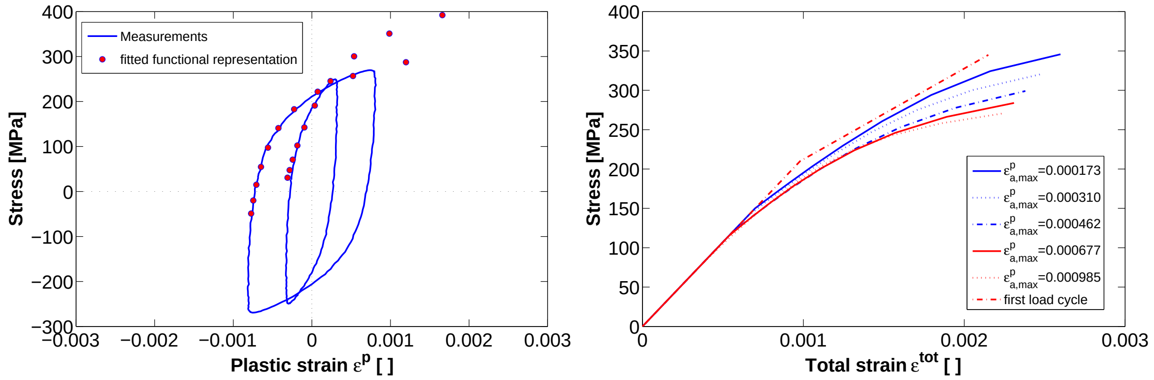

(a) saturated cyclic material behavior at two different load levels

(b) individual material models constructed of the saturated stress-strain hysteresis loops

Figure 30: Adjusted material models at different load levels for the simulation of the effects of cyclic softening

model is set to σ_{y0} the model may not represent the saturated stress-strain hysteresis loops sufficiently well. On the other hand, using the elasticity limit $\sigma_{yN} = \sigma_y(0.5 \cdot N_f)$ obtained from the saturated stress-strain hysteresis loops causes plastic deformations during the first load cycle to evolve below σ_{y0} so that the overall structural behavior becomes too soft. In order to get a fairly accurate result of the elastic-plastic material behavior around stress concentrations the reduction of the elastic domain during softening needs to be taken into account within the plasticity model.

The reduction of the elastic domain is considered here in a simplified version which yields the saturated behavior within a few load cycles. For this purpose different cyclic stress-strain curves obtained at different load levels are included into a single plasticity model. Each of the curves has its own yield limit and represents the cyclic stress-strain behavior in the saturated regime for the given stress level. Figure 30(a) shows exemplarily two measured stress-strain curves and the corresponding corner points of the fitted multi-linear material model. Similar curves are generated for each experimentally investigated load level. The determined stress-strain curves for all stress levels are summarized in figure 30(b). The first curve represents a pseudo bilinear material behavior with the yield limit σ_{y0} which is used to estimate initial yielding. Now switching between the individual stress-strain curves during the numerical calculation allows to model the complex plastic material behavior and the reduction of the elastic range. This requires the definition of an interpolation scheme between the individual curves.

The FE-program ANSYS 10.0 provides an option which allows to use different elastic-plastic material curves e.g. in order to simulate temperature dependent material behavior. This option is used here to generate an interpolation scheme between the individual cyclic stress-strain curves. As an interpolation parameter each of the stress-strain curves is associated with the maximum plastic strain amplitude which occurred in the experiment for the given stress amplitude. During the numerical simulation for each element the maximum equivalent plastic strain is calculated after each time step. For the first load cycle the initial limit of all elements is set to $\sigma_{y0} = 210$ Mpa. Thus this yield limit determines whether the material remains linear elastic or starts to plasticize. If the initial yield limit σ_{y0} is exceeded, the elastic-plastic material curve of the element is gradually adjusted during the next time steps until the applied material behavior corresponds to the stress-strain curve that is associated with the calculated maximum plastic strains. In order to prevent convergence problems and to guarantee a smooth transition between the individual material models only softening is allowed and the material models are changed gradually over 10 to 20 time steps if the initial yield limit σ_{y0} is exceeded.

5.5.4 Verification of the plasticity model

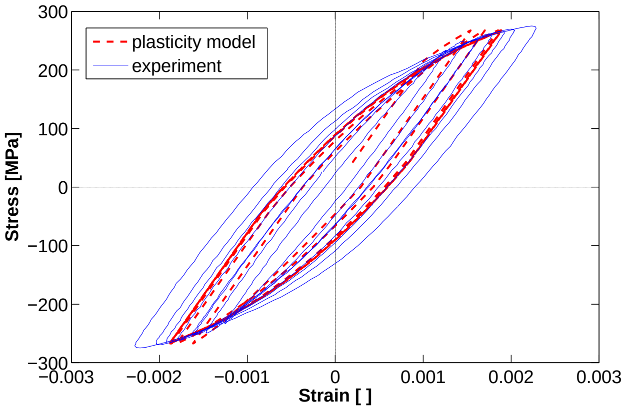

Figure 31: Convergence of the plasticity model in a 1-D test case; specimen type I; F_a=21 kN, f_L=2.5 Hz, comparison with the stabilized hysteresis loops of figure 28(a)

Figure 31 shows a convergence study of the cyclic behavior for specimen type I subjected to fully reversed sinusoidal loading at a frequency of 2.5 Hz and a load amplitude of 21.0 kN. As before the values are given for a surface point in the middle section of the specimen i.e. for a 1-D stress state. To demonstrate the convergence towards the experimental results the numerical results are compared with the stabilized hysteresis loops of figure 28(a). Note that each of the loops has been on a single specimens tested at certain load amplitude. During the first load cycle plastic deformations set on once the initial yield limit σ_{y0} is reached. Then the plasticity model converges quickly towards the experimentally observed saturation behavior. After convergence the stress-strain relation gives a close representation of the experimentally measured saturated behavior at the corresponding load amplitude. Depending on the magnitude of the applied loading, convergence of the plasticity model is generally reached within the first 2 to 3 load cycles. Next the performance of the plasticity model is evaluated for the more complex situation of the notched specimen type II.

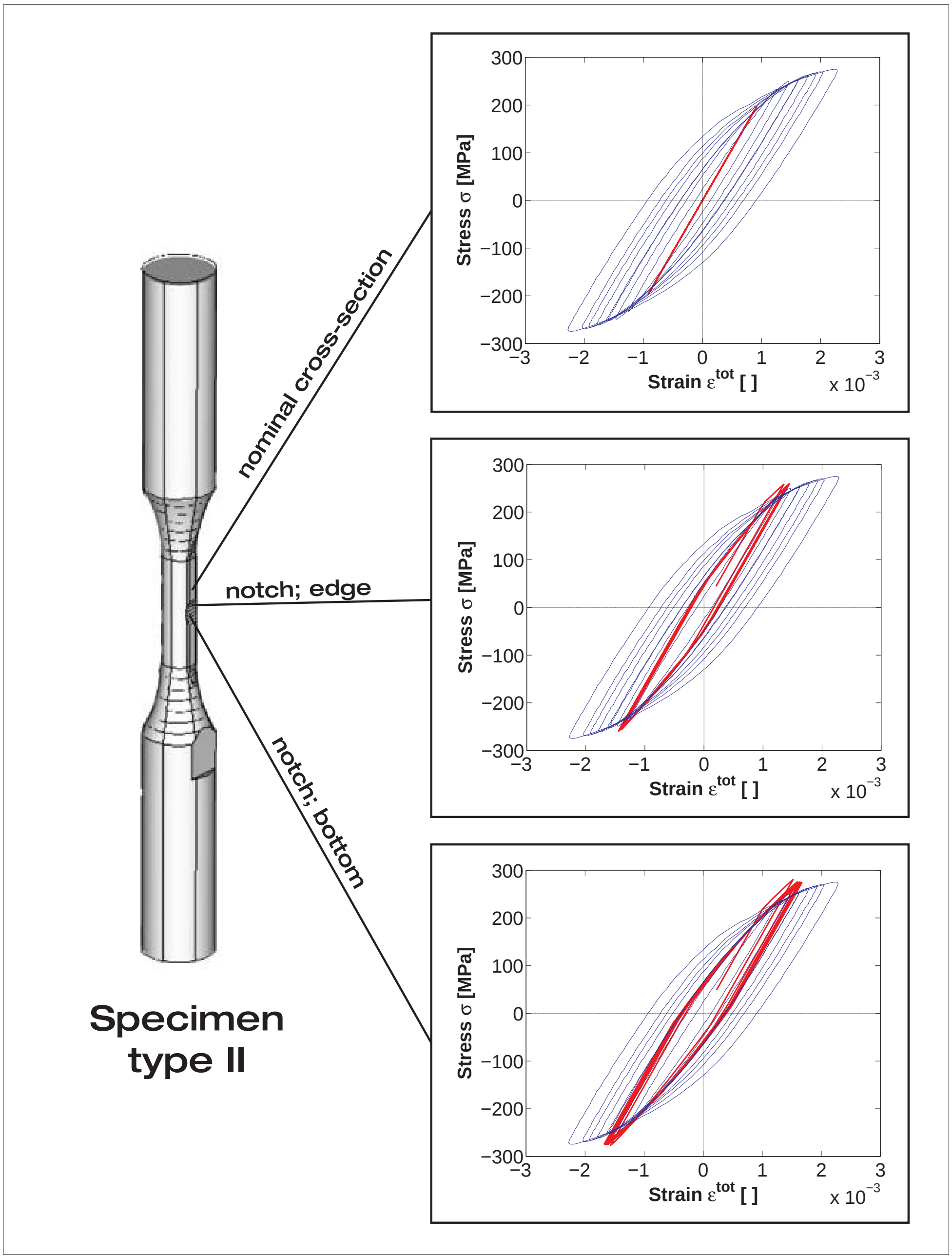

Figure 32: Convergence of the plasticity model for the notched specimen type II; F_a=16 kN, f_L=15 Hz

As a test case a load amplitude of 16.0 kN and a frequency of 15 Hz is chosen. Under these loading conditions pretests show that plastic deformations remain confined to the bottom of the notch. Figure 32 shows the cyclic stress-strain curve in terms of the maximum principal stress and strain at different surface points on the centerline $y = 0$ of the specimen. As before the experimental stress strain hysteresis loops of figure 28(a) are given to demonstrate the convergence behavior of the model. The results demonstrate that plastic deformations and the corresponding cyclic material behavior varies gradually from the bottom of the notch to the nominal cross-section of the specimen. At all surface points the plasticity model gives a good representation of the underlying experimental cyclic stress-strain hysteresis loops. Convergence is reached a little slower than for the 1-D case but within the first 4 to 5 load cycles. As intended the material remains linear elastic within the nominal cross-section of the specimen and plastic deformations are localized to the bottom of the notch. The plasticity model with interpolation scheme leads to a smooth and steady transition between areas with plastic flow and elastic regions.

The localization of the plastic deformations for the present case becomes obvious by figures 33(a) and 33(b) which show the simulated distribution of the first principal plastic strain amplitude across the surface of the specimen and at the symmetry lines $x = 0$ and $y = 0$. With the chosen plasticity model the plastic deformations are restricted to the bottom of the notch and small areas close to the shoulders of the specimen whereas the rest of the specimen remains linear elastic.

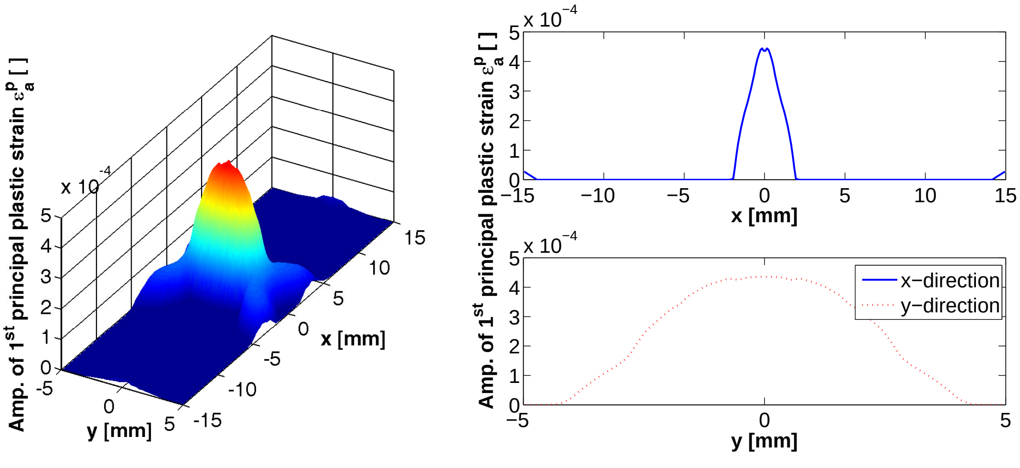

(a) spatial distribution

(b) distribution along y=0 and x=0

Figure 33: Distribution of the principal plastic strain amplitude; specimen type II, F_a=16 kN, f_L=15 Hz

5.5.5 Effects of plastic dissipation - specimen type I

According to equation (57) plastic dissipation can be taken into account within the heat equation (57) by applying the plastic work rate $\sigma_{ij}\frac{\varepsilon^p_{ij}}{\partial t}$ as additional volumetric heat source in the numerical model. The plastic work rate is calculated from the converged mechanical elastic-plastic model and updated at each time step. Thermoelastic coupling is taken into account in its linear form e.g. neglecting the influences arising due to the temperature dependency of the Young's modulus and other nonlinearities. For an upper limit estimation it is assumed that the entire plastic work is converted into heat. In reality a small portion of the dissipated work alters the hardening state and the inherent damage of the material and will therefore not be released as heat [CC04]. This portion of the dissipated work is rather small (10-20 %) and is therefore neglected during the following phenomenological investigations.

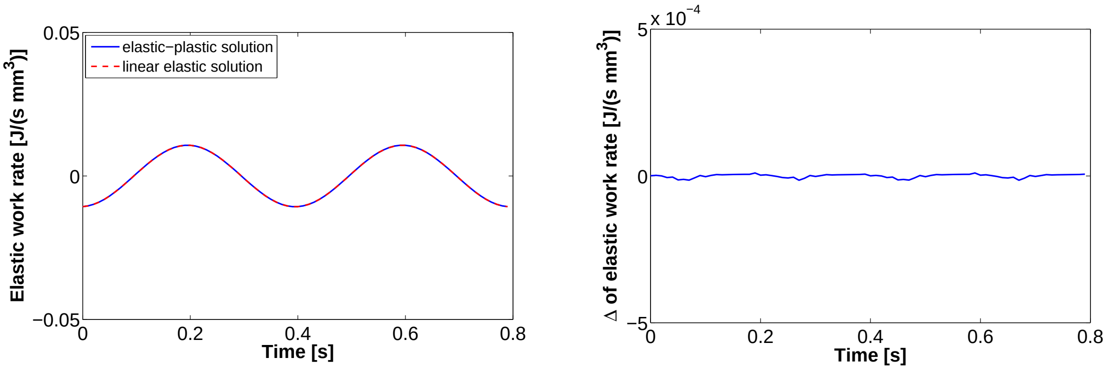

(a) elastic coupling term (b) difference

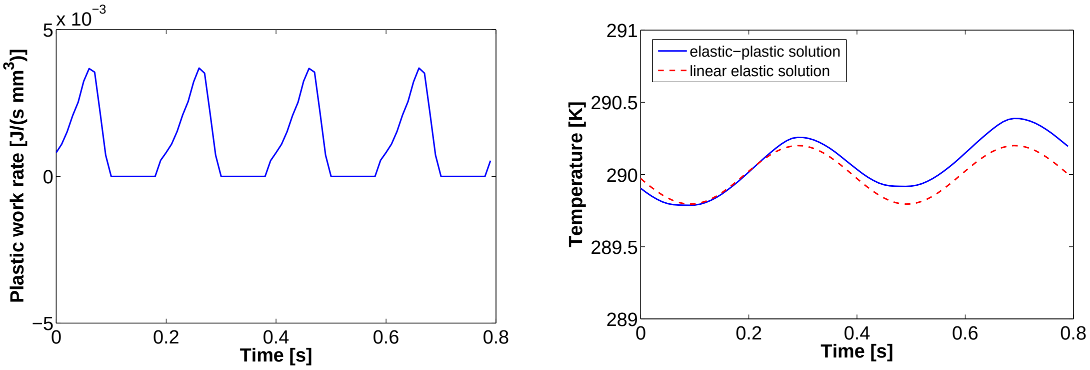

(c) plastic work rate (d) temperature evolution

Figure 34: Evolution of the thermoelastic/thermoplastic heat generation and temperature evolution for the elastic-plastic and the linear-elastic model; specimen type I, F_a=21 kN, f_L=2.5 Hz

As test case the temperature evolution of specimen type I subjected to sinusoidal loading with 21 kN at 2.5 Hz is calculated. Figure 34(a) compares the evolution of the elastic heat generation of an elastic-plastic numerical model with a corresponding linear-elastic model. Figure 34(b) provides the difference in the thermoelastic coupling term between both solutions. Figures 34(c) and 34(d) give the evolution of the plastic work rate and the final temperature evolution of the elastic-plastic and the linear-elastic model. The results presented in figures 34(a) and 34(b) show that the elastic work rate remains quasi-constant despite the onset of plastic deformations compared to the linear elastic solution. Accordingly the difference of the elastic coupling term between the elastic-plastic and the linear elastic model remains close to zero.

Figure 34(c) demonstrates that the plastic dissipation is always positive and becomes nonzero whenever the local yield limit is exceeded during compression and tension. During elastic unloading the plastic work rate drops to zero which causes distinct peaks in the temporal evolution. The positive plastic work rate causes an ongoing increase of the mean temperature with respect to the linear-elastic solution which is superimposed by temperature oscillations (figure 34(d)).

Figure 35(a) shows the temperature difference between the elastic-plastic and the linear elastic solution. The linear elastic solution has been calculated based on the same loading conditions but assuming linear elastic material behavior. In order to check the convergence of the model, different results obtained for time stepping with 1/40, 1/80 and 1/120 of a complete load cycle are given. For a time step size smaller than 1/80 of a load cycle the results can be regarded as converged. A time step size of 1/40 of a load cycle gives a good approximation of the converged results at relatively low computational costs. From figure 35(a) the linear trend in the elastic-plastic solution becomes clearly visible but the results also indicate an additional cyclic variation which is superimposed on the linear temperature trend.

During the first few load cycles the underlying trend in the temperature evolution can be considered as linear for specimen type I. This allows to remove the trend by subtracting a linear function of type $T_m(t) = T_0 + (\partial T/\partial t) \cdot t$ which can be easily fitted to the temperature evolution shown in figure 35(a). After trend removal the local effects of plastic dissipation on the temperature signal can be studied. Figure 35(b) shows a cyclic difference signal which represents the local effects of plastic dissipation compared to the linear elastic solution. It can be seen that plastic dissipation leads to characteristic nonlinear changes of the temperature evolution within one load cycle. The resulting peaks in the temperature difference appear both during tensional and compressional plastic flow so that their natural frequency is $2 \cdot f_L$, with f_L being the loading frequency. The amplitude of the temperature difference signal between the elastic-plastic solution and the corresponding linear elastic solution is around 16 mK for the given loading conditions.

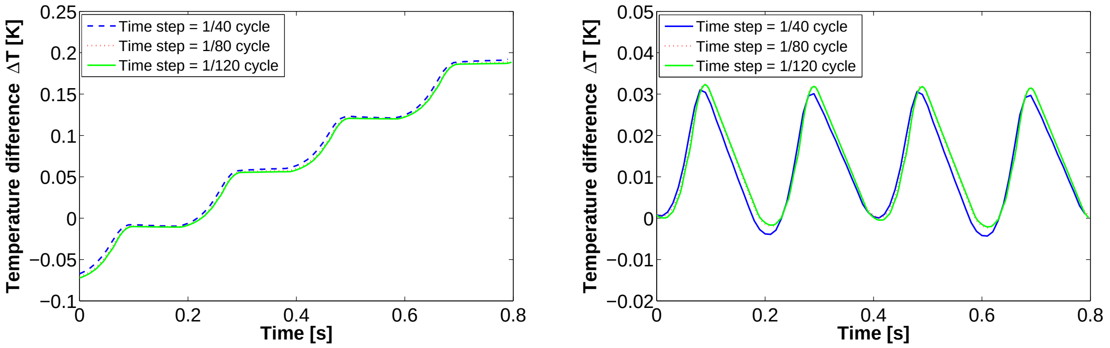

(a) temperature difference (b) temperature difference without trend

Figure 35: Temperature difference between the elastic-plastic and the linear-elastic model before and after trend removal; specimen type I, F_a=21 kN, f_L=2.5 Hz

5.5.6 Effects of plastic dissipation - specimen type II

Next it is verified that comparable effects can also be found for specimen type II for which plastic deformations remain strongly localized. The loading is harmonic with F_a=16 kN and f_L=15 Hz. Figures 36(a) and 36(b) give the temperature difference between the elastic-plastic solution and the corresponding linear elastic solution for a point at the bottom of the notch, i.e. at x=0 and y=0, and for a surface point within the nominal cross-section of specimen II. The principal evolution of the temperature difference within the notch is comparable to the results for specimen type I discussed earlier. Note that a different temperature scale has been chosen for figure 36(a) compared to figure 35(a) for representation purposes.

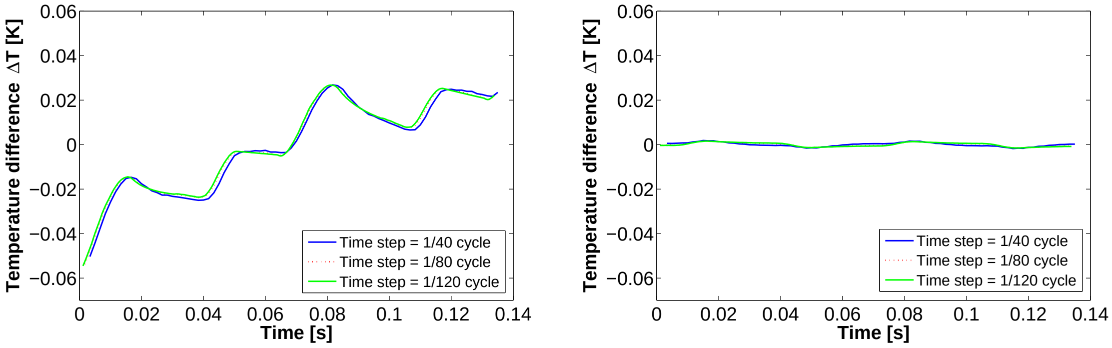

(a) x=0 and y=0 (notch) (b) nominal cross-section

Figure 36: Temperature difference between the elastic-plastic and the linear-elastic model at x=0 and y=0 and at a point in the nominal cross-section; specimen type II, F_a=16 kN, f_L=15 Hz

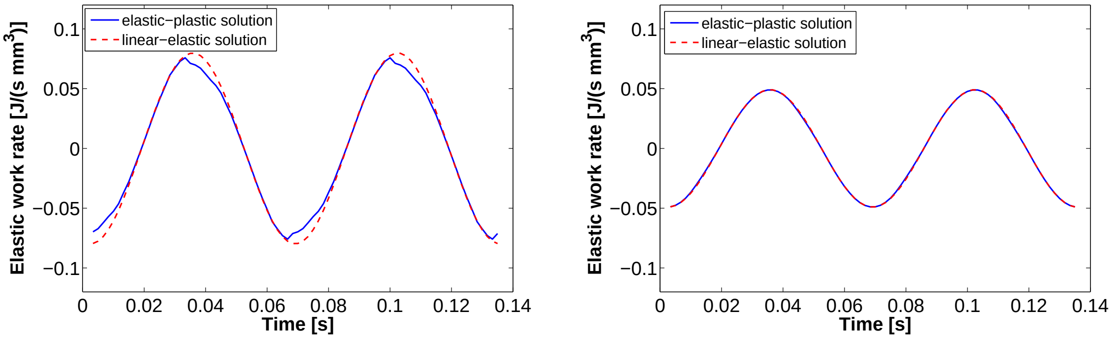

(a) x=0 and y=0 (notch)

(b) nominal cross-section

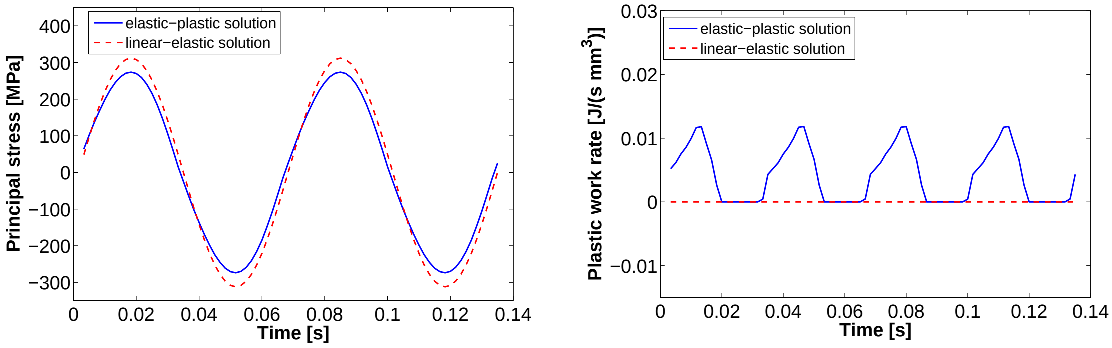

(c) first principal stress

(d) plastic work rate

Figure 37: Value of the thermoelastic coupling term for the elastic-plastic and the linear-elastic model at x=0 and y=0 and at a point in the nominal cross-section (a, b). First principal stress and plastic work rate for the elastic-plastic and the linear-elastic model at x=0 and y=0 (c, d); specimen type II, F_a=16 kN, f_L=15 Hz

The increase of the mean temperature within the notch is much weaker than for the cylindrical specimen type, as the overall plastic dissipation is smaller due to the localization of plastic deformations to the vicinity of the notch. Outside the notch no increase of the mean temperature can be found after the first two load cycles. The trend in the evolution of the mean temperature within the notch is strongly nonlinear even during the first two load cycles. This indicates strong influences of heat diffusion within the specimen. Therefore trend removal becomes more difficult and has not been performed at this point. The evolution given in figure 36(a) shows that the local temperature effects caused by plastic dissipation are different during compressional and tensional half load cycles. During tension the peaks in the temperature difference are more pronounced than during compression, so that the shape of the nonlinearities in temperature evolution becomes more complex. The overall amplitude of the nonlinear temperature difference is about 10 mK, i.e. small compared to the thermoelastic temperature variations.

Note that a similar phenomena has not been observed for the cylindrical specimen type I and therefore needs further clarification. Figures 37(a) and 37(b) show the evolution of the thermoelastic coupling term within the notch and at a point in the nominal cross-section of specimen II under the same loading conditions. For a better orientation figures 37(c) and 37(d) provide the evolution of the first principal stress and the plastic work rate for the same surface point within the notch. Whereas for specimen type I no effect of cyclic plasticity has been found on the evolution of the thermolastic coupling term, figure 37(a) demonstrates that the elastic coupling term within the notch is strongly influenced by the onset of plastic deformations. By contrast the difference in the thermoelastic coupling of the elastic-plastic model and the linear elastic solution is negligible for the nominal cross-section of the specimen. The nonlinearities in the thermoelastic coupling term can be attributed to load redistributions and/or residual stresses due to the localization of plastic deformations. Note that this effect cannot be observed in the uniaxial case investigated on specimen type I. Effectively the load redistributions cause a reduction of the thermoelastic coupling term close to the zero-crossings of the mechanical loading. Both effects are superimposed within the notch and lead to rather complicated nonlinearities of the thermomechanical coupling within the notch. This is demonstrated by figure 38 which gives the difference evolution of the nonlinear thermoelastic coupling term with respect to a linear solution, together with the plastic work rate and the superposition of both nonlinear effects. The superposition of the different nonlinearities in the thermomechanical coupling explains the complicated shape of the temperature difference presented in figure 36(a). In fact the discrepancies found for the coupling during tension and compression result from two distinct effects, both associated with the localized onset of plastic deformations within the notch.

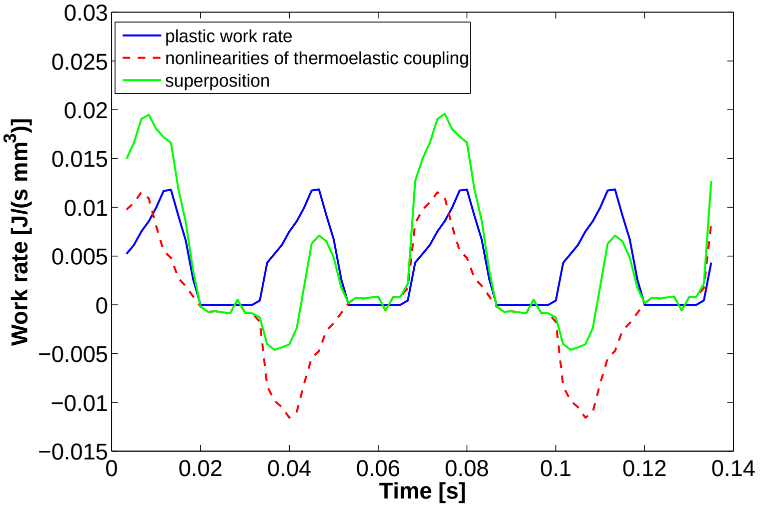

Figure 38: Superposition of the different nonlinear coupling phenomena for plastic material behavior within the notch, x=0 and y=0; specimen type II, F_a=16 kN, f_L=15 Hz

5.5.7 Effects of plastic dissipation - convergence of the mean temperature

Since the convergence of the mean temperature towards the stabilized temperature is very slow, a step-by-step solution procedure becomes very inefficient in order to study the stabilization behavior. However experimental investigations of plastic dissipation will in general be performed under quasi-stationary conditions. It is therefore interesting to verify the above mentioned effects of plastic dissipation under stationary conditions. As an alternative to the direct numerical simulation two different time scales can be introduced. For this purpose the initial time step size is extended to one or multiple excitation periods. Since the thermoelastic heat generation equals zero over a complete excitation period, thermoelastic temperature variations become negligible on this time scale. For the calculation of the temperature convergence only the dissipated plastic energy integrated over one period is applied as heat source. After stabilization of the mean temperature the time stepping is refined again and the complete thermoelastic-plastic problem is calculated as before around the new thermal equilibrium.

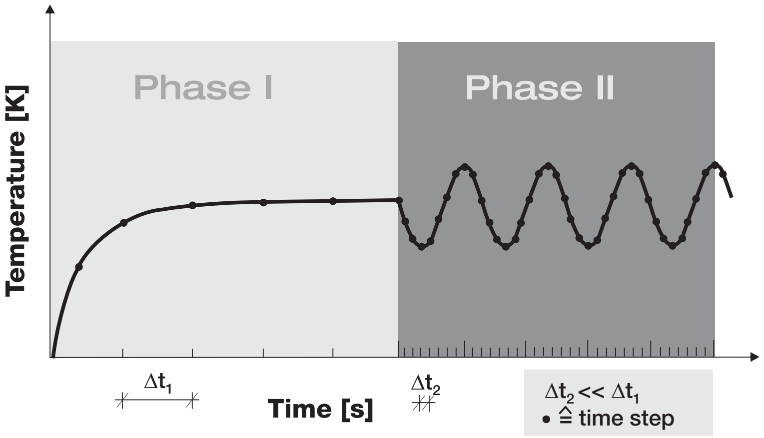

Figure 39: Time stepping procedure for the evaluation of temperature convergence during plastic dissipation

For the following investigations an initial time step size Δt of 15 periods equal to one second has been used. The dissipated plastic energy is calculated based on a converged solution of the elastic-plastic mechanical model. The applied loading conditions are as before, i.e. F_a=16 kN, f_L=15 Hz. With the applied loading and boundary conditions thermal convergence could be reached within 500 load steps. After this initial calculation the time steps Δt are reduced to 1/40 of a load cycle which allows to study the elastic/plastic temperature evolution as before. Figures 40(a) and 40(b) show the temperature evolution of two points on the surface of specimen II obtained at different time step sizes. Figure 40(a) demonstrates the convergence of the surface mean temperature towards a stabilized value which is approximately 1 K above the initial temperature T_0 =290 K. Figure 40(b) shows the transition between both time scales. The refinement to smaller time step sizes allows to calculate the thermoelastic/thermoplastic temperature variations around the new equilibrium. No significant change of the mean temperature occurs during refinement of the time step size after 500 s which proves the validity of the chosen approach.

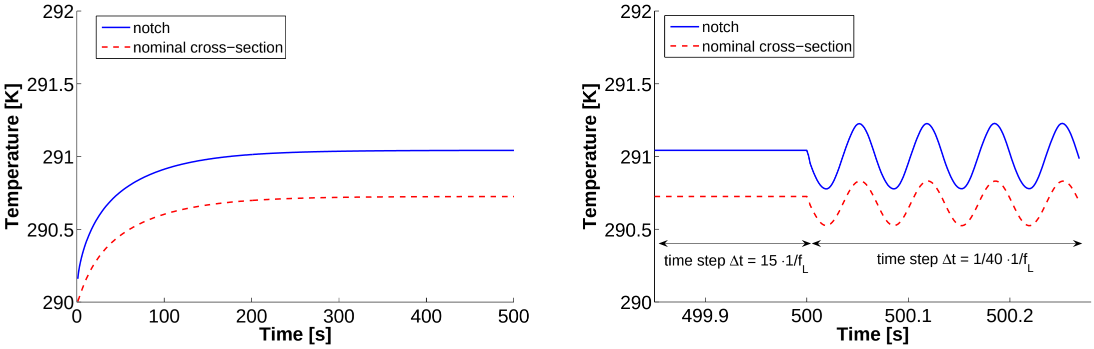

(a) time step Δt=$15\cdot\frac{1}{f_L}$ (b) time step Δt=$1/40\cdot\frac{1}{f_L}$

Figure 40: Temperature evolution at two different points of specimen type II for different time step sizes Δt; specimen type II, F_a=16 kN, f_L=15 Hz

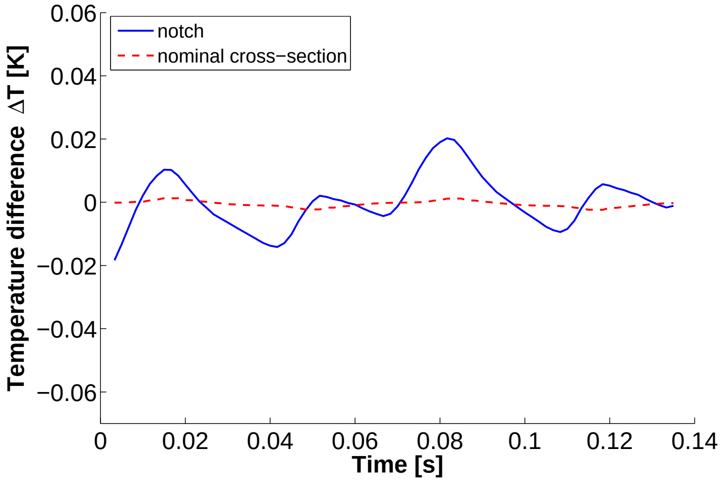

Figure 41: Temperature difference between the converged elastic-plastic model with respect to the linear-elastic solution; specimen type II, F_a=16 kN, f_L=15 Hz

Figure 41 gives the difference of the temperature evolution of the elastic-plastic model under quasi-stationary conditions with respect to a corresponding linear elastic model. The difference of the mean temperature has been subtracted a priori so that only the varying parts of the difference signal are represented. The results are similar to the difference signals given in figures 36(a) and 36(b) but with negligible trend in the temperature evolution. Within the notch the difference signal shows the typical discrepancies between tensional and compressional loading discussed earlier for the transient solution. Possible small discrepancies of the converged solution with respect to the initial transient behavior e.g. due to different effects of heat conduction are not discussed here further.

5.6 Chapter summary

For the investigation of the general heat equation a numerical solution procedure has been implemented in the commercial FE-program ANSYS 10.0. The adopted procedure allows to consider linear and non-linear thermoelastic coupling and plastic dissipation. Based on the numerical model the most important linear and nonlinear coupling phenomena and their effect on the local temperature evolution during mechanical loading have been discussed for two different specimen geometries. From the investigations the following conclusions can be drawn:

- Heat diffusion needs to be considered for the notched specimen type for which adiabatic conditions cannot be assumed. For harmonic loading non-adiabatic conditions can be identified by a phase shift $\neq \pi$ between the mechanical loading and the temperature evolution. Heat diffusion causes a nonlinear behavior if the load frequency is changed whereas linearity is maintained for a change of the load amplitude.
- The nonlinear effect due to the temperature dependency of the thermoelastic coupling terms is negligible for experimental investigations. The results obtained for different mean temperature $T_{0,n}$ can be directly compared if the measured temperature changes are scaled linearly by $T_0^*/T_{0,n}$, where T_0^* is a reference mean temperature.
- The consideration of bidirectional coupling leads to a reduction of the observable temperature variations with respect to the uncoupled problem in the range of 1 %. It can be taken into account by adjusting either the coefficient of thermal expansion in the decoupled problem or the Young's modulus in the coupled problem. The results show that with adjusted material parameters no additional nonlinearities are to be expected in the temperature evolution due to bidirectional coupling.

- Based on a literature review it can be concluded that for most material parameters the influences from the temperature and stress state become negligible. The temperature dependency of the Young's modulus causes the appearance of a higher harmonic at $2 \cdot f_L$ for harmonic loading with a magnitude of a few mK. The amplitude of the higher harmonic depends solely on the square of the applied load amplitude. The temperature variation at f_L becomes dependent on the stress amplitude and the mean stress level. Negative mean stresses cause a reduction of the thermoelastic temperature variations, positive mean stresses causes an increase with respect to the temperature amplitude at zero mean stress. The evaluation of mean or residual stresses based on thermoelastic coupling is doubtful for the given mild steel, since a distinction between the effects of the mean stresses and the load amplitude is experimentally not possible.

- For the study of local plastic behavior a new modeling technique has been developed which allows to take into account the reduction of the elastic regime during softening. The procedure shows good convergence properties and a suitable representation of the saturation behavior in the vicinity of geometric notches.

- Plastic dissipation leads to characteristic changes in the temperature evolution. Besides the increase of the mean temperature non-linearities in the order of a few mK arise in the local temperature evolution. The nonlinearities can be observed both during the initial transient phase and during thermal equilibrium and allow to study the local material behavior. For localized plastic deformations the nonlinearities remain strongly confined to the locations of highest stresses. In the vicinity of stress concentrations changes of the thermoelastic coupling are to be expected with the onset of plastic flow due to stress redistributions. In the temperature evolution the effects of these stress redistributions are superimposed on the effects from plastic dissipation.

6 Experimental analysis

Based on the numerical investigations in chapter 5 it can be concluded that most mechanical phenomena related to the fatigue behavior of metals such as the onset of plastic deformations, reduction of the elastic range, changes of the mean stresses/strains and structural nonlinearities cause corresponding variations in the surface temperature evolution during mechanical loading. The presented numerical studies allow to estimate the magnitude of the different linear and nonlinear temperature signals and show whether and how these phenomena might be detected during mechanical testing. The results confirm the high potential of thermal measurements by non-contacting full-field infrared thermography as a supplementary tool for the evaluation of localized damage phenomena during fatigue loading.

Infrared thermography can be regarded as a powerful tool in testing situations where other well established measurement techniques fail to provide valuable information of ongoing damage phenomena. The purpose of the following experimental investigations is the application of infrared measurements for the assessment of localized fatigue damage phenomena. The intent is a proof of concept with respect to the detection of typical coupling phenomena by thermographic measurements. In contrast to former approaches the investigations concentrate on localized phenomena which are typically involved in the mid to high-cycle fatigue regime. The experimental investigations start with a verification of the numerical model introduced in chapter 5. Then thermographic measurements are subsequently applied to situations with increasing complexity. This includes fatigue testing of cylindrical, notched and welded specimens. Specialized data processing techniques are introduced which allow to capture and separate different linear and non-linear coupling phenomena. In order to judge the results, thermographic measurements are compared with conventional techniques as strain gauge measurements and in-situ light microscopy. The author is aware that adiabatic conditions will never be reached due to the strong localization of the investigated damage phenomena. Therefore no further attempt is undertaken to calculate quantitative values as stresses, strains or dissipated energy based on the temperature measurements. The exclusive focus is therefore laid on the analysis of the temperature data.

6.1 Experimental verification on the modeling of thermoelastic coupling

6.1.1 Experimental approach

The purpose of the first test campaign is the verification of the numerical findings on thermoelastic coupling presented in chapter 5. For this purpose a series of cyclic tests on specimen types I and II has been conducted. The geometries of the specimens and a description of the preparation is given in appendix I. Testing was performed under load-control in a digitally controlled servohydraulic testing machine which is described further in appendix II. For the first test small load levels were chosen so that the specimens were loaded within their elastic range and no softening of the material is to be expected. For the thermographic measurements the investigated specimen surface was coated with a dull gray graphite layer (Graphit 33, Kontakt Chemie) which ensured a uniform and high emissivity $\epsilon \approx 0.85$. The graphite coating was chosen based on a study of different black dull coatings and was found to provide the best tradeoff between emissivity, thermal conductivity and applicability. The effect of the coating on the measured temperature variations can be estimated by a formula given by [Mac89] based on the solution of the 1-D heat diffusion problem. As mentioned before two distinct effects have to be distinguished, namely the thermoelastic response of the coating and the attenuation of the heat due to heat conduction within the coating layer. It is assumed that the thermoelastic response of the graphite layer (which consists of individual graphite particles) is negligible. The thermal lag caused by the heat conduction through the coating can be estimated by:

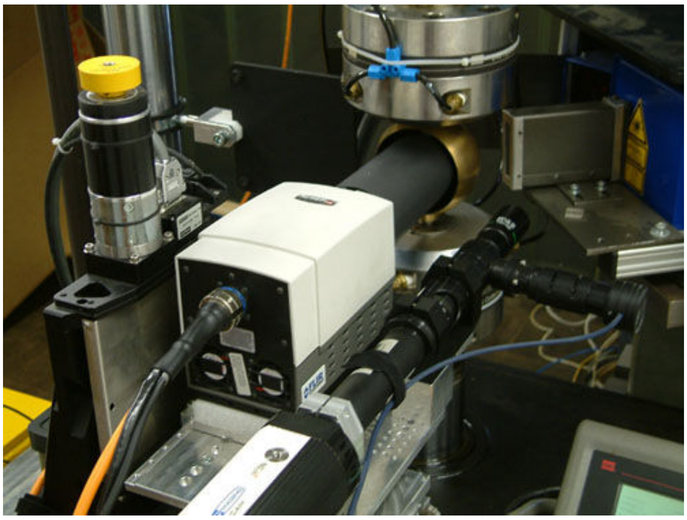

Figure 42: Experimental setup used for the thermographic investigations

$$\frac{T_{a,o}}{T_{a,i}} = abs\left[\frac{cosh[\mu\, x(1+i)]}{cosh[\mu\, d(1+i)]}\right]; \quad \mu = \left[\frac{\pi f_L}{\lambda_T}\right]^{0.5} \tag{76}$$

where d is the coating thickness. The surface of the coating is given by $x = 0$. In this case $T_{a,o}$ and $T_{a,i}$ represent the temperature amplitudes at the outside and the inside of the coating. For an upper limit estimation a thermal diffusivity $\lambda_T = k/(\rho C_P)$ of $0.5 \cdot 10^{-6} \frac{m^2}{s}$ and a maximum thickness of 50 μm is assumed [McK87]. In this case equation (76) gives an attenuation ratio of 0.982 which means that the coating has negligible effect on the surface temperature amplitudes.

The infrared camera system used for the investigations is described and characterized in appendix II. For the quantitative temperature measurements the camera was calibrated so that the grey values could be converted into corresponding temperature values. Calibration was performed by a digitally controlled black body which has been coated with the same graphite layer as that used for specimen preparation. The calibration process is described further in appendix II. The sampling rate of the camera was adjusted to ensure that more than 30 data points per load cycle could be acquired for all loading frequencies. During testing a brass half-sphere coated with a dull black color at the inside was attached around the specimen. This guaranteed a uniform thermal background radiation and avoided unwanted reflections during recording (figure 42). Data processing consisted in the application of a non-uniformity correction to the raw images, conversion into temperature values and calculation of the temperature amplitudes [4].

6.1.2 Linear thermoelastic coupling

For loading at stress levels below σ_{y0} it has been shown in chapter 5 that the only relevant nonlinearities within the temperature evolution to be expected for $F_m = 0$ are due to the temperature dependency of the Young's modulus E. For harmonic loading the temperature dependency of E causes the appearance of a higher harmonic in the temperature evolution. According to the numerical simulation in chapter 5 they are two or threes orders of magnitude smaller than the thermoelastic coupling itself. For the verification of the linear numerical model the contribution of the higher harmonic to the total temperature amplitude is considered to be negligible.

Figure 43(a) shows numerical and experimental values for the temperature amplitudes at a surface point in the center section of specimen type I. For the numerical simulation the geometry parameters have been adjusted according to the measured geometry of the tested specimen. The specimen is harmonically loaded at a loading frequency

---

[4] The methodology used for the calculation of the temperature amplitudes is discussed in section 6.2.4.

of 15 Hz, a mean load $F_m = 0$ (corresponding to a load ratio $R = -1$) and load amplitudes between 10 and 15 kN. The loading is small enough to ensure linear elastic conditions throughout the entire specimen.

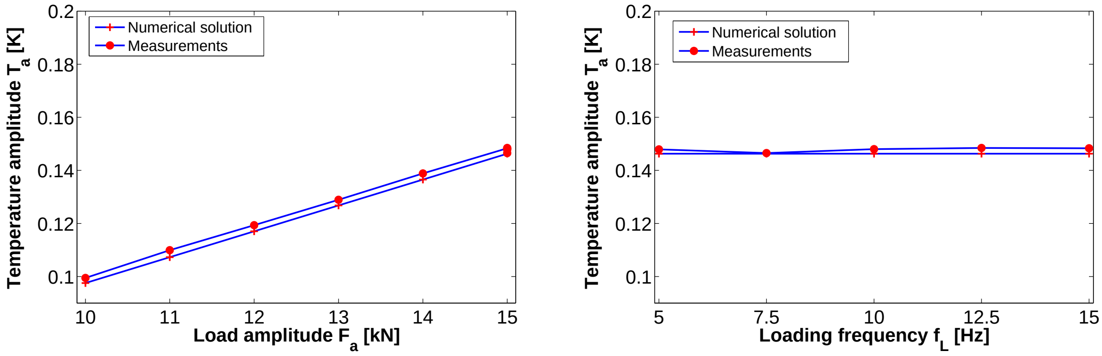

(a) temperature amplitudes vs. loading amplitudes; f_L=15 Hz

(b) temperature amplitudes vs. loading frequency; F_a=15 kN

Figure 43: Comparison of numerical and experimental temperature amplitudes; specimen type I, F_a=var., f_L=var.

Figure 43(b) gives the temperature amplitudes for the same specimen but this time at a constant load amplitude of 15 kN and varying loading frequencies. The experimental results confirm linearity of the temperature variations and adiabatic conditions throughout the investigated section of the specimen for all frequencies. Since the measured temperature amplitudes are independent of the loading frequency the results also confirm that the coating effect is indeed negligible. The overall agreement of the numerical and experimental results is very good with discrepancies below 2 %.

The numerical results discussed in section 5.3.2 show that the thermoelastic temperature variations on the surface of the notched specimen type become more complex due to the stress concentration at the notch and heat conduction within the specimen. In order to verify the appropriate consideration of heat diffusion in the numerical model further tests have been conducted on the notched specimen type II under harmonic fully reversed loading and similar testing conditions as given earlier. Figure 44 shows a comparison of numerical and experimental temperature amplitudes along the surface line x=0 on the specimen surface under harmonic loading with F_a=15 kN and loading frequencies of 15 Hz, 10 Hz, 5 Hz and 2.5 Hz. As before the geometry of the numerical model has been adjusted according to the actual geometry of the physical specimen measured after manufacturing.

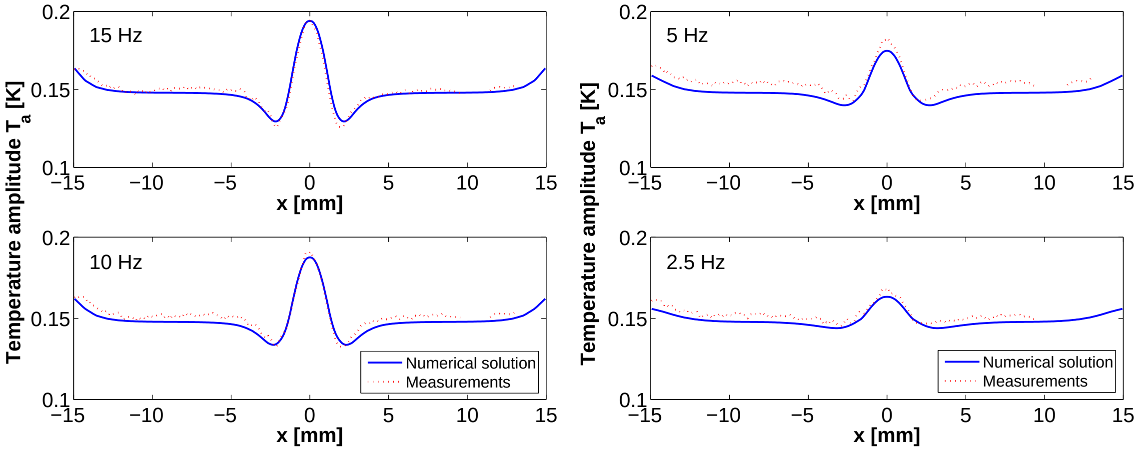

Figure 44: Comparison of numerical and experimental temperature amplitudes at symmetry line x=0; specimen type II, F_a=15 kN, f_L=var.

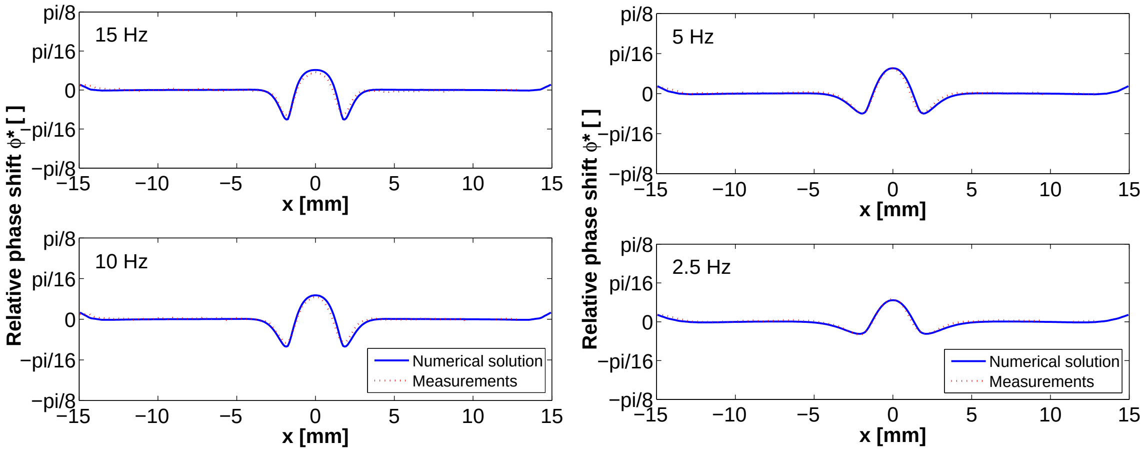

Figure 45: Comparison of numerical and experimental relative phase shifts; specimen type II, F_a=15 kN, f_L=var.

Figure 45 gives the corresponding relative phase shift at the central line x=0 on the surface of the same specimen. Both the numerical and experimental amplitudes and the relative phase shifts plot close together at all loading frequencies. The coincidence between the numerical model and the experimental results is very good, with typical discrepancies in the amplitudes below 3 % and in the phase shifts below 1 %.

6.1.3 Influence of mean stresses

Further tests have been performed to validate the occurrence of nonlinear effects due to the temperature dependency of the Young's modulus. Figure 46(a) gives a comparison of the total temperature amplitudes obtained numerically and experimentally on the surface of specimen type I for sinusoidal loading with a load amplitude F_a= 7.5 kN and a frequency f_L=15 Hz. During the experiments the mean load has been varied between -7.5 kN and 7.5 kN. All load levels are small enough to ensure purely elastic deformations throughout the specimen. Both experimental results and numerical calculations exhibit a linear variation of the temperature amplitudes with respect to the mean loading. The slope obtained from the numerical results is slightly higher than that from the measurements, which is probably due to a slight over-estimation of the temperature dependency of the Young's modulus.

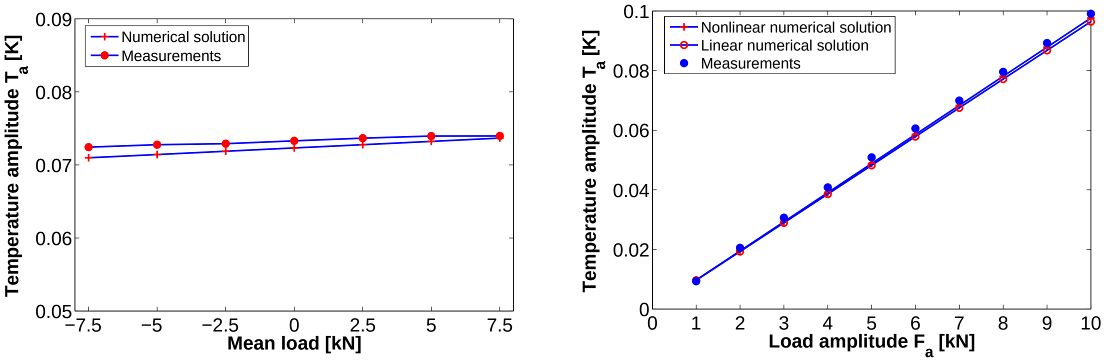

(a) temperature amplitudes vs. mean load; F_a= 7.5 kN

(b) temperature amplitudes vs. load amplitude; F_m= 5 kN

Figure 46: Temperature amplitudes vs. mean load and temperature amplitudes vs. load amplitude; specimen type I, F_a= var., F_m= var., f_L=15 Hz

Figure 46(b) gives the temperature amplitudes of the same specimen but at a constant mean load of 5 kN and varying load amplitudes. The experimental results fall close together with the numerical calculations for which the mean stress dependency has been taken into account. By contrast the simple linear numerical model shows larger discrepancies to the experimental results in case of non-zero mean stresses. This verifies that the temperature dependency of the Young's modulus needs to be taken into account to obtain accurate numerical results for varying testing conditions.

The experimental results given in this section confirm that the numerical model is able to predict qualitatively and quantitatively the local temperature field for linear thermoelastic coupling including the effects of heat conduction within the specimen.

6.2 Cyclic testing with zero mean load

6.2.1 Specimen preparation and testing procedure

The intention of the following investigations is the assessment of fatigue related properties by thermographic means. The examinations start with the study of the temperature evolution on cylindrical specimens during fully reversed fatigue loading. The material of all specimens was unalloyed low-carbon steel S355J2G3 under annealed conditions, according to the specifications given in appendix I. All specimens were mechanically polished before final annealing and then tested under the conditions as received after heat treatment. In the middle section of each specimen a strain gauge of 20 mm grid length was attached which allowed to measure the integral strains in the nominal cross-section of the specimen so that the softening behavior could be investigated. Influences from temperature changes during testing were compensated by an additional unloaded strain gauge attached to a piece of the same steel which was brought in close thermal contact with the center section of the specimen. Heat conduction between the specimen and the temperature compensation was improved by heat conductive paste. The preparation for the radiometric temperature measurements by infrared thermography consisted of coating the investigated side of the specimen with high emissivity graphite spray (compare figure 47).

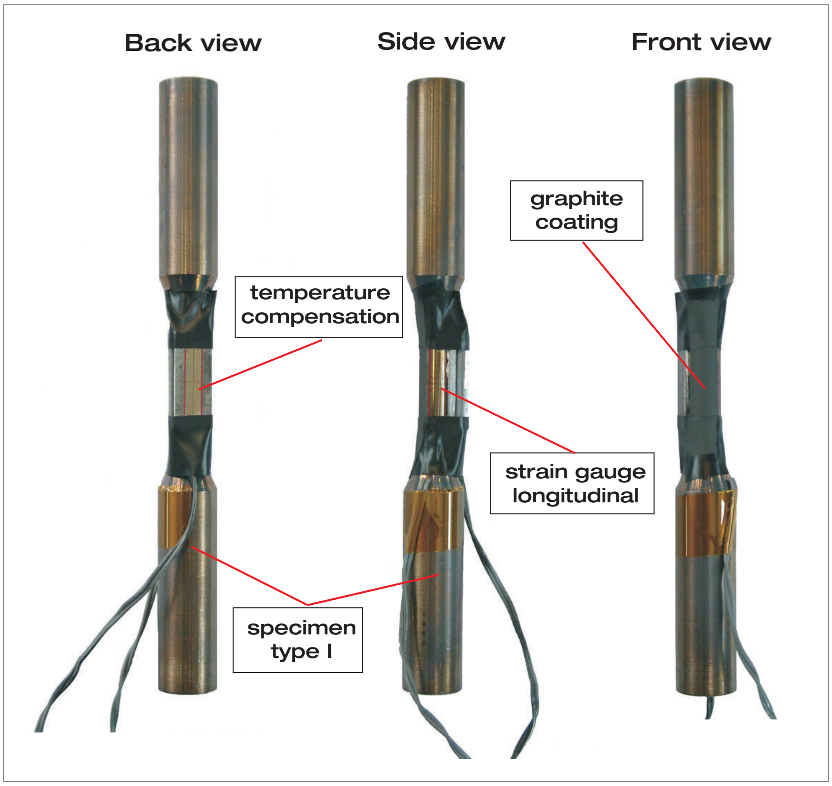

Figure 47: Specimen preparation; specimen type I

The experimental setup used for the fatigue testing of the specimens is described in more detail in appendix II. During the long-term testing the grips of the testing machine were temperature controlled by a thermostat which provided a constant water flow of 290 K. Room temperature was stabilized and kept constant at around 294 K by air-conditioning of the laboratory. During fatigue testing strain measurements were triggered every 100 load cycles. Thermal measurements were triggered every 500 load cycles for $N \leq 20000$ and every 5000 load cycles for $N > 20000$. During each acquisition interval the strain and the load signal provided by the load cell of the testing machine were recorded by a National Instruments SCXI-1520 data acquisition card during two complete load cycles. The acquisition rate was adjusted so that every load cycle was sampled with 200 data points. Thermal measurements compromised the acquisition of 2000 frames of the coated specimen surface under the applied fatigue loading. The camera frame rate was set to approximately 206 $^{\text{frames}}/_{\text{s}}$.

The fatigue loading was applied under load control as fully-reversed ($R = -1$) harmonic single-step loading at different load amplitudes. The testing frequency was set to 2.5 Hz for all specimens which guaranteed that the mean temperature of the specimens did not increase by more than 20 K at all load levels. All stress levels were below the initial monotonic yield limit of the steel so that only elastic strains occurred during the first load cycles upon onset of primary softening. Testing was terminated by failure of the specimens, typically between 20000 and 700000 load cycles. The testing conditions and the failure load cycles of all tested specimens are summarized in table 2. The stress values are calculated based on the diameter of the specimens measured after manufacturing and the applied loading based on the records of the load cell.

Table 2: Loading and testing conditions for fatigue testing on specimen type I with $\sigma_m = 0$

Specimen No.	σ_a [MPa]	σ_m [MPa]	f_L [Hz]	N_f [lc]
RR0706	261.5	0	2.5	124,870
RR0713	252.5	0	2.5	326,400
RR0715	269.6	0	2.5	61,260
RR0717	234.6	0	2.5	632,000
RR0719	274.8	0	2.5	33,210

6.2.2 Macroscopic softening/hardening behavior

Figures 48(a) through 48(c) show the evolution of the total strain amplitudes, plastic strain amplitudes and the mean strains for the different specimens. Plastic and elastic strains are separated according to the methodology discussed in section 5.5.2. The cyclic-stress strain behavior exhibits the general softening and hardening behavior of mild steels during stress-controlled testing as discussed schematically in section 3.2.2. Upon primary softening the steel behaves quasi-elastic on a macroscopic scale. In the tested stress range the duration of this initial incubation phase compromises between 10^3 and 10^4 load cycles. The onset of primary softening is marked by a rapid increase of the total and plastic strain amplitudes due to the evolution of plastic strains. The extent of softening depends on the applied stress amplitudes. Consequently higher stress amplitudes lead to:

- a shorter incubation interval
- a faster increase of plastic strains during primary softening
- a higher level of the plastic strain amplitudes during saturation

With completion of primary softening the cyclic stress-strain behavior is quasi-saturated and varies little until crack initiation. For small load amplitudes a slight hardening tendency can be found which is followed by a phase of secondary softening close to crack initiation. For higher stress amplitudes hardening is less pronounced. Altogether the tendency to cyclic hardening is much weaker than reported by [Gon79] and [Rei78] for comparable low-carbon steels. The different phases take the following portions of the total fatigue lifetime:

- incubation phase: 0.5 % to 1.5 % of total fatigue lifetime
- end of softening phase phase: 2 % to 5 % of total fatigue lifetime
- end of secondary hardening phase (if any): 15 % to 25 % of total fatigue lifetime
- macroscopic crack initiation (detection based on the strain gauge measurements) at around 90 % of the total fatigue lifetime

Figure 48(c) shows that together with the onset of primary softening small tensional mean strains evolve for all of the specimens. The initial increase is terminated by the end of the softening phase. In contrast to the plastic strain amplitudes the mean strains do not saturate completely during further testing, even though the overall increase remains relatively small. The results demonstrate that non-zero mean strains can evolve even during fully reversed loading ($R = -1$). These results correspond to findings discussed by [Web83] and [Rei78]. Based on a literature review [Web83] mentions that in order to reach zero mean strains during saturation small external compressional mean stresses need to be applied. He attributes the observed mean strain evolution during reversed loading partially to the temperature increase owing to plastic dissipation within the specimens. The investigations point out that the

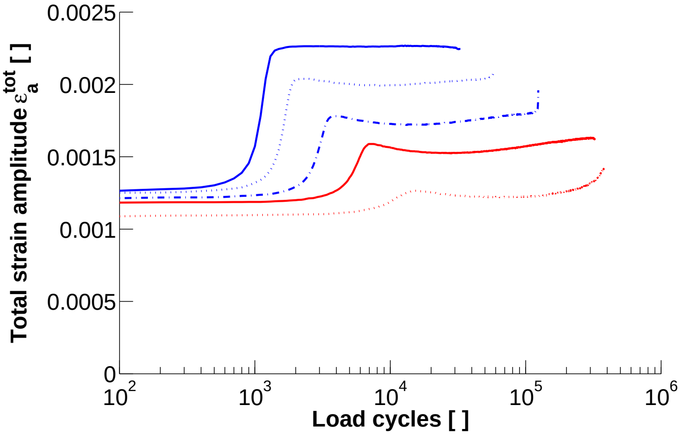

(a) total strain amplitudes

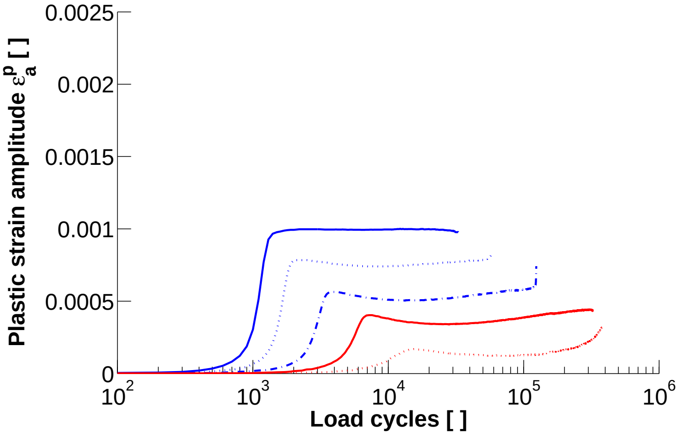

(b) plastic strain amplitudes

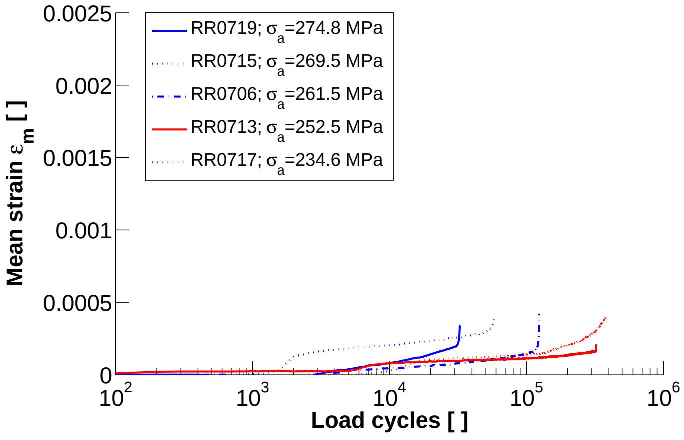

(c) mean strains

Figure 48: Evolution of cyclic total strain amplitude, plastic strain amplitude and mean strains; specimen type I, σ_m=0, σ_a=var., f_L=2.5 Hz

temperature influence generally needs to be considered for the interpretation of test results on cyclic properties. [Rei78] mentions that even small mean loads e.g. due to imperfections in the test equipment are sufficient to provoke cyclic creep and thus lead to non-zero mean strains. For the present studies temperature compensated strain gauges have been used so that effects from the temperature increase can be widely excluded for the present studies. Accordingly the observed mean strains indicate cyclic creep of the material at zero mean stress whose exact reason remains unclear.

6.2.3 Analysis of the mean temperature evolution

Figure 49 gives the increase of the mean temperature on the specimen surface relative to the initial temperature T_0 at the beginning of the testing. The values represent a spatial mean of a 5 x 5 pixel neighborhood in the center section of the specimens. Qualitatively the evolution of the mean temperatures resembles closely the evolution of the plastic and total strains discussed earlier. The onset of primary softening is accompanied by an increase of the mean temperature which, based on the findings of the strain gauge measurements, can be associated with plastic dissipation.

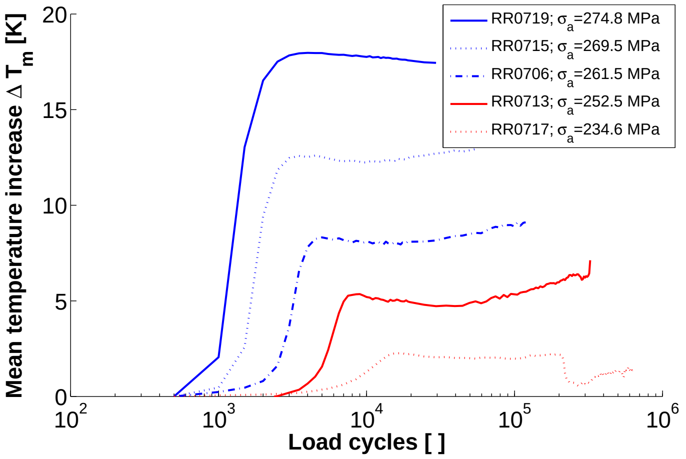

Figure 49: Evolution of the mean temperature with respect to T_0; specimen type I, σ_m=0

For specimens with high plastic strain amplitudes the relative temperature increase with respect to T_0 is more pronounced during softening than for specimens with overall small plastic strain amplitudes. After primary softening the mean temperature of the specimens remains quasi-constant during saturation of the cyclic softening/hardening curve. For specimens which exhibit secondary hardening the mean temperature evolution follows the hardening curve. The mean temperature decreases slightly during the saturation phase and increases again with the onset of secondary softening. The jump in the mean temperature of specimen RR0717 is due to an unintended interruption of the test which led to a cooling-down of the hydraulic circuit and the hydraulic grips. This interruption shows that the stabilized relative mean temperature and the absolute temperature depend strongly on the specific testing conditions and the thermal equilibrium of the testing device. Note that at the same point the cyclic hardening curve does not exhibit any irregularities. The absolute mean temperature or its increase with respect to the initial temperature can therefore be regarded as rather sensitive towards variations of the testing conditions.

6.2.4 Data processing - Separation of linear and nonlinear temperature signals

The numerical investigations of chapter 5 show that plasticity causes characteristic nonlinearities within the local temperature evolution. Therefore a suitable approach for the detection of fatigue related phenomena as cyclic plasticity seems to be the separation of linear and nonlinear temperature signals at each pixel of the measured infrared sequence. The classical approach consists of the calculation of a Discrete Fourier Transform (DFT) over the temporal variation of each pixel within the recorded image sequence. Nonlinearities caused e.g. by plasticity lead to the appearance of higher harmonics in the temperature evolution which can be detected by DFT. Additionally DFT allows to calculate the phase shift of all identified harmonics. Nevertheless this classical approach has some disadvantages for practical applications which are:

- the sensible application range of DFT is limited to the analysis of harmonic loading functions
- the results obtained by DFT are directly influenced by small deviations from purely harmonic loading which are always present in the temperature evolution e.g. due to a limited control-accuracy of the servohydraulic testing machine
- the frequency resolution of DFT is determined by the sampling rate and the sampling length
- DFT provides values only at discrete frequency steps. Interpolation schemes with sub-time-step accuracy (and therefore higher frequency resolution) are complicated to implement
- DFT does not allow to identify the variation of the nonlinearities in time
- for nonharmonic signals DFT spreads information onto multiple harmonics which complicates the analysis

To avoid these disadvantages a new approach is proposed here which resembles the classical DFT but is entirely based on a signal analysis in the time domain. It has been shown in chapter 5 that the influence of different nonlinear effects on the temperature evolution can be investigated based on an analysis of the difference signal with respect to the linear solution. A comparable approach has been developed for the analysis of experimental results. The methodology requires a linear solution of thermomechanical coupling. Then this linear reference signal is subtracted from the temperature-time signal recorded for each pixel and the remaining difference is evaluated. For the practical implementation a few problems need to be solved. First for experiments it is obviously not possible to obtain both the linear and nonlinear temperature evolution for each point of the specimen surface at the same time and compare the results as we did for the numerical analysis. Therefore an additional reference signal is required for which linearity can be assumed. The linear reference can e.g. be generated from the values of the controlled variable during testing or from the temperature evolution in a section of the specimen for which linear conditions are guaranteed throughout testing.

For harmonic loading it is suitable to normalize the reference signal before further processing so that its amplitude equals unity. The assumption of linearity requires that the temperature signal of each pixel recorded at the specimen surface can be expressed by scaling the chosen reference signal. At this point the effects of heat diffusion need to be taken into account. It has been shown that for harmonic or near-harmonic loading linearity of the temperature signal is also preserved if heat conduction is not negligible. In this case heat conduction leads to a time respectively phase shift of the local temperature evolution. Therefore the two parameters to be adjusted are the magnitude (amplitude) and the time (phase) shift of the reference signal. After matching of the reference signal to the temperature evolution all additional nonlinearities are given by the difference between the actual pixel signal and the fitted (linear) reference signal. In case of a purely linear behavior the remaining difference signal equals zero. For full-field infrared measurements the fitting needs to be performed for each pixel within the recorded infrared sequence. Since the reference signal and the temperature evolution are given as discrete measurements the fitting procedure becomes rather cumbersome compared to the fitting of an analytical function.

The developed fitting procedure follows a two step approach and has been implemented as Matlab routine. First, the phase shift between the reference signal and the measured pixel temperature signal is evaluated by analyzing the zero crossings of both signals at sub-time-step accuracy. Then both signals are interpolated onto a common time scale so that their zero-crossings fall together. After interpolation the discrete values of the reference function and the pixel signal are given at the same phase angles without any additional time lag. Next the linear scaling factor for the reference is calculated based on a linear least-square fit which minimizes the mean-square-root residual between the values of the reference function and the pixel signal. The calculated scaling factor represents the linear amplitude of the temperature signal. Finally the nonlinear

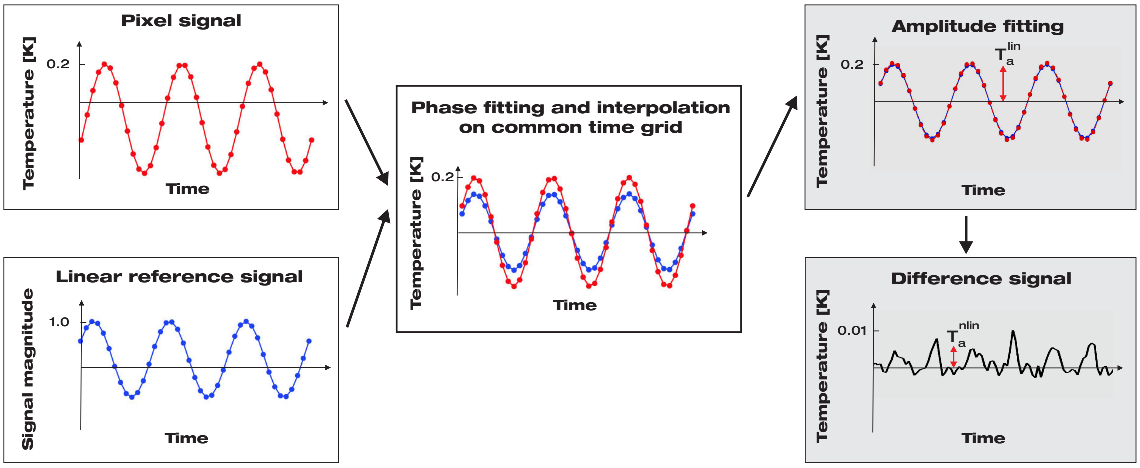

Figure 50: Working principle of the fitting procedure used for the separation of linear and nonlinear temperature signals

signal contributions are obtained by calculating the difference signal between the original temperature evolution and the fitted reference. The entire procedure is sketched schematically in figure 50.

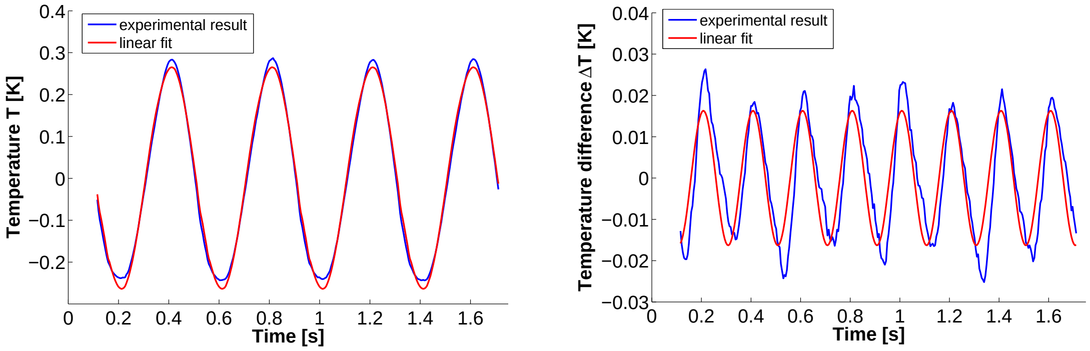

(a) fitting of the linear reference signal

(b) fitting of the search function to the difference signal

Figure 51: Definition of linear and nonlinear temperature amplitudes and fitting procedure; specimen type I, σ_m=0.

As an example figure 51(a) shows the original nonlinear temperature signal and the fitted reference signal. The temperature signal represents the temporal temperature evolution of a surface point of specimen RR0719 in the saturated regime at $0.5 \cdot N_f$. For the given example the reference signal has been extracted from the load signal of the testing machine. The representation shows that the fitted load signal and the temperature variation of the specimen fall together for most parts of the temperature signal. Nevertheless clear discrepancies appear close to the minimum and the maximum of the temperature evolution. These differences are mainly attributed to local nonlinearities due to plastic dissipation as discussed in chapter 5. Figure 51(b) gives the difference calculated by subtracting the fitted reference of the original temperature signal. Note that the evolution of the difference signal is very similar to the numerical results given for specimen type I in figure 35(b).

For representation purposes it is useful to reduce the linear and nonlinear parts of the temperature signal to a single parameter. Convenient parameters are the amplitudes of the linear and the nonlinear temperature signals. The amplitude of the linear temperature signal is given directly as the scaling factor of the reference signal. The amplitude of the nonlinear temperature signal is obtained by fitting a suitable 'search' function to the difference signal shown in figure 51(b). The shape of the search function to be chosen should provide a close representation of the difference signal. Its scaling factor can then be used to characterize the magnitude of the nonlinear temperature evolution. For the given shape of the nonlinearities a suitable search function is a sinus with a frequency of $2 \cdot f_L$, where f_L is the natural loading frequency (compare figure 51(b)). The phase shift of the difference signal is not calculated at this point. Instead it is assumed that the harmonic temperature evolution at $2 \cdot f_L$ has coincident zero crossings with the fitted reference signal. In contrast to the discrete linear reference used before, the search function is now given in an analytical form which allows to apply a standard fitting procedure. The amplitude of the fitted sinus at $2 \cdot f_L$ will be referred to as nonlinear temperature amplitude in the following. For the analysis of a complete sequence of infrared images the described analysis is repeated for each individual pixel.

6.2.5 Analysis of the temperature amplitudes

Figure 52(a) shows the evolution of the linear temperature amplitude obtained for the different specimens during fatigue testing. The values represent a spatial mean value of the center section of the specimen. As discussed in detail in chapter 5, the magnitude of linear thermoelastic coupling depends on the mean temperature T_0. Since the mean temperature varies considerably during fatigue testing (figure 49) its variability needs to be taken into account for the comparison of the linear temperature amplitudes. Therefore the amplitudes given in figure 52(a) are normalized to a 'standard temperature' $T_0 = 290$ K by applying a normalizing scaling factor T_0/T_m, where T_m represents the actual values of the local mean temperature.

Prior to the onset of softening the linear temperature amplitudes are directly proportional to the applied loading which indicates purely elastic material behavior. This is demonstrated by figure 53 which gives the dependency of the temperature amplitude on the elastic strain amplitude after 500 load cycles, i.e. before the onset of primary

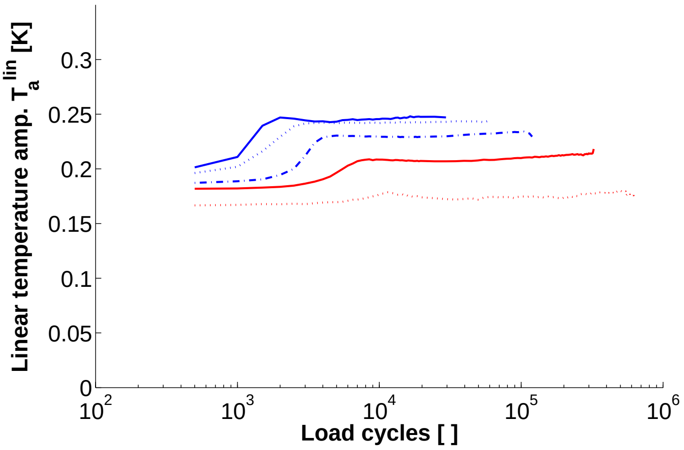

(a) amplitude of linear temperature variations

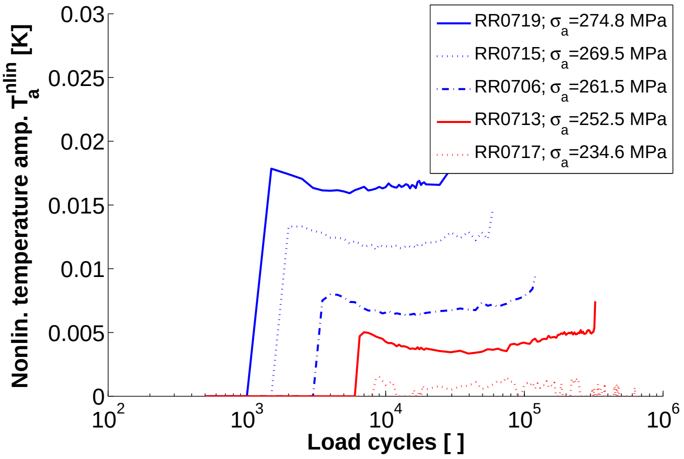

(b) temperature amplitude of nonlinear temperature variations

Figure 52: Evolution of linear and nonlinear temperature amplitudes; specimen type I, σ_m=0, σ_a=var., f_L=2.5 Hz

softening. Due to the proportionality of thermoelastic coupling and mechanical loading under adiabatic conditions the temperature amplitudes at the surface of the specimens increase quasi linearly with the applied load amplitude.

Figure 52(a) shows that with the onset of softening the linear temperature amplitudes increase significantly and thus follow the trend of the total strain amplitudes. This result is rather surprising and cannot be explained with the theoretical and numerical considerations given so far. Possible explanations will be discussed in more detail later on.

Figure 52(b) provides the corresponding evolution of the nonlinear temperature amplitudes. Pseudo-amplitudes obtained by fitting the search function to an unstructured

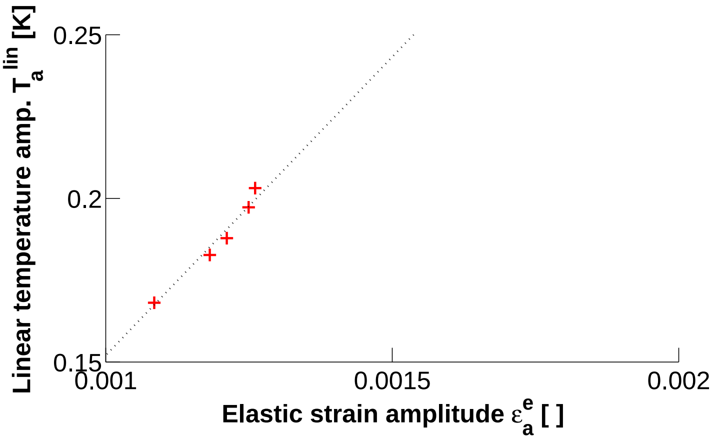

Figure 53: Linearity of the temperature amplitude with respect to the elastic strain amplitude before softening; specimen type I, σ_m=0, σ_a=var., f_L=2.5 Hz

(random) difference signal have been set to zero for representational purposes. Generally poor fitting is assumed if the regression coefficient of the fitting procedure becomes less than 50 %. The results show clearly that the nonlinear temperature amplitudes become non-zero with the onset of softening and exhibit a similar shape as the evolution of the plastic strain amplitudes. Together with the numerical investigation in chapter 5 the occurrence of these nonlinearities can be attributed to plastic dissipation associated with the onset of softening. Note that the nonlinear temperature amplitudes are very small compared to the linear temperature amplitudes. The results indicate that the developed data analysis procedure allows to investigate nonlinear temperature amplitudes below 5 mK. Together with the results of the strain gauge measurements (figure 55) it can be concluded that the thermal resolution is high enough to detect small plastic strain amplitudes below 0.05 %.

Figures 54(a) through 54(f) show the spatial distribution of the linear and the nonlinear temperature amplitudes in the center part of specimen RR0706 after 500, 2500, 3000, 3500, 4000 and 74500 load cycles. The nonlinear temperature amplitudes reveal that the softening process starts heterogeneously. In the present case plastic deformations set on at the lower end of the specimen and spread over the entire central part of the specimen as a cyclic Lüders band within fewer than 500 load cycles. At the end of the softening phase the nonlinearities are homogeneously distributed over the entire specimen and remain quasi-constant throughout further testing. The rapid spread-out of the nonlinear temperature signals corresponds to the localization of plastic deformations during the primary softening phase investigated by [Gon79]. The analysis of nonlinearities in the temperature signal is thus considered to give a very good insight into the localization effects during cyclic loading. Figures 54(a) through 54(f) reconfirm that the onset of nonlinearities in the temperature evolution is accompanied

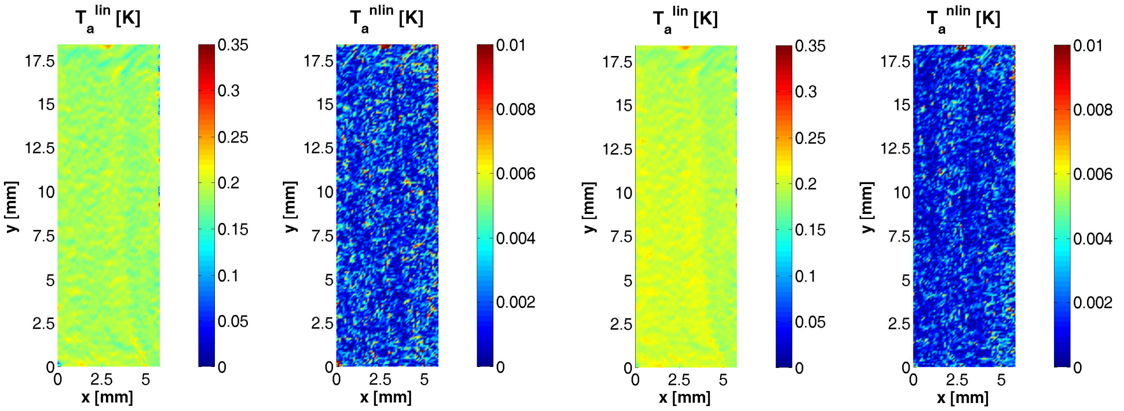

(a) 500 load cycles

(b) 2500 load cycles

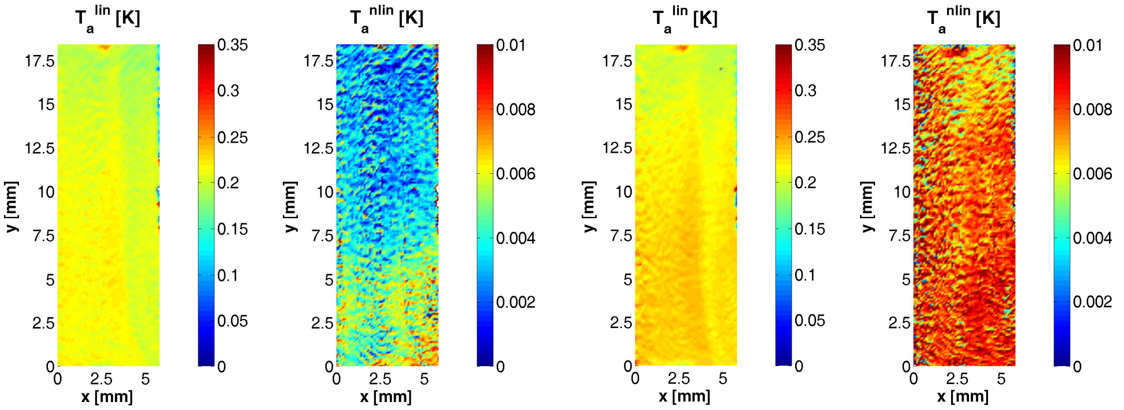

(c) 3000 load cycles

(d) 3500 load cycles

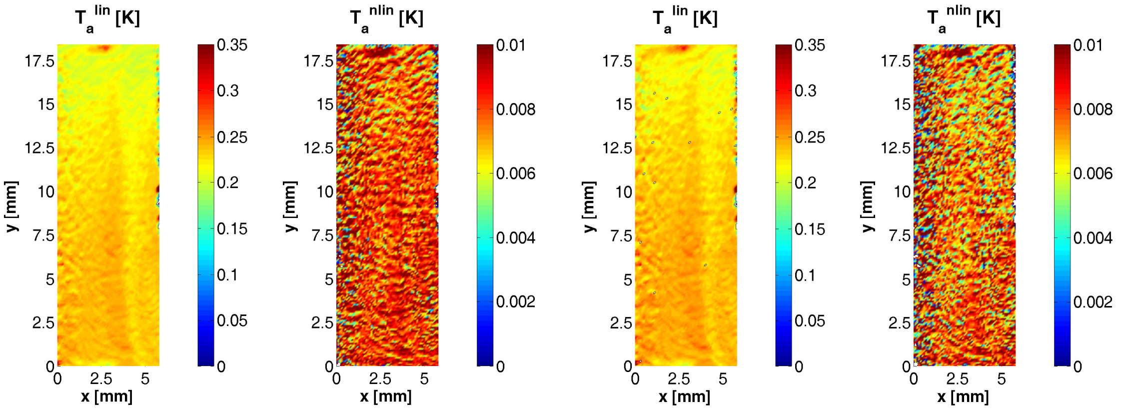

(e) 4000 load cycles

(f) 74500 load cycles

Figure 54: Distribution and evolution of the linear and nonlinear temperature amplitudes; specimen RR0706.

by a sudden increase of the linear temperature amplitudes which cannot be explained in the context of the presented linear theory.

The distribution of the linear and nonlinear temperature amplitudes in figures 54(a) through 54(f) exhibits a characteristic repeatable ripple structure which appears in all images. These ripples appear in a fixed pattern and are not associated with the typical detector noise of the camera. Possible explanations for these ripples are influences from the relative motion and/or deformation of the specimen with respect to the fixed camera position together with inhomogeneities in the surface coating or inhomogeneities in the material itself. The influence of the relative motion within the scenery will be discussed later on.

6.3 Cyclic testing with positive and negative mean stresses

6.3.1 Testing conditions

The next test series was conducted on the same specimen type and similar specimen preparation but at nonzero mean stresses during sinusoidal loading. The load amplitude was held constant at 250 Mpa for all specimens. Different mean loads were used so that the load ratios varied between -0.80 and -1.25. The testing frequency was 2.5 Hz for all specimens as before. The testing conditions of all tests are summarized in tables 3 and 4. The results of specimen RR0721 have been used as reference at zero mean stress for both test series and are therefore repeated in the two tables for convenience.

Table 3: Loading and testing conditions for fatigue testing on cylindrical specimens with $\sigma_m \geq 0$; specimen type I, $\sigma_a \approx 250$ Mpa

Specimen No.	σ_a [MPa]	σ_m [MPa]	R	f_L [Hz]	N_f [lc]
RR0707	251.7	13.3	-0.90	2.5	107.870
RR0714	249.8	20.2	-0.85	2.5	192.550
RR0716	251.5	28.0	-0.80	2.5	100.480
RR0721	254.5	0.0	-1.00	2.5	201.570
RR0726	253.5	6.5	-0.95	2.5	135.260

Table 4: Loading and testing conditions for fatigue testing on cylindrical specimens with $\sigma_m \leq 0$; specimen type I, $\sigma_a \approx 250$ Mpa

Specimen No.	σ_a [MPa]	σ_m [MPa]	R	f_L [Hz]	N_f [lc]
RR0721	254.5	0.0	-1.00	2.5	201.570
RR0728	255.0	-6.5	-1.05	2.5	164.990
RR0729	249.7	-20.3	-1.18	2.5	450.300
RR0730	251.3	-13.2	-1.11	2.5	542.190
RR0731	252.0	-28.0	-1.25	2.5	385.100

6.3.2 Cyclic behavior for $\sigma_m \geq 0$

Figures 55(a), 55(b) and 55(c) show the evolution of the total strain amplitude, the plastic strain amplitude and the mean strains for testing with $\sigma_m \geq 0$. Up to a mean stress level of 20.2 Mpa the evolution of the total strain and plastic strain amplitudes do not show any significant difference to the evolution observed for zero mean stresses. All test results of the plastic and the total strain amplitudes for the four specimens with $\sigma_m \leq 20.2$ MPa fall closely together. Additionally the number of load cycles spent until primary softening is almost the same for all specimens. Apparently the mean stresses did not affect the cyclic stress-strain curve of these four specimens. By contrast the evolution of the plastic strain amplitude of specimen RR0716 subjected to the highest mean stresses differs significantly from the other specimens. For this specimen the total and plastic strain amplitudes are higher with respect to the other specimens and primary softening sets on earlier. The results give evidence to the supposition of [Rei78] that a critical value of the mean stress level exists for which the mean load considerably affects the cyclic stress-strain behavior.

Figure 55(c) shows that with the onset of primary softening positive mean strains evolve for all specimens. For the four specimens with $\sigma_m \leq 20.2$ Mpa the increase rate of the mean strains drops after completion of initial softening. The further growth of the mean strains becomes much smaller than during primary softening. In contrast to the plastic strain amplitudes the mean strains do not completely saturate although the increase of the mean strains becomes relatively small after initial softening. Shortly before failure the mean strains increase rapidly, which might also be caused by crack initiation. The mean strain level reached just before the point of crack initiation increases with growing mean load level but remains within the same order of magnitude as the plastic strain amplitudes. For specimen RR0716 subjected to the highest mean load the increase rate of the mean strains is very high during primary softening and remains high even beyond the initial softening period. In this case the mean strain evolution does not exhibit any saturation although a short phase of retardation in the

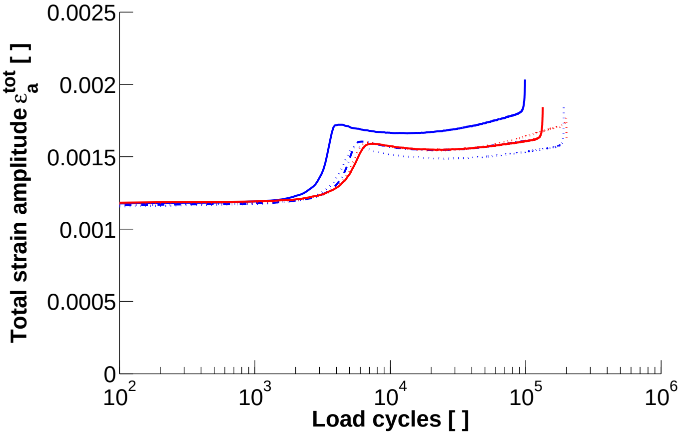

(a) total strain amplitudes

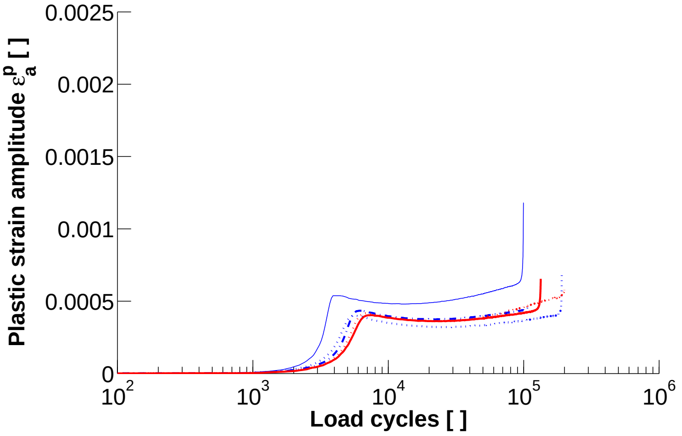

(b) plastic strain amplitudes

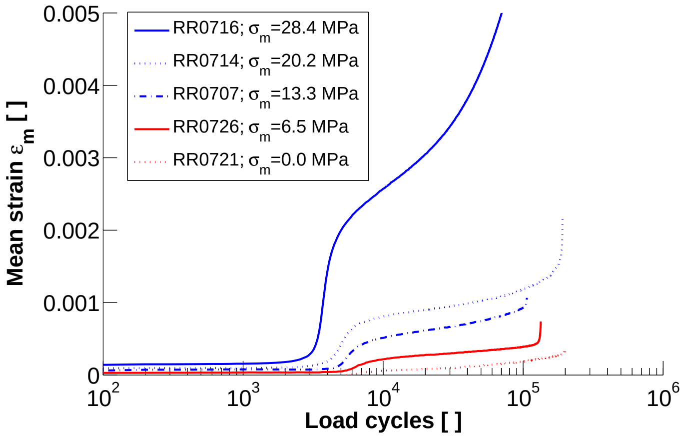

(c) mean strains

Figure 55: Evolution of cyclic total strain amplitudes, plastic strain amplitudes and mean strains; specimen type I, $\sigma_m \geq 0$

mean strain evolution follows onto primary softening. For this specimen the mean strains reach values up to 0.5 % before crack initiation and are therefore significantly larger than the plastic strain amplitude.

6.3.3 Cyclic behavior for $\sigma_m \leq 0$

Figures 56(a), 56(b) and 56(c) show the evolution of the total strain amplitudes, the plastic strain amplitudes and the mean strains for testing with $\sigma_m \leq 0$. The evolution of the total and the plastic strain amplitudes of the two specimens with $\sigma_m = 0$ Mpa and $\sigma_m = -6.5$ Mpa fall close together. By contrast the specimens with higher compressional mean stresses exhibit smaller total and plastic strain amplitudes which indicates an influence of the mean stress on the hardening and softening behavior. However the influence of the compressional mean stresses on the plastic strain amplitudes and on the hardening/softening behavior is less pronounced and less distinct than for tensional mean stresses. Additionally the results indicate that the onset of softening is shifted towards higher load cycle numbers with higher compressional mean stresses.

With the onset of primary softening significant negative mean strains evolve which cause cyclic creep of the specimens (figure 56(c)). The mean strains reach higher compressional values with increasing superimposed mean stresses. The first strong increase of the mean strains ends with the phase of primary softening. After this point the increase rate of the mean strains diminishes significantly. Similar to the results for tensional mean stresses the mean strains do not completely saturate during testing. For the highest compressional mean stress of -28.0 MPa the growth of the means strains is less severe than for comparable tensional mean stresses.

6.3.4 Analysis of the temperature evolution

Similar to the results obtained for loading at $\sigma_m = 0$ the temperature evolution recorded for $\sigma_m \neq 0$ is analyzed with respect to the linear and nonlinear temperature amplitudes. Figures 57(a) and 57(b) show the evolution of the linear and the nonlinear temperature amplitudes for $\sigma_m \geq 0$ according to the conventions for the amplitude values made earlier. Figures 58(a) and 58(b) give the corresponding results for $\sigma_m \leq 0$. As before the linear and nonlinear temperature amplitudes increase with the onset of primary softening and mirror the general softening and hardening behavior.

Interestingly some particularities found for the softening behavior are also reflected by the evolutions of the temperature amplitudes. Specimen RR0730 reached smaller plastic strain amplitudes during testing with $\sigma_m \leq 0$. Accordingly it exhibits smaller nonlinear temperature amplitudes (figure 58(b)). For specimen RR0716 it has been

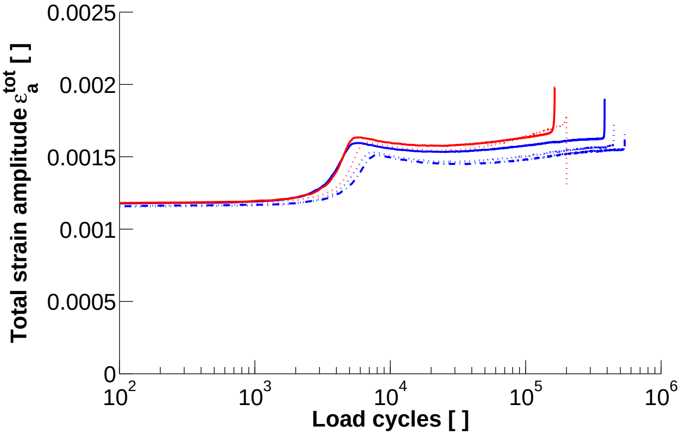

(a) total strain amplitudes

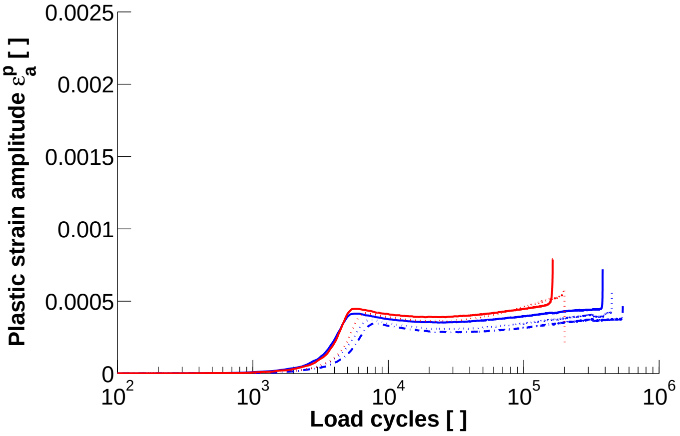

(b) plastic strain amplitudes

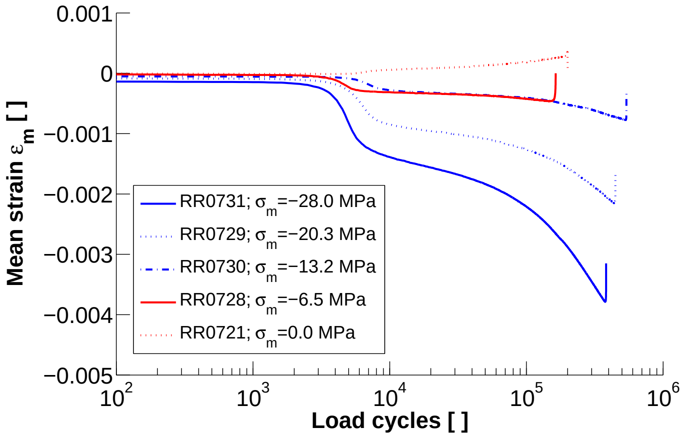

(c) mean strains

Figure 56: Evolution of cyclic total strain amplitudes, plastic strain amplitudes and mean strains; specimen type I, $\sigma_m \leq 0$

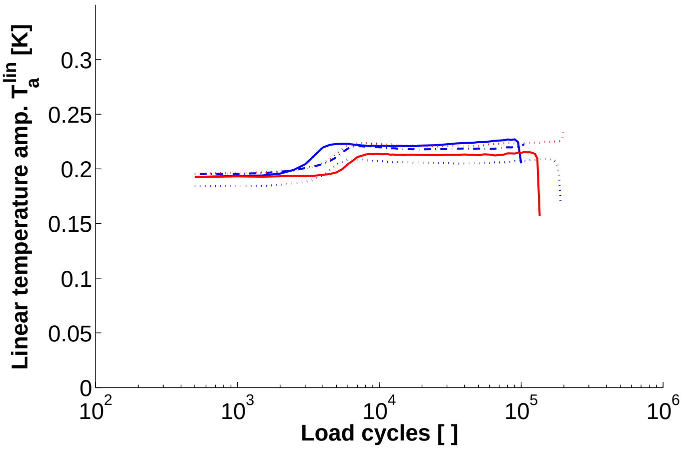

(a) amplitude of linear temperature variations

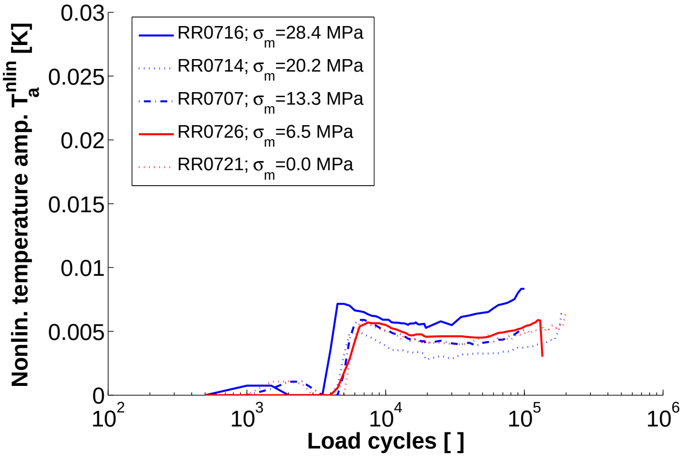

(b) temperature amplitudes of nonlinear temperature variations

Figure 57: Evolution of linear and nonlinear temperature amplitudes; specimen type I, $\sigma_m \geq 0$

shown that the applied mean stress influenced the cyclic behavior and led to higher plastic strain amplitudes. Similar to the strain measurements the corresponding nonlinear temperature amplitude reaches higher values for this specimen compared to the other specimens. By contrast the strong increase of the mean strains observed for this specimen due to cyclic creep does not cause any noticeable change in the general evolution of the linear and nonlinear temperature amplitudes.

From the comparison of the temperature values with the strain measurements it can be concluded that the nonlinearities in the temperature evolution give a close representation of the plastic strain amplitudes. By contrast the evolution of the mean strains do not significantly alter the temperature signals. Potential changes of the linear tem-

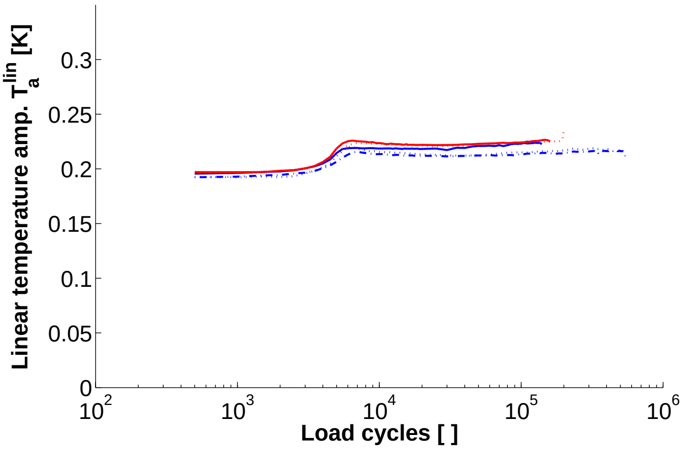

(a) amplitude of linear temperature variations

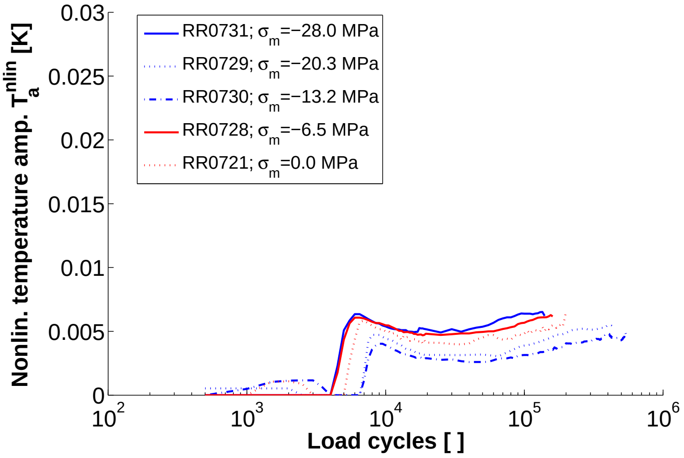

(b) temperature amplitude of nonlinear temperature variations

Figure 58: Evolution of linear and nonlinear temperature amplitudes; specimen type I, $\sigma_m \leq 0$

perature amplitude due to the mean loading cannot be distinguished from the natural scatter between the individual specimens. For a single specimen the assessment of the mean strain evolution based on the analysis of the evolution of the linear temperature amplitudes is complicated due to the variability of the thermoelastic coupling associated with the onset of softening. Possible contributions at higher harmonics are small compared to the effects of plastic dissipation and cannot be retrieved by the proposed data processing. Under thermal aspects fatigue loading at $\sigma_m = 0$ and $\sigma_m \neq 0$ is therefore to be considered as coequal. However the nonlinear temperature amplitudes can be used to study how superimposed mean stresses affect the evolution of the plastic strain amplitudes.

6.3.5 Discussion of the variability of the linear temperature amplitudes

The results for testing with $\sigma_m = 0$ and $\sigma_m \neq 0$ show a significant increase of the linear temperature amplitudes with the onset of primary softening. This increase cannot be explained in the context of the given thermomechanical theory and is discussed here in more detail.

Based on a review of the underlying mechanisms one of the following reasons for the variation of the linear temperature amplitudes is likely:

1 The increase is caused by an increase of the thermoelastic coupling term due to the mean temperature rise with the onset of softening.

2 The data processing is not able to distinguish clearly between linear and nonlinear signal parts which provokes some crosstalk between the linear and nonlinear contributions to the local temperature evolution.

3 The onset of plastic deformations involves some higher order thermomechanical coupling and/or the variation of some material constants.

Explanation 1 can be discarded since all linear temperature amplitudes have been normalized to a standard temperature T_0 according to the explanations given in section 5.4.3.

Explanation 2 is not probable either. The given data processing technique represents a modified version of the classic DFT. Whereas for DFT purely harmonic fitting functions are used the proposed methodology is based on nearly harmonic functions. The ability to separate linear and nonlinear phenomena is comparable for both approaches. The numerical calculations show that the main effect of plastic dissipation is concentrated to the second harmonic in the temperature evolution. A brief check of the orders of magnitude shows that even in case of minor crosstalk (i.e. nonlinearities due to plastic dissipation are partially miss-interpreted as a contribution to the linear temperature variation) all possible influences on the linear temperature amplitude would be at least two orders of magnitude smaller than the observed changes. It can therefore be excluded that the observed variation in the linear coupling is solely based on a miss-interpretation due to crosstalk during data processing.

Explanation 3 needs some further discussion. Figure 59(a) shows the relative increase of the linear temperature amplitudes as a function of the plastic strain amplitude ε_a^p. Figure 59(b) relates the increase to the absolute maximum plastic strains $abs(\varepsilon_{max}^p) = abs(\varepsilon_m) + \varepsilon_a^p$ reached during the fatigue loading. All values represent the measurements after 40000 load cycles, which correspond to a quasi-saturated regime of the plastic strain amplitudes for all specimens. The results show that the increase of the 'linear' temperature amplitudes can reach values which are up to 25 % higher than those due to the original thermoelastic coupling. This is much larger than any possible effect of plastic dissipation on the temperature amplitudes. From figure 59(a) it becomes obvious that the relative increase of the 'linear' temperature amplitudes is strongly dependent on the actual plastic strain amplitude. By contrast its dependency on the maximum plastic strains is rather vague (figure 59(b)).

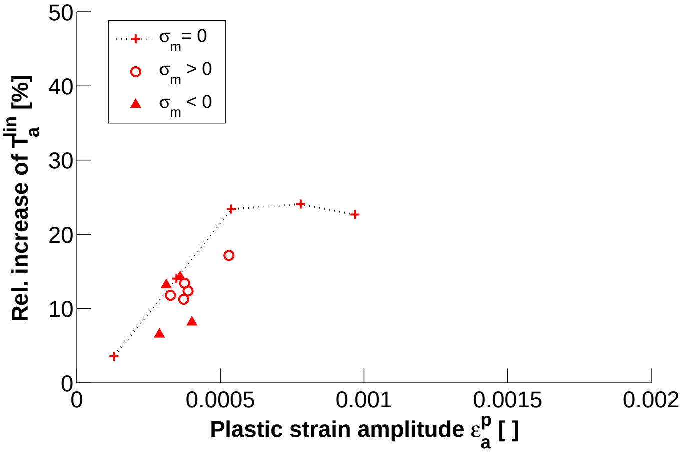

(a) linear temperature amplitudes vs. plastic strain amplitudes

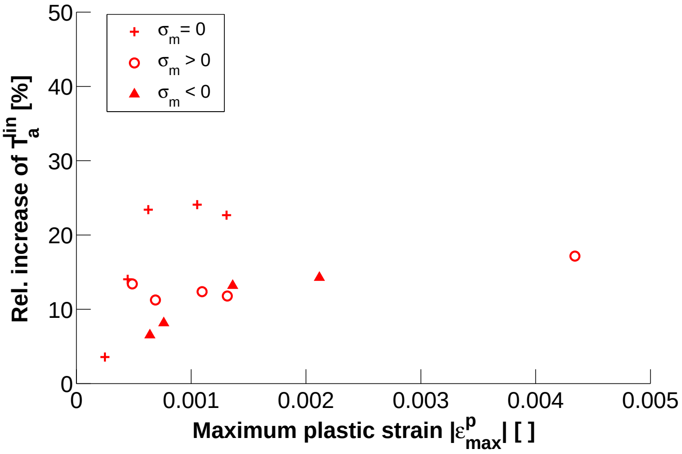

(b) linear temperature amplitudes vs. maximum plastic strains

Figure 59: Relative increase of the linear temperature amplitudes after softening with respect to plastic strains; specimen type I

The observed characteristics suggest a higher order coupling phenomena which has not been taken into account yet. In the framework of the thermomechanical theory given in chapter 4 the observed phenomena manifests in an apparent rise of the thermoelastic coupling term with ongoing evolution of plastic deformations. This indicates that one or more of the material parameters depend on the hardening state. The most suspicious material parameter is the coefficient of thermal expansion for which [RS50] and [RA56] reported a significant increase with ongoing plastic deformation. Additionally the observed phenomenon explains to some extent the findings of [KP02] that the fatigue limit of different metals is indicated by an increase of the first harmonic temperature amplitude. In a more elaborated thermomechanical framework the observed changes can possibly be associated with additional coupling terms which depend on the damage state, the hardening state or other factors. Since the variation of the linear temperature amplitudes is rather pronounced and relatively easy to assess experimentally, its incorporation in a thermomechanical framework bears high potential for future thermographic assessment of damage or hardening states. The observed phenomenon will be referred to as variation of the thermoelastic coupling with the onset of plastic deformations.

6.4 Fatigue testing of notched specimens

6.4.1 Testing conditions and parameter variation

Next the observations made above are generalized to the mildly notched specimen type II which involves localized plastic deformations. Fatigue testing was performed as single-step test under load-controlled harmonic loading at zero mean stress. Pretests showed that the localization of plastic dissipation allowed to increase the testing frequency up to 15 Hz without risking excessive self-heating of the specimens. Testing was terminated by failure of the specimens or after completion of $2.5 \cdot 10^6$ ($1.3 \cdot 10^6$ for specimen RK0621) load cycles. Crack initiation occurred within the notch for all failed specimens.

During fatigue testing IR measurements and additional light-microscopic investigations of the surface changes were performed. The light-microscopic observations were conducted in situ either within the nominal cross-section of the specimens or within the notch, without removing the specimens from the testing machine. The preparation of the specimens consisted of mechanical polishing and annealing of the specimens after manufacture. As preparation for the microscopic investigation the center part of the specimens was slightly etched before testing with a 3 % Nital solution which revealed the ferritic-perlitic grain structure. Graphite coating (Graphit 33, Kontakt Chemie) was applied to all specimens to ensure high emissivity. The microscopic investigations were performed at an un-coated reference window, where the metallic surface was directly accessible. The window was prepared by attaching a small (1.5 mm x 8 mm) self-adhesive strip to the specimen surface before coating. The strip was removed before testing and left a small un-coated window of the blank metallic surface (compare figure 60).

The microscopic investigations consisted of a surface scan of the un-coated reference

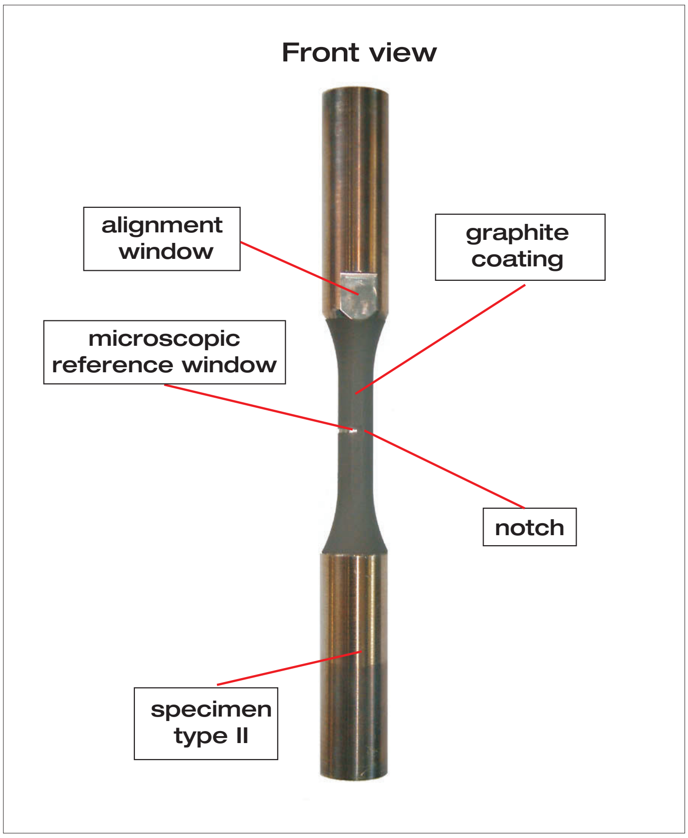

Figure 60: Specimen preparation; specimen type II

window. During each scan multiple contiguous images were taken which covered the entire width of the reference window. The microscopic investigations required an interruption of the fatigue testing during which loading was held constant at zero force. The microscopic scan and positioning of both camera systems was realized with an automated 3-axes positioning system described in appendix II. Prior to each scan the position of the axes were corrected based on an image correlation procedure of the microscopic scene with respect to a reference image of the same surface detail taken at the beginning of the test. The procedure corrected for small drifts in the positioning system and ensured an overall repositioning accuracy around 1 μm. This guaranteed that identical surface details were investigated each time. The IR measurements compromised the acquisition of 2000 single pictures with an image size of 192 x 300 pixels which were taken at the maximum camera frame rate achievable at this resolution (412.5 Hz). At the chosen loading frequency of 15 Hz this corresponded to sampling of a load cycle by approximately 27 single IR measurements which has been found to be sufficient over-sampling for further data processing. The IR measurements were triggered just before interrupting the fatigue loading for the microscopic investigations. All IR measurements were conducted during thermal equilibrium conditions. Table 5

Table 5: Loading conditions for notched specimens

Specimen No.	F_a	$\sigma_{a,0}$ [MPa]	$\sigma_{a,N}$ [MPa]	$\sigma_{m,0}$ [MPa]	f_L [Hz]	N_f [lc]
RK0603	17000	217	293	0	15	1,400,900
RK0605	18000	233	308	0	15	406,170
RK0606	18500	239	319	0	15	264,540
RK0608	17250	223	298	0	15	711,540
RK0614	16500	212	286	0	15	$>$ 2,500,000
RK0617	17000	223	293	0	15	783,380
RK0618	18000	231	305	0	15	477,140
RK0621	16500	215	290	0	15	$>$ 1,300,000
RK0624	18500	242	319	0	15	218,180
RK0625	17500	226	302	0	15	486,930
RK0626	17750	233	304	0	15	388,690
RK0627	17500	225	298	0	15	619,640
RK0628	16750	214	281	0	15	$>$ 2,500,000
RK0631	18250	237	307	0	15	256,050

summarizes the loading parameters, the failure load cycles N_f and the corresponding von Mises stress amplitudes in the nominal cross-section $\sigma_{a,0}$ and at the center of the notch $\sigma_{a,N}$ for all specimens. The stress values have been calculated based on a linear elastic FEM-analysis using the actual geometry of the specimens measured after manufacturing. Table 6 gives an overview of the corresponding sampling conditions used for the different specimens.

6.4.2 Data processing - Motion compensation

The IR measurements are analyzed with the processing procedure described in section 6.2.4. As earlier linear and non-linear temperature amplitudes,the phase shift with respect to the linear reference signal and the mean temperature are calculated. Here only the amplitude values are discussed further. The linear reference signal is generated of the recorded temperature values itself using the spatial mean value of a 3 x 3 pixel neighborhood within the nominal cross-section of the specimens at the beginning of fatigue testing. At this time linear-elastic conditions can be assumed for all specimens. In addition to the fitting procedure discussed earlier, the recorded data is preprocessed by a motion compensation scheme which has been implemented in Matlab R14. The motion compensation assures that subsequent pictures of the recorded picture stream represent an identical surface detail of the specimen, so that the following temperature analysis is not distorted by blur effects within the scenery.

Table 6: Testing parameters for notched specimens

Specimen No.	IR-measurements after [lc]	micro. pictures @
RK0603	100, 500, 1000, 2500, 5000, 7500, 10000, 12500, 15000 ... every 15000	nominal cross-sect.
RK0605	100, 500, 1000, 2500, 5000, 7500, 10000, 12500, 15000 ... every 15000	nominal cross-sect.
RK0606	100, 500, 1000, 2500, 5000, 7500, 10000, 12500, 15000 ... every 15000	nominal cross-sect.
RK0608	every 15000	notch
RK0614	every 30000	notch
RK0617	every 15000	notch
RK0618	every 15000	notch
RK0621	500, 5000, 10000, 20000 ... every 20000	notch
RK0624	every 15000	notch
RK0625	every 15000	notch
RK0626	every 15000	notch
RK0627	100, 500, 1000, 2500, 5000, 7500, 10000, 12500, 15000 ... every 15000	nominal cross-sect.
RK0628	every 20000	notch
RK0631	every 15000	notch

This compensation is applied off-line after recording and before further analysis of the temperature values. The scheme is based on normalized cross-correlation between the individual pictures of the recorded stream with respect to a reference picture taken of the unloaded specimen at the beginning of the fatigue test. The compensation takes into account solid body motion whereas possible deformations of the specimen surface due to the mechanical loading are ignored. Since the regular cross-correlation scheme operates at discrete pixel intervals an additional interpolation scheme has been developed. The scheme allows for sub-pixel accuracy and achieves a typical resolution of the displacement vector in the order of 1/100 pixel. The working principle of the compensation scheme is clarified in figure 61. For the motion compensation the cross-correlation with interpolation is used to retrieve the position of the highly reflective un-coated steel surface used for the microscopic investigations. This surface detail represents the only high-contrast template of the otherwise uniformly coated specimen.

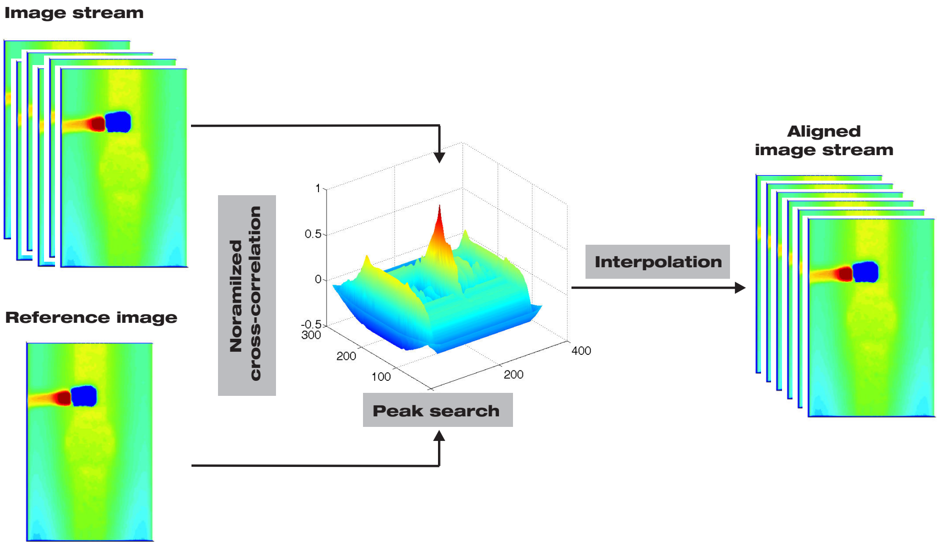

Figure 61: Motion compensation scheme

Without motion compensation severe blur effects have been observed which have been mainly attributed to small emissivity heterogeneities of the surface. These heterogeneities cause apparent periodic temperature changes if the surface moves parallel to the camera position due to mechanical loading and vibrations of the setup. To demonstrate the necessity for a motion compensation scheme, figure 62 shows a 3-D view of the linear and the nonlinear temperature amplitudes calculated for the same IR-sequence with (figure 62(b)) and without (figure 62(a)) motion compensation. Both results have been obtained using the separation procedure for linear and non-linear temperature amplitudes discussed earlier. The (meaningless) temperature values associated with the un-coated blank reference window and the pixel rows/columns directly located at the border of the scenery - which are strongly affected by motion - have been set to zero.

The linear temperature amplitudes without motion compensation exhibit an unequal distribution between the left and the right side of the specimen surface and contain additional noise. Even after clipping the 5 outermost pixel rows of the images the borderlines of the scenery are still strongly affected by motion blur. The calculated nonlinear temperature amplitudes are very noisy, unstructured and do not allow to retrieve any meaningful information (figure 62(a)) regarding local damage processes. Figure 62(b) shows that the applied motion compensation almost completely removes the uneven distribution of the linear temperature amplitudes and reduces all disturbances at the borderline of the images. After clipping of the 5 outermost pixel lines no disturbances appear any longer at the borders of the scenery and the spatial distribution of the linear temperature amplitudes becomes much more homogenous. The

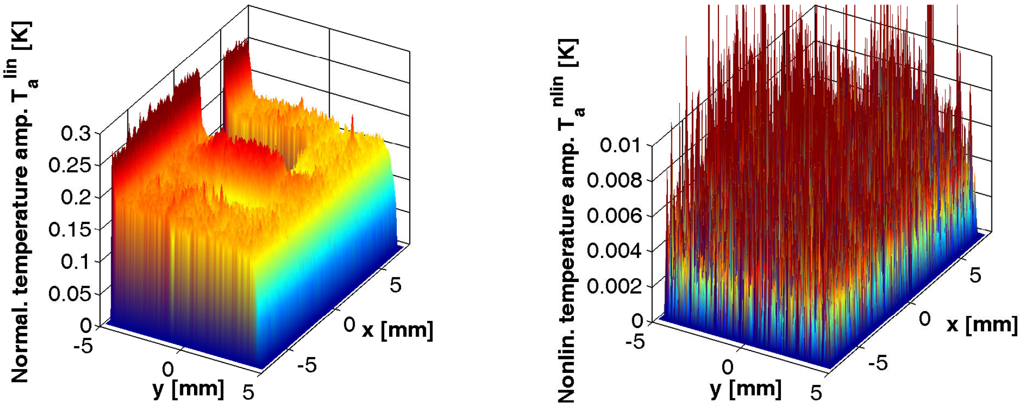

(a) without motion compensation

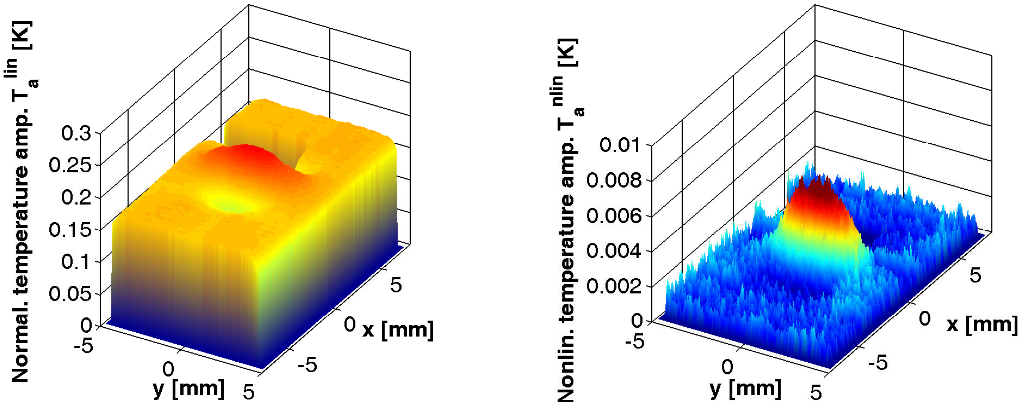

(b) with motion compensation

Figure 62: Comparison of linear and nonlinear temperature amplitudes evaluated with and without motion compensation scheme; specimen type II

non-linear temperature amplitudes are strongly smoothed and reveal significant nonlinearities at the bottom of the notch. This indicates localized plastic dissipation in this area (figure 62(b)).

Figures 63(a) and 63(b) show the reconstructed displacement vectors in the x and y directions for the individual frames with respect to the initial reference scenery. The displacements are periodic with a near sinusoidal variation in the y-direction and non-harmonic variation in the x-direction. The offset of the mean displacement in the x-direction indicates long-term changes with respect to the initial configuration. This is mainly caused by settling effects of the IR camera which has been bedded on a foam-like shock-absorbing material. The varying component of the displacement is small with an amplitude of approximately 2 pixels in the x-direction and 1.2 pixels

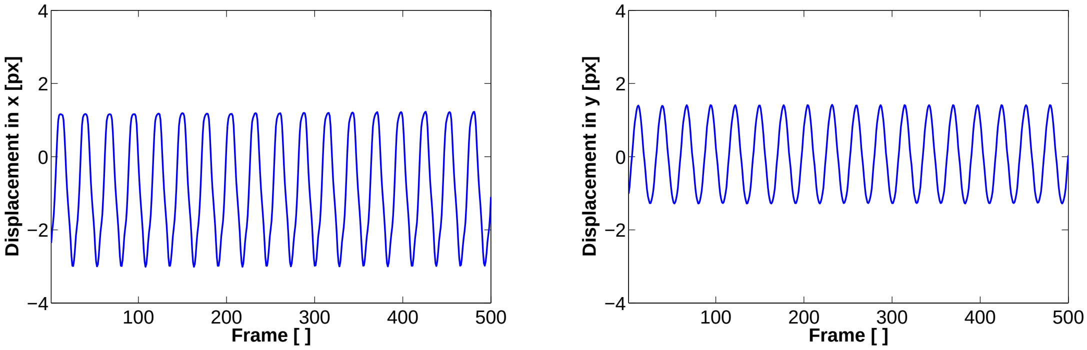

(a) displacement in x-direction

(b) displacement in y-direction

Figure 63: Displacements in x and y- direction calculated by motion compensation scheme; specimen type II.

in the y-direction. The significant influence of these small displacement values on the amplitude distribution shown in figure 62 points out the necessity to compensate even for small movements in between the individual frames of the IR-recording prior to further analysis of the temporal evolution.

6.4.3 Analysis of the temperature evolution

Figures 64(a) and 64(b) show the evolution of the linear and the nonlinear temperature amplitudes of a single point within the center of the notch. Both amplitude values exhibit a very good repeatability from one measurement to another with small fluctuations. The evolution of the nonlinear temperature amplitudes within the notch shows some difference to the results obtained for the unnotched specimens. Similar to the unnotched specimens softening sets on within the notch after a phase of linear elastic behavior and leads to increasing nonlinearities in the temperature signal. For small load amplitudes the nonlinear behavior nearly saturates after an initial phase and remains relatively constant upon crack initiation. For higher load amplitudes the nonlinear behavior within the notch does not come to complete saturation or only exhibits a short period of saturation. Compared to the cylindrical specimens the phase of primary softening is more extended. For most of the higher loaded specimens the plastic strain amplitudes increase until crack initiation. This shows that the behavior at the notch bottom is dominated by softening processes until crack initiation.

For none of the specimens any indication of hardening (a reduction of the nonlinear temperature amplitudes) of the material within the notch could be found. All findings correspond well to results reported by [Böh85] based on strain gauge measurements at specimens wit different notch factors. The extension of the softening phase can be explained by the stress gradient in the vicinity of the notch. Softening starts

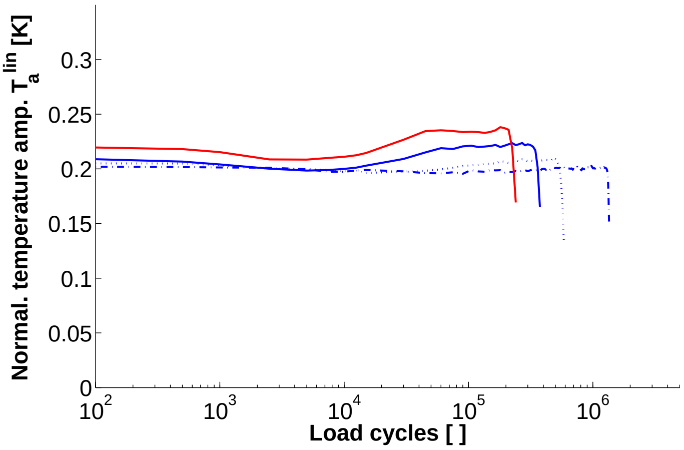

(a) linear temperature amplitude

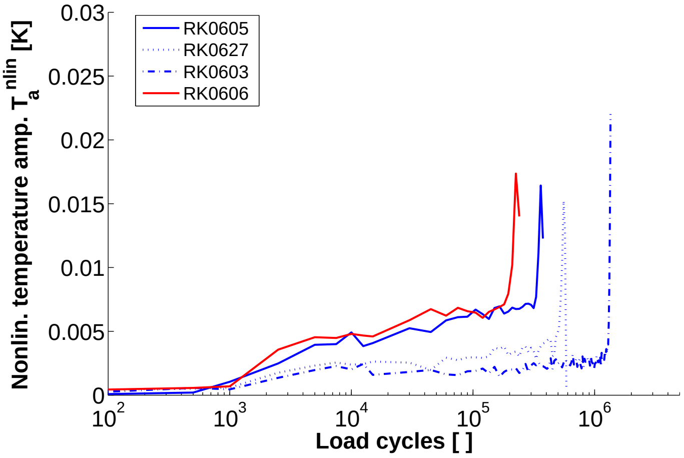

(b) nonlinear temperature amplitude

Figure 64: Evolution of the linear and nonlinear temperature amplitudes at the center point of the notch; specimen type II

at the bottom of the notch where the highest stress amplitudes are present. Due to the stress gradient the plastically deformed areas are initially supported by the surrounding stiffer elastic material until softening subsequently moves on to points with lower stress amplitudes. With the propagation of plastic deformations to the surrounding areas the support of the material within the notch becomes weaker which causes an overall increase of plastic strains. Accordingly the softening behavior for a given location within the notch depends not only on the cyclic material behavior itself but is also affected by the complicated stress redistribution associated with the onset of plastic flow. Overall the interdependency of the softening behavior and the local stress situation causes a slower saturation of plastic strains.

The evolution of the linear temperature amplitudes given in figure 64(a) exhibits a remarkable difference to the evolution of the unnotched specimens. Whereas for the cylindrical specimens the linear temperature amplitudes increase directly with the onset of primary softening, the linear amplitudes within the notch initially drop with the onset of plastic flow before they increase again after a certain number of load cycles. The increase following onto softening is more pronounced for specimens with higher stress amplitudes. After this initial phase the linear temperature amplitudes remain relatively constant until crack initiation. Depending on the applied stress amplitude the linear temperature amplitudes saturate below or above the initial value at the beginning of the test.

It is supposed that the observed behavior within the notch is caused by a superposition of two individual phenomena. First, together with the onset of plastic deformations within the notch, stresses are redistributed to stiffer areas so that the stress exposition within the notch becomes smaller. Accordingly the linear temperature amplitudes drop. A similar drop of the temperature amplitudes within geometric notches has been reported by [Mül89] on specimens of St37-2 based on measurements with thermocouples. In contrast to these results the decrease of the temperature amplitudes observed during the present studies starts much earlier and is not as pronounced. This suggests that different phenomena have been observed. It is supposed that the reduction of the temperature amplitudes observed by [Mül89] might have been caused by an early crack initiation.

The subsequent increase of the temperature amplitudes cannot solely be explained by the softening behavior. Instead it is assumed that during initial softening the reduction of the stresses at the notch bottom is not fully compensated by the variation of the thermoelastic coupling discussed in section 6.3.5. With further softening higher overall plastic strain amplitudes are reached in the vicinity of the notch which cause a subsequent rise of the thermoelastic coupling. Accordingly the observable linear temperature amplitudes start to grow again if the rise of the linear thermoelastic coupling exceeds the drop of the stress amplitudes within the notch.

Figure 65 shows the evolution of the linear and nonlinear temperature amplitudes along the longitudinal surface centerline y=0 of specimen RK0603 against the number of applied load cycles. The dark lines in the diagram represent the measured values. The intermediate color shading is based on temporal interpolation of the results which gives a better impression of the evolution. The notch bottom and the edges of the notch are marked by elevated and lower linear temperature amplitudes respectively, with respect to the nominal cross-section. The zero values around x=5 mm are associated with the microscopic reference window with negligible thermal emissivity. The representation confirms the general trend in the linear and nonlinear temperature amplitudes as discussed earlier for the single point evolution. A comparison of the evolution of the

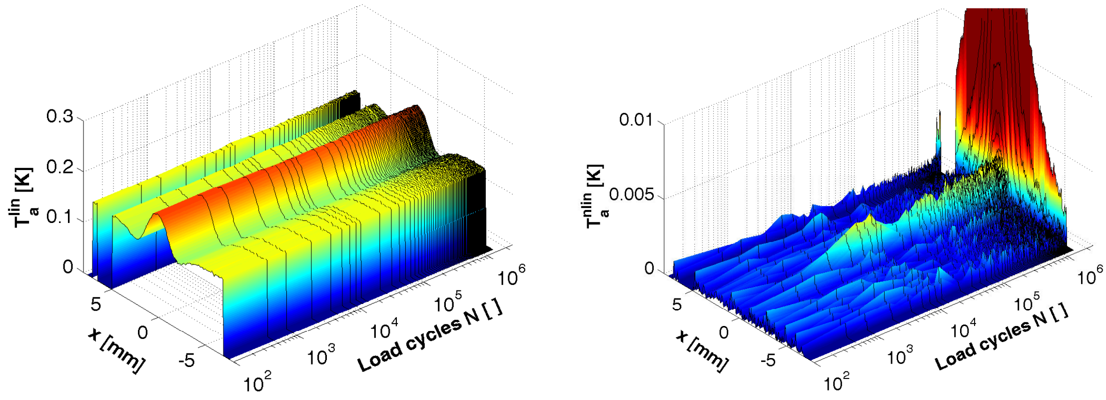

Figure 65: Evolution of linear and nonlinear temperature amplitudes at the centerline y=0; specimen RK0603

linear and nonlinear temperature amplitudes verifies a slight decrease of the linear temperature amplitudes within the notch which falls together with the appearance of nonlinearities in the temperature signal. The crack initiation is marked by a strong increase of the nonlinear temperature amplitudes.

6.4.4 Discussion of the fatigue behavior and comparison with microscopic investigations - example

Based on a typical example (specimen RK0618) figure 66-4 compares the infrared thermographic results with corresponding microscopic observations. The infrared results are given as the distribution of the linear and nonlinear temperature amplitudes. The left microscopic image shows the characteristic damage evolution on the un-coated surface within the notch of the specimen. Due to the etching with Nital ferritic and pearlitic grains appear bright and dark respectively in the microscopic images. The right microscopic image is a difference picture of the actual scenery with respect to the same surface detail taken at the beginning of the fatigue testing. The calculation of the difference images requires exact matching of the microscopic images. This has been realized by applying the sub-pixel motion compensation scheme developed for the IR sequences to the microscopic images. In the difference image variations with respect to the reference scenery appear dark and equal (constant) parts are bright.

The spatial distribution of the linear temperature amplitudes reveals the stress concentration at the notch as shown in chapter 5 by the numerical investigations. The first IR-images have been taken at 3 % of the total fatigue lifetime of the specimen. At this point softening has already set on within the notch which is indicated by the elevated nonlinear temperature amplitudes which remain concentrated to the notch bottom. The microscopic images show that at this point the first slip bands appear

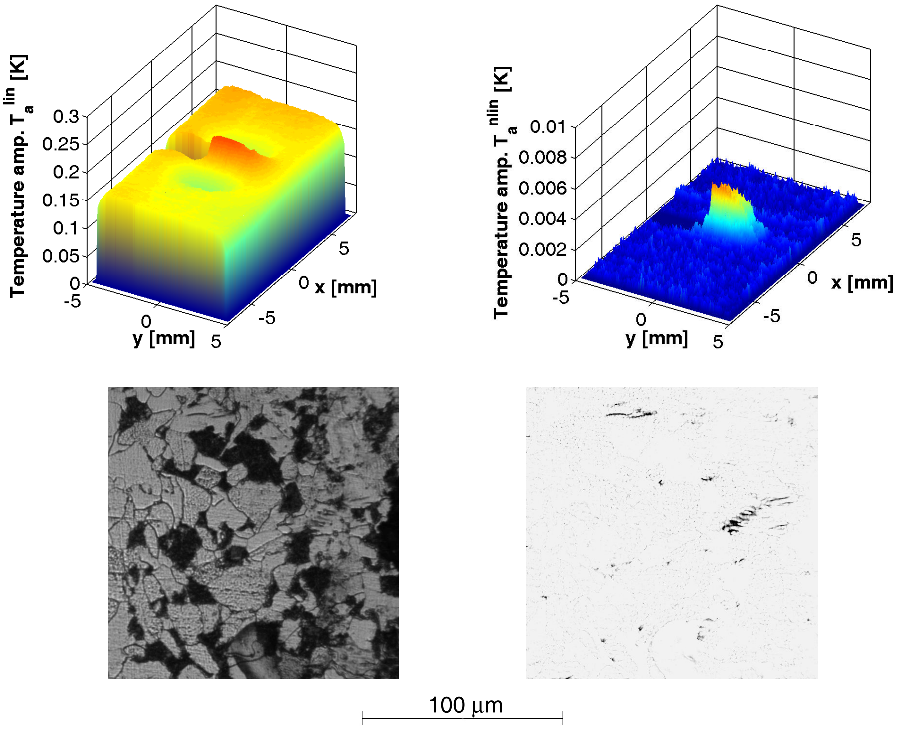

$N = 15000;\ N/N_f = 0.03$

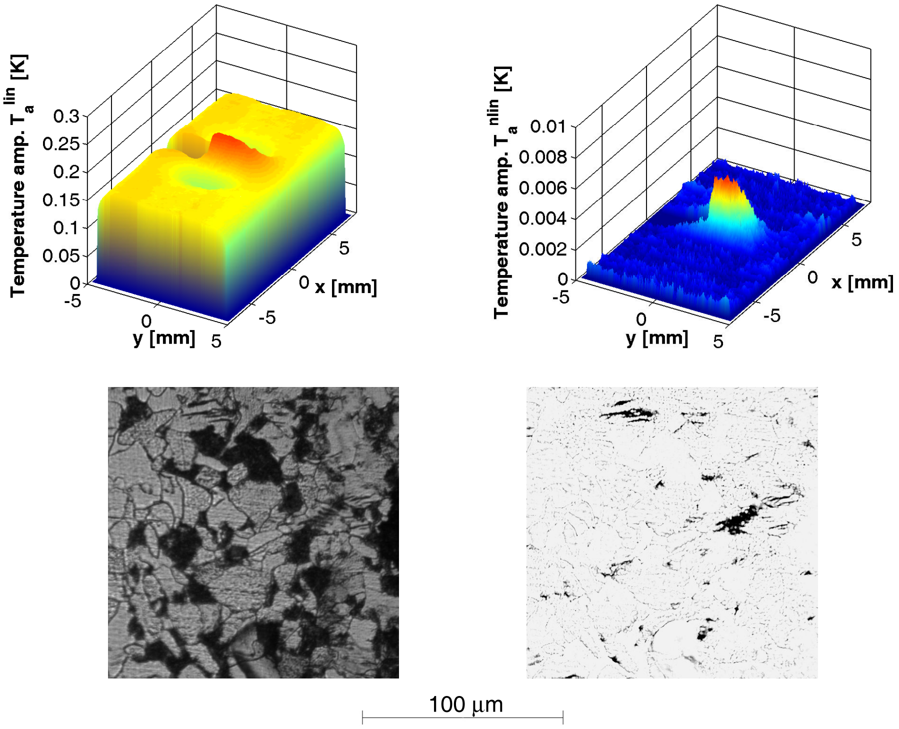

$N = 45000;\ N/N_f = 0.094$

Figure 66-1: Linear and nonlinear temperature amplitudes and microscopic images of the notch showing the typical damage evolution; specimen RK0618

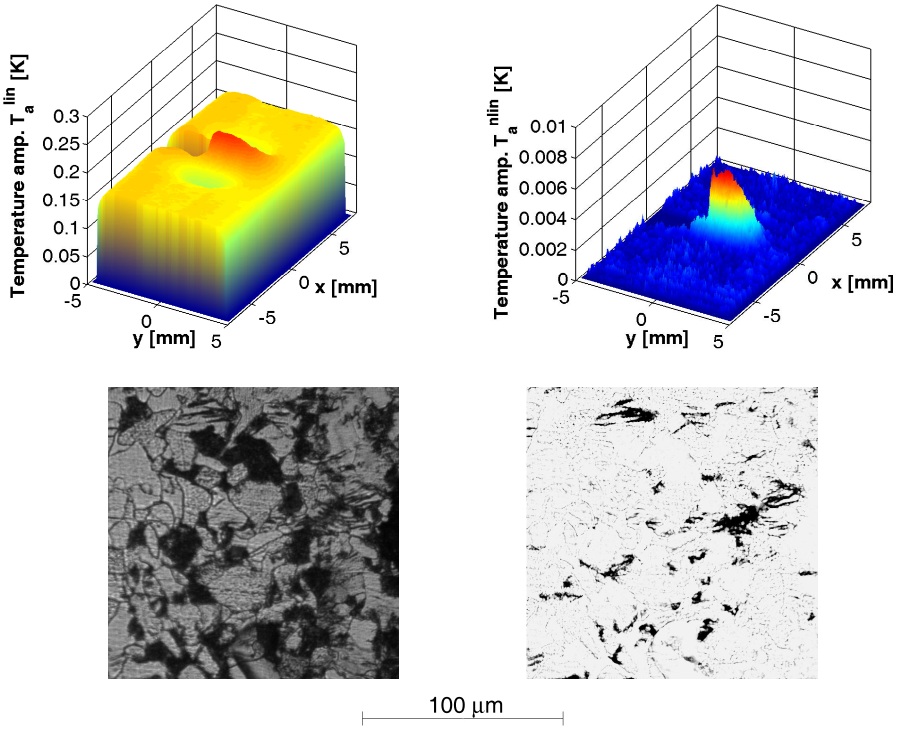

$N = 105000;\ N/N_f = 0.224$

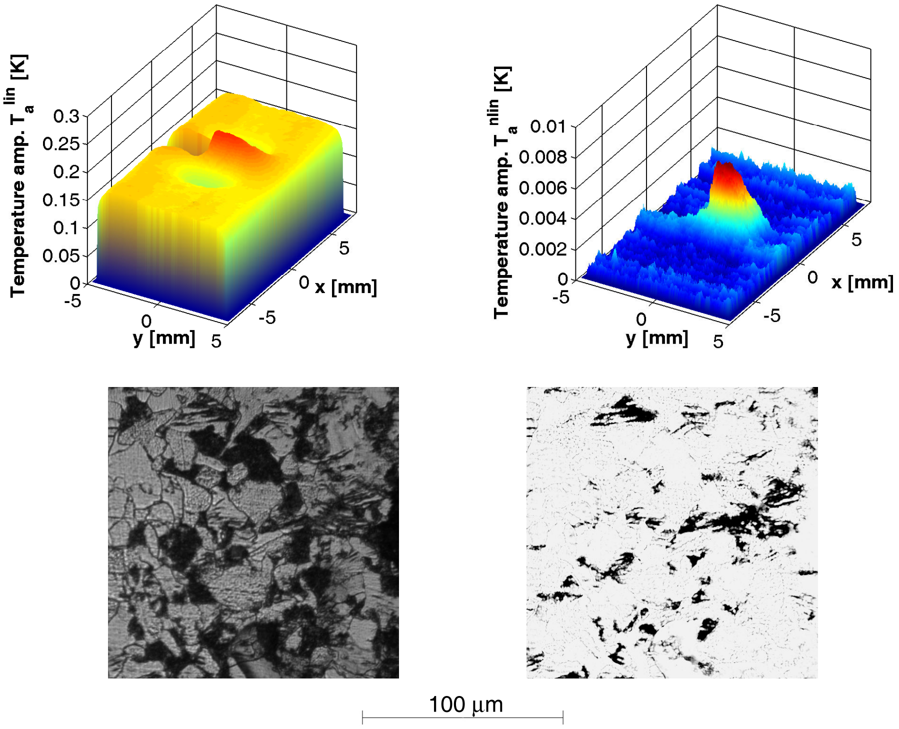

$N = 225000;\ N/N_f = 0.47$

Figure 66-2: Linear and nonlinear temperature amplitudes and microscopic images of the notch showing the typical damage evolution; specimen RK0618

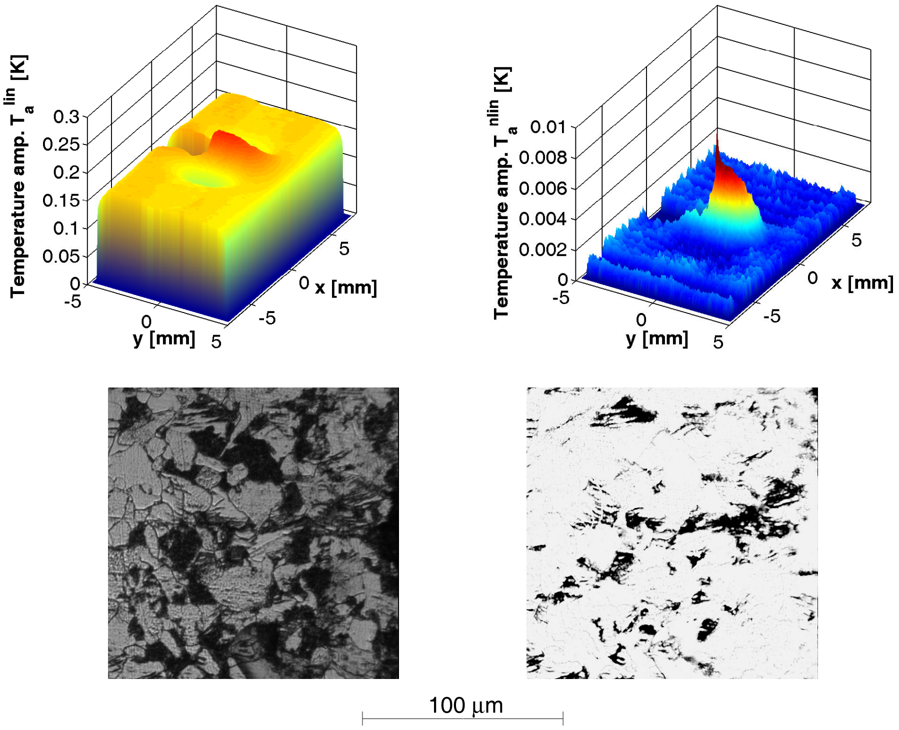

$N = 330000;\ N/N_f = 0.69$

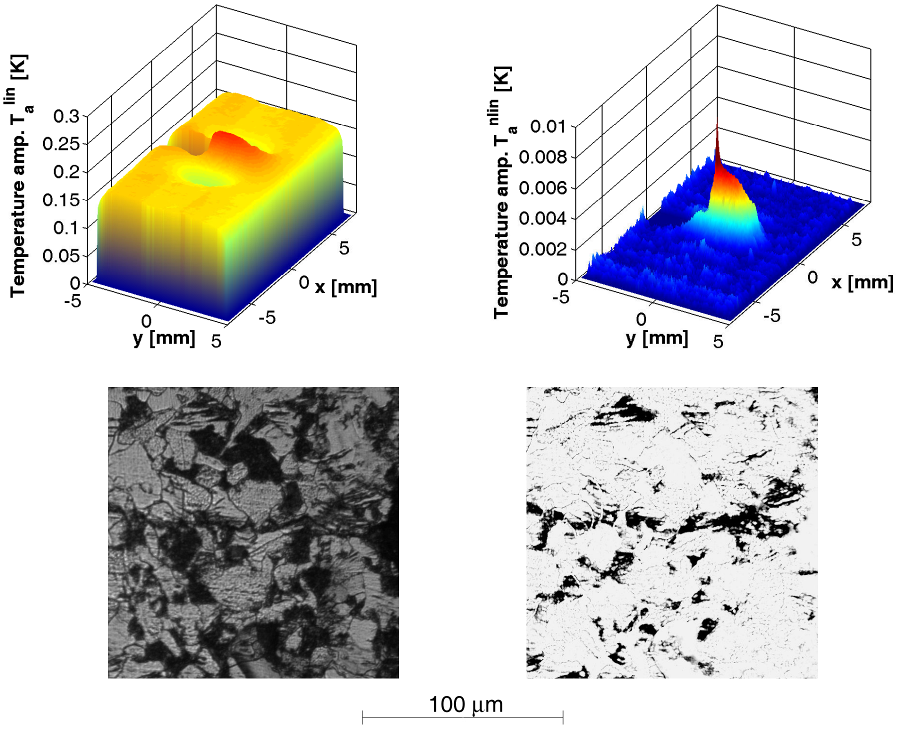

$N = 390000;\ N/N_f = 0.82$

Figure 66-3: Linear and nonlinear temperature amplitudes and microscopic images of the notch showing the typical damage evolution; specimen RK0618

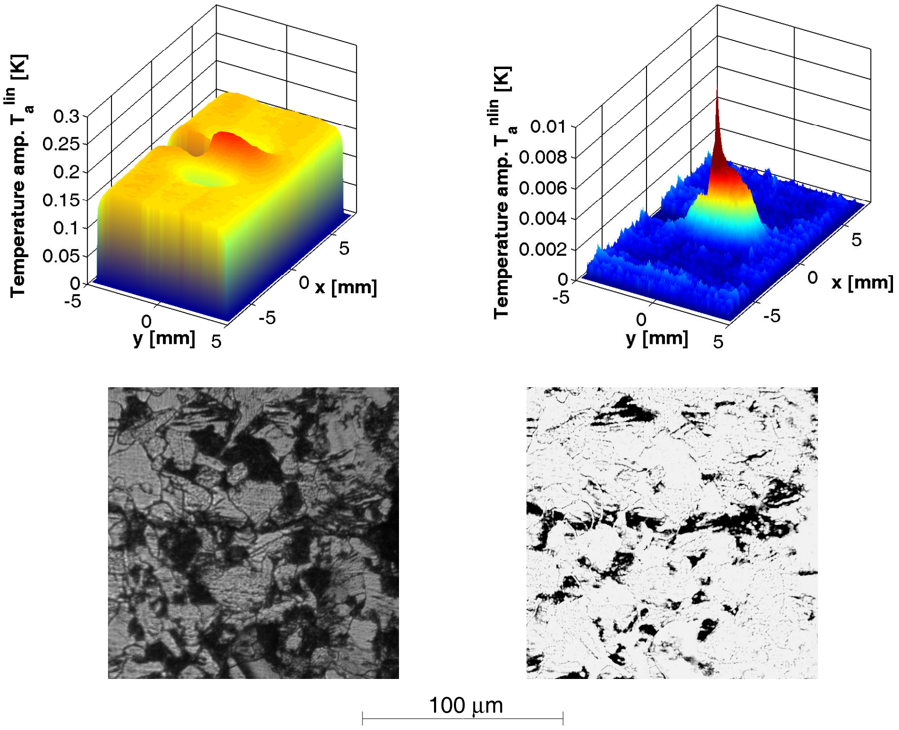

$N = 405000;\ N/N_f = 0.85$

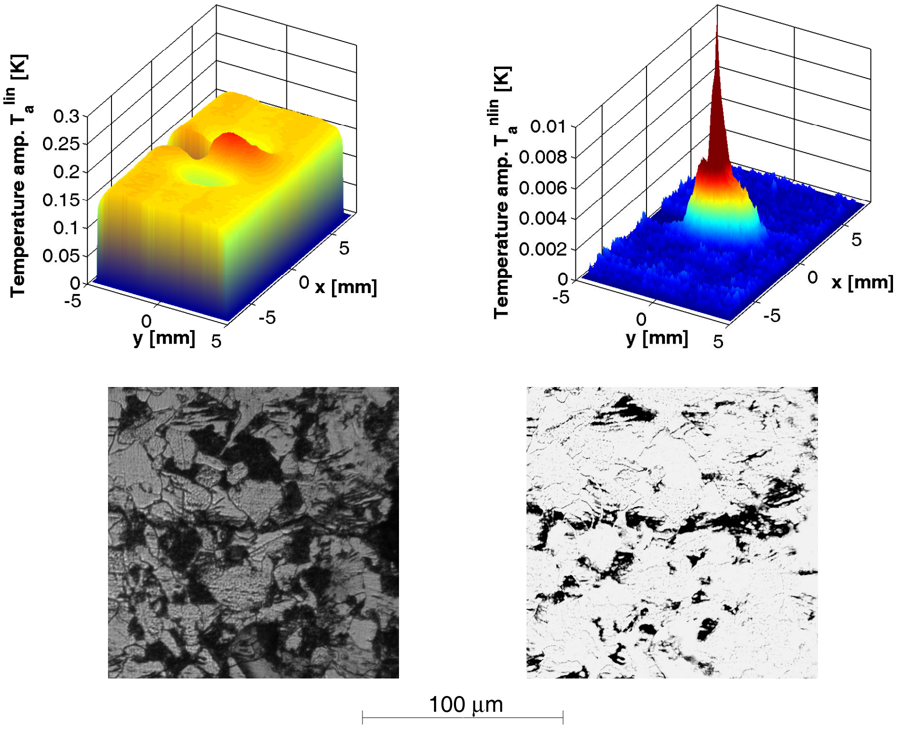

$N = 420000;\ N/N_f = 0.88$

Figure 66-4: Linear and nonlinear temperature amplitudes and microscopic images of the notch showing the typical damage evolution; specimen RK0618

within individual ferritic grains. The overall number of slip bands within individual grains and the number of grains displaying slip bands is still small. The poor contrast of the images in the pearlitic phase does not allow for an investigation of slip band formation in the pearlitic grains. However based on the discussion given in chapter 3 it can be assumed that plastic deformations remain mostly confined to the softer ferritic phase.

At around 10 % of the relative lifetime softening is mostly terminated and the nonlinear temperature amplitudes have reached a quasi-saturated state. The microscopic images reveal that the slip band density and the number of grains with slip bands has increased with respect to the situation at the beginning of softening.

At 22.5 % of the fatigue lifetime the number of ferritic grains with clearly distinguishable slip bands does not change significantly anymore. By contrast the number of individual slip bands within the grains is still growing. At the right border of the microscopic image an area with high slip band density has formed. In this area multiple grains are concentrated with a high overall slip band density. No indication of an inclusion or any other surface flaws could be found by closer microscopic examination of this area.

At around 47 % of the fatigue lifetime the microcrack has grown to a size of 4 grain diameters within the microscopic investigation area. Its potential growth beneath the graphite coating at the right border of the surface detail is unclear. The number of grains with slip bands and the number of slip bands within individual grains has completely saturated in the investigated surface area with the exception of grains in the direct path of the microcrack. The slip bands in all grains are still growing and seem to be deepening. Based on the microscopic investigations a clear distinction between slip bands and beginning microcracks is not completely possible.

At 69 % of the fatigue lifetime the nonlinear temperature amplitudes next to the microscopically inspected surface detail suggest the presence of a crack which has reached a length of approximately 80 μm in the microscopic image. In the following the nonlinear temperature amplitudes increase strongly in the close vicinity of the crack. The increase of the nonlinear temperature amplitudes is not caused solely by plastic deformation at the crack tip but also by geometric nonlinearities as crack closure due to the presence of the crack. The investigations of [Hus94] show that these geometric nonlinearities can exceed by far the nonlinear behavior due to crack tip plastic dissipation.

At around 85 % of the total lifetime the linear temperature amplitudes show small variations due to the presence of the crack. Now, beside the increase of the nonlinearities in the temperature evolution, the stress concentration at the crack tip also causes an elevation of the linear temperature amplitudes. The flanks of the propagating crack are indicated by reduced linear temperature amplitudes. The rest of the specimen lifetime is governed by crack propagation.

6.4.5 Discussion of the fatigue behavior and comparison with microscopic investigations - summary of the fatigue behavior

The reduction of information to a single characteristic line (figure 65) allows to represent the results of the temperature evolution of all specimens in relatively compact form. In appendix III the evolution of the temperature amplitudes at the centerline y=0 and the corresponding microscopic surface images at different relative lifetimes are given for each specimen. The microscopic images represent a small characteristic detail of the entire surface scan. If possible a detail which contains the final macro-crack initiation has been chosen. For all specimens pseudo temperature values associated with the un-coated reference window used for the microscopic investigations are set to zero as earlier. Note that the last microscopic difference pictures are often corrupted by the large distortions of the image associated with crack formation and propagation. These distortions cannot be completely compensated by the chosen matching procedure and lead to false results in the difference image.

All specimens show a comparable softening behavior to that discussed above. Generally cyclic softening at the notch sets on within the first thousands of load cycles. For some specimens softening has already come to an end before the first infrared images were taken and can therefore not be characterized in more detail. From the available results it can be concluded that the onset of softening is shifted towards higher load cycle numbers with decreasing stress amplitudes. For stress amplitudes below 230 Mpa in the nominal cross-section plastic deformations remain confined to the notch during the entire test. For higher nominal stress amplitudes the IR measurements reveal that plastic deformations also occur within the nominal cross-section (specimens RK0605, RK0606, RK0624 and RK0631). This is indicated by a minor increase of the nonlinear temperature amplitudes outside the notch for higher load cycle numbers. Softening in the nominal cross-section occurs later as within the notch and the overall nonlinear temperature amplitudes in the nominal cross-section remain small. For specimens RK0605 and RK0606 the microscopic investigations performed in the nominal cross-section of the specimens do not indicate slip band formation as might have been expected from the thermal results. However this finding might have been caused by the relatively poor surface finish of these specimens.

Based on the results it can be concluded that for the notched specimens the initial yield limit σ_{y0} is significantly higher than the value of 210 Mpa given as cyclic yield limit for the unnotched specimens. This result suggests a rate sensitivity of the cyclic behavior as mentioned by [Rei78] and [Eif81] since material, specimen preparation and surface treatment are similar as for the cylindrical specimens.

The microscopic investigations within the notch demonstrate slip band formation for all specimens. Note that even for the three specimens which did not fail during testing (RK0614, RK0621, RK0628) the microscopic observation within the notch demonstrate a significant number of slip bands within the ferritic grains. The formation of the slip bands is accompanied by clearly distinguishable nonlinearities in the temperature evolution. For all specimens the first slip bands generally appear within the first 5 % of the fatigue lifetime. At around 30 % of the fatigue lifetime the number of grains with slip bands does not change anymore. The number of distinguishable slip bands within the individual grains saturates within the first 50 % of the fatigue lifetime, whereas further growth of the slip bands and deepening might go on until fracture. The saturation of the slip bands does therefore not follow the saturation of the nonlinearities in the evolution of the temperature signal and the macroscopic softening behavior, respectively. It can be concluded that the saturation of the slip band formation and of the cyclic material behavior do not fall together.

The microscopic investigations show that grain boundaries often form an obstacle for the further growth of the slip bands. This become especially obvious for the specimens which did not fail (RK0614, RK0621, RK0628). For all of these specimens several ferritic grains are present which clearly exhibit slip bands. The slip band density and potentially their depth increases during ongoing loading. However most of these 'micro-cracks' are not able to overcome the grain boundaries and join across multiple grains, so that their growth is obviously blocked by the grain boundaries. Together with the thermal investigations it can be concluded that damage processes are present even within the specimens that have been loaded close to the endurance limit. The overall importance of the slip band formation and the grain boundaries for the early fatigue process on defect free surfaces becomes apparent by the results obtained on specimens RK0608 and RK0618. For both specimens the initiation of the final fatigue crack could be directly observed. Crack initiation occurred at a grain boundary for RK0608 and in an area of high slip band density for RK0618. For both specimens a well-defined micro-crack was present after 20 % to 30 % of the fatigue lifetime.

The results discussed so far show that infrared investigations during fatigue testing provide valuable information regarding the local material and fatigue behavior. In contrast to other experimental techniques in situ IR measurements during fatigue loading require minimal effort and specimen preparation. Therefore it seems promising to set the findings of the IR measurements in context to the general fatigue behavior of the tested specimens.

Figure 67 shows the Wöhler curve (S/N-curve) constructed from the test results on the notched specimen type II. In a double logarithmic representation the test results fall together within a narrow band. According to the classical Wöhler diagram the results can be approximated by a linear function of the type (compare [Hai02]):

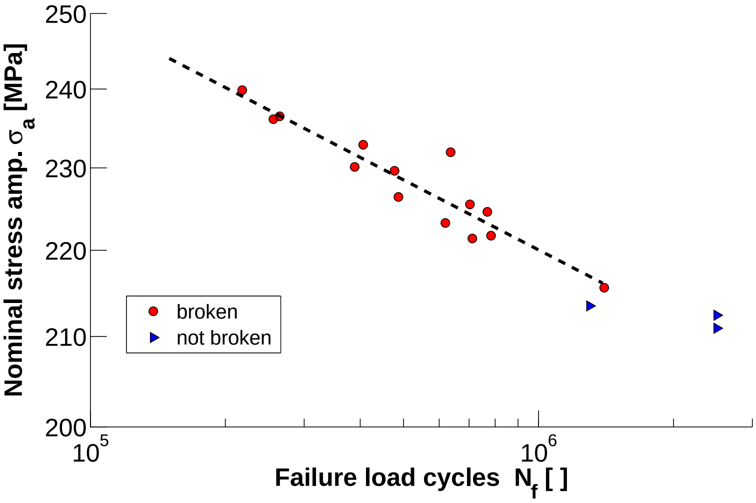

Figure 67: Wöhler curve for specimen type II (double-logarithmic representation)

$$log(N_f) = a - b \cdot log(\sigma_a) \tag{77}$$

where a and b are two coefficients to be evaluated by linear least squares fitting. In the present case σ_a represents the stress amplitude in the nominal cross-section of the specimens. Due to computational purposes the fitting is performed for the inverse of equation (77). The fitted Wöhler curve gives a close representation of the fatigue strength of the specimens. The slope b of the Wöhler curve has been evaluated to 18.36 for $\sigma_a > 210$ Mpa and a is approximately 49.0. The three specimens that did not fail at nominal stress amplitudes around 210 MPa indicate that the slope of the Wöhler curve changes significantly at this stress amplitude which is therefore the range of the endurance limit. However the few test results in this stress range do not allow for the proper evaluation of the slope of the Wöhler curve for $\sigma_a < 210$ Mpa.

The investigations show that the stress concentration and the localization of plasticity within the notch are the decisive factors for the fatigue behavior of the notched specimen type II. It can therefore be expected that the nonlinear temperature amplitudes associated with plastic dissipation are related directly to the local fatigue behavior until crack initiation. Figure 68 gives the nonlinear temperature amplitudes at $0.5 \cdot N_f$ of a small reference area at the bottom of the notch with respect to the fatigue lifetime of the specimens.

Figure 68 demonstrates that the amplitude of the nonlinear temperature amplitudes and accordingly the associated plastic dissipation can be directly related to the local fatigue performance of the specimens upon crack initiation by

$$log(N_f) = a - b \cdot T_{a,nlin} \tag{78}$$

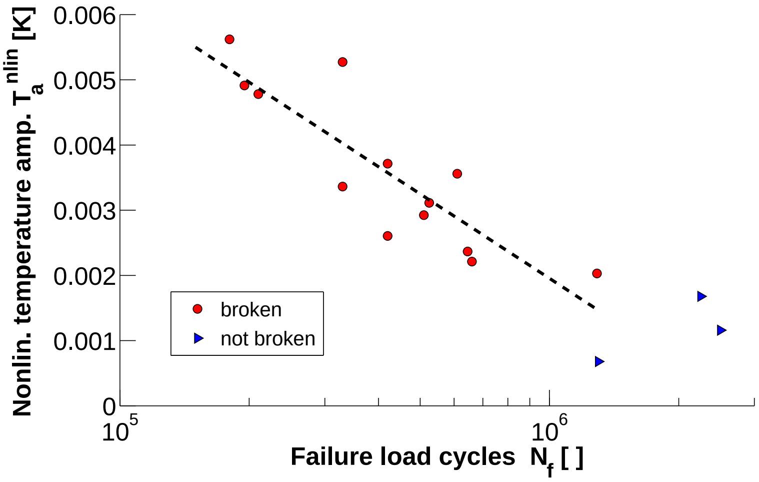

Figure 68: Dependency of the fatigue lifetime on the nonlinear temperature amplitude within the notch (single-logarithmic representation)

Equation (78) indicates that the local fatigue lifetime until (macro-)crack initiation can be characterized by local parameters as the accumulated plastic dissipation or the maximum plastic strain amplitudes if no significant flaws are present. This suggests the extendability of approaches based on the quantification of energy or plastic dissipation to the prediction of local fatigue properties. The experimental verification can - especially in the case of localized plastic deformations - be performed based on thermographic investigations. This requires the quantification of the dissipated energy on a local scale, taking into account the heat diffusion within the tested specimens.

The thermal results show that the location and the point of macro-crack initiation can be easily inferred from the IR measurements using the proposed data processing technique. Figure 69 relates the relative lifetime at the point of crack initiation estimated from the infrared measurements to the failure load cycles of the specimens. The results demonstrate that the phase of macro-crack propagation compromises typically less than 25 % of the complete fatigue lifetime for the notched specimen type under the premiss of polished surfaces. With an increasing number of load cycles up to failure the portion of crack propagation on the entire fatigue lifetime decreases. Obviously fatigue crack initiation and propagation are not affected to the same extent by an increase of the stress amplitude.

6.5 Fatigue testing of welded specimens

The results of the notched specimens show that thermographic analysis of the surface temperature evolution during fatigue loading provides a suitable tool for the assessment of localized damage effects. For most engineering structures welding seams constitute

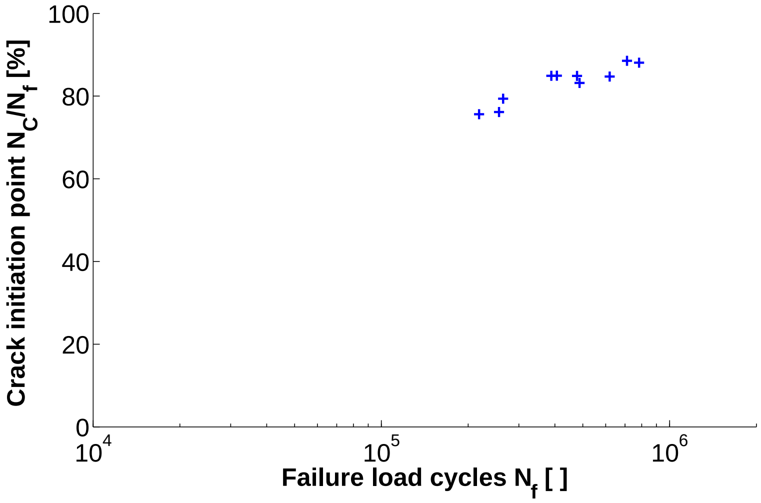

Figure 69: Relation of the point of crack initiation to the number of failure load cycles; specimen type II

especially critical details which determine the fatigue resistance of the structures. In the following section results of fatigue testing on small welded specimens with dimensions according to figure 75(c) in appendix I are presented. Generally it can be expected that the local fatigue properties within the weld toe are influenced by different factors such as:

- stress concentrations due to the geometric notch
- variations of geometry
- local material changes and increasing brittleness as result of the extreme heat treatment and rapid cooling
- variable residual stress field after cooling down
- potential flaws within the weld seam

6.5.1 Testing conditions and parameter variation

The welded specimens were machined as a single piece of a 20 mm steel plate of S355J2G3 with the material properties given in appendix I and cut into two pieces afterwards. The flanks of the specimens were prepared for welding according to the specification given in figure 75(c). To ensure constant and repeatable conditions during welding, the two specimen halves were clamped onto a mounting plate. Two additional pieces of steel were attached to both sides of the specimen and were used as the starting and ending point for the arc welding. Both extension plates were removed after welding of the specimens from both sides. The weld seam on one side of the specimen was milled down to the nominal cross-section afterwards. This prevented crack initiation on the uninvestigated backside of the specimen. All specimens were tested without annealing after manufacture. Obvious welding-splashes were removed before testing. As described earlier all specimens were coated with graphite spray as preparation for the thermographic investigations. On the weld bead a small reference window was left un-coated which gave a sufficiently high contrast in the IR-pictures for the application of the motion compensation (compare figure 70).

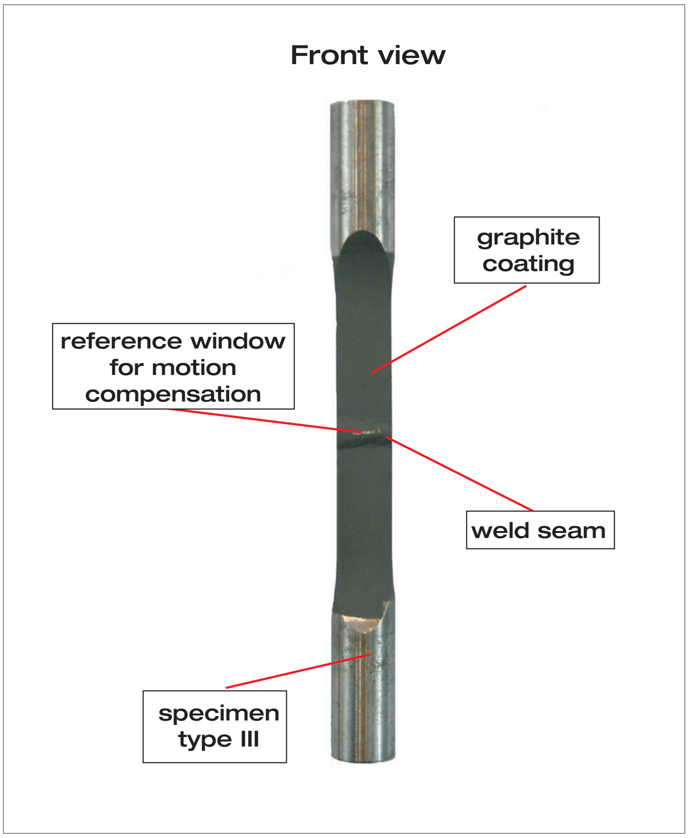

Figure 70: Specimen preparation; specimen type III

Fatigue loading was applied load-controlled as fully reversed harmonic loading ($R = -1$) at different load amplitudes using a testing frequency of 15 Hz. IR-images were recorded every 15000 load cycles with the same camera settings as described earlier. For some of the specimens the light microscope was used to acquire macro images of the weld seam in order to investigate whether crack initiation could be assessed visually. The investigations proofed that with the light microscope the crack initiation in the weld toe could not be assessed and the results will therefore not be presented here. Similar to the investigations on the notched specimens the acquisition of the pictures required an interruption of the fatigue testing during which the load was kept close to zero. For all specimens the fatigue testing was terminated by failure which occurred at the weld seam for all specimens. In most cases crack initiation occurred within the weld toe from the investigated side of the specimen. One specimen failed by crack initiation from the backside. This gives the opportunity to discuss both failure modes here.

Table 7 summarizes the loading conditions, the failure load cycles and the location of failure initiation. The nominal stress amplitudes are calculated from the measured dimensions of the individual specimens and the applied load amplitudes.

Table 7: Loading conditions for welded specimens

Specimen No.	F_a	$\sigma_{a,0}$ [MPa]	f_L [Hz]	N_f [lc]	Failure
SK0601	17750	142	15	885,390	front
SK0602	16500	130	15	151,870	front
SK0603	17500	141	15	796,110	front
SK0604	18000	149	15	340,830	front
SK0607	17500	137	15	675,130	front
SK0608	16500	132	15	734,680	front
SK0611	17500	140	15	252,430	front
SK0612	16500	134	15	1,043,740	front
SK0613	16000	127	15	580,516	backside
SK0615	17500	140	15	1,493,900	front

6.5.2 Discussion of the results

Form the recorded IR sequences the mean temperature, the linear and nonlinear temperature amplitudes and the relative phase shift with respect to the linear reference signal were calculated by the same data processing procedure as earlier. Here only the values of the linear and nonlinear temperature amplitudes will be presented. Prior to the analysis of the temperature values the motion compensation was applied to the recorded IR sequences. The linear reference signal is generated as spatial mean value of the temperature readings of a 3 x 3 pixel neighborhood in the nominal cross-section of the specimen at the beginning of testing.

Figure 71 shows the typical distribution of the linear temperature amplitude (figure 71(a)), the nonlinear temperature amplitude (figure 71(b)), the relative phase shift (figure 71(c)) recorded during fatigue testing and a corresponding surface image 71(d) of the weld seam. The results represent the state of specimen SK0608 after 75000 load cycles. Instead of the 3-D representation adopted for the notched specimen type a 2-D representation of the thermal results is preferred at this point to prevent

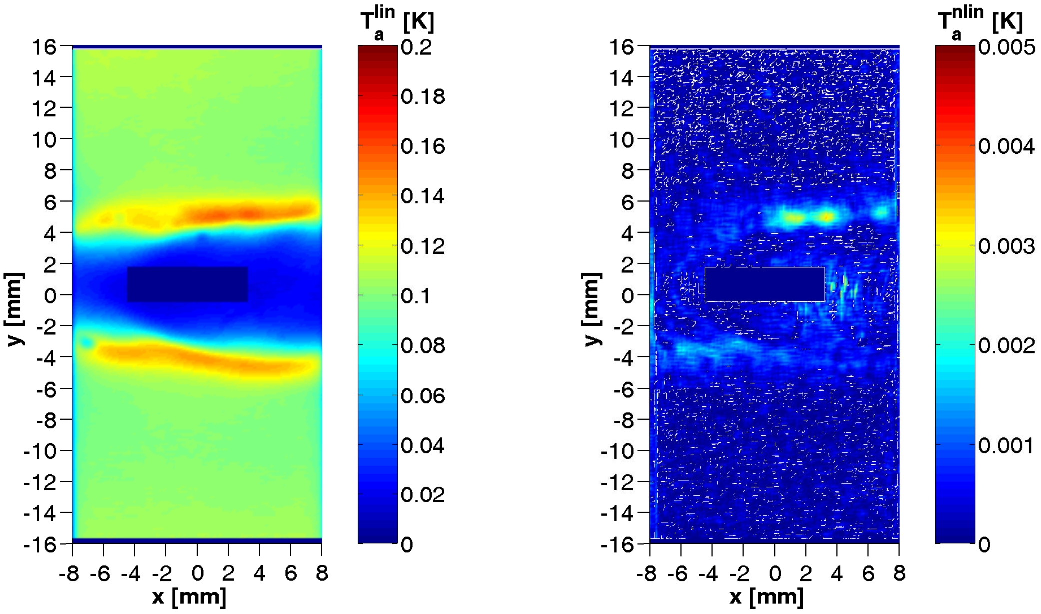

(a) linear temperature amplitude

(b) nonlinear temperature amplitude

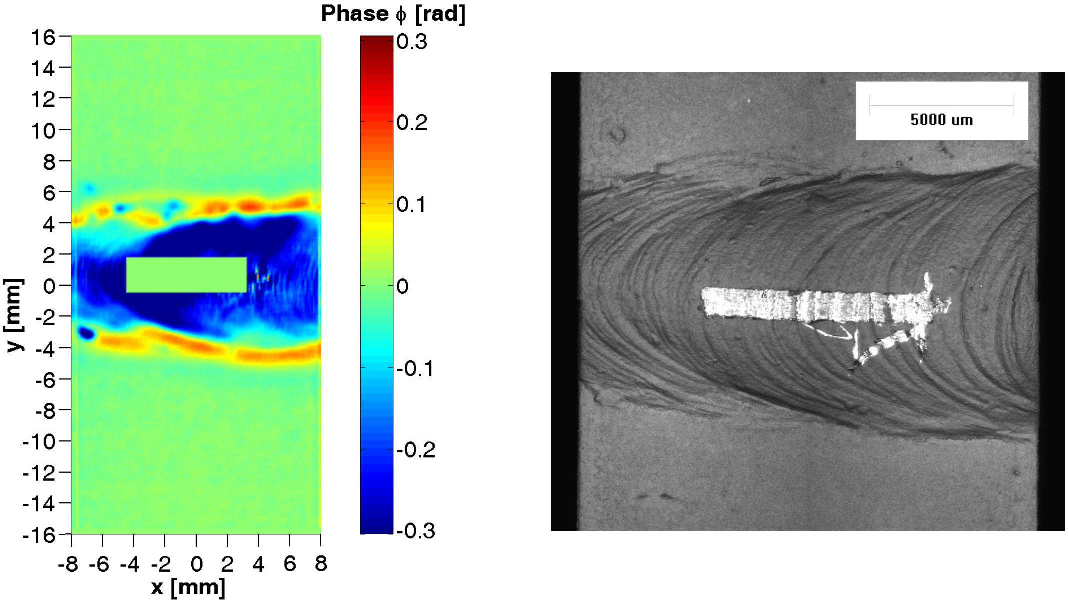

(c) relative phase shift

(d) microscopic surface image

Figure 71: Distribution of linear, nonlinear temperature amplitudes, the relative phase shift at a welded specimen and visual surface image of the weld seam

that local inhomogeneities in the temperature distribution become hidden due to the perspective.

In figure 71(a) the two toes of the welding seam are distinguished by elevated linear temperature amplitudes with respect to the nominal cross-section which indicates local stress concentrations. At the surface of the weld bead the linear temperature amplitudes drop which shows that these areas of the welding seam are subjected to smaller mechanical stresses. The rectangular section in the center of the weld bead corresponds to the un-coated reference window used as a high contrast feature for cross-correlation of the images during motion compensation. Figure 71(a) reveals several spot-like areas at the weld toe that exhibit strongly decreased temperature amplitudes with respect to the rest of the weld toe. These areas can either be attributed to remaining welding-splashes or local flaws. The distribution of the nonlinear temperature amplitudes reveals several spots within the weld toe which exhibit elevated nonlinearities in the temperature evolution. For the given example the nonlinearities are confined to small areas, which indicates localized damage effects. The nature of these nonlinearities will be discussed later on. The distribution of the relative phase shift of the temperature signal confirms adiabatic conditions in the nominal cross-section of the specimen. By contrast the weld toe and the weld bead are corrupted due to local heat conduction and are therefore not in an adiabatic state at the given loading frequency. At the weld toe the relative phase shift is positive which indicates local heat losses due to heat conduction. At the weld bead it becomes negative which indicates that heat flows to this area from the surroundings according to the conventions of chapter 5.

6.5.3 Discussion of the fatigue behavior

The evolution of the temperature values during fatigue testing is investigated on the example of specimen SK0601. For this purpose figure 72-3 shows exemplarily the evolution of the linear and nonlinear temperature amplitudes with ongoing fatigue damage.

The images taken at 15000 load cycles and $N/N_f = 0.017$, respectively shows the undamaged weld seam shortly after the beginning of the fatigue testing. The spatial distribution of the amplitude values resembles the general situation discussed before.

At $N/N_f = 0.102$ the linear temperature amplitudes start to drop within a small section at the weld toe. This local drop is the first indicator of a degradation process due to fatigue within the weld toe. However at this point the temperature evolution is still completely linear and no significant nonlinearities appear in the temperature evolution.

At $N/N_f = 0.203$ two more 'hot spots' can be found where the linear temperature amplitudes start to drop locally. At this point small nonlinearities in the temperature signal can be found for all three initiation sites. Note that all three 'hot spots' are located within the central section of the weld toe and do not start close to the edges of the specimen as might have been expected.

At $N/N_f = 0.305$ the two uppermost damage areas have joined. The unified damage area extends across half of the width of the specimen. The nonlinearities in the temperature signal grow rapidly and are no longer confined to the very vicinity of the suspected fatigue crack. In the following the 'hot spot' areas spread out further and grow towards the edges of the specimen. The linear temperature amplitudes are increased at the crack tips and drop close the flanks of the fatigue cracks in the weld toe.

At $N/N_f = 0.695$ the upper damage area reaches the edge of the specimen. The nonlinearities reach relatively high values above 15 mK and are spread out across the entire mid-section of the specimen. The proper distinction of the crack tips by investigation of the nonlinearities becomes difficult, since nonlinear behavior is not confined to the crack tips anymore. In this stage it becomes easier to estimate the crack tip position from the linear temperature amplitudes. As before the crack tips are characterized by a local increase of the linear temperature amplitudes. The further damage evolution is characterized by fast lateral growth of the fatigue cracks. Final failure occurred shortly after the linear temperature amplitudes indicated that the crack runs across the entire width of the specimen within one of the weld toes.

In similar fashion to figure 72-3 the results of all welded specimens are summarized in appendix III. The general fatigue behavior of all specimens resembles the damage evolution discussed earlier. Besides specimen SK0613 all specimens show clear signs of fatigue damage initiation within the weld toe. For specimens with higher fatigue lifetimes damage evolution is strongly localized and starts at several distinct initiation points (compare specimen SK0615). After their first appearance these initiation sites grow during the ongoing fatigue loading and finally join to a relatively large macro crack. The specimens generally fail rapidly if the fatigue crack spans across the entire width of the specimen. By contrast specimens with a short fatigue lifetime often exhibit only a single initiation point which dominates the fatigue behavior until final failure (compare e.g. specimen SK0604). For all specimens for which failure initiated at the investigated side both weld toes were equally affected by damage processes.

Some of the investigated specimens show small zones of nonlinearities in the temperature evolution close to the zones of maximum stresses prior to crack initiation (specimens SK0602, SK0603, SK0604, SK0608, SK0611). In these cases relatively widespread but small and more stable nonlinearities are present in the weld toe during the early stages of fatigue loading. These zones do not necessarily preindicate the location of later crack initiation. For some of the specimens the nonlinearities in the weld toe completely disappear during the early stages of the fatigue loading. The

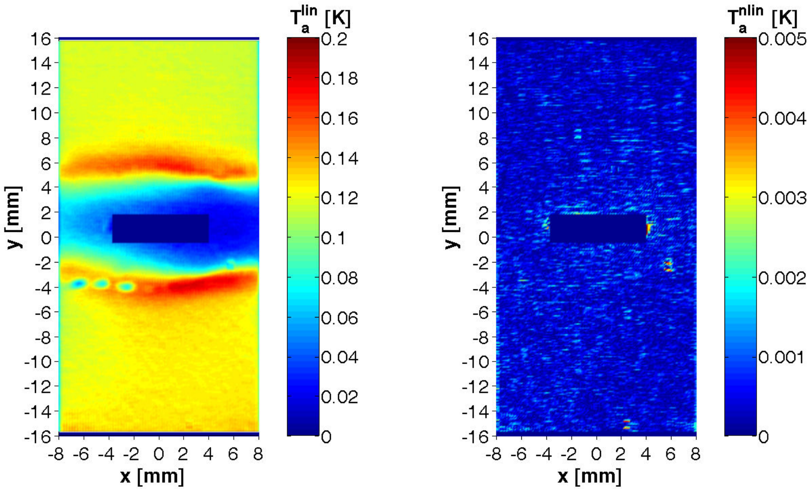

$N = 15000;\ N/N_f = 0.017$

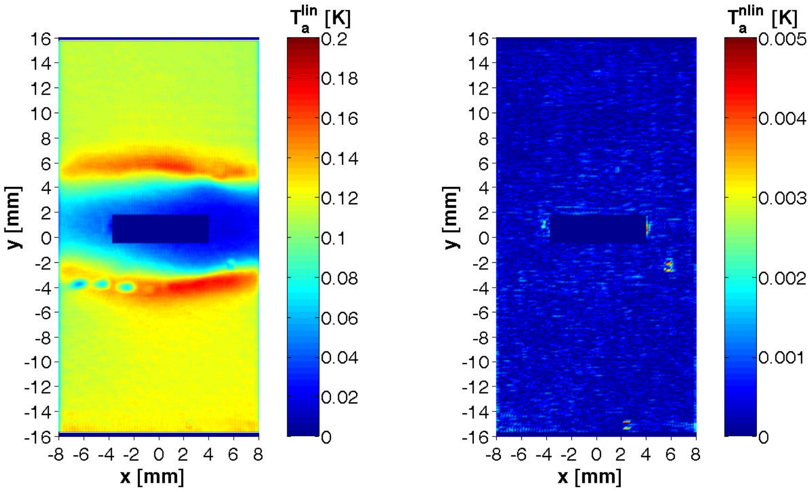

$N = 45000;\ N/N_f = 0.051$

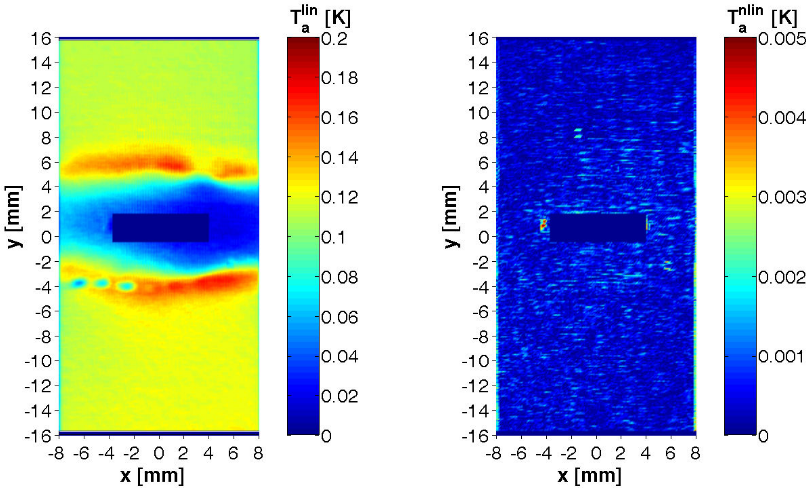

$N = 90000;\ N/N_f = 0.102$

Figure 72-1: Linear and nonlinear temperature amplitudes showing the fatigue damage evolution of a welded specimen; specimen SK0601

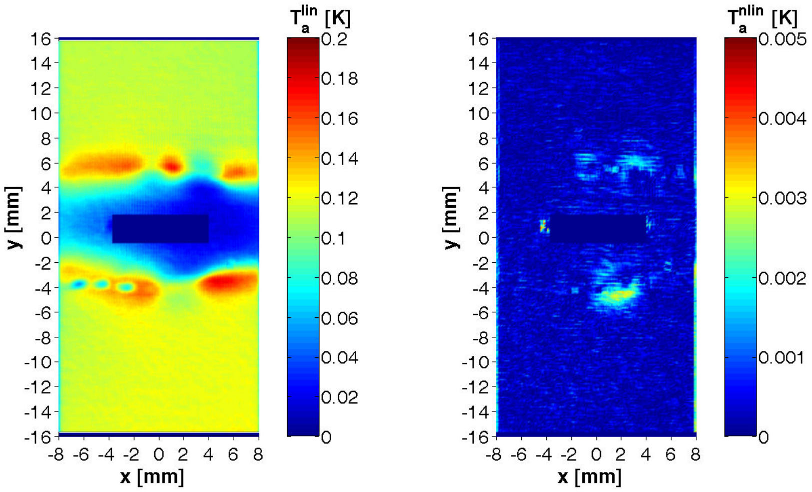

$N = 180000;\ N/N_f = 0.203$

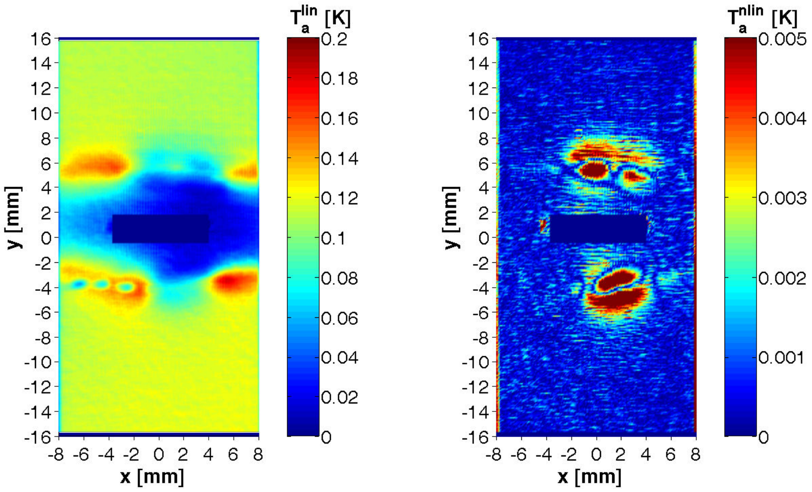

$N = 270000;\ N/N_f = 0.305$

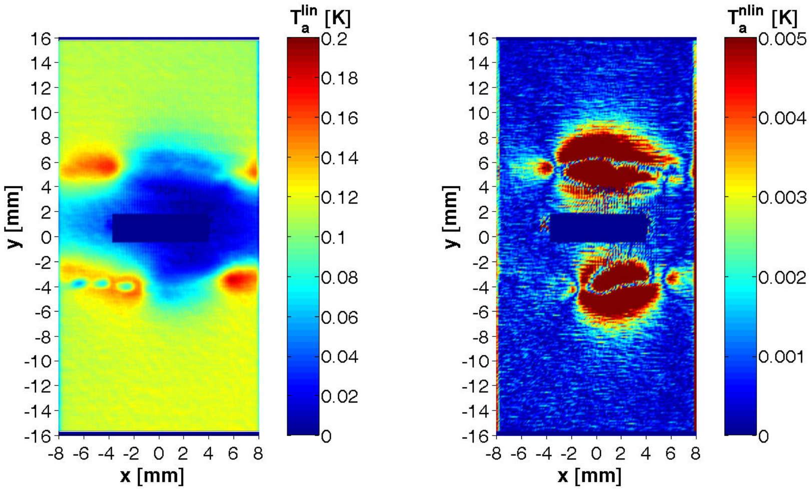

$N = 360000;\ N/N_f = 0.407$

Figure 72-2: Linear and nonlinear temperature amplitudes showing the fatigue damage evolution of a welded specimen; specimen SK0601

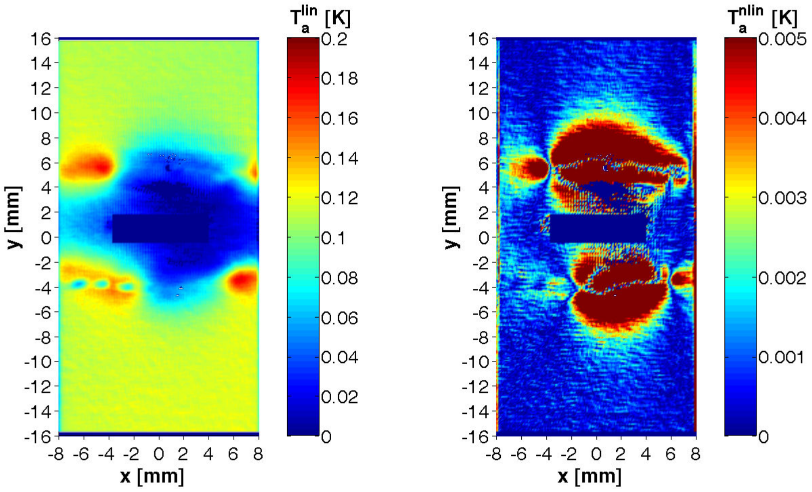

$N = 450000$; $N/N_f = 0.508$

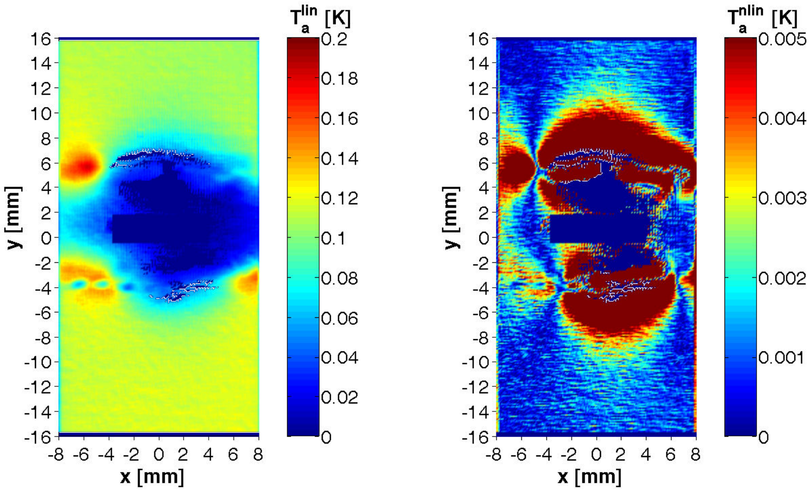

$N = 615000$; $N/N_f = 0.695$

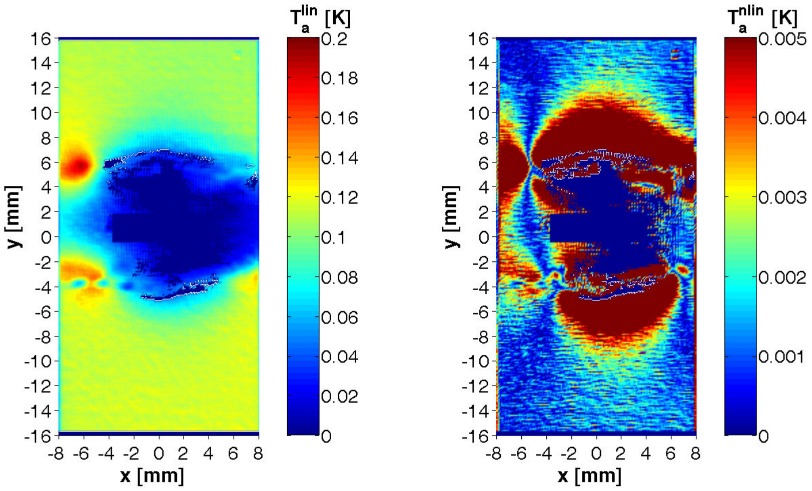

$N = 705000$; $N/N_f = 0.796$

Figure 72-3: Linear and nonlinear temperature amplitudes showing the fatigue damage evolution of a welded specimen; specimen SK0601

mechanism behind these nonlinearities and its relation to cyclic plasticity within the weld toe is still unclear.

The results of specimen SK0613 show that the damage evolution from the backside of the specimen leads to completely different characteristics in the thermal behavior. In this case the damage evolution on the opposite side of the specimen leads to an ongoing increase of the nonlinear temperature amplitudes throughout the entire welding seam. This phenomenon can be associated with ongoing load redistributions with growing fatigue cracks and subsequent structural nonlinearities which might be superimposed by additional local plasticity.

For all specimens crack initiation within the weld toe leads to very localized and fast growing nonlinearities in the temperature evolution. Generally the location of crack initiation is first indicated by a local drop of the linear temperature amplitude. This first variation of the linear temperature amplitude is not directly accompanied by observable nonlinearities in the temperature signal. The first nonlinearities generally appear later during the fatigue process. Based on the results it can therefore not be inferred whether or not cyclic plasticity occurs in the weld toe prior to crack initiation. However from the results it becomes obvious that cyclic plasticity - at least on a macroscopic scale - does not play the important role as for notched or unnotched specimens.

The point of crack initiation can be estimated by a strong localized increase of the nonlinearities. The investigations demonstrate that in contrast to the unnotched or mildly notched specimen type, crack propagation plays a significant role for the damage evolution at the weld toe. This is demonstrated by figure 73 which relates the relative lifetime at the point of crack initiation to the failure load cycles of the specimens.

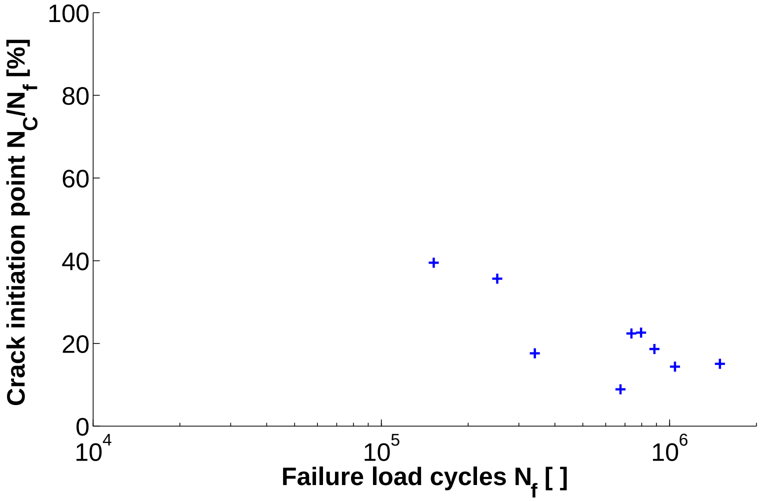

Figure 73: Crack initiation with respect to the number of failure load cycles; specimen type III

The first clear indication of fatigue cracks is given at approximately 10 % to 40 % of the fatigue lifetime of the specimens. Therefore approximately 60 % to 90 % of the fatigue lifetime is spent for crack growth, joining and propagation. Figure 73 indicates that the relative lifetime spent for crack propagation decreases with decreasing total lifetime. As a result of the investigations it can be concluded that the fatigue damage evolution within the weld toe exhibits significant difference to the findings for the mildly notched specimen type. For the welded specimens the fatigue damage process is governed by crack initiation and propagation rather than by localized cyclic plasticity.

The distribution of the nonlinearities associated with crack initiation shows that the nonlinearities in the temperature evolution are not restricted to the crack tips as would be expected for purely plasticity-induced nonlinearities. From the investigations of [Hus94] it can be inferred that the nonlinearities at both flanks of the crack are caused to a significant extent by local geometric nonlinearities due to crack opening and closure. [Hus94] shows that these nonlinearities generally exceed the effects of plasticity by an order of magnitude. The analysis methodology introduced primarily for the analysis of nonlinearities due to cyclic plasticity does not allow to distinguish between different origins of nonlinear behavior.

6.6 Chapter summary

In the preceding chapter thermographic investigations on the surface temperature evolution during fatigue loading of unnotched, geometrical notched and welded specimens have been presented. For the analysis of the recorded infrared images a data processing method has been introduced which allows to distinguish between linear temperature variations associated with thermoelasticity and additional nonlinearities in the temperature signal. The approach is based on a fitting procedure of a linear reference signal which can either be generated from additional equipment such as load cells, strain gauges etc. or from the temperature evolution of a reference area of the loaded specimens and avoids problems associated with a DFT. The application of a motion compensation scheme significantly improves data quality. The data processing method is suitable to detect very small nonlinearities in the temperature evolution but does not allow to clearly identify the source of the underlying mechanism which causes the nonlinear behavior.

The numerical findings of chapter 5 could be verified experimentally. In the elastic range very good coincidence between experimental and numerical results with overall discrepancies below 2 % could be achieved. The mean stress effect on the first harmonic due to the temperature dependency of the Young's modulus could be verified for investigations on a single specimen. For different specimens the small contributions to the magnitude of thermoelastic coupling cannot be distinguished from the natural scatter between the individual specimens. The contribution to the second harmonic could not be detected.

For unnotched specimens the evolution of the nonlinearities in the surface temperature variations can be attributed to the elastic-plastic cyclic material behavior measured by strain gauges. The onset of plastic strains causes a corresponding increase of the nonlinearities in the temperature signal which allows to identify cyclic plasticity. The characteristics of these nonlinearities are in good agreement with the numerical predictions of chapter 5. Investigations into the localization of the nonlinearities show that softening takes place in the form of rapidly growing cyclic Lüders bands. The end of the softening phase coincides with the homogenization of the spatial distribution of nonlinearities and the associated plastic strains.

The investigations reveal a significant increase in the linear temperature variations associated with thermoelastic coupling. To the authors best knowledge this increase has not been reported or studied yet in the context of fatigue loading. The results show that the increase correlates roughly with the plastic strain amplitudes. After a review of possible mechanisms the observation has been attributed to additional coupling phenomena. In the context of the presented theory the additional coupling manifests in an apparent change of some of the material coefficients. Particularly a hardening dependency of the coefficient of thermal expansion has been suspected.

The thermographic investigations on the notched specimen type prove that there is a localization of plastic strains to the bottom of the notch. Compared to the unnotched specimen type the softening process within the notch requires more load cycles and occurs gradually. This has been explained by effects of load redistribution within the notch as a result of the local onset of plastic deformations. Crack initiation causes a strong increase of the local nonlinearities in the temperature signal. The crack tip can be best inferred from the thermographic investigations by a local increase of the linear temperature amplitudes. Additional microscopic investigations reveal that the appearance of measurable nonlinearities in the temperature signal is accompanied by the initiation of persistent slip bands within the notch. Temporally the evolution and growth of the slip bands does not fall together with the hardening and softening behavior. For some of the specimens the crack initiation could be directly observed microscopically. For the notched specimens the major span of the lifetime (70 % to 85 %) is spent before macroscopic crack initiation. The microscopic results show that microcracks can develop earlier in the fatigue process.

The fatigue behavior of welded specimens is dominated by the early initiation of cracks in the toe of the weld seam. The weld toe is distinguished from the rest of the specimen by elevated linear temperature amplitudes due to stress concentrations. It is characterized by strongly non-adiabatic conditions. Fatigue damage initiation is generally first indicated by a local drop of the linear temperature amplitudes. At this point generally no significant nonlinearities can be measured, so that no clear indication of local cyclic plasticity within the weld toe prior to crack initiation can be found. For all investigated specimens fatigue cracks develop at around 10 % to 30 % of the fatigue lifetime on both sides of the weld seam. The initiation of the cracks can be inferred by a strong increase of nonlinearities in the temperature signal. A clear distinction of the different mechanisms causing the nonlinearities at the crack is not possible based on the adopted data processing methodology.

7 Conclusions

7.1 Summary

The purpose of the presented thesis is to contribute to the stronger integration of thermographic measurements in experimental mechanics. The work is motivated by an apparent gap between recent advances in damage modeling and the lack of suitable experimental techniques for the assessment of local damage processes e.g. due to fatigue in complex engineering structures. The focus of the work is the assessment of local fatigue properties in mild steel during high cycle fatigue testing by thermography.

Chapter 2 provides a comprehensive review of known applications of infrared thermography in thermomechanical studies.

In chapter 3 the material behavior of mild steel under load controlled cyclic loading in the high cycle fatigue regime is reviewed and various influencing factors are discussed. The review shows that in the absence of defects or sharp notches the evolution of plastic strains dominates the fatigue behavior of mild steels. For relatively small load amplitudes the material behavior becomes highly heterogenous even for simple specimen geometries.

Chapter 4 gives a review of basic thermomechanical principles and introduces the heat diffusion equation with thermoelastic coupling and plastic dissipation. The equation constitutes the thermomechanical background for the present studies. The derivation highlights several simplifications which provide starting points for more rigorous thermomechanical formulations and damage modeling in the future.

In chapter 5 a numerical solution procedure for the simulation of thermomechanical coupling based on a standard FE program is presented. The numerical approach solves the heat equation with coupling terms based on the subsequent solution of a mechanical and a thermal model. The numerical procedure has been used to study mechanical-thermal coupling and the effect of different nonlinearities on the local temperature evolution. After adjustment of the material parameters very good coincidence of numerical and experimental results could be achieved.

Chapter 6 presents results of experimental thermographic investigations during load controlled fatigue testing on unnotched, geometrically notched and welded specimens. For the analysis of experimental records a new data processing methodology based on a pixel-wise fitting procedure is introduced which has been applied to separate linear and nonlinear contributions to the temperature evolution during fatigue testing. The thermographic results are compared to results of strain gauge measurements and microscopic investigations.

7.2 Results

- The numerical studies show that of the investigated nonlinear effects only the mean stress dependency of the thermoelastic coupling term and thermoplastic dissipation cause technically relevant variations of the thermomechanical coupling during fatigue loading. The occurrence and the magnitude of both effects could be verified experimentally for mild steel. Additionally the effects of bidirectional coupling are significant. They can be taken into account by either adjusting the coefficient of thermal expansion in the decoupled problem or the Young's modulus in the coupled problem. The magnitude of further nonlinear effects such as the temperature dependency of the thermoelastic coupling term and the temperature dependency of different material parameters have been found to be below the detection capabilities of current infrared imaging systems. Therefore the consideration of these effects for experimental studies is currently not necessary.

- By direct comparison of the results obtained on a single specimen subjected to different mean stress levels the change of the first harmonic owing to the temperature dependency of the Young's modulus has been verified experimentally. The assessment of unknown mean and residual stresses on different specimens based on thermographic measurements does not seem to be feasible at the time since the mean stress effect is too weak and not distinguishable from the natural scatter in thermoelastic coupling.

- The onset of plastic flow leads to distinct nonlinearities in the temperature signal which are caused by plastic dissipation. In contrast to the measurement of the mean temperature rise the assessment of the nonlinearities allows to retrieve information of the localized cyclic material behavior. The experimental detection is demanding since the magnitude of the nonlinearities is one to two orders smaller than the temperature changes caused by thermoelastic coupling.

- For the experimental detection of these small nonlinearities in the temperature evolution a newly developed fitting procedure is suitable. Compared to an approach based on DFT the procedure exhibits better thermal and temporal resolution and is not influenced by deviations from pure harmonic loading. Data quality can be significantly improved by the application of a motion compensation scheme before further evaluation of the temperature evolution.

- Load-controlled fatigue tests on unnotched specimens confirm the typical softening and hardening behavior for mild steel as reported in the literature. The tendency to primary hardening is relatively weak for the investigated load amplitudes. Non-zero mean stresses significantly influence the evolution of the mean strains due to cyclic creep. Upon a certain higher level the plastic strain amplitudes are significantly altered by the presence of mean stresses. Small mean stresses do not affect the plastic strain amplitudes. In contrast to the plastic strain amplitudes the mean strains do not completely saturate during testing.

- The onset of plastic strains during primary softening is accompanied by an increase of the mean temperature, the linear temperature amplitude and the nonlinear temperature amplitude. The increase of the mean temperature and the occurrence of nonlinearities in the temperature evolution can be attributed to plastic dissipation. The nonlinearities in the temperature signal are directly associated with the evolution of plastic strains. Higher plastic strains cause higher nonlinearities and vice versa. The softening and hardening behavior found by strain gauge measurements has corresponding effects on the magnitude of the nonlinearities.

- The increase of the linear temperature amplitudes associated with the onset of softening can be up to 25 % with respect to the initial values. It is suspected that the effect is caused by further coupling phenomena which have not yet been taken into account. Within the context of the presented classical theory the phenomenon can be associated with the dependency of some material parameters (as e.g. the coefficient of thermal expansion) on the hardening state.

- The analysis of the nonlinearities in the temperature signal allows to resolve localization phenomena as the spread-out of cyclic Lüders bands and the localization of plastic flow within geometric notches. For the notched specimen type a direct relation of the thermal measurements to the evolution of slip bands in the ferrite grains of the metal matrix could be proved.

- Slip bands evolved in all specimens for which measurable nonlinearities in the temperature evolution are found. The formation of slip bands does not fall together with primary softening but starts and ends later during the fatigue process. For some of the specimens zones with high slip band density cause the initiation of fatigue micro- and macro-cracks. The grain boundaries have been found to act as barriers for slip band and microcrack propagation.

- Within the notch the initiation of macro-cracks typically occurred after 70 % to 85 % of the fatigue lifetime. Crack growth therefore plays a minor role for the fatigue lifetime of the notched specimens. The point of crack initiation can be inferred by a strong increase of the nonlinearities in the temperature evolution. After crack initiation the nonlinearities are not caused solely by plastic dissipation but also by crack closure. Based on the presented data processing approach, a distinction between the different sources of nonlinearities in the vicinity of a fatigue crack is not possible.

- The fatigue behavior of the investigated weld seams is characterized by the early initiation of fatigue cracks in the weld toe. The initiation of these cracks is first indicated by a decrease of the local linear temperature amplitude and later by an increase of the nonlinearities in the temperature signal. The current results do not give any clear indication of local cyclic plasticity in the weld toe prior to crack initiation. The first fatigue cracks develop at around 10 % to 30 % of the fatigue lifetime. In contrast to the un-welded specimens, fatigue crack propagation dominates the fatigue behavior of the weld seam.

7.3 Outlook and potential for future work

As a result of the investigations high overall potential can be attributed to the application of thermography to localize and eventually quantify local material properties or damage phenomena. The assessment of thermomechanical coupling phenomena by infrared thermography offers a broad range of possible applications during experimental fatigue studies. Especially the applications to geometric notches and welded joints are promising since the method reveals unique information of the local fatigue processes. In this context the fatigue processes in the weld toe should be further investigated. The present studies indicate that with respect to local approaches for the fatigue analysis of weld seams it might become more appropriate to concentrate on crack propagation by adopting concepts from fracture mechanics than to apply elastic-plastic concepts in the weld toe. For the further development of the experimental technique more effort needs to be put into the quantification of the results.

First the exact location of the crack tip needs to be retrieved from the thermal images. This might be achieved by analysis of the spatial distribution of the linear temperature amplitudes. The development of such a technique allows for the study of crack propagation in complicated geometries without the need of special specimen preparation or modifications of the testing procedure.

Second the analysis of the temperature evolution around the crack might be appropriate to reveal crack closure and other aspects of the fatigue damage evolution under realistic operating conditions. For crack and crack tip investigations the quantification of the locally dissipated energy seems to be a suitable approach. Eventually it will allow for the separation of the nonlinearities caused by geometric effects such as crack closure and plastic dissipation at the crack tip.

Third, regarding the analysis of cyclic plasticity, future work should focus on the back-calculation of the energy balance of the recorded temperature images. For complex 3-D situations this requires the correction of local non-adiabatic behavior and the effects of heat diffusion. Quantitative energy-based approaches become especially promising for the investigation of very localized damage processes, e.g. at weld seams and geometric notches, where other experimental techniques such as strain gauge measurements can not be applied.

From the theoretical point of view, high-resolution thermal measurements need to be accepted and incorporated as experimental tool for the verification of advanced thermomechanical models. In this context especially the nature of the observed variability of the linear coupling term with the onset of plastic deformations needs to be clarified. The results need to be incorporated into new approaches for fatigue damage analysis and lifetime prediction. Due to the manifold tasks to be solved interdisciplinary experimental and numerical-theoretical approaches are strongly recommendable.

Literature

[ACI03] Andrianopoulos, N.P., K.T. Champidis and A.P. Iliopoulos: *Detection of crack nucleation in sheet metalforming by monitoring infrared radiation.* Fatigue and Fracture of Engineering Materials and Structures, 26(4):323–328, 2003.

[ACZ03] Audenino, A.L., V. Crupi and E.M. Zanetti: *Correlation between thermography and internal damping in metals.* International Journal of Fatigue, 25(4), 2003.

[ANS05] *Ansys: Release 10.0 Documentation for ANSYS.* 2005.

[Ask91] Askegaard, V.: *Prediction of initial crack location in welded fatigue test specimens by the thermoelastic stress analysis technique*, Volume 276 of *Serie R.* Technical University of Denmark, 1991.

[BCMG04] Boulanger, T., A. Chrysochoos, C. Mabru and A. Galtier: *Calorimetric analysis of dissipative and thermoelastic effects associated with the fatigue behavior of steels.* International Journal of Fatigue, 26(3):221–229, 2004.

[Bel68] Belgen, M.: *Infrared radiometric stress instrumentation application range study*, Volume CR-1076 of *Nasa contractor report.* NASA, 1968.

[Bes58] Besseling, J.F.: *A theory o elastic, plastic and creep deformations of an initially isotropic material showing anisotropic strain-hardening, creep recovery and secondary creep.* Journal of applied mechanics, 26:529–536, 1958.

[Bil93] Bily, M.: *Cyclic Deformation and Fatigue of Metals*, Volume 78 of *Materials Science Monographs.* Elsevier, 1993.

[Böh85] Böhmer, H.J.: *Vergleichende Unterschungen zum Ermüdungsverhalten von glatten und gekerbten Stäben aus CK45.* Dissertation, Universität Karlsruhe, Karlsruhe, 1985.

[Böt02] Böttcher, C.: *Geschwindigkeitssensitivität des mechanischen Verhaltens unlegierter Baustähle bei wiederholter Beanspruchung bis in den inelastischen Bereich - experimentelle Untersuchung und Modellierung*, Volume 654 of *Fortschritts-Berichte VDI.* VDI-Verlag, Düsseldorf, 2002. Dissertation.

[BP96] Barone, S. and E.A. Patterson: *Full-field separation of principal stresses by combined thermo- and photoelasticity.* Experimental Mechanics, 36(4), 1996.

[BP01] Brémond, P. and P. Potet: *Lockin thermography: a tool to analyse and locate thermo-mechanical mechanism in materials and structures.* Proceedings of SPIE, the International Society for Optical Engineering, 4360(560-566), 2001.

[BR01] Bougaut, O. and D. Rittel: *On crack-tip cooling during dynamic crack initation.* International Journal of Solids and Structures, 38(15):2517–2532, 2001.

[BZH03] Bhalla, K.S., A.T. Zehnder and X. Han: *Thermomechanics of slow stable crack growth: Closing the loop between experiments and computational modeling.* Engineering fracture mechanics, 70(17):2439–2458, 2003.

[CAF75] Charles, J.A., F.J. Appl and J.E. Francis: *Using the infrared camera in experimental fatigue studies.* Experimental Mechanics, 15(4):133–138, 1975.

[CC04] Charkaluk, E. and E. Constantinescu: *Dissipation and fatique damage - a unified method to treat fatique damage.* MP Materialprüfung, 46(10):524–530, 2004.

[Chr91] Christ, H.J.: *Wechselverformung von Metallen.* Springer-Verlag, 1991.

[Dan99] Dannemeyer, S.: *Zur Veränderung der Fließfläche von Baustahl bei mehrachsiger plastischer Wechselbeanspruchung.* Dissertation, TU Braunschweig, Braunschweig, 1999.

[DBEQC06] Dulieu-Barton, J.M., T.R. Emery, S. Quinn and P.R. Cunningham: *A temperature correction methodology for quantitative thermoelastic stress analysis and damage assessment.* Measurement Science and Technology, 17:1627–1637, 2006.

[DBQ98] Dulieu-Barton, J.M. and S. Quinn: *The effect of plastic deformation on the thermoelastic response of steel.* Conference Proceedings of Mechanics in Design, Nottingham, July 1998, pages 327–336, 1998.

[Del07] *Deltatherm 1000:*. http://www.sti.nasa.gov/tto/spinoff1996/39.html, last checked: June 2007.

[DLS89] Dunn, S.A., D. Lombardo and J.G. Sparrow: *The mean stress effect in metallic alloys and composites.* In: Stanley, P. [Sta89], pages 129–142.

[Dun93] Dunn, S.A.: *On the effects of through-thickness thermal conduction on stress measurement by thermoelastic techniques.* Experimental Mechanics, 33(1):32–36, 1993.

[Dun97] Dunn, S.A.: *Using nonlinearities for improved stress analysis by thermoleastic techniques.* Applied Mechanics Review, 50(2):499–513, 1997.

[DYP04a] Diaz, F.A., J.R. Yates and E.A. Patterson: *Measuring stress intensity factors during fatigue crack growth using thermoelasticity.* Fatigue and Fracture of Engineering Materials and Structures, 27(7):571–583, 2004.

[DYP04b] Diaz, F.A., J.R. Yates and E.A. Patterson: *Some improvments in the analysis of fatigue cracks using thermoelasticity.* International Journal of Fatigue, 26(4):365–376, 2004.

[Eif81] Eifler, D.: *Inhomogene Deformationserscheinungen bei Schwingbeanspruchung eines unterschiedlich wärmebehandelten Stahles des Typs 42Cr-Mo4.* Dissertation, Universität Karlsruhe, Karlsruhe, 1981.

[Esc80] Eschermann, K.H.: *Infrarot-Temperaturmessungen an schwingend beanspruchten Stahlproben.* Dissertation, TU Berlin, Berlin, 1980.

[Fei94] Feickert, W.: *Ermittlung des vollständigen Spannungszustands mit dem Verfahren der Thermoelastischen Spannungsanalyse*, Volume Vol. 18 No.154. VDI - Fortschritt Berichte, 1994.

[FLI05] *User's manual for ThermCam RDac.* Version 2.0, 2005.

[FZRS92] Feng, Z., D. Zhang, R.E. Rowlands and B.I. Sandor: *Thermoelastic determination of individual stress components in loaded composites.* Experimental Mechanics, 32(2):89–95, 1992.

[Gal93] Galione, K.A. (editor): *Proceedings of the 50th spring conference on experimental mechanics, Dearborn, Michagan*, Conference proceedings. SEM-Society for experimental mechanics, 1993.

[Gas87] Gasper, B.C. (editor): *Stress analysis by thermoelastic techniques*, Volume 731 of *Conference proceedings*, Bellingham, 1987. Proceedings of SPIE - The international society for optical engineering.

[GB99] Gyekenyesi, A.L. and G.Y. Baaklini: *Thermoelastic stress analysis: the mean stress effect in metallic alloys.* NASA/ TM, (1999-209376), 1999.

[GB01] Gyekenyesi, A.L. and G.Y. Baaklini: *Quantifying residual stresses by means of thermoelastic stress analysis.* NASA/ TM, (2001-210697), 2001.

[GMS05] Galietti, U., D. Modugno and L. Spagnolo: *A novel signal processing method for TSA applications.* Measurement Science and Technology, 16(11):2251–2260, 2005.

[Gon79] Gonzales, D.P.: *Zum Wechselverformungsverhalten normalisierter unlegierter Stähle mit Kohlenstoffgehalten von 0,01 bis 1,02 Gew. %.* Dissertation, Universität Karlsruhe, Karlsruhe, 1979.

[GP03] Greene, R.J. and E.A. Patterson: *Integrating thermoelastic and numerical stress methods for reliable analysis.* Journal of Strain analysis, 38(4):303–312, 2003.

[GS05] Gallotti, A. and A. Salerno: *Automatic procedure for the correction of thermoelastic stress analysis data acquired in nonadiabatic conditions.* Review of Scientific Instruments, 76(12), 2005.

[GZRR01] Guduru, P.R, A.T. Zehnder, A.J. Rosakis and G. Ravichandran: *Dynamic full field measurements of crack tip temperatures.* Engineering fracture mechanics, 68(14):1535–1556, 2001.

[Hai02] Haibach, E.: *Betriebsfestigkeit.* Springer-Verlag, Heidelberg, 2 Edition, 2002.

[Har75] Harig, H.: *Zur Bedeutung der Thermometrie bei der mechanischen Prüfung metallischer Werkstoffe.* Habilitation, TU Berlin, Berlin, 1975.

[HAR90] Huang, Y.M., H.H. Abdelmohsen and R.E. Rowlands: *Determination of individual stresses thermoelastically.* Experimental Mechanics, 30(1):88–94, 1990.

[HC87] Harwood, N. and W.M. Cummings: *The theoretical basis of the use of random excitation signals for thermoelastic stress analysis.* In: Gasper, B.C. [Gas87], pages 32–43.

[HC91] Harwood, N. and W.M. Cummings (editors): *Thermoelastic stress analysis*, Bristol, Philaselphia, New York, 1991. National Engineering Laboratory, Adam Hilger.

[Hol98] HOLST, G.: *Testing and evaluation of infrared imaging systems.* SPIE optical engineering press, 2 Edition, 1998.

[HRRR00] HODOWANY, J., G. RAVICHANDRAN, A.J. ROSAKIS and P. ROSAKIS: *Partition of plastic work into heat and stored energy in metals.* Experimental Mechanics, 40(2):113–123, 2000.

[Hus94] HUSS, A.: *Rissdetektion und -bewertung mit dem Verfahren der thermoelastischen Spannungsanalyse*, Volume 18 No. 147. VDI - Fortschritt Berichte, 1994.

[HW90] HERRMANN, K. and L. WALTHER: *Wissenspeicher Infrarottechnik.* Fachbuchverlag Leipzig, Leipzig, 1 Edition, 1990.

[Ino04] INOUE, H.: *Stress separation in thermoelastic stress analysis using nonlinearity of the thermoelastic effect.* International Journal JSME, 47(3):305–311, 2004.

[Jou59] JOULE, J.P.: *On some thermodynamic properties of solids.* Philosophical Transactions of the Royal Society of London, 149, 1859.

[JWL$^+$01] JIANG, L., H. WANG, P.K. LIAW, C.R. BROOKS and L. KLARSTROM: *Characterization of the temperature evolution during high-cycle-fatigue of the Ultimet superalloy. Experiment and theoretical modelling.* Metallurgical and Materials Transactions, 32A, 2001.

[JWL$^+$04] JIANG, L., H. WANG, P.K. LIAW, C.R. BROOKS, L. CHEN and L. KLARSTROM: *Temperature evolution and life prediction in fatigue of superalloys.* Metallurgical and Materials Transactions, 35A(3):839–848, 2004.

[KH95] KHAN, A.S. and S. HUANG: *Continuum theory of plasticity.* Wiley-Interscience puplication, New York, Chichester, Brisbane, Toronto, Singapore, 1995.

[KISS97] KISHIMOTO, K., H. INOUE, H. SHINBO and T. SHIBUYA: *Inverse analysis related to stress separation in thermoelastic stress analysis.* JSME International Journal, 40(2):108–116, 1997.

[KP02] KRAPEZ, J.C. and D. PACOU: *Thermography detection of damage initation during fatigue tests.* Volume 4710 of *Proceedings of SPIE*, pages 435–449. 2002. 1-4 April 2002, Orlando, Florida.

[KPB99] Krapez, J.C., D. Pacou and C. Bertin: *Application of lock-in thermography to rapid evaluation of fatigue limit in metals.* 1999. 5th International Workshop on Advanced Infrared Technology and Applications, September 1999, Venice, Italy.

[Kuc95] Kuck, D.: *Experimentelle Untersuchungen zum Ratchetting-Verhalten bei Baustahl ST52-3.* Dissertation, TU Braunschweig, Braunschweig, 1995.

[LB95] Lesniak, J.R. and B.R. Boyce: *A high-speed differential thermographic camera.* http://stressphotonics.com/TSA/Download.html, 1995. downloaded: June 2007.

[LBH98] Lesniak, J.R., B.R. Boyce and G. Howenwater: *Thermoelastic measurement under random loading.* http://stressphotonics.com/TSA/Download.html, 1998. downloaded: June 2007.

[LC90] Lemaitre, J. and J.L. Chaboche: *Mechanics of solid materials.* Cambridge University Press, Cambridge, 1990.

[LC01] Louche, H. and A. Crysochoos: *Thermal and dissipative effects accompanying Lüders band propagation.* Material Sciences and Engineering, A307(1):15–22, 2001.

[LMR97] Lin, S.T., J.P. Milles and R.E. Rowlands: *Image enhancement and stress separation of thermoelastically measured data under random loading.* Experimental Mechanics, 37(3):225–231, 1997.

[LRR00] La Rosa, G. and A. Risitano: *Thermographic methodology for rapid determination of the fatigue limit of materials and mechanical components.* International Journal of Fatigue, 22(1):65–73, 2000.

[Luo98] Luong, M.P.: *Fatigue limit evaluation of metals using an infrared thermographic technique.* Mechanics of Materials, 28(1):155–163, 1998.

[LWJ+00] Liaw, P.K., H. Wang, L. Jiang, B. Yang, J. Y. Huang, R. C. Kuo and J. G. Huang: *Thermographic detection of fatigue damage of pressure vessel steels at 1,000Hz and 20Hz.* Scripta Materialia, 42(4):389–395, 2000.

[Mac89] Mackenzie, A.: *Effects of surface coatings on infrared measurements of thermoelastic responses.* In: Stanley, P. [Sta89], pages 59–71.

[Mat05] *Online help to: Matlab Release 14 with Service Pack 2.* 2005.

[Mau99] Maugin, G.A.: *The thermomechanics of nonlinear irreversible behaviors*, Volume 27A of *World Scientific Series on Nonlinear Science*. World Scientific Puplishing Co., Singapore, 1999.

[McK87] McKelvie, J.: *Consideration of the surface temperature response to cyclic thermoelastic heat generation*. In: Gasper, B.C. [Gas87], pages 44–53.

[Med04] *Online help to: Image-Pro Plus 5.1 and StagePro; V5.1.0.20.* 2004.

[MF05] Müller, W.H. and F. Ferber: *Technische Mechanik für Ingenieure*. Fachbuchverlag Leipzig, Leipzig, 2 Edition, 2005.

[MRKS02] Meyendorf, N.G.H, H. Rösner, V. Kramb and S. Satish: *Thermoacoustic fatigue characterization*. Ultrasonics, 40(1):427–434, 2002.

[MS93] Miles, J.P. and B.I. Sandor: *Thermoelastic stress analysis of structures under random loading*. In: Galione, K.A. [Gal93], pages 605–616.

[MSS87a] Machin, A.S., J.G. Sparrow and M-G. Stimson: *Mean stress dependence of the thermoelastic constant*. Strain, 23:27–29, 1987.

[MSS87b] Machin, A.S., J.G. Sparrow and M-G. Stimson: *The thermoelastic constant*. In: Gasper, B.C. [Gas87], pages 26–31.

[Mül89] Müller, K.: *Thermometrische Untersuchungen an Kerben und Rissspitzen zyklisch beanspruchter Stähle*. Dissertation, Universität Gesamthochschule Essen, Essen, 1989.

[OBBF97] Offermann, S., J.L. Beaudoin, C. Bissieux and H. Frick: *Thermoelastic stress analysis under nonadiabatic conditions*. Experimental Mechanics, 37(4):409–413, 1997.

[Par03] Parish, H.: *Festkörper-Kontinuums-Mechanik*. Teubner, Stuttgart, Leipzig, Wiesbaden, 2003.

[Pas03] Pasternak, H.: *Untersuchung des thermoplastischen Verhaltens verschiedener Baustoffe mit Hilfe der Thermovision*. Bauingenieur, 78(5):221–230, 2003.

[PE95] Piotrowski, A. and D. Eifler: *Bewertung zyklischer Verformungsvorgänge metallischer Werkstoffe mit Hilfe mechanischer, thermometrischer und elektrischer Meßverfahren*. Materialwissenschaft und Werkstofftechnik, 26:121–127, 1995.

[Pip82] Pippan, R.: *Das Temperaturfeld um die Rissfront eines Ermüdungsbruches.* Dissertation, Montanuniversität Loeben, Loeben, 1982.

[PP03] Pitarresi, G. and E.A. Patterson: *A review of the general theorey of thermoelastic stress analysis.* Journal of Strain analysis, 38(5):405–417, 2003.

[PPLS+05] Plekhov, O., T. Palin-Luc, N. Saintire, S. Uvarov and O. Naimark: *Fatigue crack initiation and growth in a 35CrMo4 steel investigated by infrared thermography.* Fatigue and Fracture of Engineering Materials and Structures, 28(1-2):169–178, 2005.

[PRMM77] Pilo, D., W. Reik, P. Mayr and E. Macherauch: *Inhomogene Deformationserscheinungen in der anrißfreien Ermüdungsphase unlegierter Stähle.* Archiv für Eisenhüttenwesen, 48(11):575–578, 1977.

[PRMM78] Pilo, D., W. Reik, P. Mayr and E. Macherauch: *Zum Mittelspannungseinfluss auf das Wechselverformungsverhalten unlegierter Stähle.* Archiv für Eisenhüttenwesen, 49(1):31–36, 1978.

[PW04] Peil, U. and M. Wichers: *Schweißen unter Betriebsbeanspruchung - Werkstoffkennwerte für einen S355J2G3 unter Temperaturen bis 1200C.* Stahlbau, 73(6):400–415, 2004.

[PW05] Peil, U. and M. Wichers: *Schweißen unter Betriebsbeanspruchung - Werkstoffkennwerte zur Temperaturfeldberechnung für einen S355J2G3.* Stahlbau, 74(4):249–257, 2005.

[QDB02] Quinn, S. and J.M. Dulieu-Barton: *Identification of the sources of non-adiabatic behaviour for practical thermoelastic stress analysis.* Journal of Strain analysis, 37(1):59–71, 2002.

[QDBL04] Quinn, S., J.M. Dulieu-Barton and J.M. Langlands: *Progress in thermoelastic residual stress measurement.* Strain, 40(3):127–133, 2004.

[RA56] Rosenfield, A.R. and B.L. Averbach: *Effect of stress on the expansion coefficient.* Journal of Applied Physics, 27(2):154–156, 1956.

[Rei78] Reik, W.: *Zum Wechselverformungsverhalten des Edelstahls CK 45 im normalisierten Zustand.* Dissertation, Universität Karlsruhe, Karlsruhe, 1978.

[Rei94] Reininghaus, M.: *Baustahl St52 unter zweiachsiger plastischer Wechselbeanspruchung.* Dissertation, TU Braunschweig, Braunschweig, 1994.

[Rös03] Rösner, H.: *Thermographic nondestructive evaluation of early stages fatigue damage in titanium material.* Dissertation, Universität des Saarlandes, Saarbrücken, 2003.

[RR93] Rauch, B.J. and R.E. Rowlands: *Recent advances in determining individual stresses from thermoelastically measured isopaches.* In: Galione, K.A. [Gal93], pages 740–748.

[RS50] Rosenholtz, J.L. and D.T. Smith: *The effect of compressive stresses on the linear thermal expnasion of magnesium and steel.* Journal of Applied Physics, 21:396–399, 1950.

[RW93] Ryall, T.G. and A.K. Wong: *Infrared starring arrays and digital signal processing.* In: Galione, K.A. [Gal93], pages 730–739.

[RWL93] Rajic, N., A.K. Wong and Y.C. Lam: *A thermomechanical technique for measuring residual stress.* In: Galione, K.A. [Gal93], pages 492–501.

[SC85] Stanley, P. and W.K. Chan: *Quantitative stress analysis by means of the thermoelastic effect.* Journal of Strain analysis, 20(3):129–137, 1985.

[Sch90] Scheibe, H.J.: *Zum zyklischen Materialverhalten von Baustahl und dessen Berücksichtigung in Konstruktionsberechnungen.* Dissertation, TU Braunschweig, Braunschweig, 1990.

[Sch98] Schlicht, O.: *Einsatz der thermoelastischen Spannungsanalyse zur Untersuchung an Rissen in Platten*, Volume 18 No.225. VDI - Fortschritt Berichte, 1998.

[SD04] Salerno, A. and S. Desiderati: *Procedure proposal for the correction of nonadiabatic thermoelastic stress analysis results.* Review of Scientific Instruments, 75(2):507–514, 2004.

[SDS96] Stanley, P. and J.M. Dulieu-Smith: *Devices for the experimental determination of individual stresses from thermoelastic data.* Journal of Strain analysis, 31(1):53–63, 1996.

[SGOC00] Silva, L.F.M, J.P.M. Goncalves, F.M.F. Oliveira and P.M.S.T. de Castro: *Applicability of the SPATE technique to the detection of hidden cracks.* NDT&E International, 33:7–13, 2000.

[SH04] Stosch, R. and U. Hammerschmidt: *A new statistical approach to thermal conductivty evaluation of transeint hot-wire and transient hot-strip signals.* High Temperatures - High Pressures, 35/36:55–66, 2003/2004.

[Spa08] *Spate 4000:*. http://www.bam.de/microsites/zfp_kompendium/geraete/g046/g046.html, last checked: January 2008.

[Stä80] Stärk, F.: *Thermometrische Untersuchungen zum zyklischen Verformungsverhalten metallischer Werkstoffe*. Dissertation, Universität Stuttgart, Stuttgart, 1980.

[Sta89] Stanley, P. (editor): *Stress and vibration*, Volume 1084 of *Conference proceedings*. SPIE-The international society for optical engineering, 1989.

[Ste58] Stephenson, N.: *A review of the literature on the effect of frequency on the fatigue properties of metals and alloys*. 1958. Memorandum M320.

[Tho53] Thomson, W.: *On the dynamical theory of heat - with numerical results deduced from Mr. Joule's equivalent of a thermal unit and M. Regaut's observations on steam*. Royal Society of Edinburgh, Transactions of the Royal Society, pages 261–288, 1853.

[TK83] Traiser, H. and K.H. Kloos: *Wechselverformungsverhalten und Gefügeänderung von Ck 15 und Ck 45*. Zeitung für Werkstofftechnik, 14:157–163, 1983.

[UM06] Ummenhofer, T. and J. Medgenberg: *Numerical modelling of thermoelasticity and plasticity in fatigue-loaded low carbon steels*. QIRT Journal, 3(1):71–93, 2006.

[Web83] Weber, M.: *Untersuchungen zum zyklischen Verformungsverhalten von Stahl*. Dissertation, Universität Gesamthochschule Essen, Essen, 1983.

[WJS87] Wong, A.K., R. Jones and J.G. Sparrow: *Thermoelastic constant or thermoelastic parameter?* Journal of Physics and Chemistry of Solids, 48(8):749–753, 1987.

[WR95] Wong, A.K. and T.G. Ryall: *Design of a focal-plane array thermographic system for stress analysis*. Experimental Mechanics, 35(2):144–147, 1995.

[WSD88] Wong, A.K., J.G. Sparrow and S.A. Dunn: *On the revised theory of the thermoelastic effect*. Journal of Physics and Chemistry of Solids, 49(4):395–400, 1988.

[WZ93] Welch, C.S. and M. Zickel: *Thermal coating characterization using thermoelasticity*. Review of progress in quantitative nondestructive evaluation, pages 1923–1929, 1993. Conference proceedings.

[Yan03a] Yang, B.: *Thermographic detection of fatigue damage of reactor pressure vessel (RPV) steels.* Journal of Materials Engineering and Performance, 12(3):345–353, 2003.

[Yan03b] Yang, B.: *Thermography detection on the fatigue damage.* Dissertation, University of Tennesse, Knoxville, 2003.

[YLW$^+$01] Yang, B., P.K. Liaw, H. Wang, L. Jiang, J.Y. Huang, R.C. Kuo and J.G. Huang: *Thermographic investigation of the fatigue behavior of reactor pressure vessel steels.* Materials Science and Engineering, 314A(1):131–139, 2001.

Appendix I - Material parameters

Material, specimen geometries and preparation

The material used for all experimental investigations reported throughout this thesis is a mild unalloyed steel S355J2G3. All specimens were manufactured out of a single hot-rolled steel plate with a format of 2000 mm x 3000 mm and a thickness of 20 mm. The chemical analysis of the delivered steel plate is given in table 8.

Table 8: Chemical analysis of the used S355J2G3 in % of the total mass

C	Si	Mn	P	S	N	Cr	Al	Cu	Ni
0.179	0.315	1.487	0.016	0.008	0.006	0.051	0.034	0.029	0.018

Figure 74 shows the typical ferrite-pearlite microstructure of the steel after annealing and etching with 3 % Nital solution. The average grain size has been determined to approximately 15 μm.

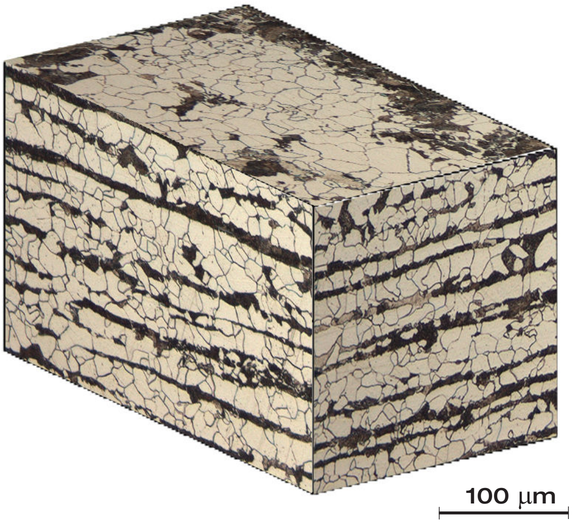

Figure 74: Microstructure of the used S355J2G3 after annealing

The experimental investigations were performed on four different specimen types shown in figures 75(a) through 75(b). Specimen types I, II and IV were tested under annealed conditions. Specimen type III was tested in the condition as received after welding. Manufacturing of the specimens included the following processing steps: first cylinders with a diameter of 19.4 mm were worked out of the steel plate. Then these raw specimens were annealed for 1 hour at 600 °C under an argon atmosphere and finished into their final shape. In order to obtain a similar surface finish all specimens were ground with wet sand paper with decreasing coarseness (grade 1000 min) and afterwards polished mechanically with diamond polish paste of a coarseness of 1 μm. After polishing all specimens were annealed again. For the microscopic investigations on specimen type II the center parts were etched with a 3 % Nital solution after annealing. Specimen type III was roughly worked out of the steel plate, brought into final shape, cut into two pieces and welded together by manual arc welding. During welding extension plates were used temporarily at both sides of the specimen. After welding the extension plates were removed and the specimens were milled into final shape. The specimens of type III were tested in the condition as received after welding without further annealing.

Monotonic stress-strain behavior

The monotonic mechanical properties of the used steel grade have been determined by quasi-static tension tests on specimen type I using the servohydraulic testing machine described in appendix II. The testing parameters have been chosen according to DIN-EN 10002-1:2001. Strains were measured within the nominal cross-section of the specimens by an optical laser-extensometer. A high resolution mode was used which limited the strain measurements to values below 1 %. Therefore the tests were performed under total strain-control for $\varepsilon \leq 0.0095$ and under displacement control for $\varepsilon > 0.0095$. The strain rate was set to 0.00005 $^1/_s$ for $\varepsilon \leq 0.0095$ and the displacement rate to 0.05 $^{mm}/_s$ for $\varepsilon > 0.0095$. Both values fall into the recommended intervals according to DIN-EN 10002-1. During the tests the voltage signals provided by the extensometer as well as the load and displacement signals of the testing machine were sampled using a National Instruments SCXI-1520 measurement card.

Table 9: Monotonic mechanical properties of the used S355J2G3

E [MPa]	$\sigma_{y,l}$ [MPa]	$\sigma_{y,u}$ [MPa]	σ_u [MPa]
214300	352	464	546

The test results of the tension tests are summarized in table 9. The values represent the mean values obtained from five specimens. All stress values are calculated based on the recordings of the load cell and the diameters of the specimens measured after annealing. The Young's modulus is obtained as the mean value of the secant slope in the elastic range between 100 and 300 Mpa. The lower yield limit represents the mean value of the yield plateau in the strain range between 0.003 and 0.009.

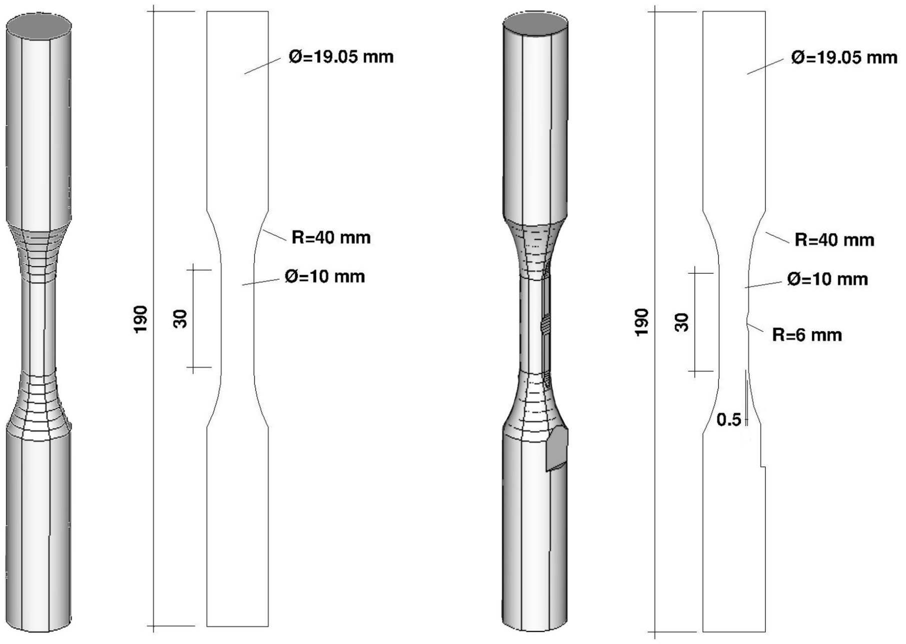

(a) specimen type I (b) specimen type II

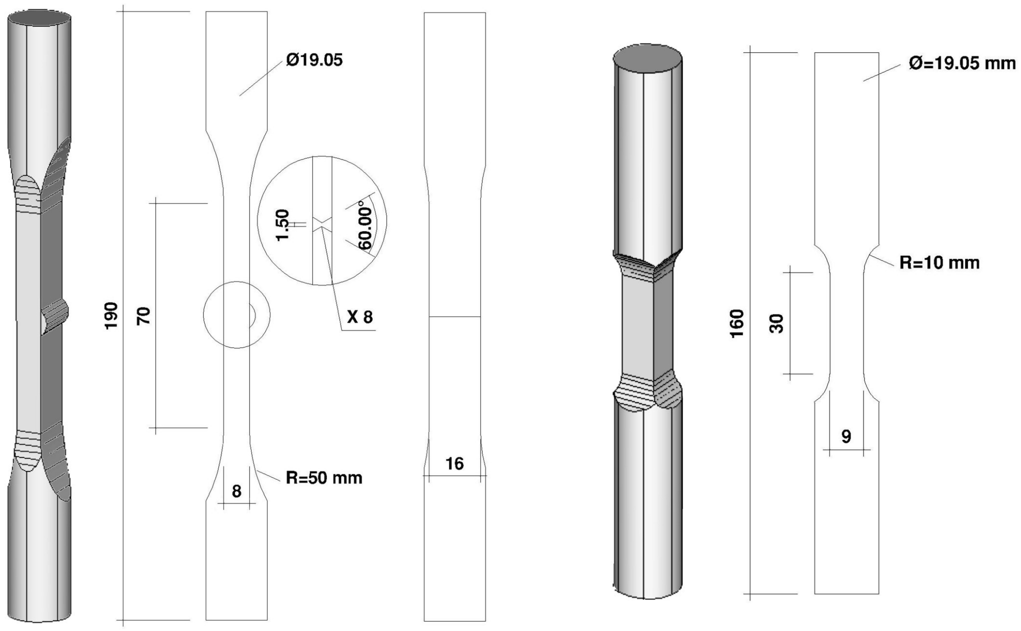

(c) specimen type III (d) specimen type IV

Figure 75: Specimen types and geometries

Temperature dependency of the elastic properties

The temperature dependency of the elastic constants around room temperature was determined by quasi-static tests on three specimens of type IV at different specimen temperatures. Temperature control was realized by heatable hydraulic grips using an external heating circulator (refer to the description of the experimental setup in appendix II). The thermostat of the heating circulator did not allow for an external control mode with an additional temperature reference. Accordingly the stabilized temperature of the specimens differs from the preset outflow temperature at the thermostat. Therefore the current stabilized temperatures of the specimens has been measured by a calibrated infrared camera at each temperature step. For this purpose a small area of the specimen surface has been coated with graphite spray. The temperature of the specimen is obtained as spatial mean value of a 20 x 40 pixel area within the coated reference section. All specimens have been equipped with two strain gauges in longitudinal and two gauges in transverse direction at two adjacent sides of the measurement section. Each strain gauge has been connected within an individual quarter bridge circuit.

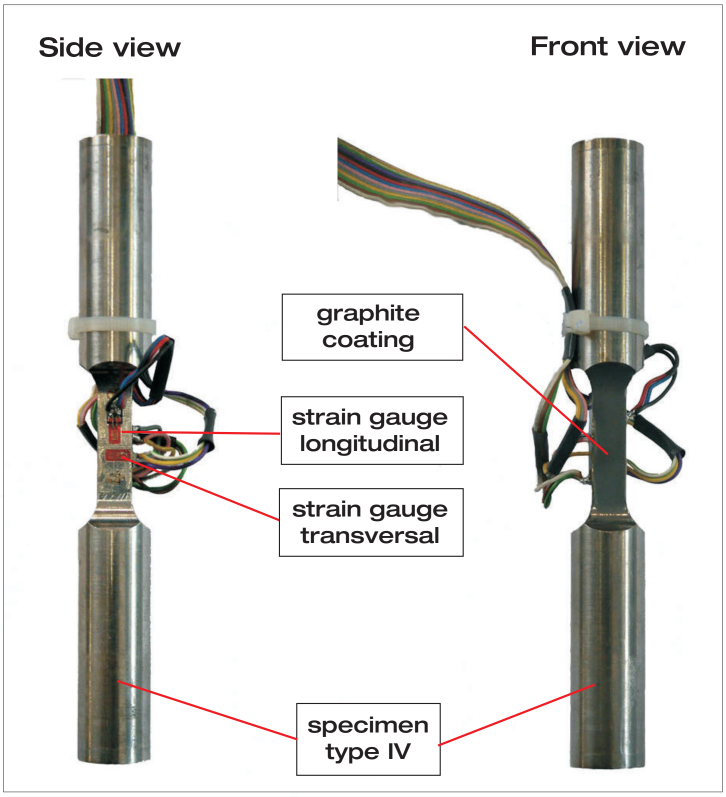

Figure 76: Specimen preparation; specimen type IV

The mean temperature of the specimens was varied between 15 °C and 35 °C in steps of approximately 1 °C by adjusting the temperature of the coolant pumped through the grips. At each temperature step the specimen was allowed to reach a steady temperature. Then the Young's modulus and the Poisson's ratio of the steel were evaluated by load-controlled quasi-static tension and compression tests within the elastic regime of the specimens. For this purpose a complete load cycle was applied, using a triangular shape function with a maximum load amplitude of 20 kN (corresponding to about 250 Mpa) applied at a constant load rate of 0.4 $^{\mathrm{kN}}/_{\mathrm{s}}$. Only a few load cycles have been applied to each specimen so that the testing can be regarded as non-destructive.

For data evaluation the temperature dependency of the gauge factor is assumed to be negligible according to the specifications provided by the manufacturer. Since no temperature compensation was used for the strain gauges the mean strain values obtained for each stabilized temperature step were set to zero at the beginning of the measurements. For each specimen two independent values of the Young's modulus and the Poisson's ratio can be determined by the four strain gauges (compare figure 76). The Young's modulus is obtained as the slope of the linear stress-strain curve which has been calculated from the test results by linear-least square fitting. The Poisson's ratio is given as the ratio of the strain variations in transverse direction and the strain variations in longitudinal direction. The results of the tests are given in figure 77(a) and 77(b) which represent the mean values of the two corresponding strain gauge measurements for each specimen.

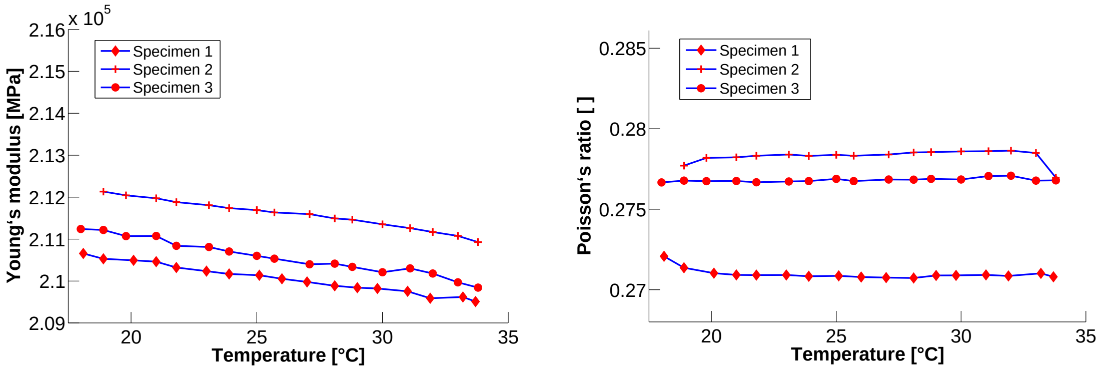

(a) Young's modulus (b) Poisson's ratio

Figure 77: Temperature dependency of the elastic material constants between 18 °C and 33 °C

The scatter in the absolute value of the Young's modulus and the Poisson's ratio is attributed to imprecision in the specimen shape, the exact orientation of the strain gauges and the natural scatter of the material properties of the individual specimens. The results in figure 77(a) confirm a clear decrease of the Young's modulus with increasing temperature. In the investigated temperature range a linear relation can be assumed. The temperature dependency of the Young's modulus dE/dT is obtained as the linear slope of the curves given in figure 77(a) which is evaluated by a linear-least-squares fitting of a linear curve to the experimental results. The corresponding values for the individual measurements are summarized in table 10. For the numerical calculations the mean value of the three measurements $\frac{\partial E}{\partial T} = -76.6$ $^{\mathrm{MPa}}/_{\mathrm{K}}$ has been used. Figure 77(b) shows that the Poisson's ratio remains quasi-constant throughout the observed temperature range. The temperature dependency of the Poisson's ratio is negligible and a constant value of $\nu = 0.275$ is used for all calculations. This value corresponds to the mean value of the measurements given in figure 77(b).

Table 10: Temperature dependency of the elastic material constants

Measurement	Specimen 1	Specimen 2	Specimen 3	Mean value
$\frac{\partial E}{\partial T}$ [$^{\mathrm{MPa}}/_{\mathrm{K}}$]	-72.9	-73.5	-83.6	-76.6

Thermal material properties

The thermal conductivity k and the thermal diffusivity λ_T have been obtained from transient heat stripe tests. The method has been recently developed at the Physikalisch-Technische Bundesanstalt Braunschweig (PTB) (see [SH04]). The experiments were conducted on cubic un-annealed specimens with the dimensions 19 mm x 40 mm x 20 mm and yield $k = 42$ $^{\mathrm{W}}/_{(\mathrm{m}\cdot\mathrm{K})}$ and $\lambda_T = 12.6 \cdot 10^{-6}$ $^{\mathrm{m}^2}/_{\mathrm{s}}$. The testing accuracy is specified by the PTB with ±5 % around the given values. The specific density of the steel is set to 7830 $^{\mathrm{kg}}/_{\mathrm{m}^3}$ based on well documented values of a comparable steel grade published recently by [PW04] and [PW05]. From the given values the heat capacity at constant pressure C_P is obtained through:

$$C_P = \frac{k}{\rho \lambda_T} \tag{79}$$

For the representation of the thermoelastic coupling term in terms of strains, the heat capacity at constant strain C_ε needs to be used in equation (49) which is related to C_P through (see [Hus94]):

$$C_\varepsilon = C_P - \frac{3E\alpha^2 T_0}{\rho(1-2\nu)} \tag{80}$$

T_0 is set to 293 K here, which represents typical laboratory conditions during testing. The coefficient of thermal expansion α is determined by an indirect approach based on measurements of the temperature variations due to thermoelastic coupling. According to the numerical investigations in chapter 5 bidirectional coupling causes a reduction of the thermoelastic temperature variations. Therefore the coefficient of thermal expansion will be slightly under-predicted by the chosen approach. For the numerical model the under-prediction of the thermoelastic temperature variations becomes negligible if decoupled numerical modeling is used instead of the bidirectional approach. The expression of linear thermoelastic coupling under adiabatic conditions is derived by combining equations (49) and (66):

$$\rho C_\varepsilon \frac{dT}{dt} = -T_0 \frac{E\alpha}{1-2\nu}\left(\frac{d\varepsilon_{ij}^{e}}{dt}\right)\delta_{ij} = -T_0 \frac{E\alpha}{1-2\nu}\left(\frac{d\boldsymbol{\varepsilon}_I^{e}}{dt}\right) \tag{81}$$

The temperature dependency of the elastic constants and the effects of heat diffusion have been neglected here. $\boldsymbol{\varepsilon}_I^{\boldsymbol{e}}$ represents the first invariant of the elastic strain tensor. Due to experimental reasons load controlled testing is preferable. Therefore an alternative representation of (81) in terms of stresses needs to be derived. For this purpose the expression for the first strain invariant $\boldsymbol{\varepsilon}_I^{\boldsymbol{e}}$ is calculated from equation (58):

$$\boldsymbol{\varepsilon}_I^{e} = \frac{1+\nu}{E}\boldsymbol{\sigma}_I - 3\left(\frac{\nu}{E}\boldsymbol{\sigma}_I - \alpha\Delta T\right) = \frac{1-2\nu}{E}\boldsymbol{\sigma}_I + 3\alpha\Delta T \tag{82}$$

The time derivative of the first invariant of the elastic strain tensor is given as:

$$\frac{d\boldsymbol{\varepsilon}_I^{e}}{dt} = \frac{1-2\nu}{E}\frac{d\boldsymbol{\sigma}_I}{dt} + 3\alpha\frac{dT}{dt} \tag{83}$$

if constant material properties with respect to time are assumed. Equation (83) is plugged into (81) which yields:

$$\rho C_\varepsilon \frac{dT}{dt} = -T_0\alpha\frac{d\boldsymbol{\sigma}_I}{dt} - T_0\frac{3E\alpha^2}{1-2\nu}\frac{dT}{dt} \tag{84}$$

If definition (80) is used, the coefficient of thermal expansion α can be determined by:

$$\alpha = -\frac{\rho C_P}{T_0}\frac{dT}{d\boldsymbol{\sigma}_I} \tag{85}$$

In a uniaxial stress state one has $\boldsymbol{\sigma}_I = \frac{F}{A}$ with F and A representing the applied force and the nominal cross-section of the specimen, respectively. For the experimental determination of α three different specimens of type I have been subjected to harmonic load-controlled loading with zero mean stress at different load amplitudes and a frequency of 15 Hz. Note that for this specimen type adiabatic conditions have been confirmed by the numerical investigations of chapter 5. The load levels were chosen low enough to ensure purely linear-elastic material behavior throughout the entire specimen.

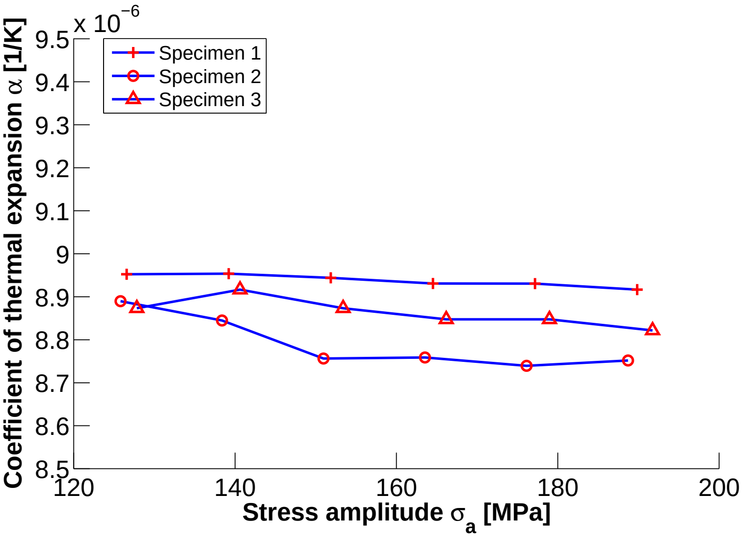

Figure 78: Coefficient of thermal expansion

During the mechanical loading the temperature variations of the specimen have been evaluated with a calibrated infrared camera. T_0 is obtained as the spatial mean value of the mean temperature of a 20 x 40 pixel reference section in the center of the specimen. Assuming linearity, the derivative $\frac{dT}{d\boldsymbol{\sigma}_I}$ can be estimated as the ratio of the measured temperature amplitude and the amplitude of the stress amplitude, which is calculated based on the load signals provided by the testing machine. Figure 78 shows the coefficient of thermal expansion calculated for three different specimens from equation (85) at different load levels and the same testing frequency. The diagram shows that the coefficient of thermal expansion remains quasi-constant in the investigated load range. For further calculations the mean value of all measurements $\alpha = 8.8 \cdot 10^{-6}\ {}^1\!/\mathrm{K}$ is used. Note that this value is significantly smaller than the value of $\alpha \approx 12.0 \cdot 10^{-6}\ {}^1\!/\mathrm{K}$ commonly used for structural calculations. Comparable values for a similar steel have also been reported by [PW04].

For convenience all values of the thermal properties of the used steel grade are summarized in table 11 again.

Table 11: Thermal properties of the used S355J2G3

k $[\mathrm{W}/(\mathrm{m{\cdot}K})]$	λ_T $[10^{-6}\ \mathrm{m}^2/\mathrm{s}]$	ρ $[\mathrm{kg}/\mathrm{m}^3]$	C_P $[\mathrm{J}/(\mathrm{kg{\cdot}K})]$	C_ε $[\mathrm{J}/(\mathrm{kg{\cdot}K})]$	α $[1/\mathrm{K}]$
42.0	12.6	7830	425	429	$8.8{\cdot}10^{-6}$

Appendix II - Testing equipment

Testing machine

The testing machine used throughout the experimental studies is a digitally controlled servohydraulic testing machine (MTS, load frame 810, 200 kN, hydraulic collet grips 646) with a maximum load capacity of 200 kN. The installed hydraulic grips limit the maximum forces to ±100 kN. The grips require cylindrical specimens with a diameter in the clamp section of 19.05 ± 0.05 mm. They are powered by an external hydraulic system, which is independent of the main hydraulic circuit. The temperature of the grips can be cooled or heated by a thermostat (Julabo, FE 1100) in order to minimize the temperature drift of the setup during long term fatigue testing. The thermostat delivers a constant water flow with stabilized temperatures between 5 and 40 °C at a setting-point resolution of 0.1 K. The control-mode of the thermostat is open-loop without external temperature reference. This means that the stabilized temperature of the grips differs from the outflow temperature of the thermostat. The coolant outflow of the lower grip - which is directly attached to the main hydraulic cylinder and therefore strongly influenced by the hydraulic circuit - has been used as inflow for the upper grip. This provides a nearly equal temperature of both grips and avoids strong temperature gradients within the clamped specimen.

The testing machine is connected to a digital controller (MTS, Teststar IIs) and a corresponding testing software (MTS, Teststar Station Manager, Version 3.4b). The controller provides load controlled, displacement controlled and strain controlled operation modes. Strain control is realized via an external non-contacting laser extensometer (Fiedler Optoelektronik GmbH). For this purpose the calibrated voltage output of the extensometer is used as an external control input for the testing machine. The controller offers different digital and analog I/O options which have been used for communication between the different components of the testing setup. All testing routines used throughout the different tests are based on a user-programmable script engine provided by the controller software. During most tests some additional parameters of the testing machine have been recorded using a National Instruments PCI-6251 or SCXI-1520 data acquisition board and National Instruments LabView 7.0.

Light-microscope and positioning unit

The microscopic investigations described in chapter 6 require the repeated inspection of the specimen surface during high cycle fatigue testing. In order to reduce the high costs and the time required for removal of the specimens and regular light-microscopic inspections, an automated testing setup has been designed and installed which allows for mechanical testing with parallel in situ visual inspection and infrared measurements. For this purpose the testing machine has been complemented by a 3-axes linear stage positioning setup (Micos, 2 x LS-180 and 1 x LS-110). The positioning unit carries a video-light-microscope and an infrared camera (FLIR Phoenix DTS). The complete experimental setup and a detailed view of the camera systems are given in figure 79.

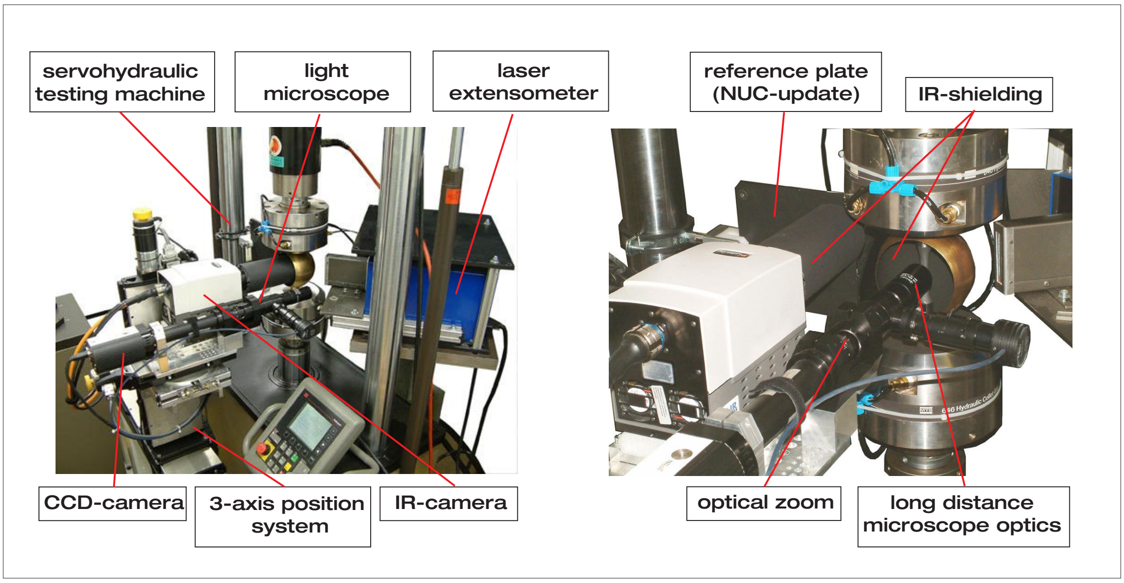

Figure 79: Overview of the experimental setup and the camera systems

The installed linear stages are based on high-precision ball screws drives. The vertical and the horizontal axis LS-180 include internal displacement measurement devices and are operated in a closed-loop mode. Both axes have been found to provide a bidirectional repetition accuracy around 4 μm. The horizontal LS-110 is used to focus the cameras and runs in open-loop mode. The stages are controlled via a serial port (RS-232 port) with an internal PCI-controller (Corvus, SMC-PCI). The positioning unit is mounted on a solid steel tripod which provides several options for leveling the entire setup. For the mounting of the cameras on the positioning system a special platform has been designed which allows for high-precision 3-axes leveling and additional rotational adjustment.

The video-light-microscope consists of a digital 12-bit grey-scale CCD-camera with an array of 1360 x 1024 pixels (QImaging, QICam) and a 12X manual zoom objective (Opto, Zoom 125). Different long-distance microscope lenses are used which provide an additional magnification between 1X and 20X. The camera is controlled by a general-purpose image processing software (MediaCybernetics, Image-Pro MC 5.1 [Med04]) which allows for several digital I/O options through an external data acquisition device.

Additionally the software can be used to control the linear stages. The automated test-procedure is realized using a program-intern macro language.

In order to isolate the test stand against environmental vibrations the entire setup has been mounted on a solid steel plate with dimensions 1200 mm x 2000 mm and a thickness of 50 mm. The plate is supported by four mechanically controlled air springs (Bilz, BIAIR 1-ED/HE) which are permanently pressurized by compressed air. The isolated mounting plate has been found to effectively damp vibrations with a frequency > 7 Hz.

Infrared camera

The infrared camera used for the investigations is a Phoenix DTS (FLIR Systems) with a 640 x 512 InSb focal plane detector built by Indigo Systems. The sensor is sensitive to thermal radiation in the wavelength range between 3 and 5 μm. The Noise Equivalent Temperature Difference (NETD) of the camera head is specified by the manufacturer with 18 mK at an integration time of 1.2 ms. A 50 mm lens with different extension rings is used for all investigations. Image recording is performed with the software bundle RTools from FLIR Systems [FLI05]. Further data processing is done with Matlab V7.0 (R14) [Mat05].

The IR camera allows the user to adjust several advanced camera settings to the specific measurement task. Generally a new camera calibration and non-uniformity correction is required if any of the settings are changed. In order to increase the frame rate of the camera a sub-array of 300 x 192 pixels is used for all investigations. The integration time is set to 2 ms and an internal gain factor of 2.0 is used for the detector. With these settings a maximum frame rate of approximately 412.5 Hz could be achieved. For each of the different lens configurations used throughout the investigations a two point non-uniformity-correction (NUC) has been performed and an individual calibration curve has been determined.

The NUC becomes necessary since individual pixels of a focal plane detector generally exhibit a different response with respect to the incident radiation. This non-uniformity of the detector is equalized by a two point (gain and offset) correction prior to any further data processing. For the NUC the gain factor (the linear response of the pixels with respect to the incident radiation) and the offset of each pixel are evaluated using a black body radiation source. The black body is set to two different temperatures T_1 and T_2 which are slightly below and above the temperature range to be calibrated. At both temperatures the grey values $\boldsymbol{G}$ of the camera must not saturate and lie within the linear range of the detector. From the grey value readings at both temperatures the gain $\boldsymbol{S}$ and the offset $\boldsymbol{O}$ of each pixel are obtained by:

$$\boldsymbol{S} = \frac{\overline{\boldsymbol{G}_{T_2} - \boldsymbol{G}_{T_1}}}{\boldsymbol{G}_{T_2} - \boldsymbol{G}_{T_1}} \tag{86}$$

$$\boldsymbol{O} = \overline{\boldsymbol{G}_{T_1} \cdot \boldsymbol{S}} - \boldsymbol{G}_{T_1} \cdot \boldsymbol{S} \tag{87}$$

$\overline{\boldsymbol{G}_{T_2} - \boldsymbol{G}_{T_1}}$ is the spatial mean gain of the uncorrected pixels and $\overline{\boldsymbol{G}_{T_1} \cdot \boldsymbol{S}}$ is the spatial mean value of the pixels after applying the gain correction. The grey value images $\boldsymbol{G}$ of the black body scenery used in equations (86) and (87) are obtained as temporal mean value of a sequence of 100 images (noise reduction). With the definition of the gain $\boldsymbol{S}$ and the offset $\boldsymbol{O}$ the corrected grey value image $\boldsymbol{G}^*$ is given through:

$$\boldsymbol{G}^* = \boldsymbol{G} \cdot \boldsymbol{S}^{-1} + \boldsymbol{O} \tag{88}$$

The offset matrix $\boldsymbol{O}$ is updated occasionally during the operation of the camera to correct for the detector drift and heating up of the camera chassis. The gain matrix $\boldsymbol{S}$ is evaluated only once for the current camera settings.

IR-detectors generally do not offer an operability of 100 % but exhibit some corrupted or dead pixels which do not meet the specifications for correct radiation measurements. For the given settings of the cameras all dead pixels within the used sub-window have been determined and corrected before further processing. The correction assigns to every dead pixel a mean value of the neighboring (uncorrupted) pixels. The analysis revealed 162 dead or corrupted pixels in the used sub-window which corresponds to a detector operability of 99.7 %.

The purpose of the calibration is to assign the corrected grey values of the camera to a specific temperature of the investigated object. For any quantitative approach special attention has to be given to the thorough calibration of the camera and the correct determination of all relevant factors. Generally a linear relationship between the grey values of the camera and the irradiance (received radiation of the detector) can be assumed. The spectral radiant exitance $\Phi(\lambda_\Phi, T)$ of a black body in $[\mathrm{W}/(\mathrm{m}^2\mu\mathrm{m})]$ is given by Planck's equation as ([Hol98], [HW90]):

$$\Phi(\lambda_\Phi, T) = \frac{c_1}{\lambda_\Phi^5}\left(\frac{1}{e^{\frac{c_2}{\lambda_\Phi T}} - 1}\right) \tag{89}$$

c_1 and c_2 are two radiation constants with $c_1 = 3.7418 \cdot 10^8\ \mathrm{W}\mu\mathrm{m}^4/\mathrm{m}^2$ and $c_2 = 1.4388 \cdot 10^4$ $\mu\mathrm{m} \cdot \mathrm{K}$. According to Planck's equation the increase of an object's temperature shifts the maximum of the emitted electromagnetic radiation towards smaller wavelengths λ_Φ and additionally causes an increase of the radiant exitance. Generally one can assume an object emissivity $\epsilon < 1$ and a transmissivity of the atmosphere and the lens system $\tau < 1$. Then the irradiance $\Phi(\lambda_\Phi, T)^*$ measured by the camera detector is given through:

$$\Phi(\lambda_\Phi, T)^* = \tau \left[\epsilon\Phi(\lambda_\Phi, T_{Object}) + (1-\epsilon)\Phi(\lambda_\Phi, T_{Background})\right] + (1-\tau)\Phi(\lambda_\Phi, T_{Lens}) \quad (90)$$

Apparently the calibration of an IR camera rather complex since the irradiance received by the IR-detector is influenced by various factors such as the emissivity of the object, the transmissivity of the atmosphere and the optical system, the thermal background radiation and the temperature of the optical system. For a correct calibration the true radiant exitance $\Phi(\lambda_\Phi, T_{Object})$ of the object under consideration has to be retrieved from equation (90). Then the object's temperature can be determined by the inversion of equation (89) which needs to be integrated over the sensitive wavelength range of the camera detector. Unfortunately the application of the radiation model (90) requires the correct determination of all relevant factors and thus involves various uncertainties.

For the present investigations an alternative and more direct approach for the calibration has been chosen: a 'black body' is coated with the graphite coating (emissivity $\epsilon \approx 0.87$) used throughout all investigations. The coated black body is set to different temperatures and the corresponding grey value readings of the camera are directly associated with the temperature of the black body. The chosen approach avoids the problems associated with the adjustment of the radiation model (90), but demands that all relevant factors (temperatures, object emissivity and transmissivity values) do not change significantly. Without going into too much detail this can be assumed for the experiments reported here, owing to the relatively constant laboratory conditions. Parameters which are difficult to control such as the temperature of the optical system and the room temperature do not have a significant influence on the differential measurements. They rather affect the absolute temperature readings which are of minor importance here.

For technical reasons a two step conversion of the grey values into temperatures has been adopted: first the grey values are converted into a (pseudo) radiant exitance $\Phi(\lambda_\Phi, T)'$ by applying Planck's equation. The calculation is based on the setting point temperature of the black body under the assumption $\epsilon = 1.0$. This pseudo radiant exitance is associated with the measured grey values by fitting a third order polynomial (figure 80(a)). The given curve has been obtained for graphite coating and a 50 mm lens with an additional extension ring of 23 mm. For the retrieval of the temperatures from a grey value image first the pseudo-radiant exitance is calculated based on the fitted calibration curve in figure 80(a). Then the temperature values are calculated back by applying the inversion of Planck's equation within the sensitive wavelength range of the detector. For computational purposes both operations are simplified by applying a fitted polynomial (figure 80(b)). Note that the radiation values given in figure 80(a) do not represent a true physical property since they have been obtained

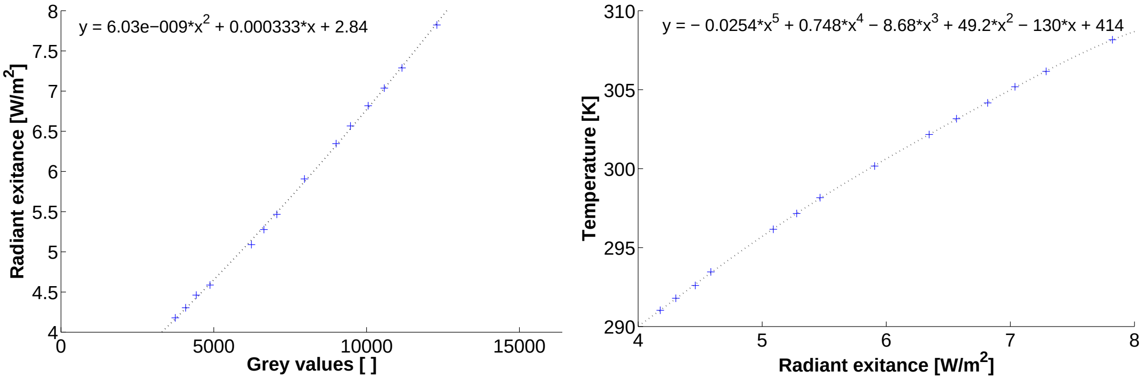

(a) conversion of the grey values into radiant exitance

(b) conversion of the radiant exitance into temperatures

Figure 80: Conversion of the grey values into temperatures

without adjusting the radiation model (90). Instead the calculation of the radiant exitance constitutes only an intermediate calculation step which is used to relate the grey values directly to the temperature readings.

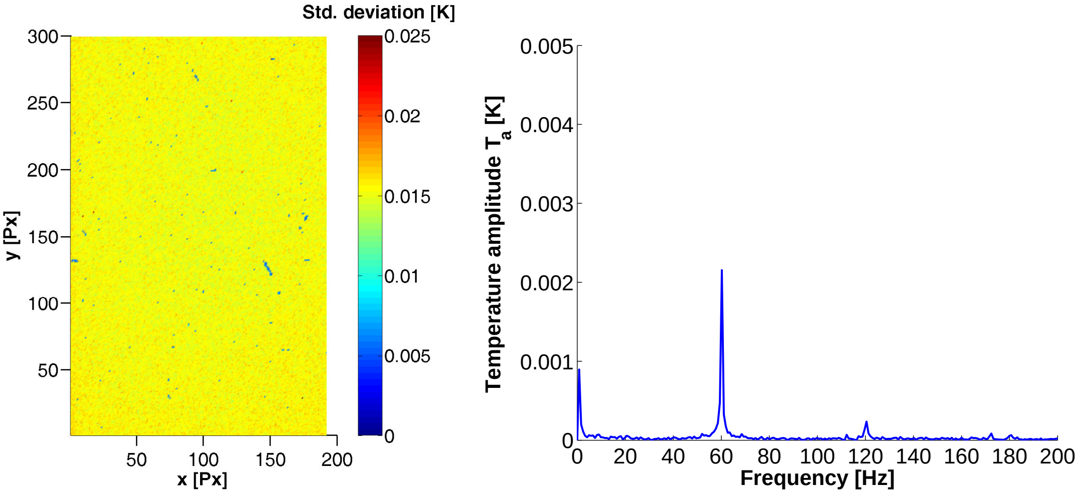

(a) spatial distribution of the standard deviation

(b) amplitude spectrum of the detector noise

Figure 81: Distribution of the standard deviation of the black body temperature readings at 24 °C and corresponding amplitude spectrum of the detector noise

As a last important point the noise behavior of the detector under the given camera settings is discussed. Figure 81(a) shows the spatial distribution of the temporal standard deviation of a sequence of 500 IR images taken of a uniform black body scenery (emissivity $\epsilon \approx 0.9713$ according to the manufacturer specifications) at 24 °C.

Most of the pixels exhibit a standard deviation of approximately 0.015 K. The standard deviation is uniformly distributed across the image which implies that all pixels exhibit a similar noise behavior. The standard deviation of the identified dead pixels is smaller since the chosen correction procedure involves the calculation of a spatial mean value for these pixels and thus reduces the inherent temporal noise. The mean standard deviation across the entire subwindow is 0.0153 K which can be regarded as the NETD for the given settings.

Figure 81(b) shows the spectral distribution of the temperature readings of the same black body scenery. The spectral distribution is obtained by applying a Fast Fourier Transform (FFT) over the temporal variation of each pixel and calculating the amplitudes at the different frequencies. Before applying the Fourier transform the temporal mean temperature of each pixel has been subtracted. The curve given in figure 81(b) represents the spatial mean value calculated from the Fourier transform of all pixels within the used sub-window.

With the exception of two distinct peaks at 60 Hz and 120 Hz the amplitude spectrum reveals that the detector noise is uniformly distributed over all frequencies. The peak close to 1 Hz is most probably caused by slow fluctuations of the black body temperature around its setting point value during the acquisition of the image sequence. The peak of the detector noise at 60 Hz reveals periodic temperature oscillations of about 2.2 mK. Further investigations showed that the mechanical cooler of the camera is operated at 60 Hz. Apparently the work cycle of the cooler causes periodic fluctuations of the temperature readings at its working frequency and associated higher harmonics (120 Hz). This has to be taken into account if temperature variations around 60 Hz are to be investigated.

Appendix III - Results

1) Damage evolution of notched specimens

The following images show the damage evolution on specimens of type II. For each specimen the evolution of the linear and nonlinear temperature amplitudes at the center line y=0 and microscopic images of a small surface detail of the specimen are given. The results are discussed in chapter 6. The following drawing clarifies the location of measurement.

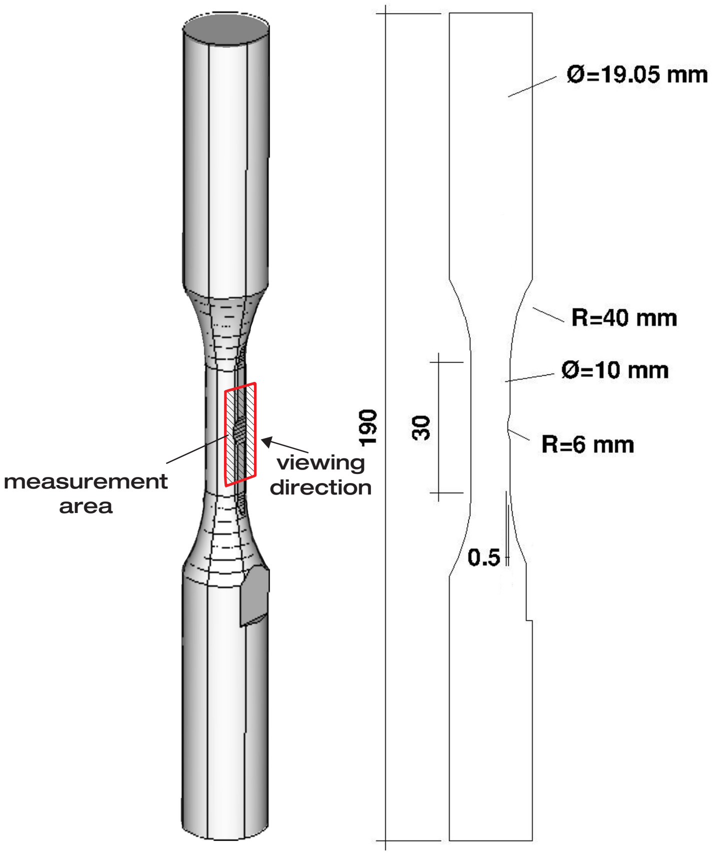

Figure 82: Definition of the measurement area; specimen type II

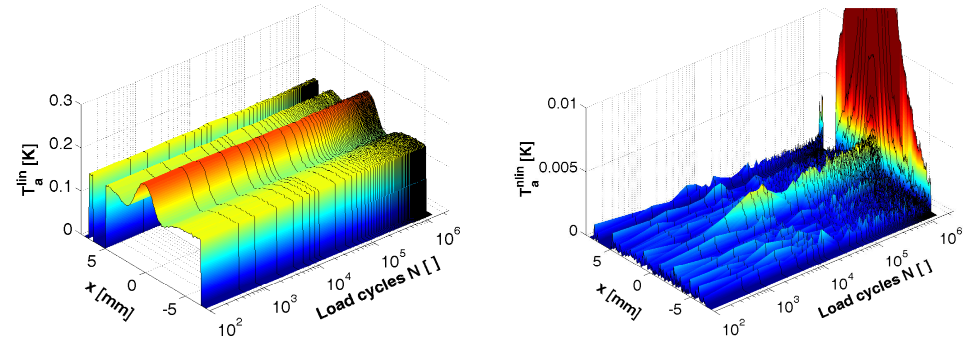

linear temperature amplitude

non-linear temperature amplitude

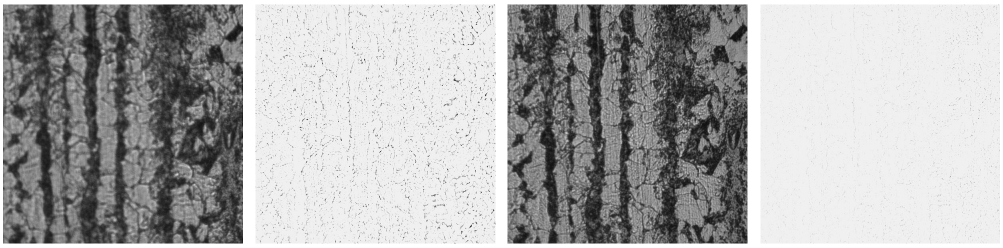

$N = 75000;\ N/N_f = 0.05$

$N = 135000;\ N/N_f = 0.10$

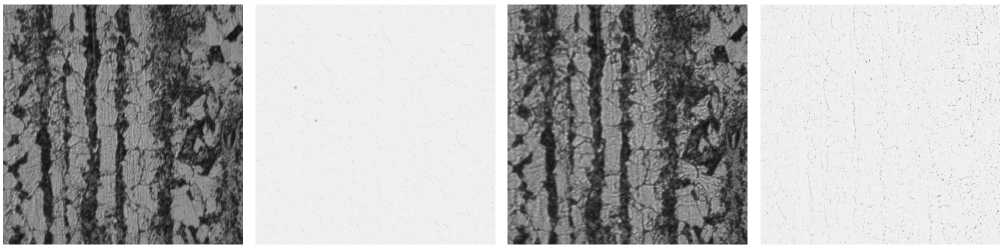

$N = 285000;\ N/N_f = 0.20$

$N = 420000;\ N/N_f = 0.30$

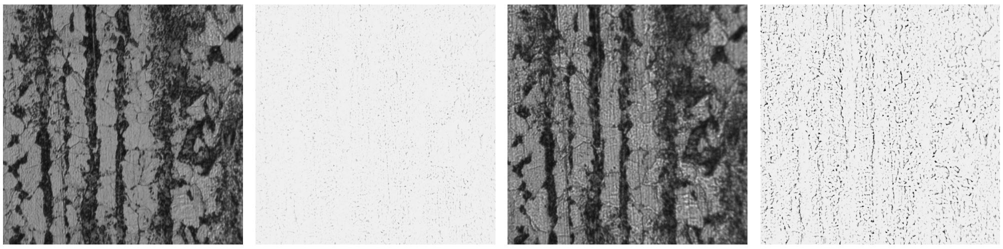

$N = 555000;\ N/N_f = 0.40$

$N = 705000;\ N/N_f = 0.50$

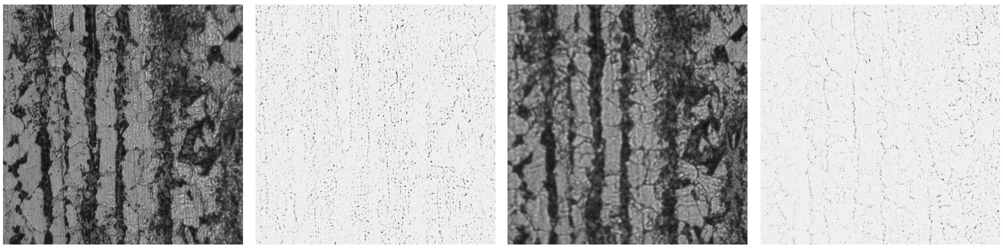

$N = 1005000;\ N/N_f = 0.75$

$N = 1335000;\ N/N_f = 0.95$

100 µm

Figure 83: Notched specimen RK0603; microscopic pictures in nominal cross-section

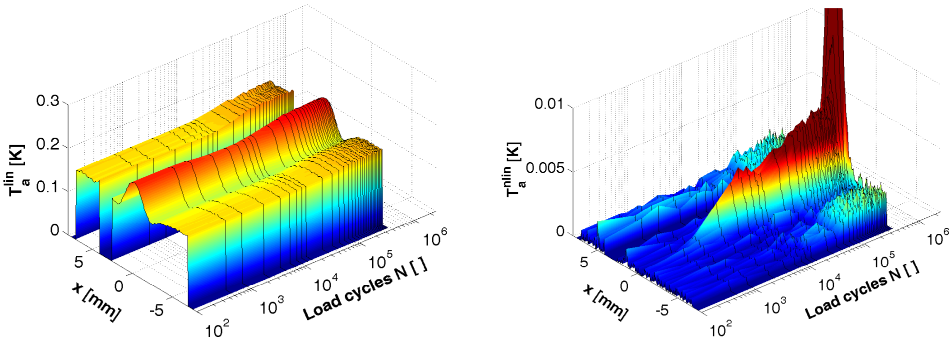

linear temperature amplitude non-linear temperature amplitude

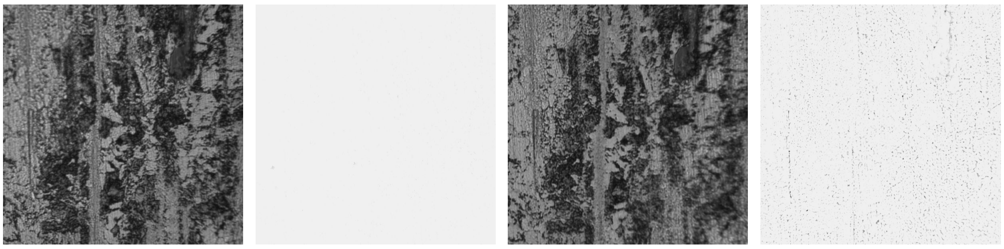

$N = 15000$; $N/N_f = 0.04$ $N = 45000$; $N/N_f = 0.11$

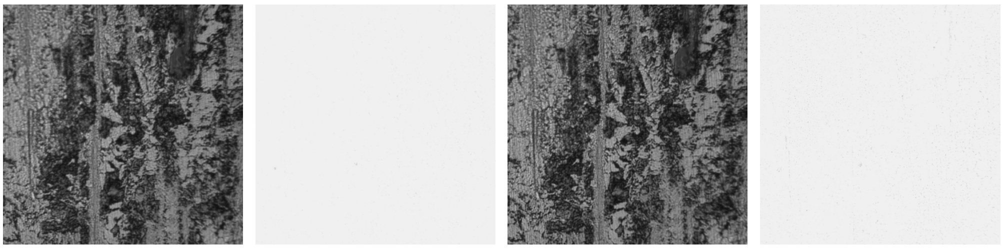

$N = 75000$; $N/N_f = 0.18$ $N = 120000$; $N/N_f = 0.30$

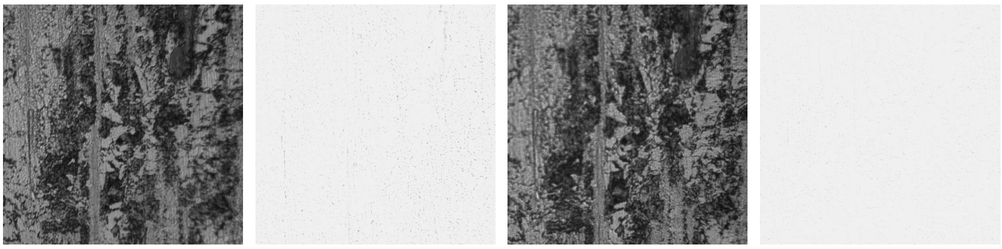

$N = 165000$; $N/N_f = 0.41$ $N = 210000$; $N/N_f = 0.52$

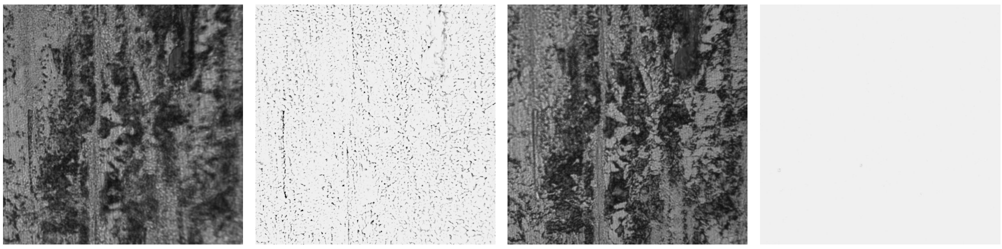

$N = 300000$; $N/N_f = 0.74$ $N = 390000$; $N/N_f = 0.96$

100 µm

Figure 84: Notched specimen RK0605; microscopic pictures in nominal cross-section

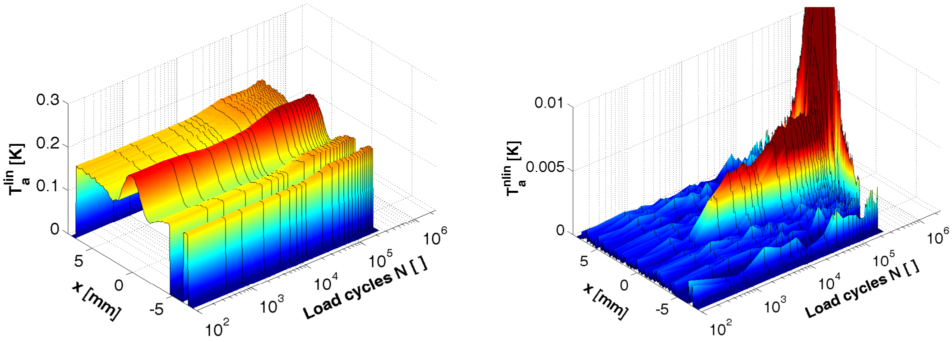

linear temperature amplitude non-linear temperature amplitude

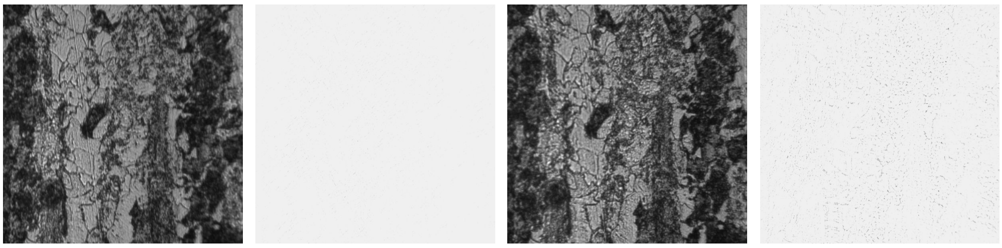

$N = 15000$; $N/N_f = 0.06$ $N = 30000$; $N/N_f = 0.11$

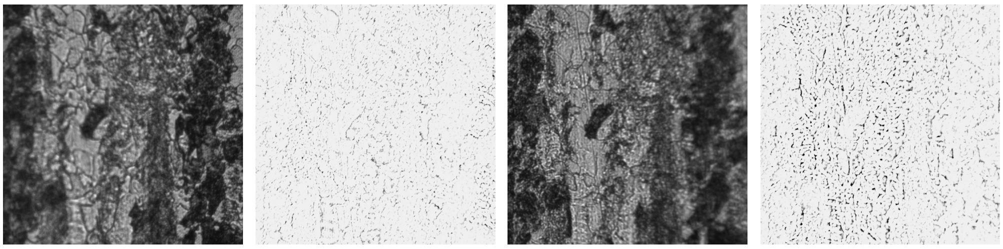

$N = 45000$; $N/N_f = 0.17$ $N = 75000$; $N/N_f = 0.28$

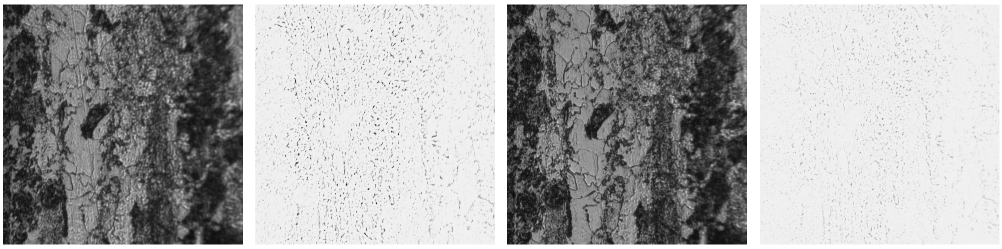

$N = 105000$; $N/N_f = 0.40$ $N = 135000$; $N/N_f = 0.51$

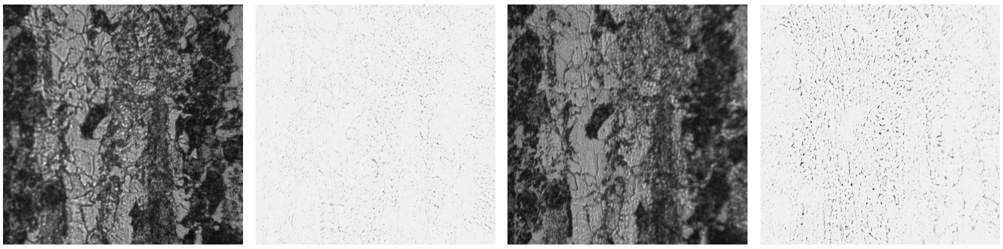

$N = 195000$; $N/N_f = 0.74$ $N = 255000$; $N/N_f = 0.96$

Figure 85: Notched specimen RK0606; microscopic pictures in nominal cross-section

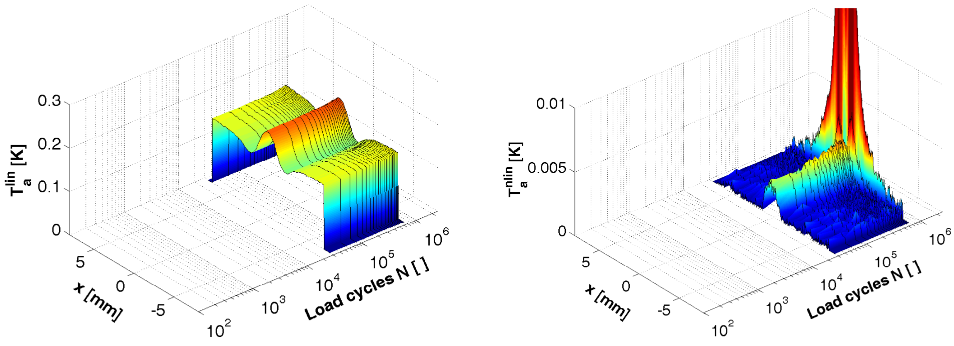

linear temperature amplitude non-linear temperature amplitude

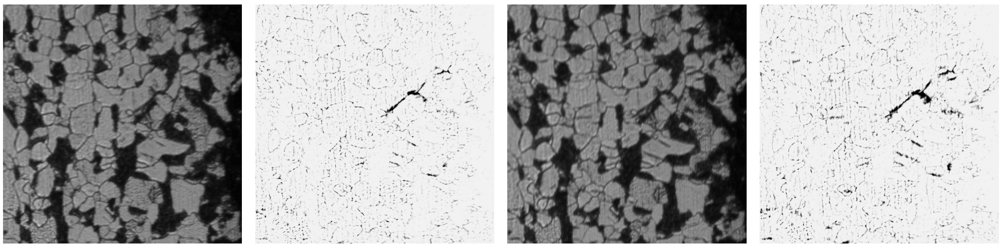

$N = 30000$; $N/N_f = 0.04$ $N = 75000$; $N/N_f = 0.11$

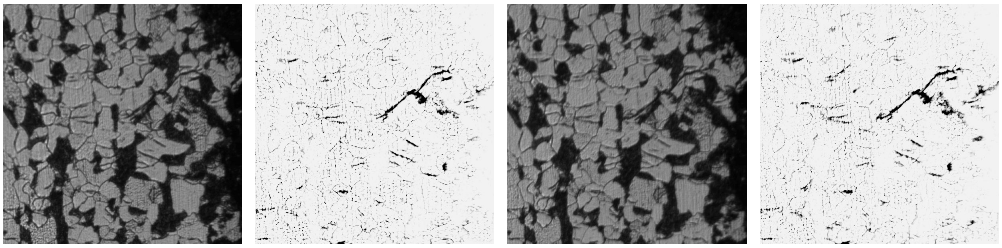

$N = 135000$; $N/N_f = 0.19$ $N = 210000$; $N/N_f = 0.30$

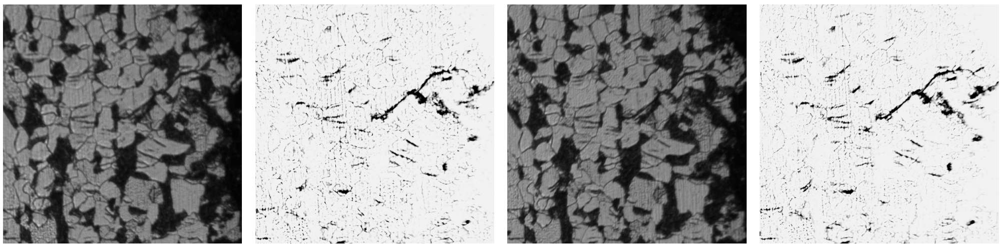

$N = 285000$; $N/N_f = 0.40$ $N = 360000$; $N/N_f = 0.51$

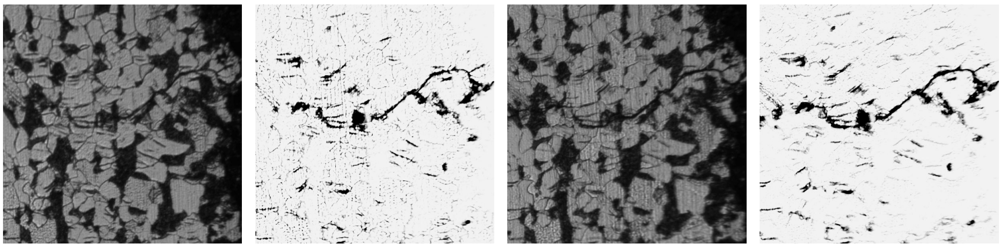

$N = 540000$; $N/N_f = 0.76$ $N = 675000$; $N/N_f = 0.95$

Figure 86: Notched specimen RK0608; microscopic pictures within the notch

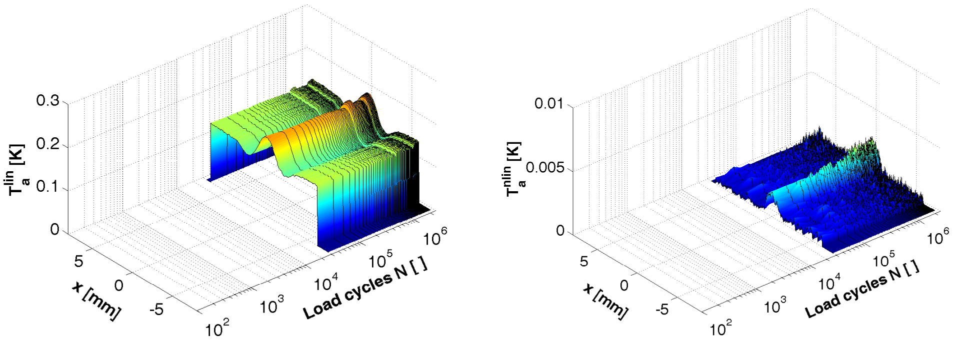

linear temperature amplitude non-linear temperature amplitude

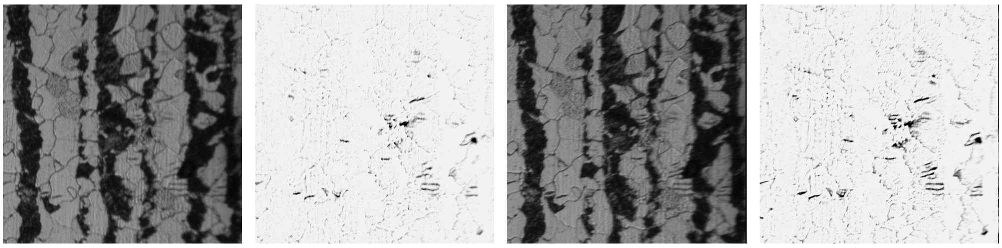

$N = 120000$; $N/N_f = 0.05$ $N = 270000$; $N/N_f = 0.11$

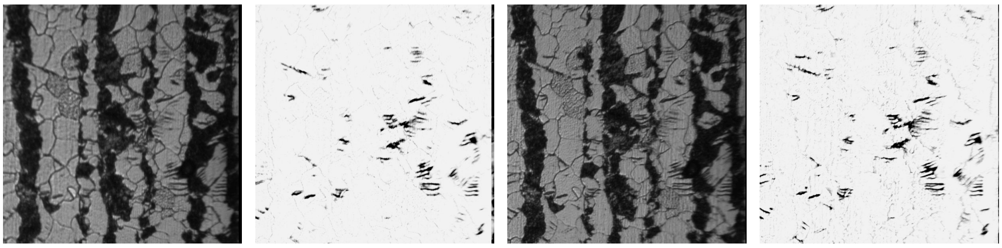

$N = 510000$; $N/N_f = 0.20$ $N = 750000$; $N/N_f = 0.30$

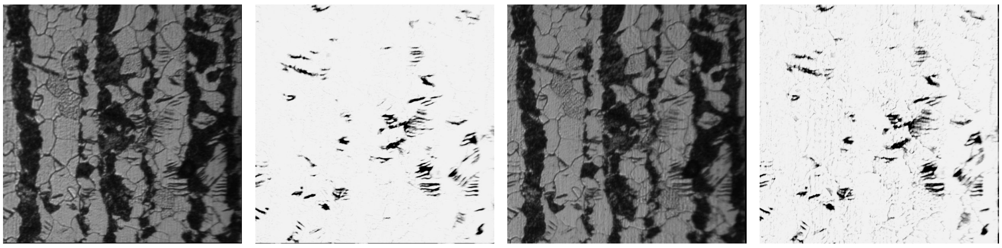

$N = 1080000$; $N/N_f = 0.43$ $N = 1230000$; $N/N_f = 0.49$

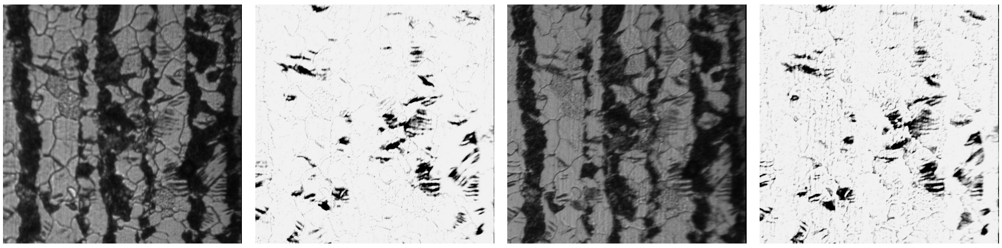

$N = 1860000$; $N/N_f = 0.74$ $N = 2370000$; $N/N_f = 0.95$

100 µm

Figure 87: Notched specimen RK0614; microscopic pictures within the notch

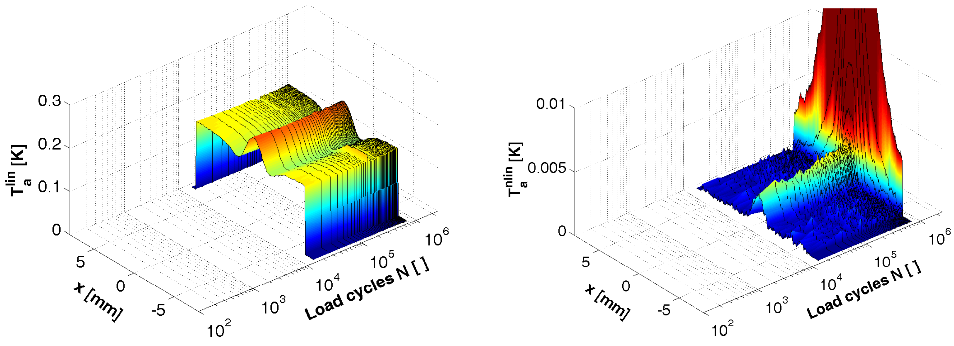

linear temperature amplitude non-linear temperature amplitude

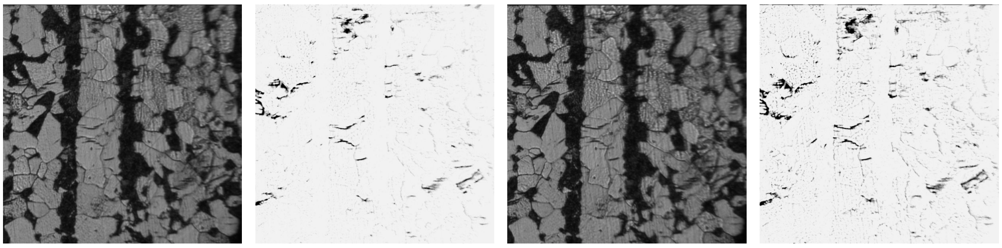

$N = 45000$; $N/N_f = 0.06$ $N = 75000$; $N/N_f = 0.10$

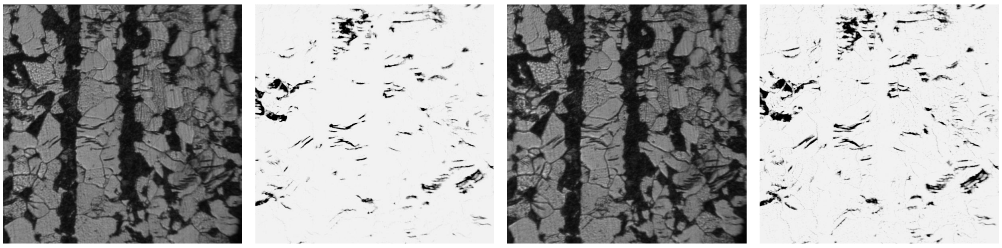

$N = 150000$; $N/N_f = 0.19$ $N = 240000$; $N/N_f = 0.31$

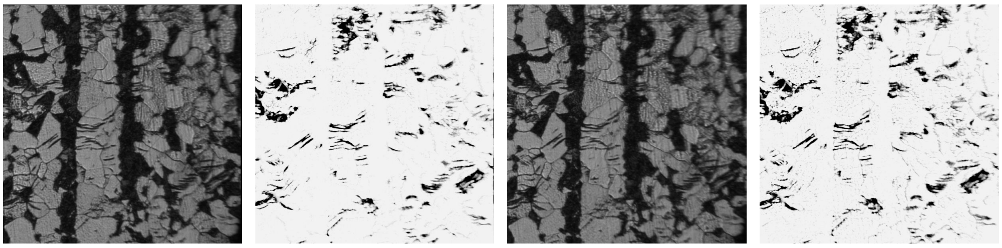

$N = 315000$; $N/N_f = 0.40$ $N = 390000$; $N/N_f = 0.50$

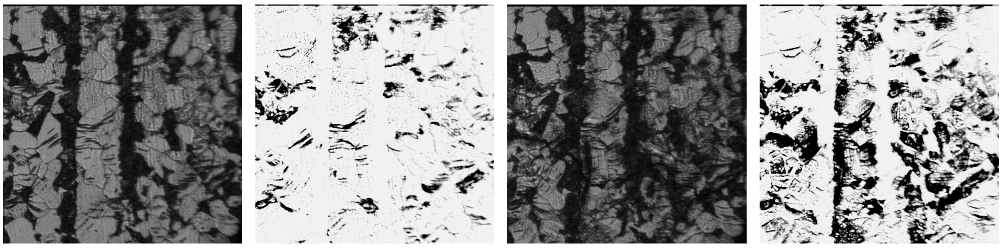

$N = 585000$; $N/N_f = 0.75$ $N = 750000$; $N/N_f = 0.96$

100 µm

Figure 88: Notched specimen RK0617; microscopic pictures within the notch

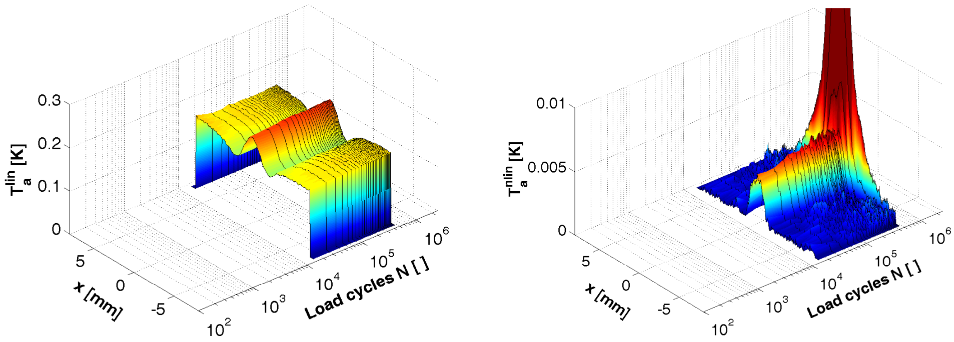

linear temperature amplitude non-linear temperature amplitude

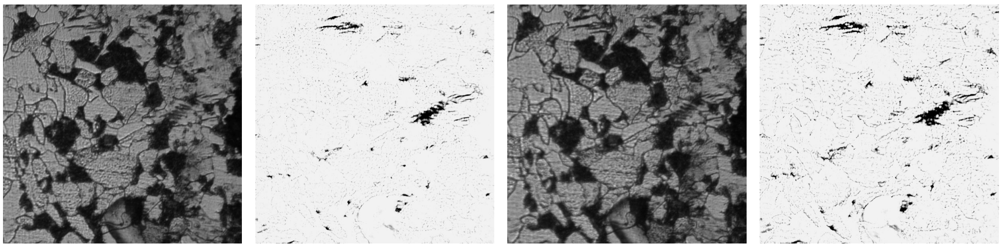

$N = 30000$; $N/N_f = 0.06$ $N = 45000$; $N/N_f = 0.09$

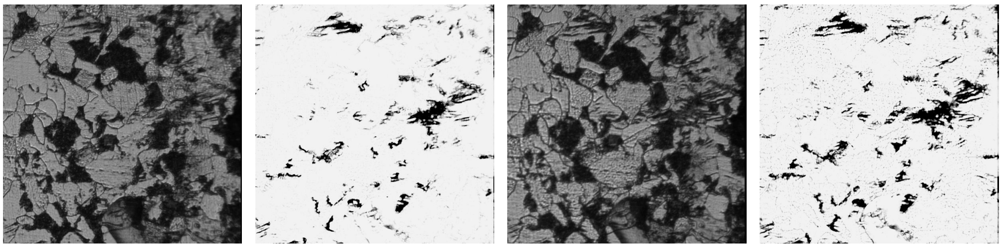

$N = 90000$; $N/N_f = 0.19$ $N = 150000$; $N/N_f = 0.31$

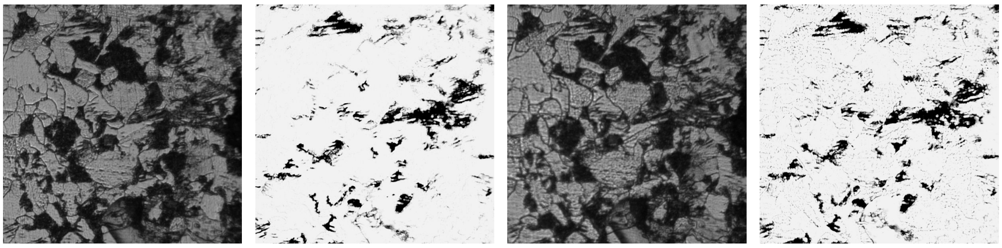

$N = 195000$; $N/N_f = 0.41$ $N = 240000$; $N/N_f = 0.50$

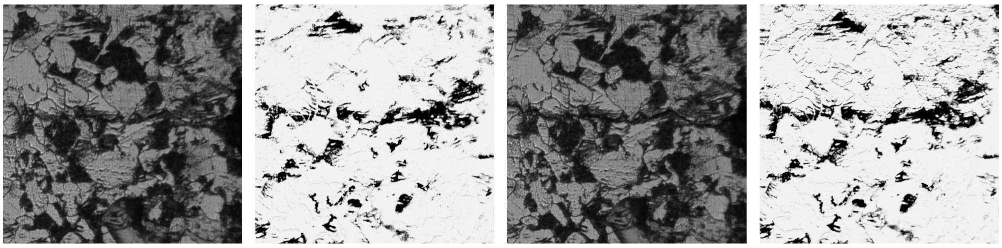

$N = 360000$; $N/N_f = 0.75$ $N = 450000$; $N/N_f = 0.94$

100 µm

Figure 89: Notched specimen RK0618; microscopic pictures within the notch

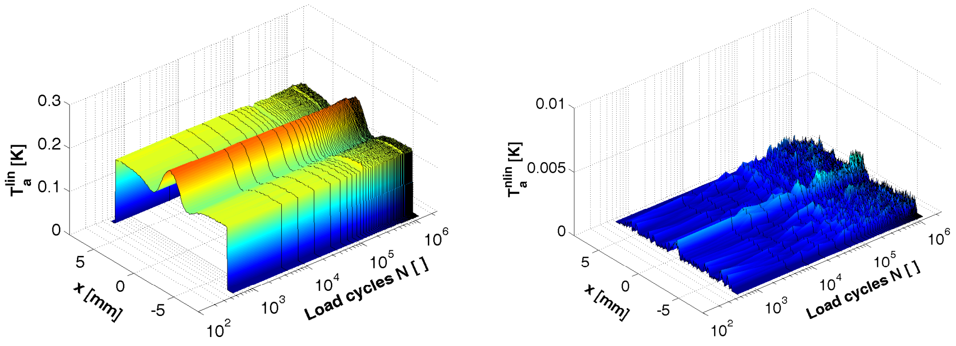

linear temperature amplitude non-linear temperature amplitude

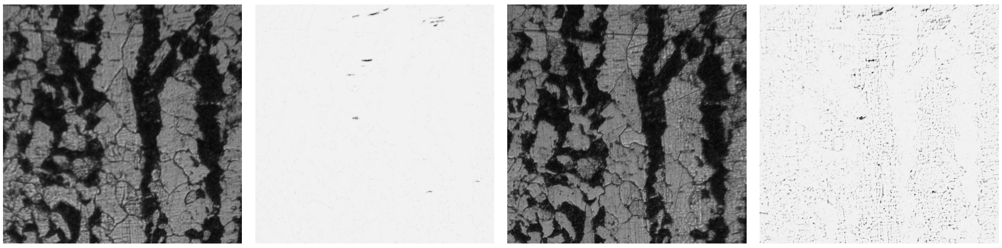

$N = 60000;\ N/N_f = 0.05$ $N = 140000;\ N/N_f = 0.11$

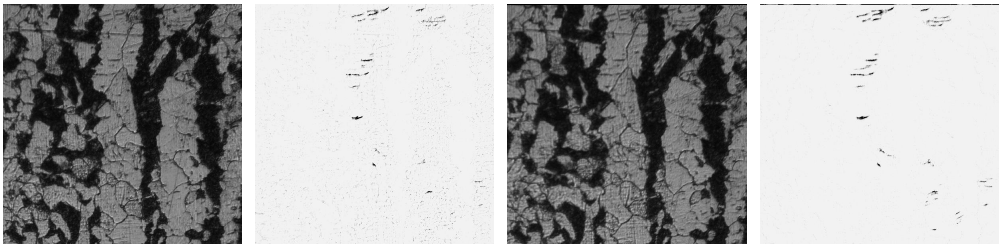

$N = 260000;\ N/N_f = 0.20$ $N = 400000;\ N/N_f = 0.31$

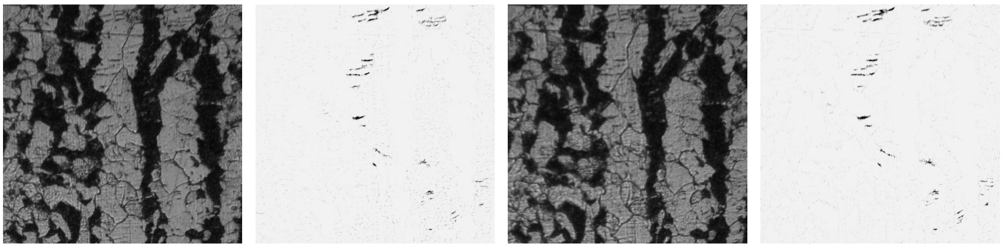

$N = 520000;\ N/N_f = 0.40$ $N = 660000;\ N/N_f = 0.51$

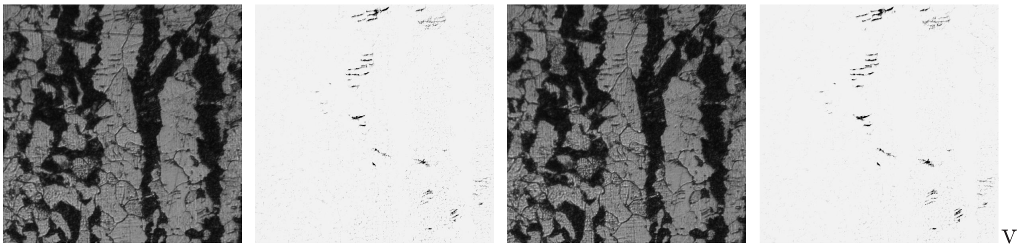

$N = 980000;\ N/N_f = 0.75$ $N = 1240000;\ N/N_f = 0.95$

Figure 90: Notched specimen RK0621; microscopic pictures within the notch

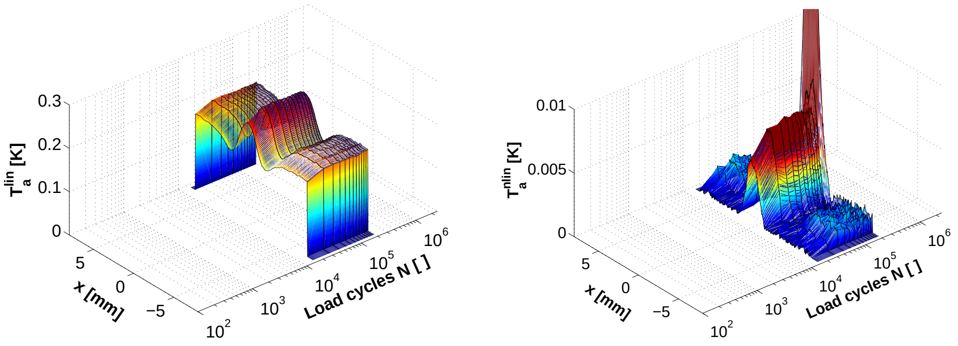

linear temperature amplitude non-linear temperature amplitude

$N = 15000;\ N/N_f = 0.07$ $N = 30000;\ N/N_f = 0.14$

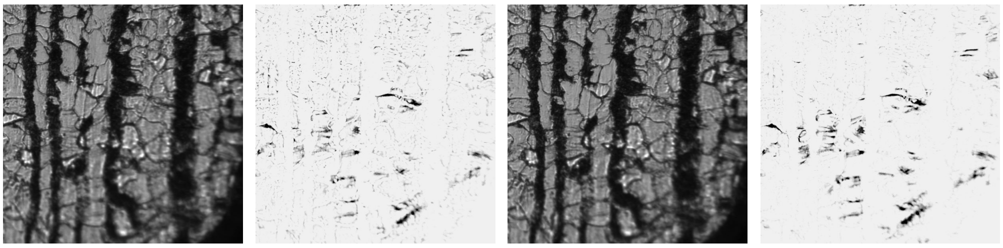

$N = 45000;\ N/N_f = 0.21$ $N = 60000;\ N/N_f = 0.28$

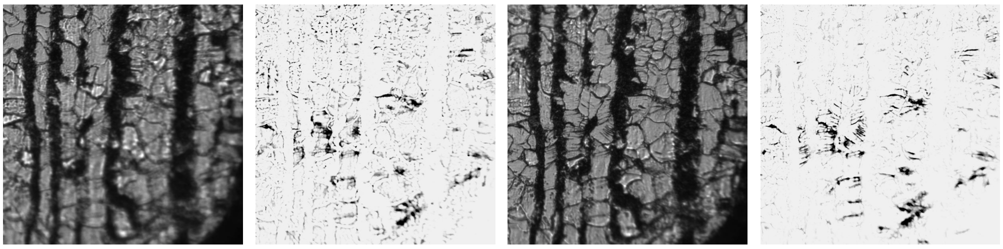

$N = 90000;\ N/N_f = 0.41$ $N = 105000;\ N/N_f = 0.48$

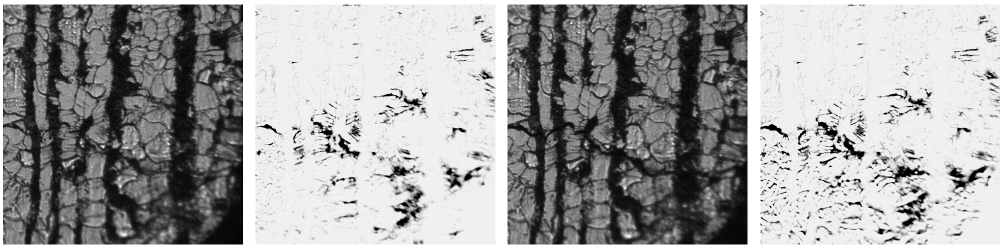

$N = 165000;\ N/N_f = 0.76$ $N = 210000;\ N/N_f = 0.96$

100 μm

Figure 91: Notched specimen RK0624; microscopic pictures within the notch

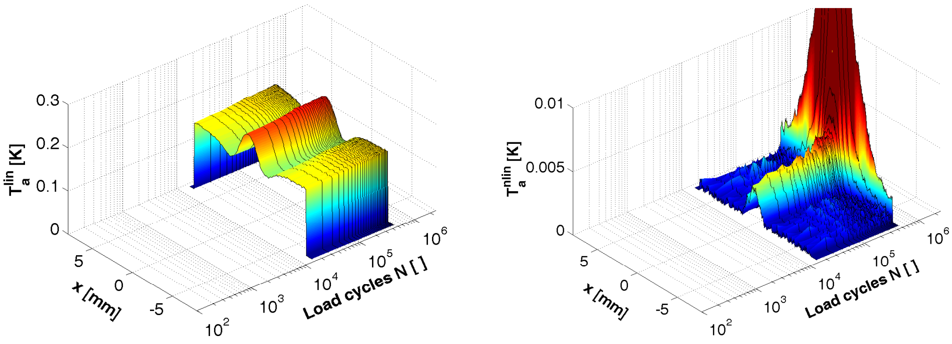

linear temperature amplitude non-linear temperature amplitude

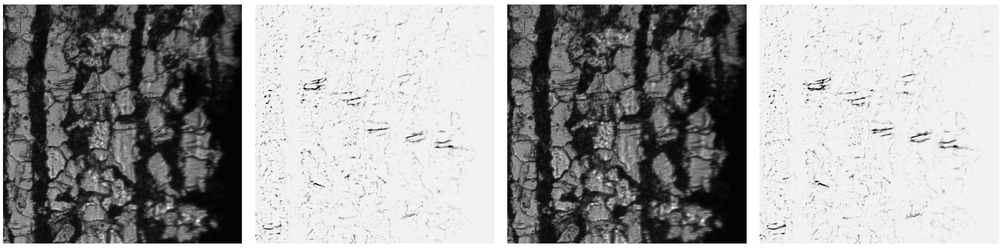

$N = 30000$; $N/N_f = 0.06$ $N = 45000$; $N/N_f = 0.09$

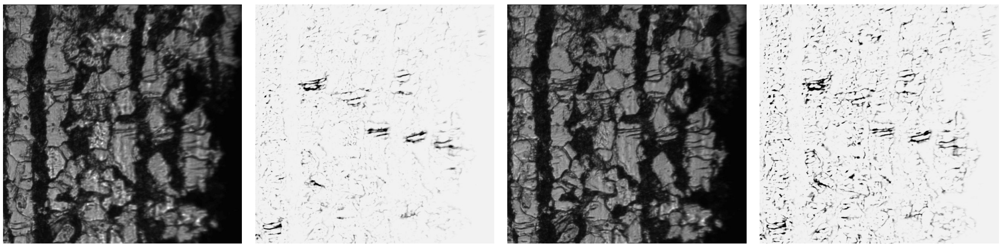

$N = 90000$; $N/N_f = 0.18$ $N = 150000$; $N/N_f = 0.31$

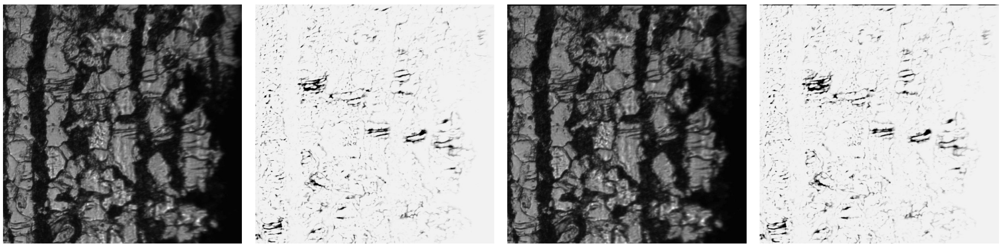

$N = 195000$; $N/N_f = 0.40$ $N = 240000$; $N/N_f = 0.49$

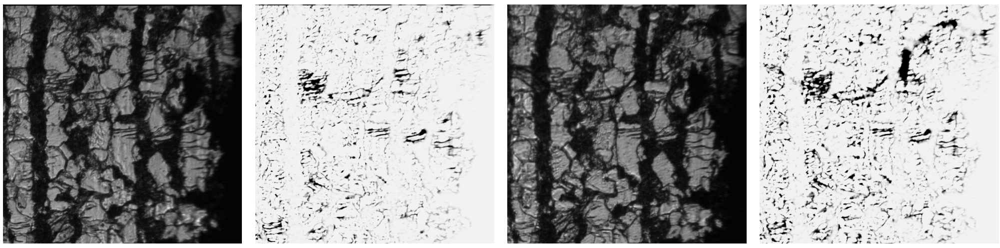

$N = 360000$; $N/N_f = 0.74$ $N = 465000$; $N/N_f = 0.95$

100 µm

Figure 92: Notched specimen RK0625; microscopic pictures within the notch

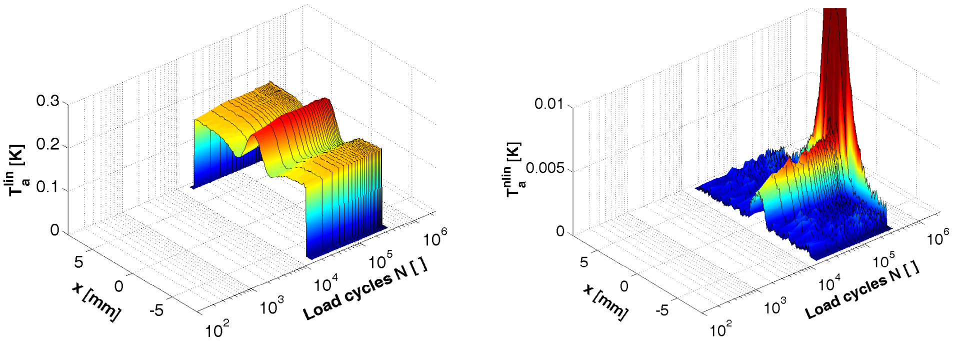

linear temperature amplitude non-linear temperature amplitude

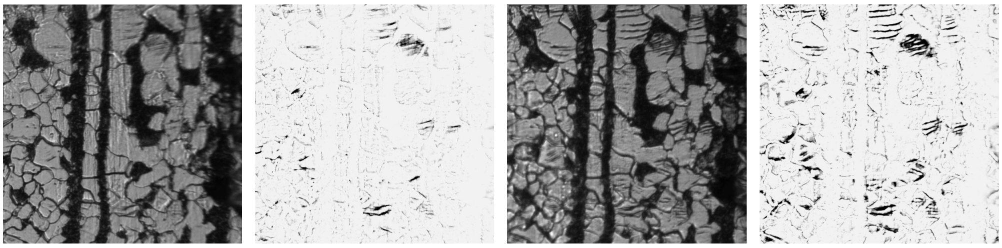

$N = 15000$; $N/N_f = 0.06$ $N = 45000$; $N/N_f = 0.12$

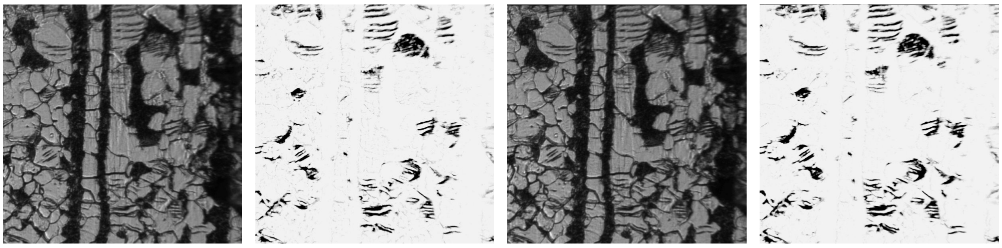

$N = 75000$; $N/N_f = 0.19$ $N = 120000$; $N/N_f = 0.31$

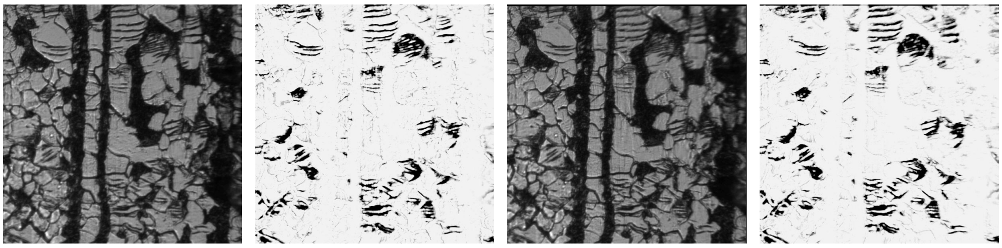

$N = 150000$; $N/N_f = 0.39$ $N = 195000$; $N/N_f = 0.50$

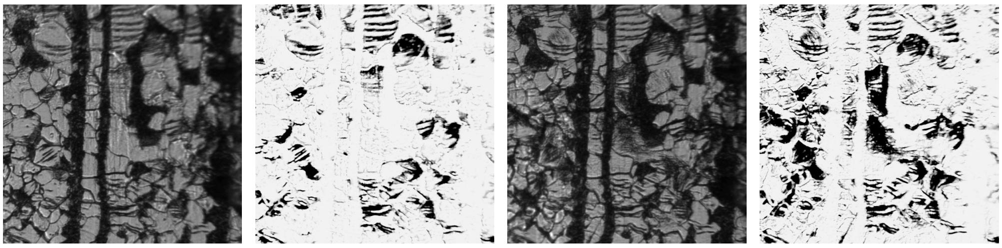

$N = 285000$; $N/N_f = 0.73$ $N = 375000$; $N/N_f = 0.96$

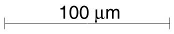

Figure 93: Notched specimen RK0626; microscopic pictures within the notch

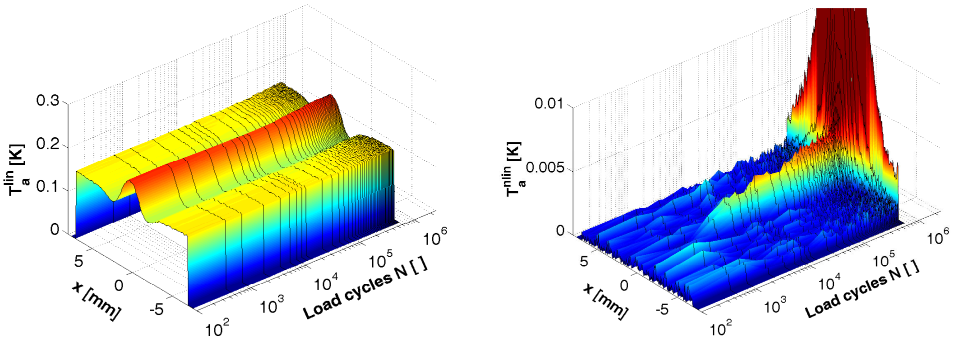

linear temperature amplitude non-linear temperature amplitude

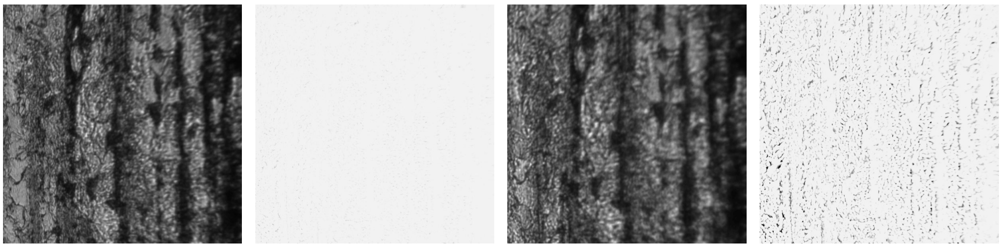

$N = 30000$; $N/N_f = 0.05$ $N = 60000$; $N/N_f = 0.10$

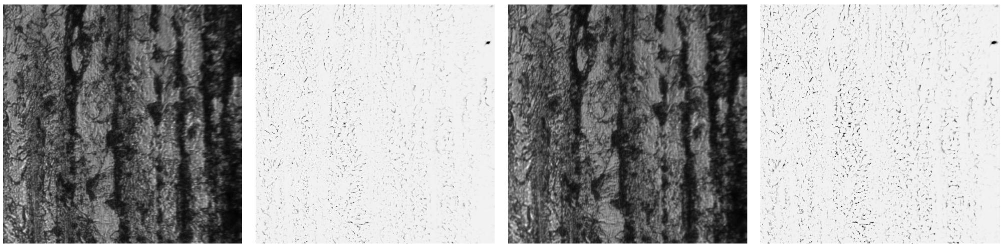

$N = 120000$; $N/N_f = 0.19$ $N = 180000$; $N/N_f = 0.29$

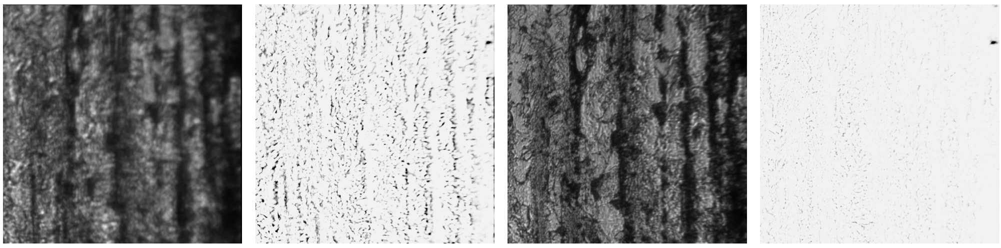

$N = 240000$; $N/N_f = 0.39$ $N = 315000$; $N/N_f = 0.51$

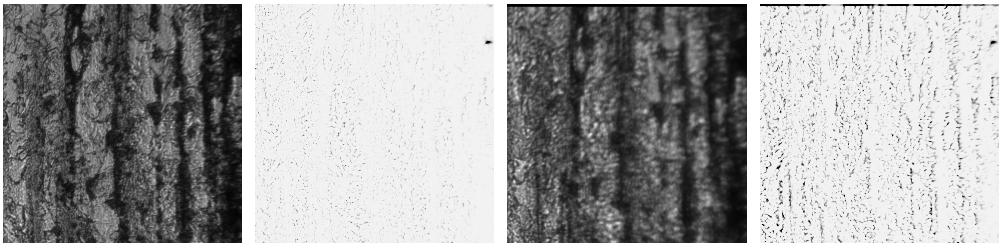

$N = 465000$; $N/N_f = 0.75$ $N = 585000$; $N/N_f = 0.94$

100 µm

Figure 94: Notched specimen RK0627; microscopic pictures in nominal cross-section

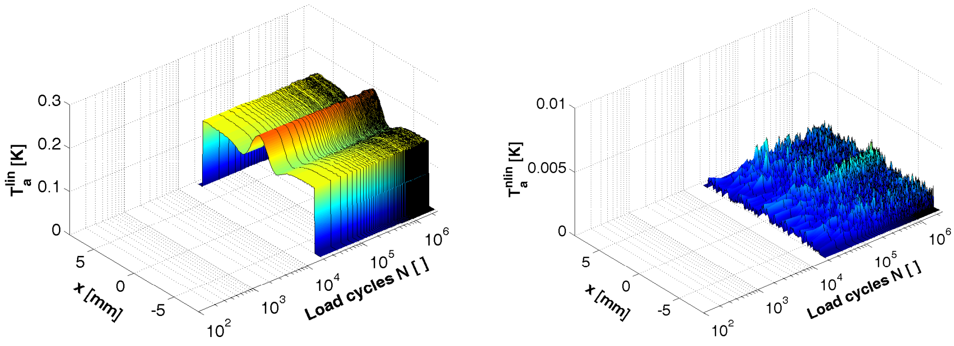

linear temperature amplitude non-linear temperature amplitude

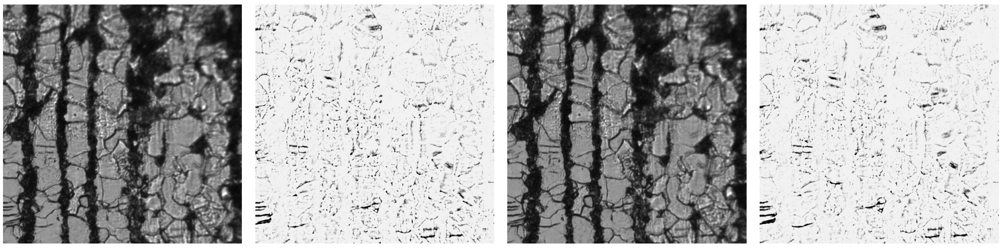

$N = 140000$; $N/N_f = 0.06$ $N = 260000$; $N/N_f = 0.10$

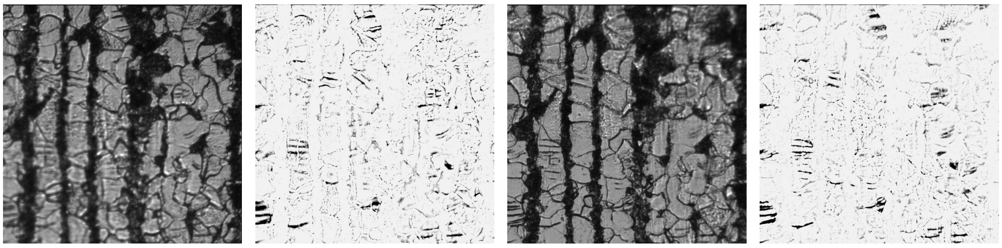

$N = 500000$; $N/N_f = 0.20$ $N = 760000$; $N/N_f = 0.30$

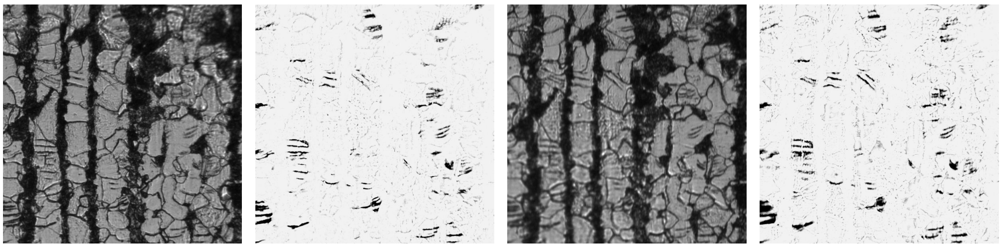

$N = 1000000$; $N/N_f = 0.40$ $N = 1260000$; $N/N_f = 0.50$

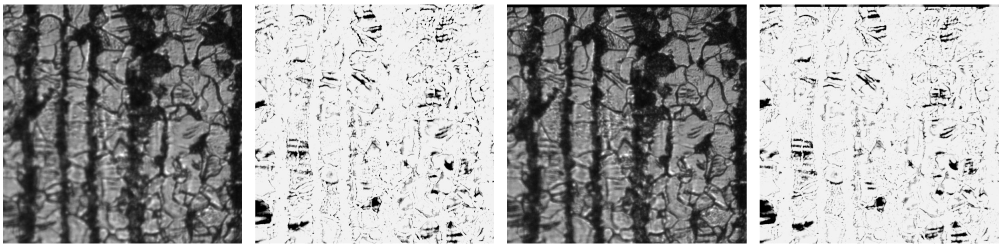

$N = 1880000$; $N/N_f = 0.75$ $N = 2380000$; $N/N_f = 0.95$

Figure 95: Notched specimen RK0628; microscopic pictures within the notch

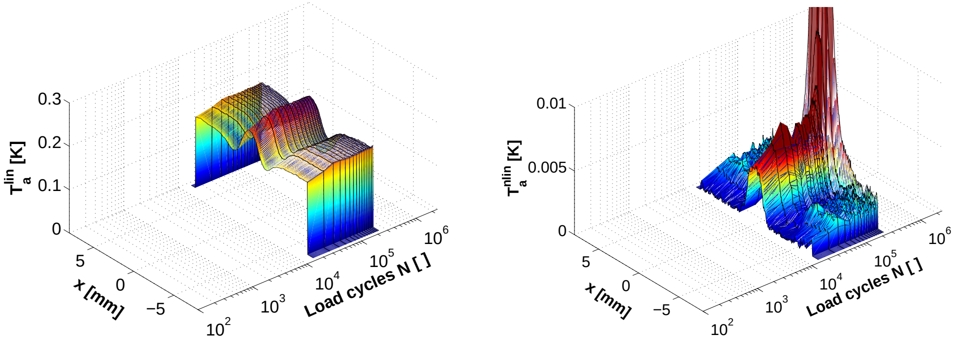

linear temperature amplitude non-linear temperature amplitude

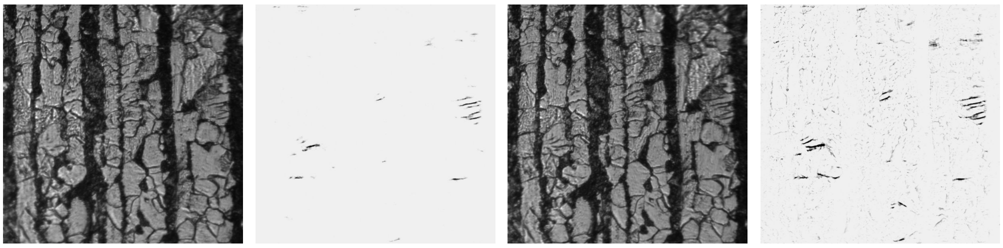

$N = 15000;\ N/N_f = 0.06$ $N = 30000;\ N/N_f = 0.12$

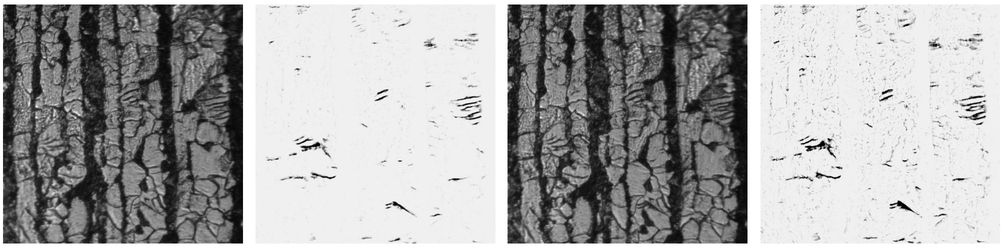

$N = 45000;\ N/N_f = 0.18$ $N = 75000;\ N/N_f = 0.29$

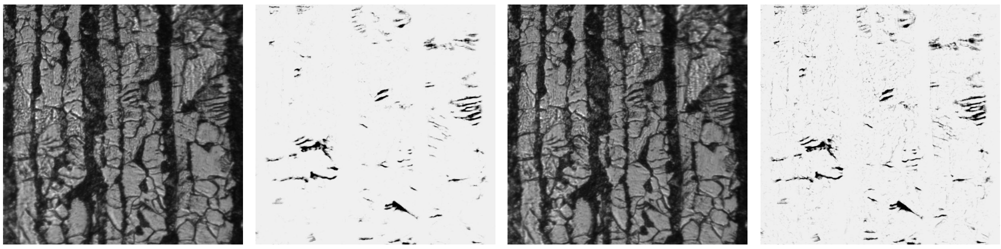

$N = 105000;\ N/N_f = 0.41$ $N = 135000;\ N/N_f = 0.53$

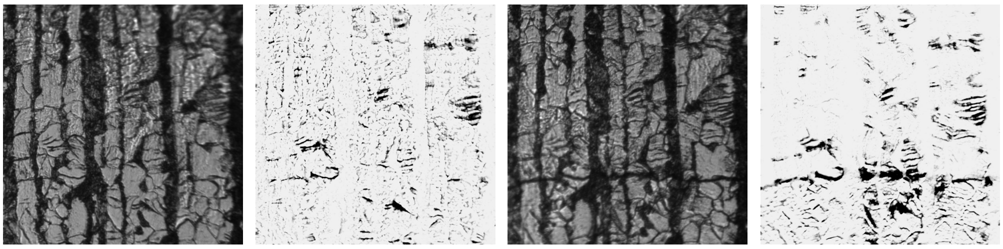

$N = 195000;\ N/N_f = 0.76$ $N = 240000;\ N/N_f = 0.94$

Figure 96: Notched specimen RK0631; microscopic pictures within the notch

2) Damage evolution of welded specimens

The following images show the damage evolution on the welded specimen type III. For each specimen the spatial distribution of the linear and nonlinear temperature amplitudes at different relative lifetimes N/N_f are given. All results are discussed in chapter 6. The following drawing clarifies the location of measurement.

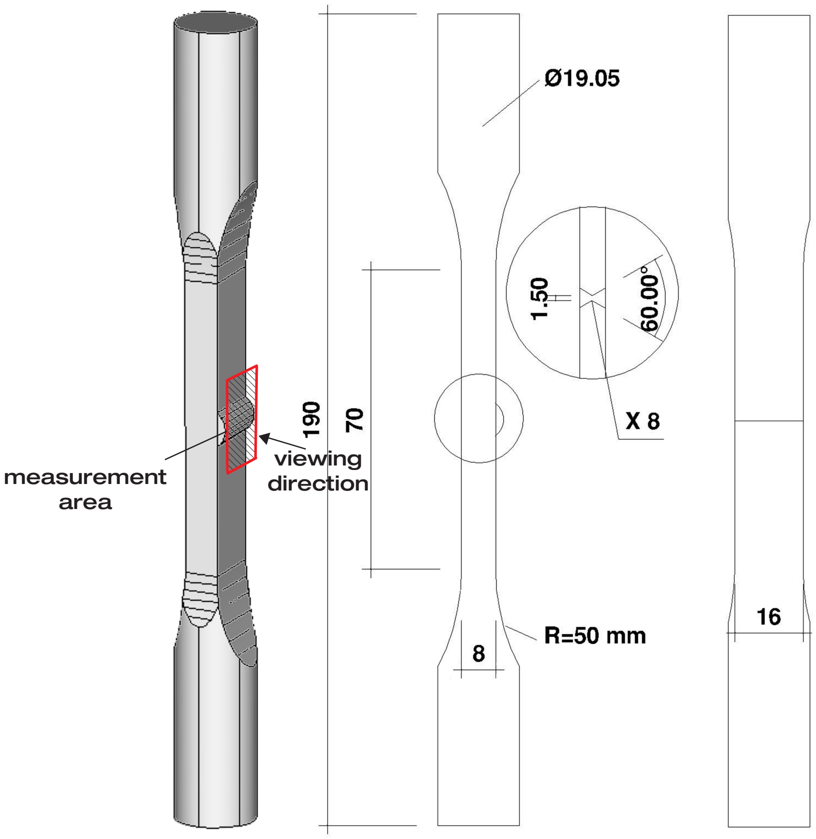

Figure 97: Definition of the measurement area; specimen type III

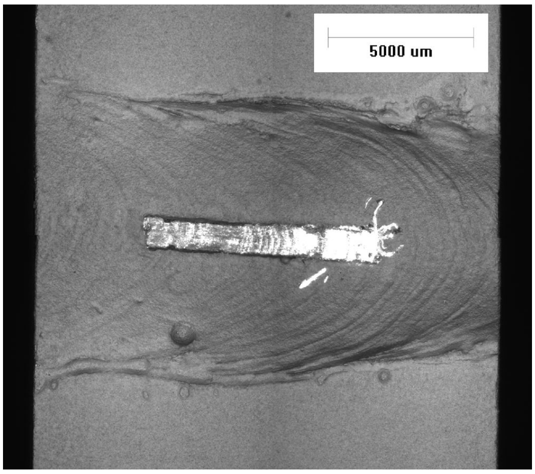

surface detail

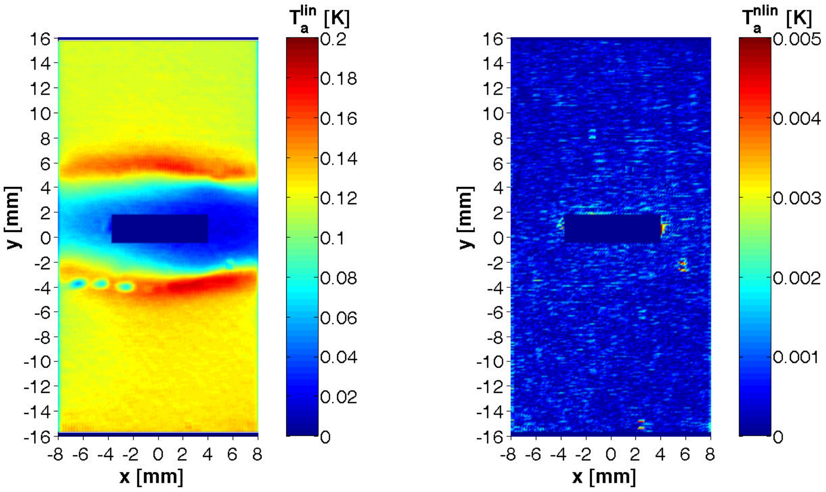

$N = 15000;\ N/N_f = 0.02$

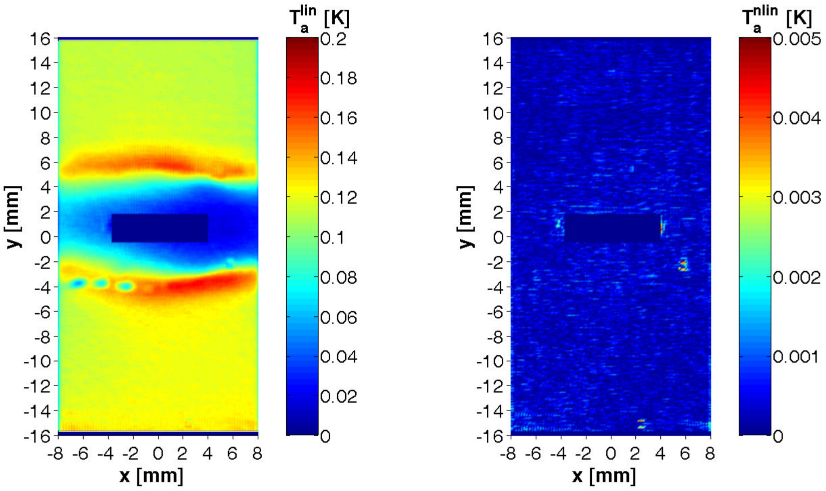

$N = 45000;\ N/N_f = 0.05$

Figure 98-1: Welded specimen SK0601; linear and nonlinear temperature amplitudes

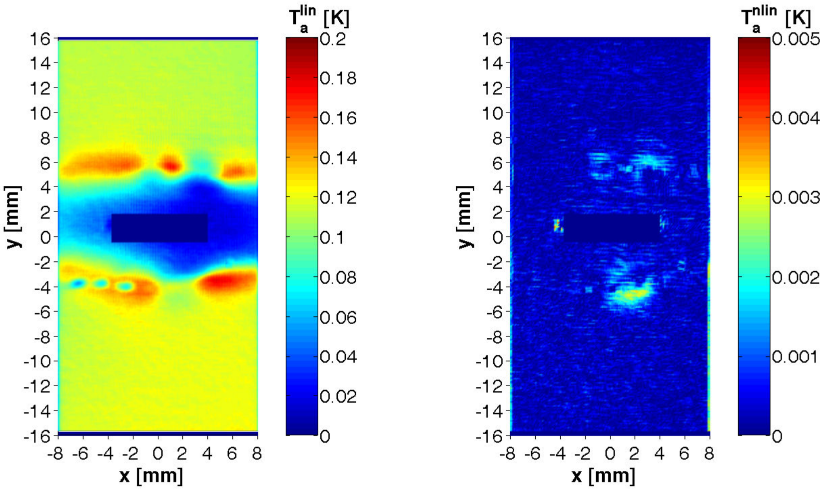

$N = 180000$; $N/N_f = 0.20$

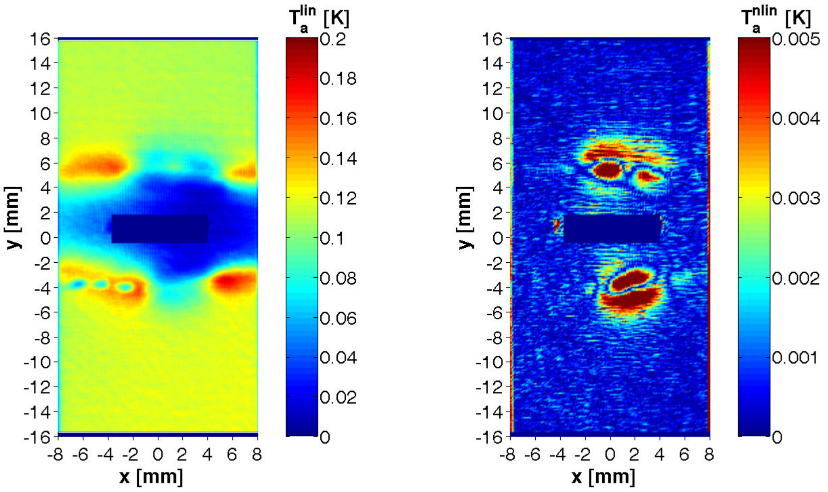

$N = 270000$; $N/N_f = 0.30$

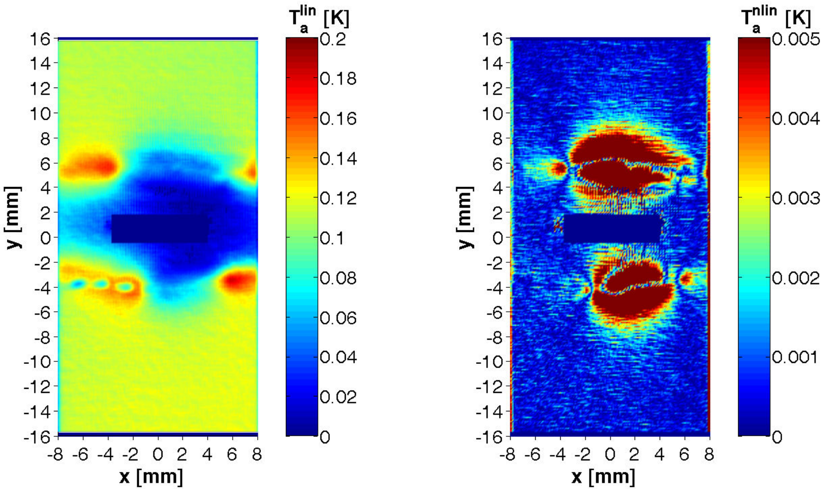

$N = 360000$; $N/N_f = 0.41$

Figure 98-2: Welded specimen SK0601; linear and nonlinear temperature amplitudes

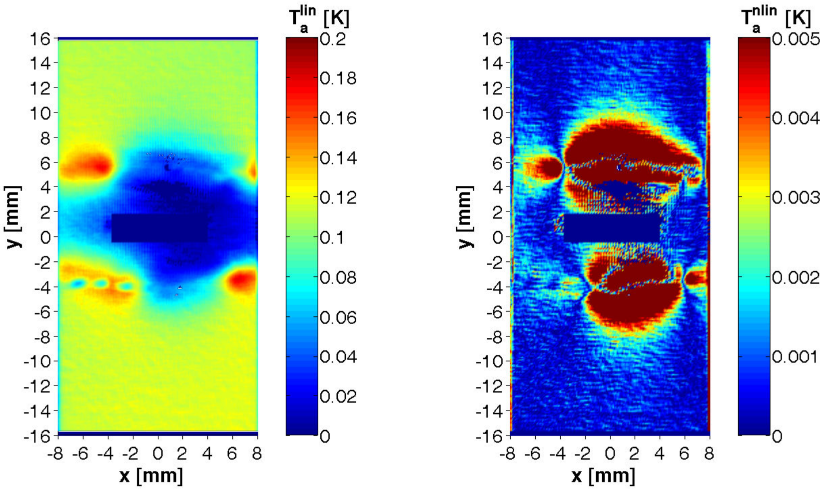

$N = 450000$; $N/N_f = 0.51$

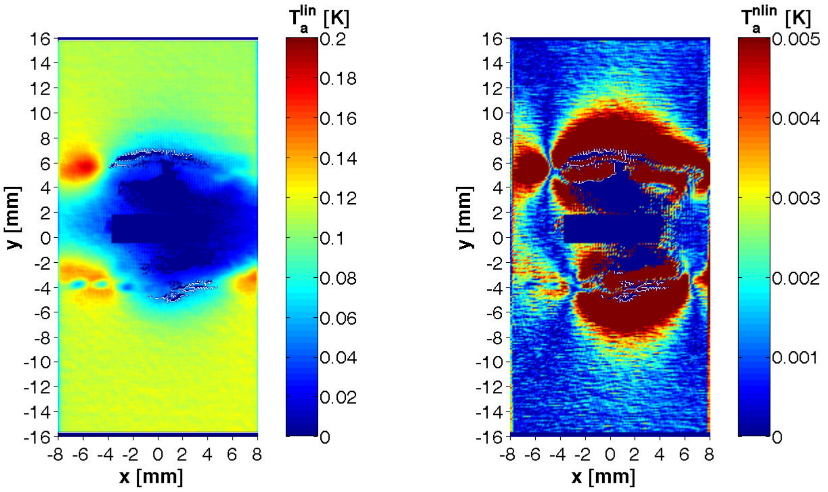

$N = 615000$; $N/N_f = 0.69$

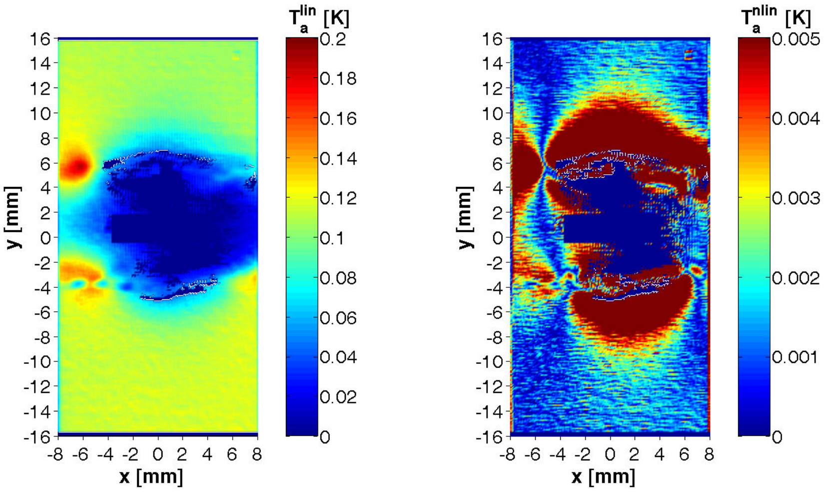

$N = 705000$; $N/N_f = 0.80$

Figure 98-3: Welded specimen SK0601; linear and nonlinear temperature amplitudes

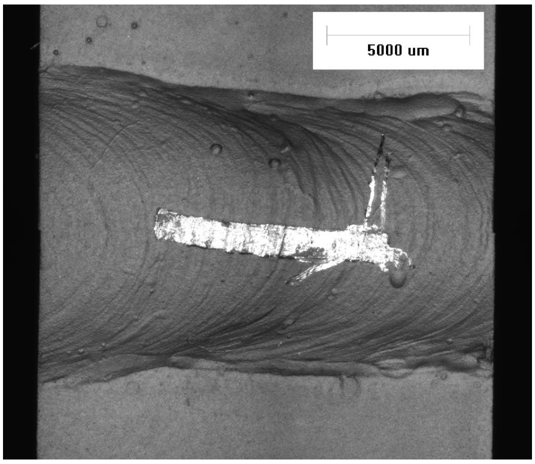

surface detail

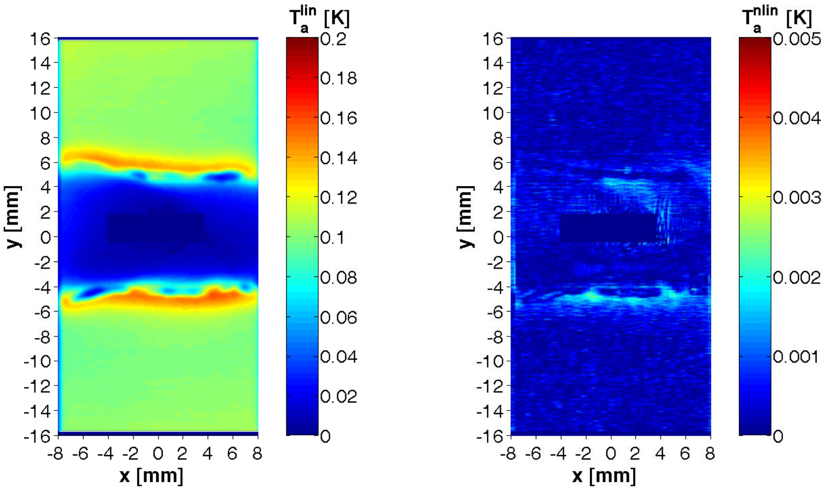

$N = 15000$; $N/N_f = 0.10$

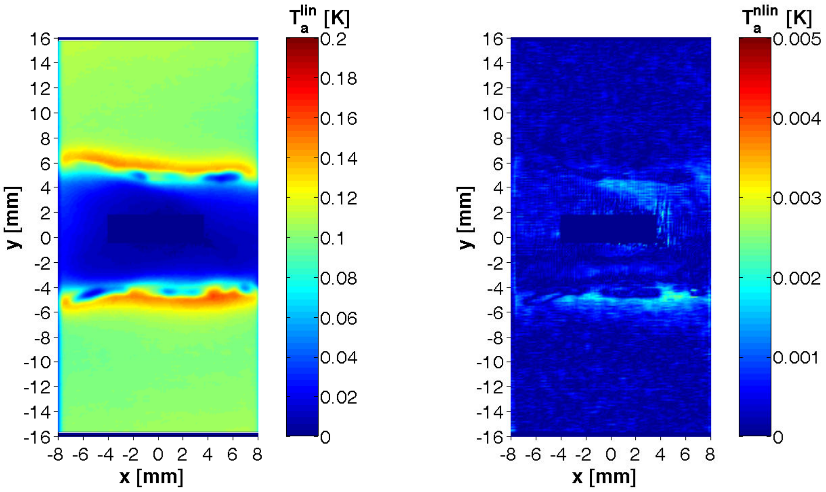

$N = 30000$; $N/N_f = 0.20$

Figure 99-1: Welded specimen SK0602; linear and nonlinear temperature amplitudes

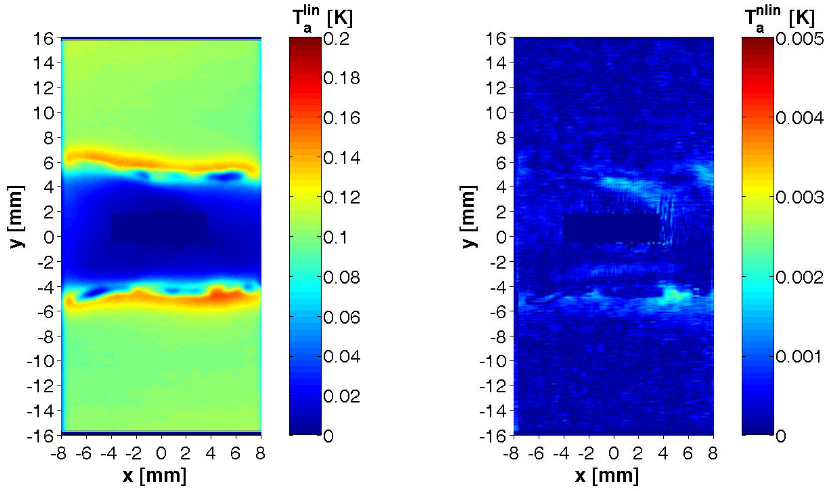

$N = 45000;\ N/N_f = 0.30$

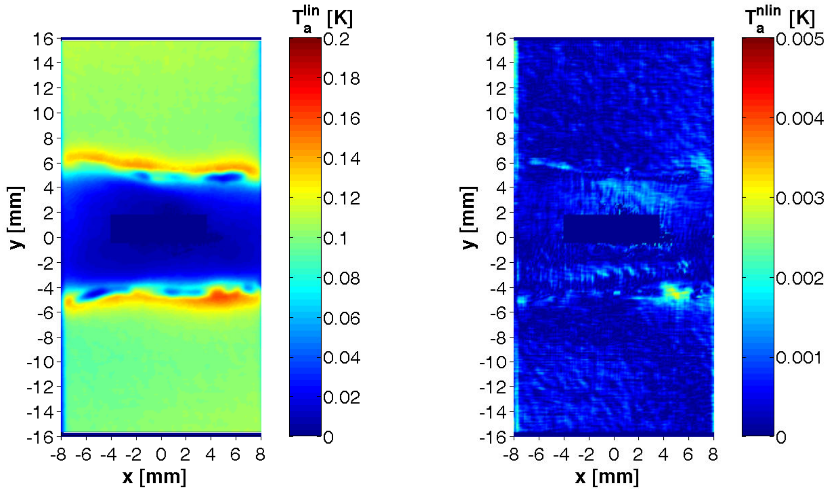

$N = 60000;\ N/N_f = 0.40$

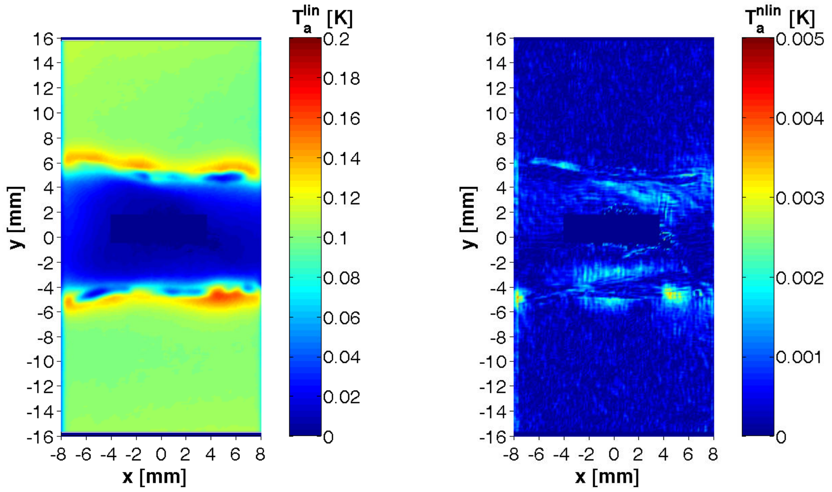

$N = 75000;\ N/N_f = 0.49$

Figure 99-2: Welded specimen SK0602; linear and nonlinear temperature amplitudes

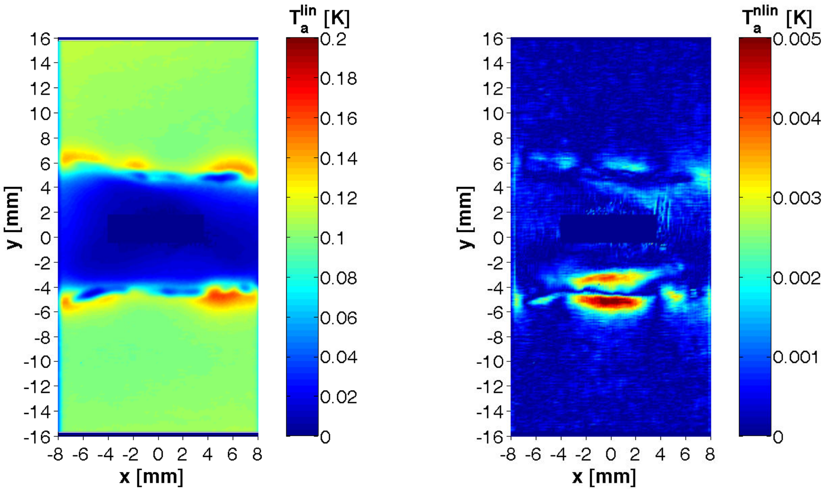

$N = 105000$; $N/N_f = 0.69$

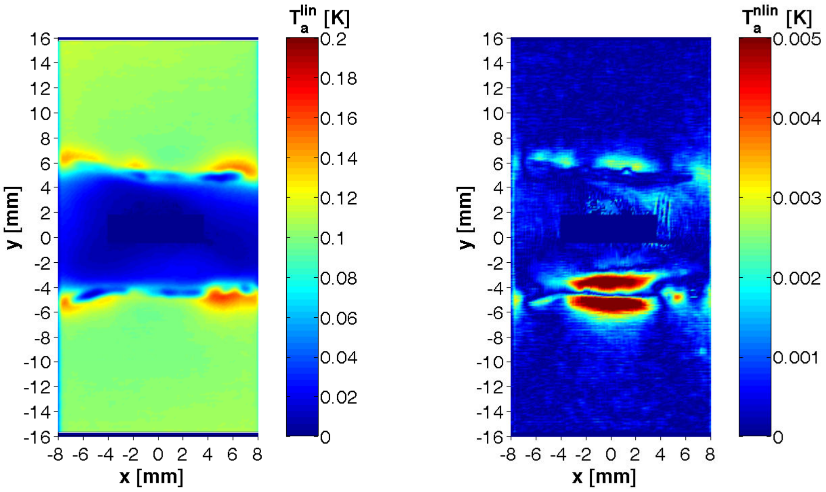

$N = 120000$; $N/N_f = 0.79$

Figure 99-3: Welded specimen SK0602; linear and nonlinear temperature amplitudes

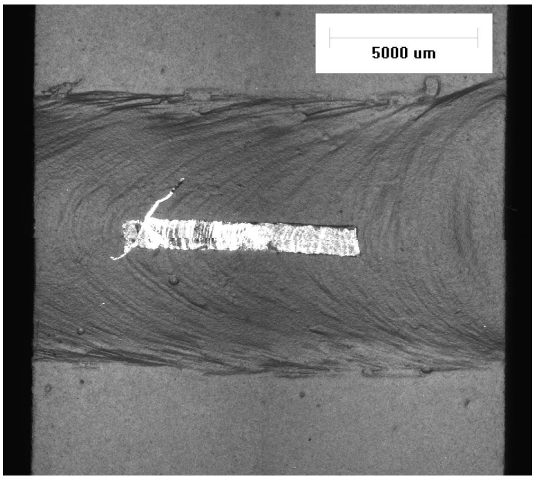

surface detail

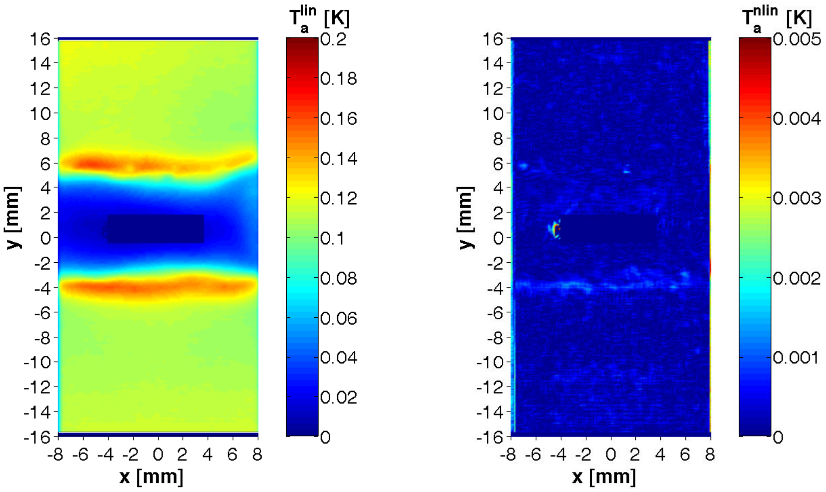

$N = 15000;\ N/N_f = 0.02$

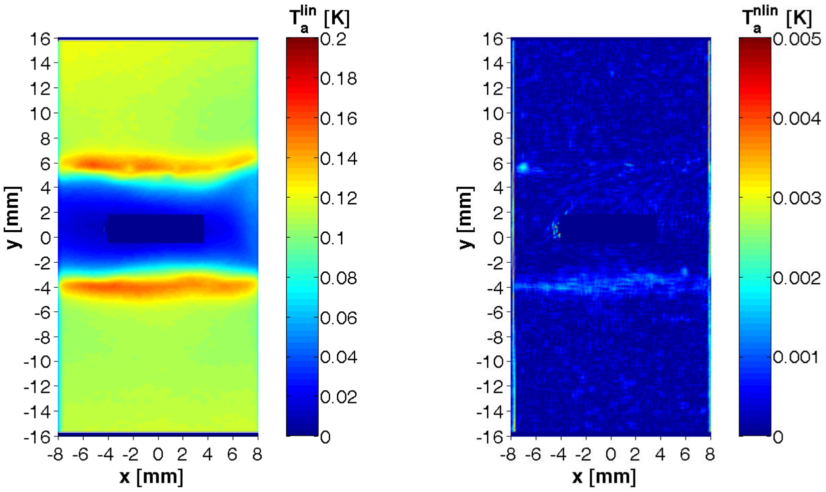

$N = 75000;\ N/N_f = 0.09$

Figure 100-1: Welded specimen SK0603; linear and nonlinear temperature amplitudes

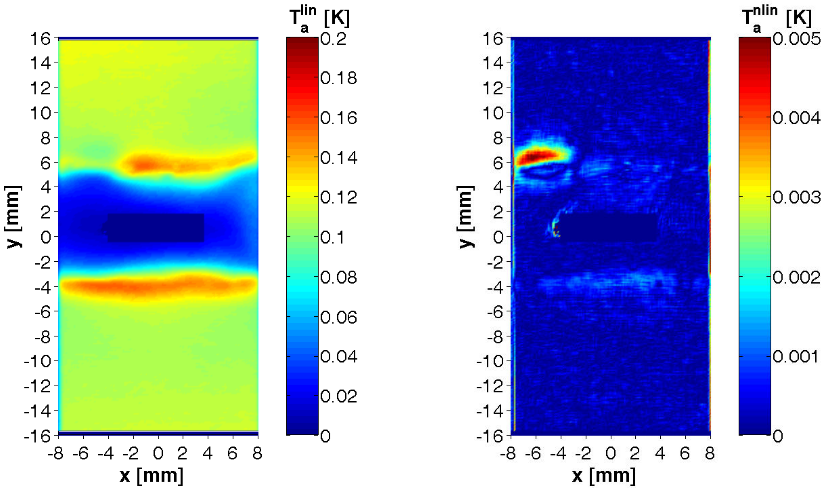

$N = 165000;\ N/N_f = 0.21$

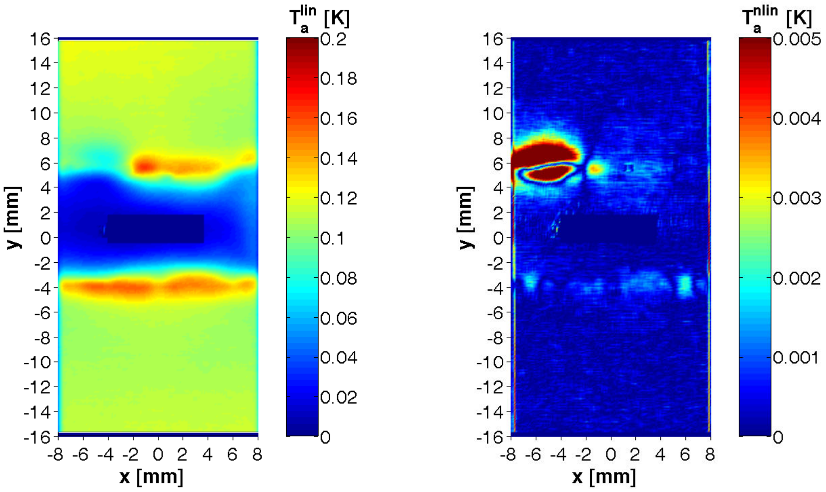

$N = 240000;\ N/N_f = 0.30$

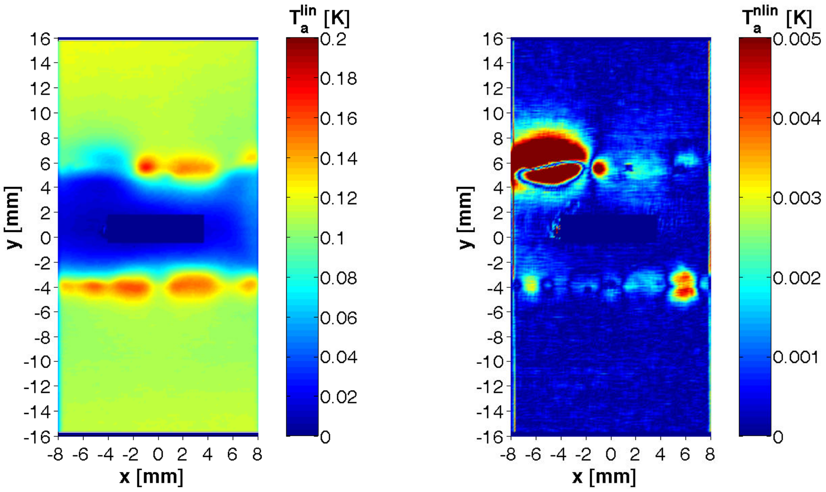

$N = 315000;\ N/N_f = 0.40$

Figure 100-2: Welded specimen SK0603; linear and nonlinear temperature amplitudes

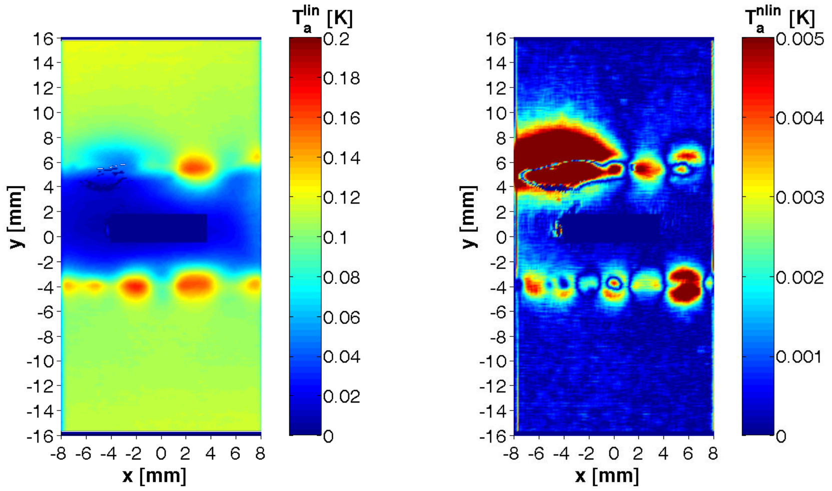

$N = 405000;\ N/N_f = 0.51$

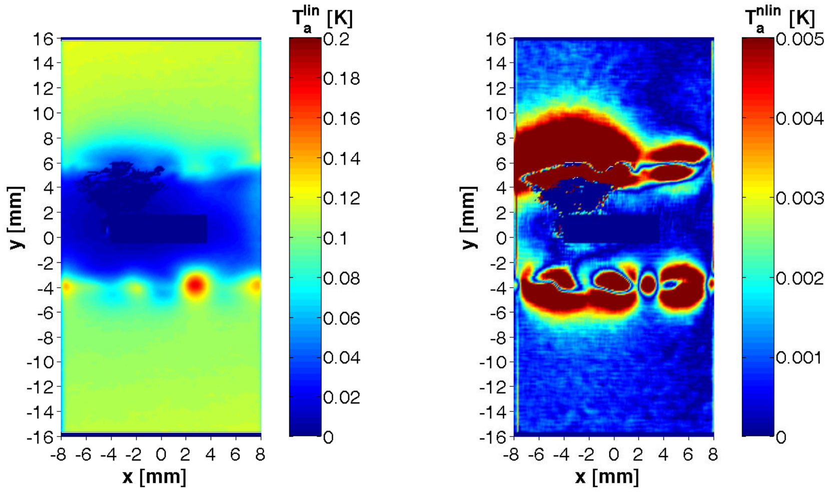

$N = 555000;\ N/N_f = 0.70$

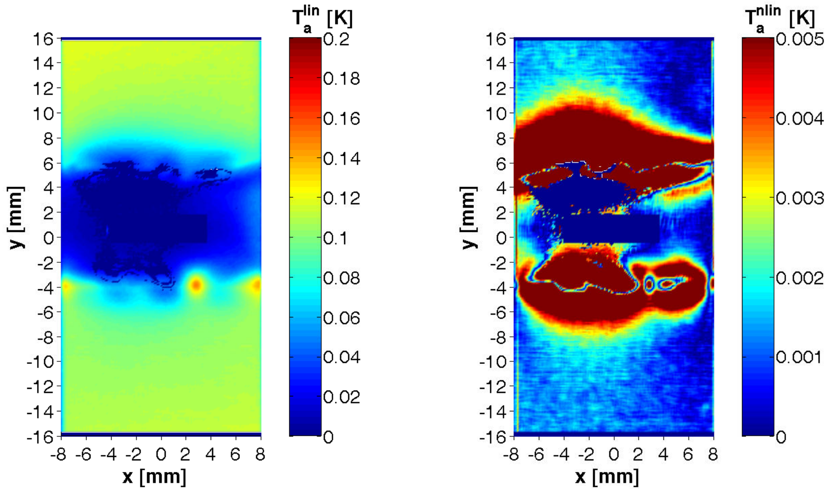

$N = 645000;\ N/N_f = 0.81$

Figure 100-3: Welded specimen SK0603; linear and nonlinear temperature amplitudes

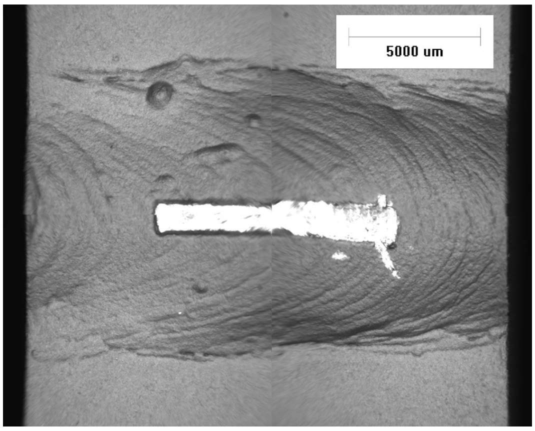

surface detail

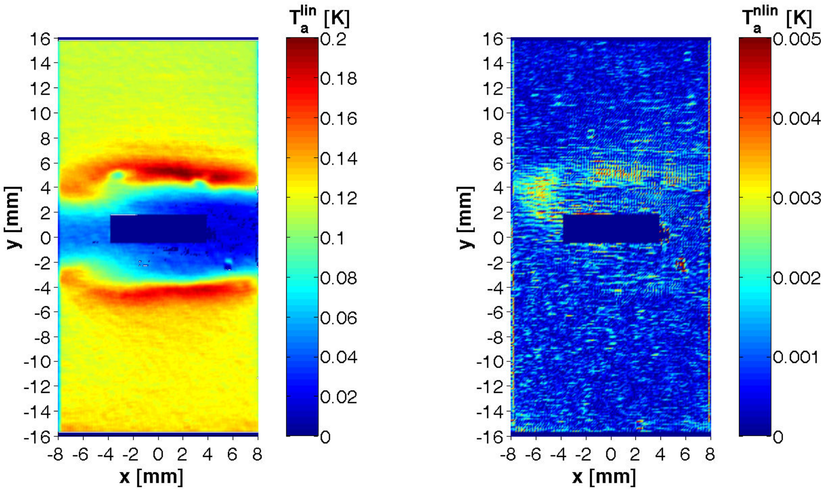

$N = 15000$; $N/N_f = 0.04$

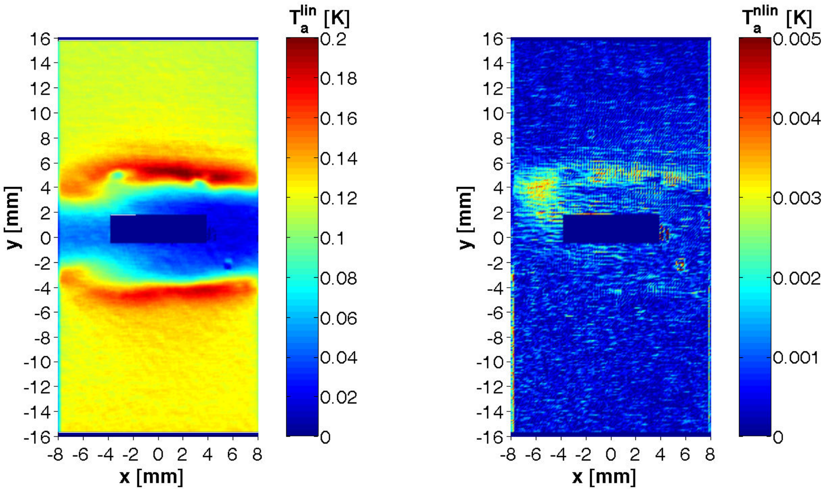

$N = 30000$; $N/N_f = 0.09$

Figure 101-1: Welded specimen SK0604; linear and nonlinear temperature amplitudes

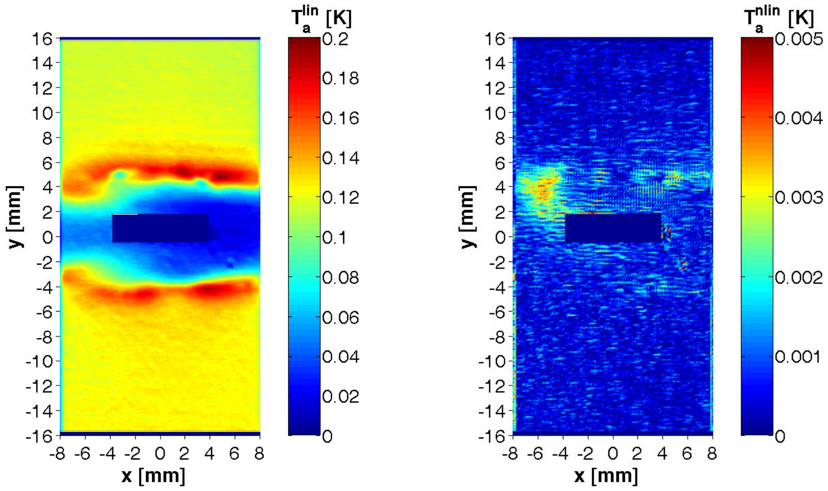

$N = 75000$; $N/N_f = 0.22$

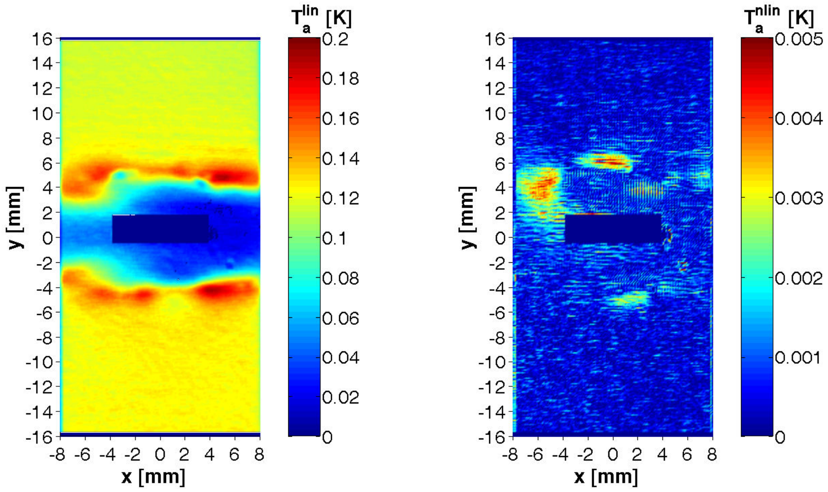

$N = 105000$; $N/N_f = 0.31$

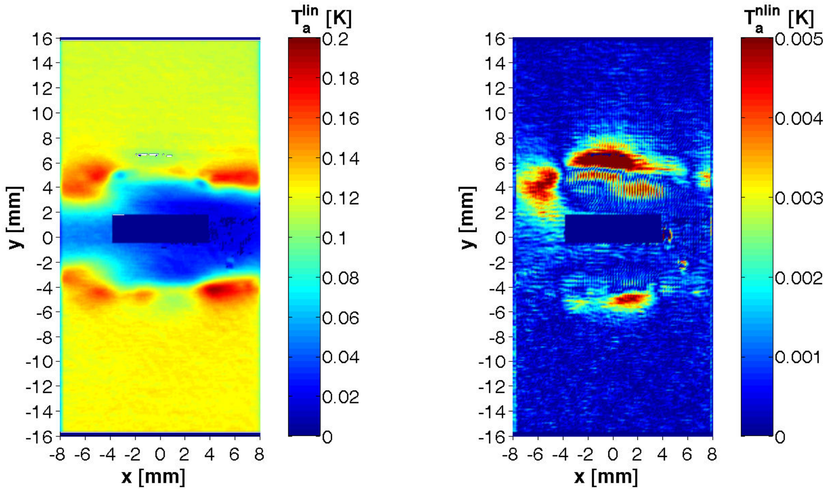

$N = 135000$; $N/N_f = 0.40$

Figure 101-2: Welded specimen SK0604; linear and nonlinear temperature amplitudes

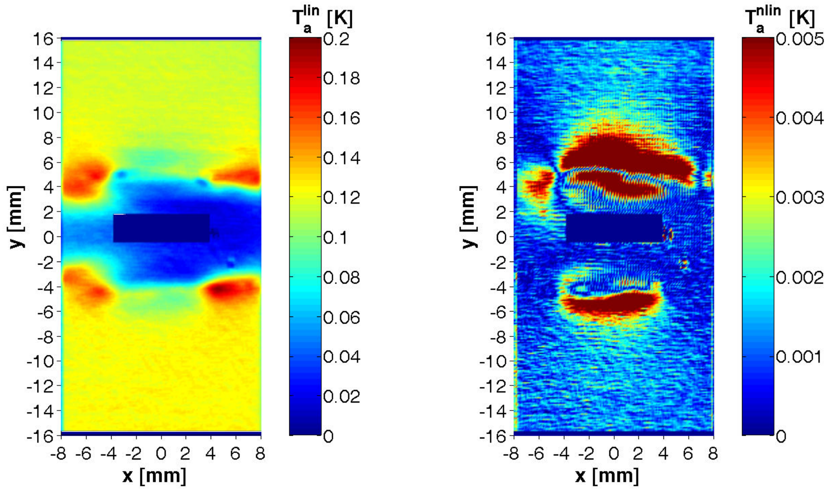

$N = 165000;\ N/N_f = 0.48$

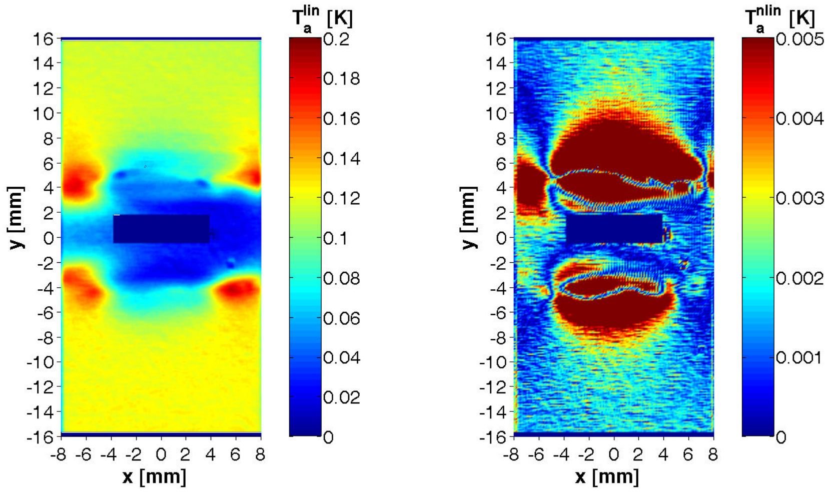

$N = 240000;\ N/N_f = 0.70$

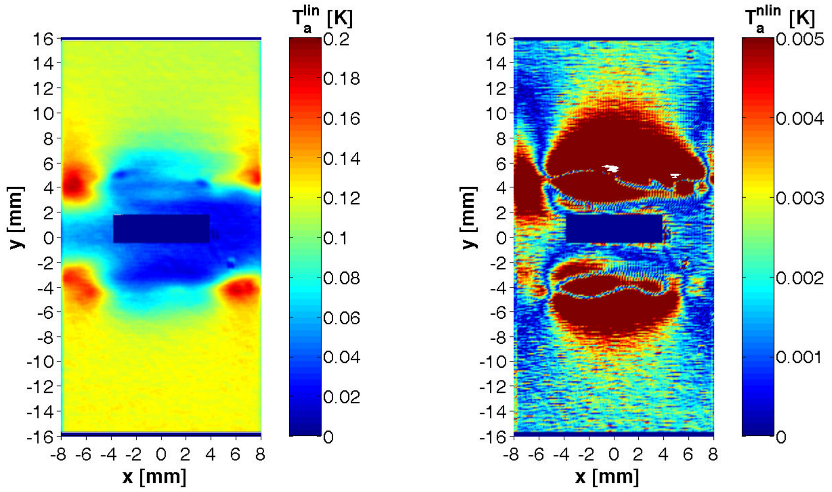

$N = 270000;\ N/N_f = 0.79$

Figure 101-3: Welded specimen SK0604; linear and nonlinear temperature amplitudes

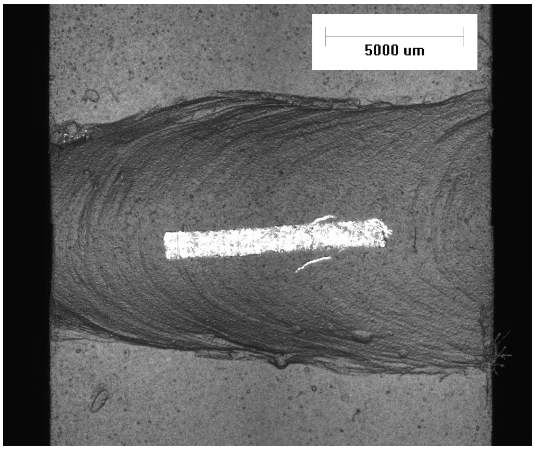

surface detail

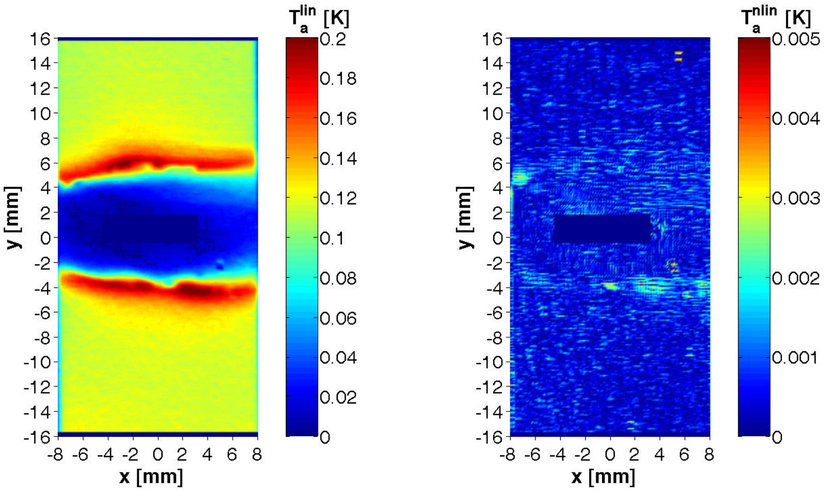

$N = 15000;\ N/N_f = 0.02$

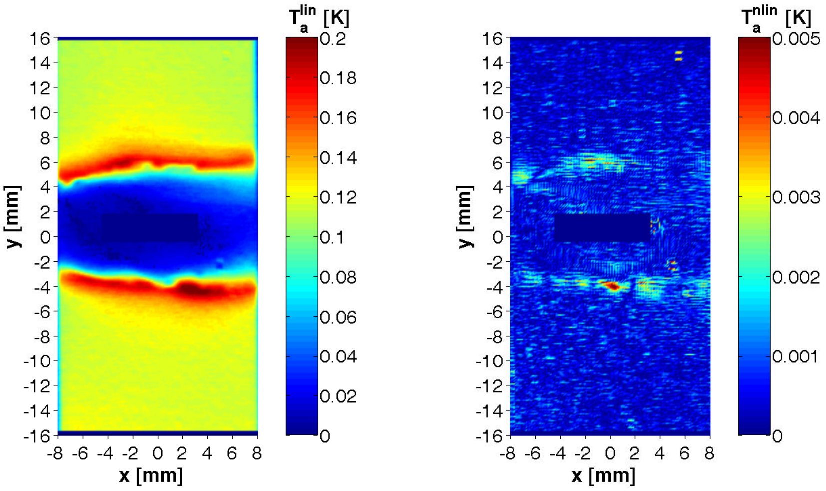

$N = 60000;\ N/N_f = 0.09$

Figure 102-1: Welded specimen SK0607; linear and nonlinear temperature amplitudes

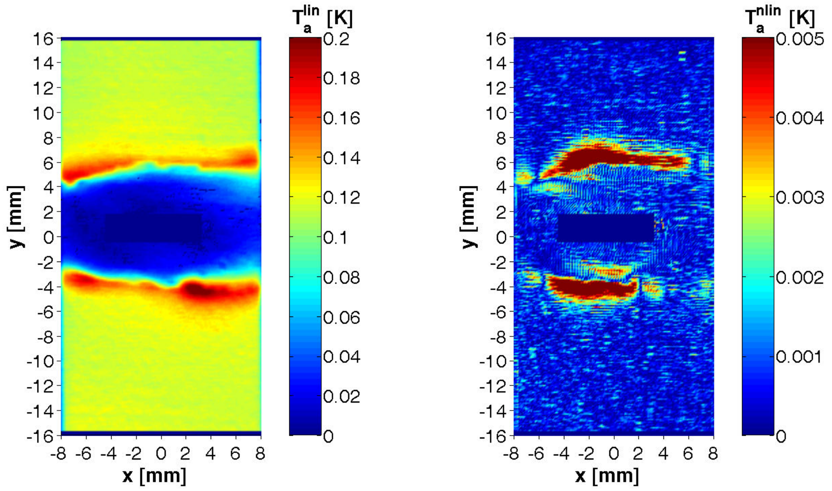

$N = 135000$; $N/N_f = 0.20$

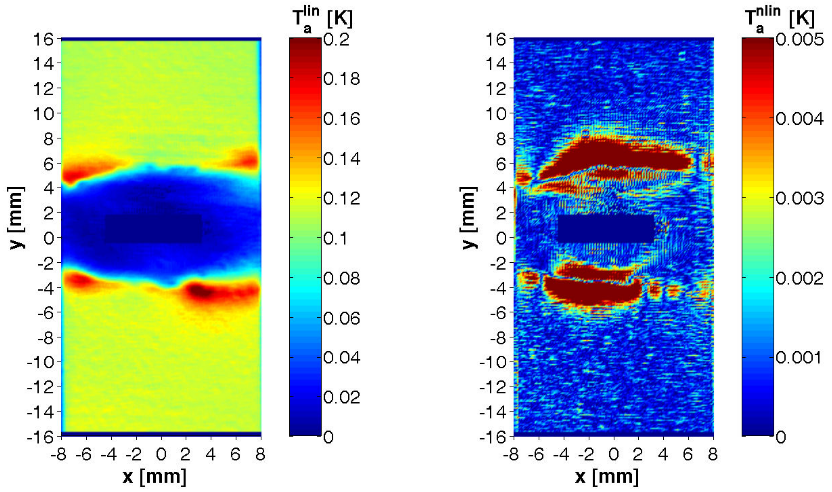

$N = 210000$; $N/N_f = 0.31$

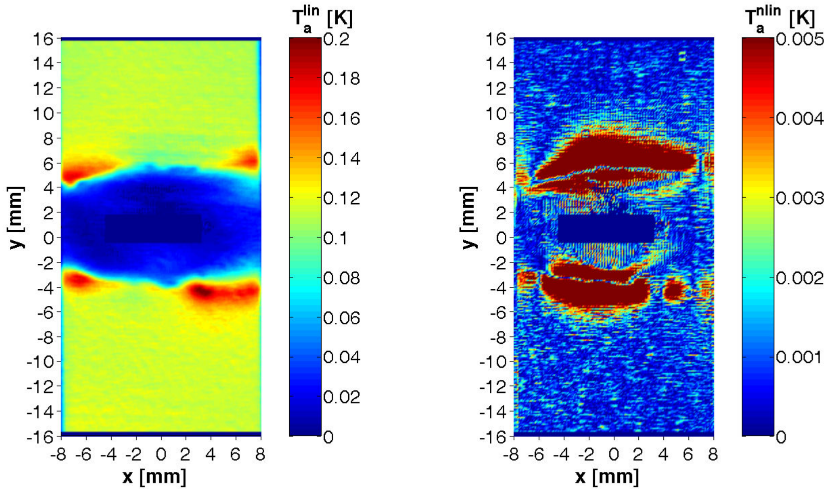

$N = 270000$; $N/N_f = 0.40$

Figure 102-2: Welded specimen SK0607; linear and nonlinear temperature amplitudes

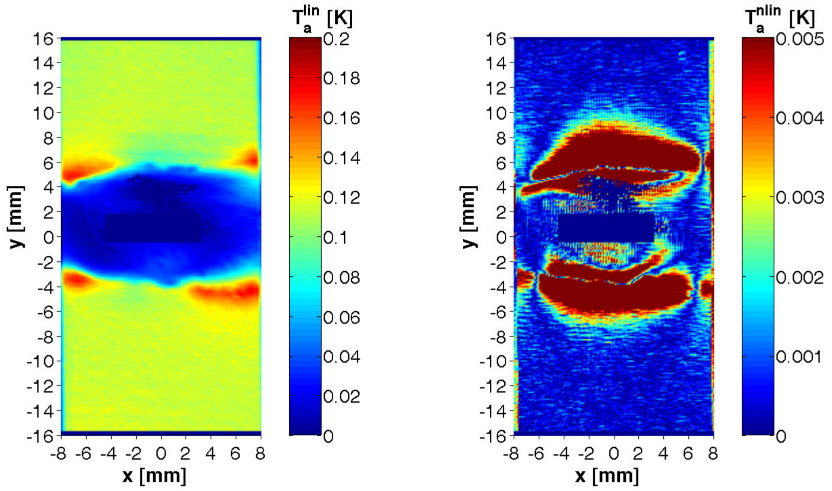

$N = 345000$; $N/N_f = 0.51$

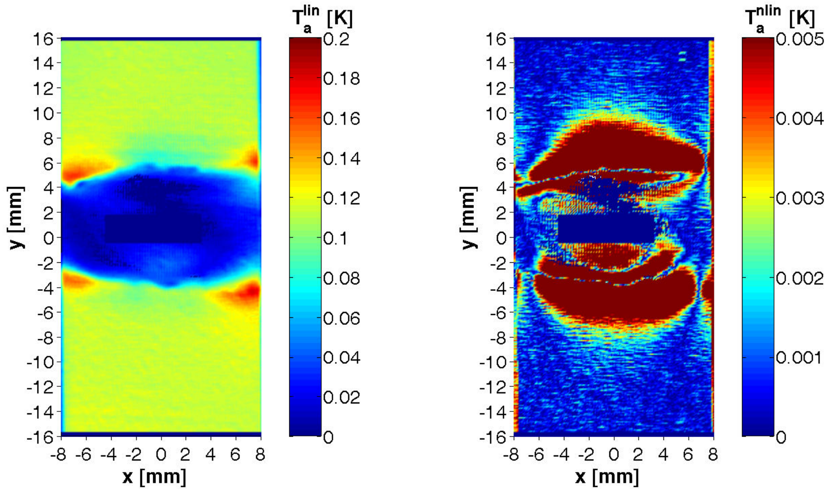

$N = 465000$; $N/N_f = 0.69$

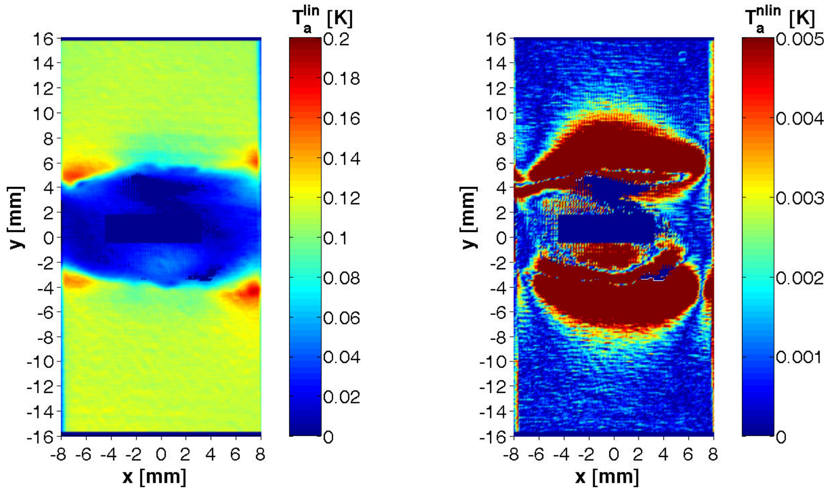

$N = 540000$; $N/N_f = 0.80$

Figure 102-3: Welded specimen SK0607; linear and nonlinear temperature amplitudes

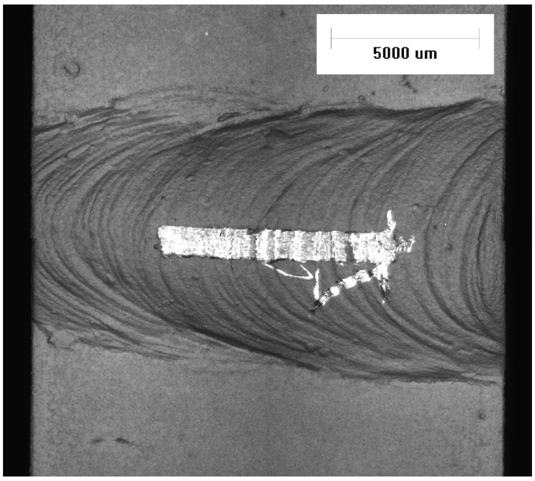

surface detail

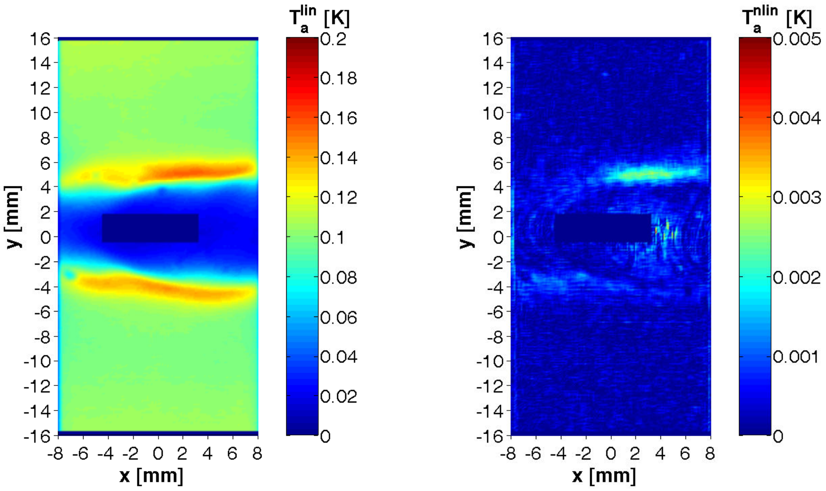

$N = 15000$; $N/N_f = 0.02$

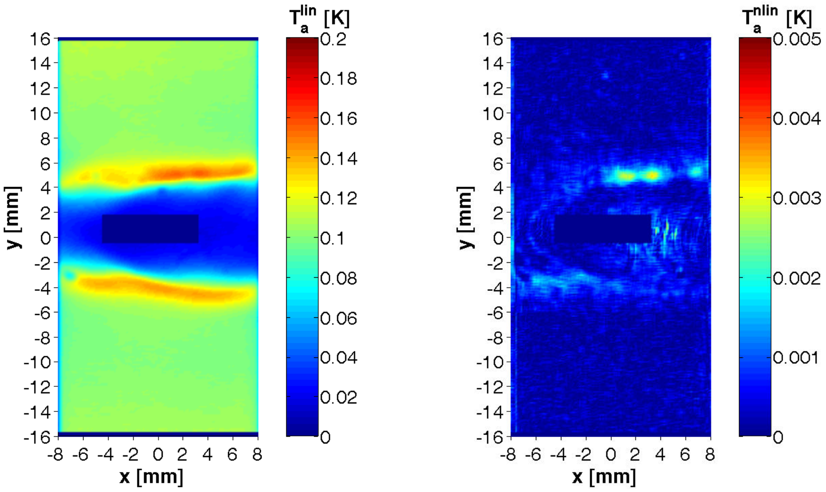

$N = 75000$; $N/N_f = 0.10$

Figure 103-1: Welded specimen SK0608; linear and nonlinear temperature amplitudes

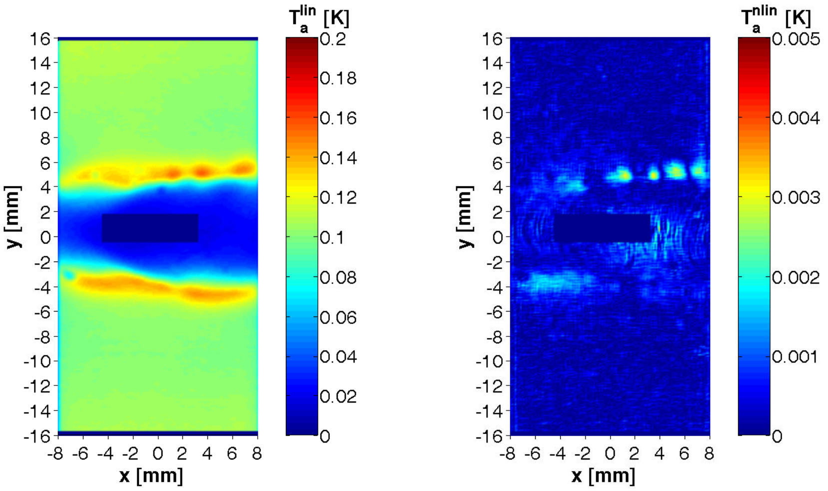

$N = 150000;\ N/N_f = 0.20$

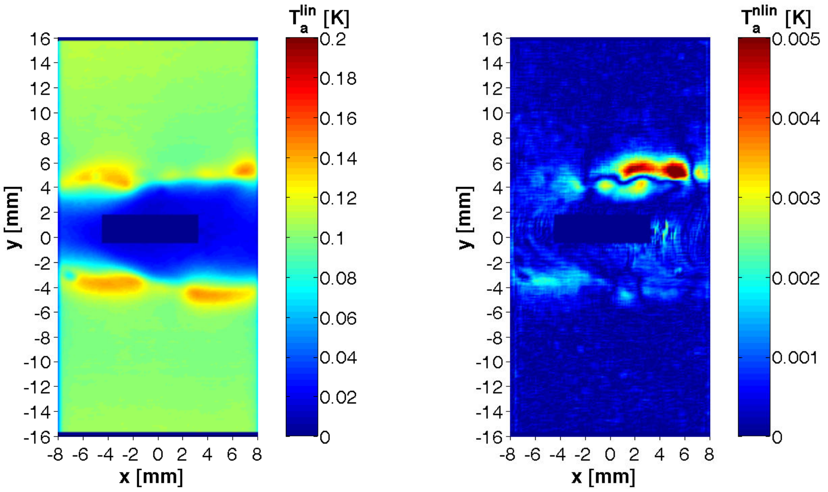

$N = 225000;\ N/N_f = 0.31$

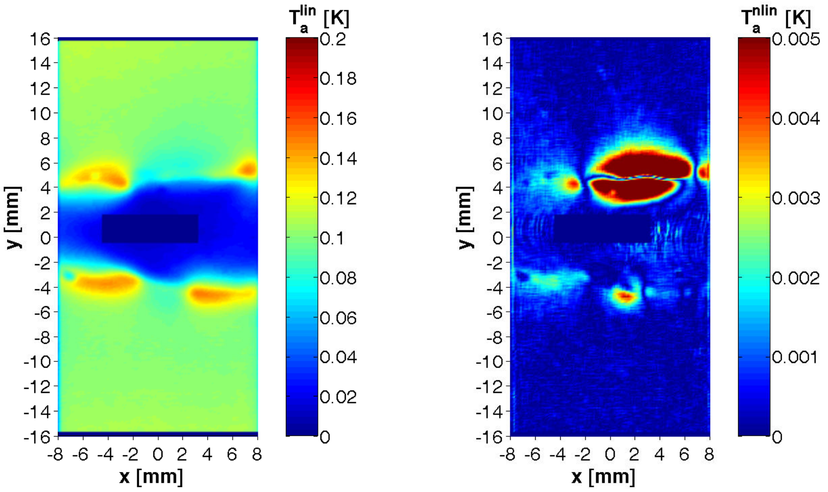

$N = 300000;\ N/N_f = 0.41$

Figure 103-2: Welded specimen SK0608; linear and nonlinear temperature amplitudes

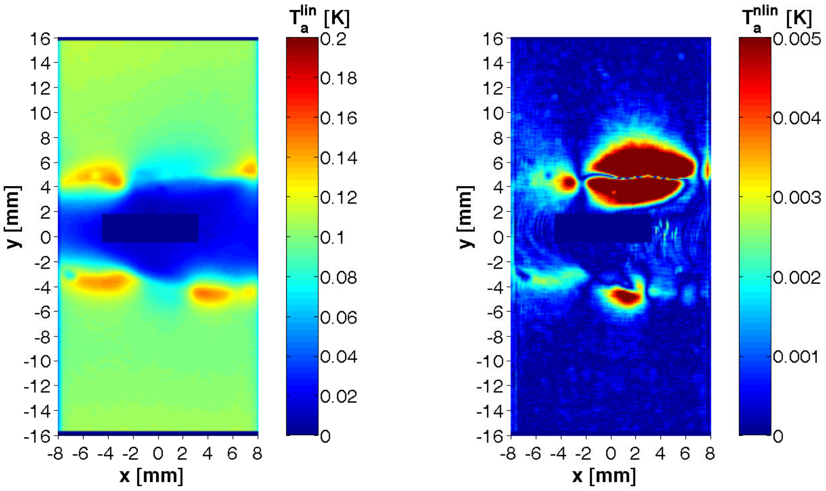

$N = 360000;\ N/N_f = 0.49$

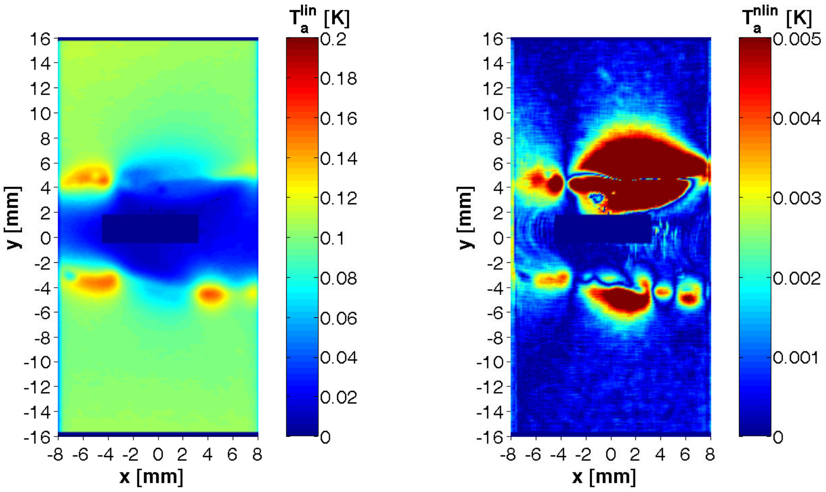

$N = 510000;\ N/N_f = 0.69$

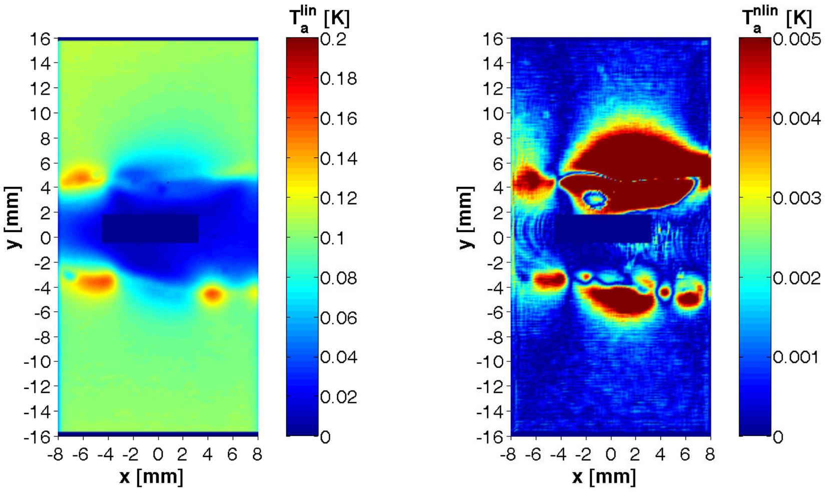

$N = 585000;\ N/N_f = 0.79$

Figure 103-3: Welded specimen SK0608; linear and nonlinear temperature amplitudes

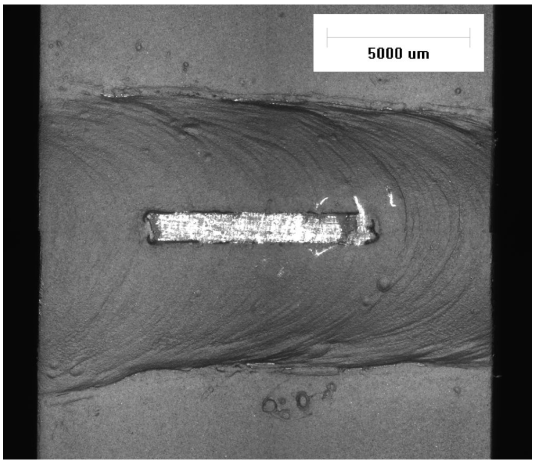

surface detail

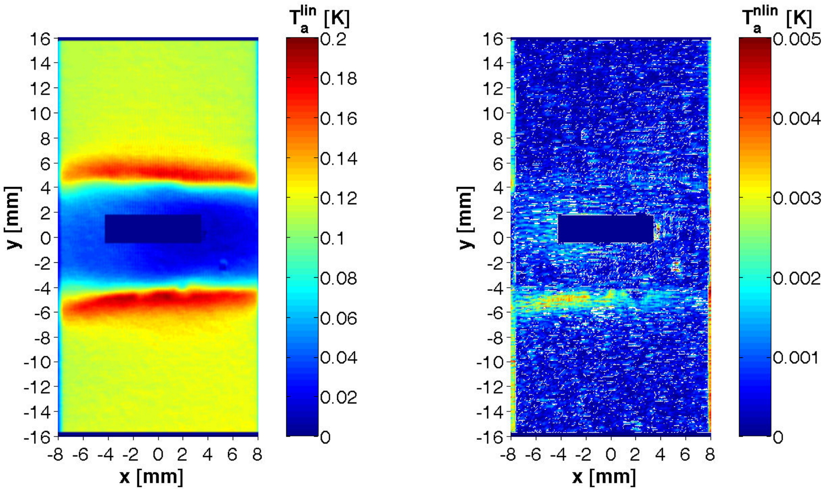

$N = 15000;\ N/N_f = 0.06$

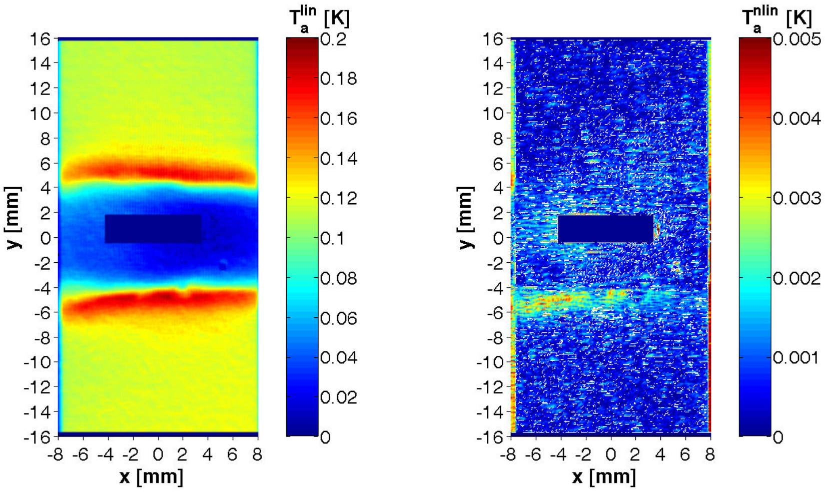

$N = 30000;\ N/N_f = 0.12$

Figure 104-1: Welded specimen SK0611; linear and nonlinear temperature amplitudes

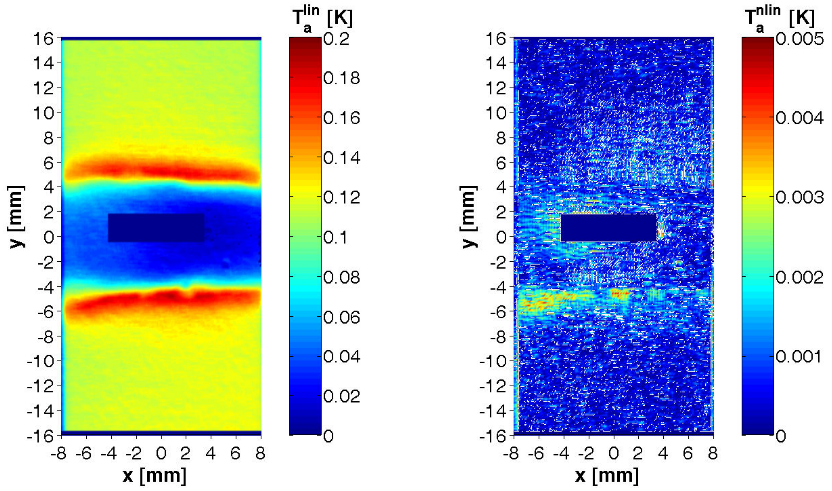

$N = 45000$; $N/N_f = 0.18$

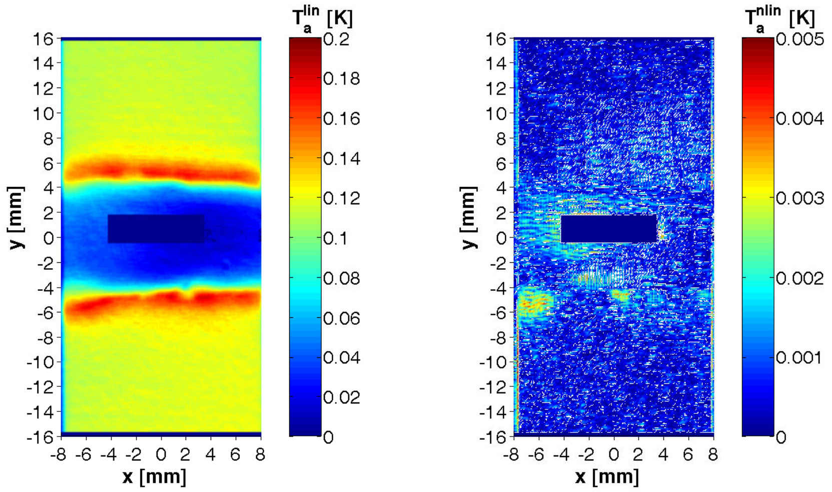

$N = 75000$; $N/N_f = 0.30$

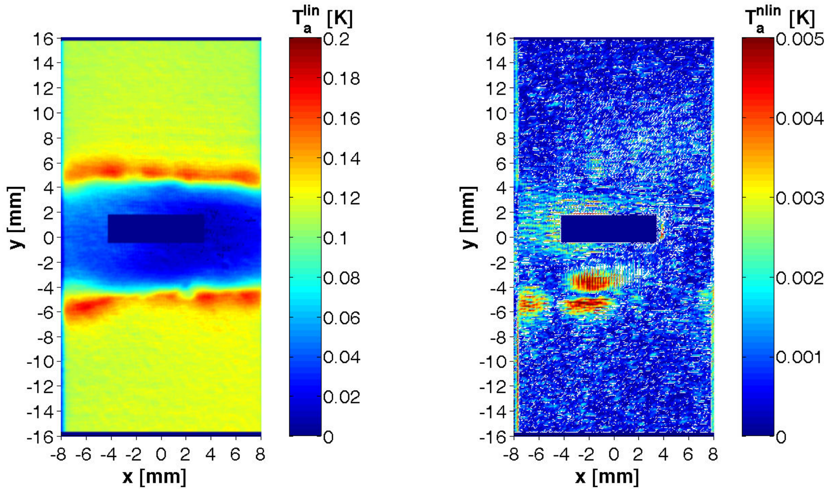

$N = 105000$; $N/N_f = 0.42$

Figure 104-2: Welded specimen SK0611; linear and nonlinear temperature amplitudes

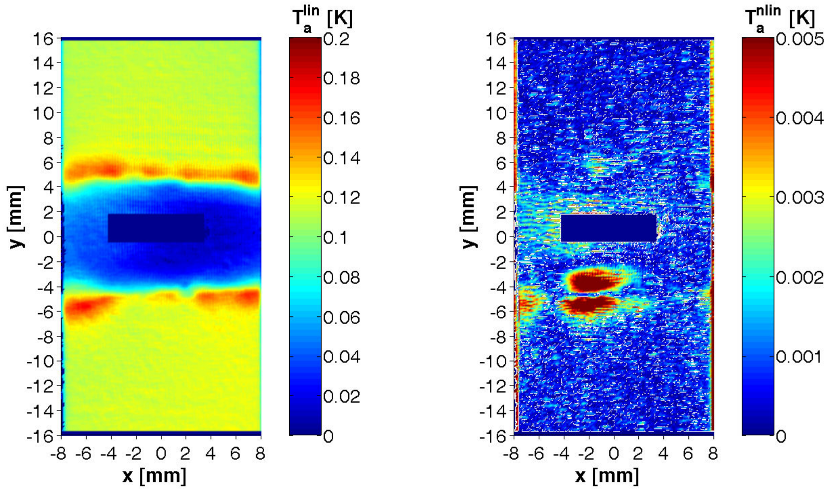

$N = 120000$; $N/N_f = 0.48$

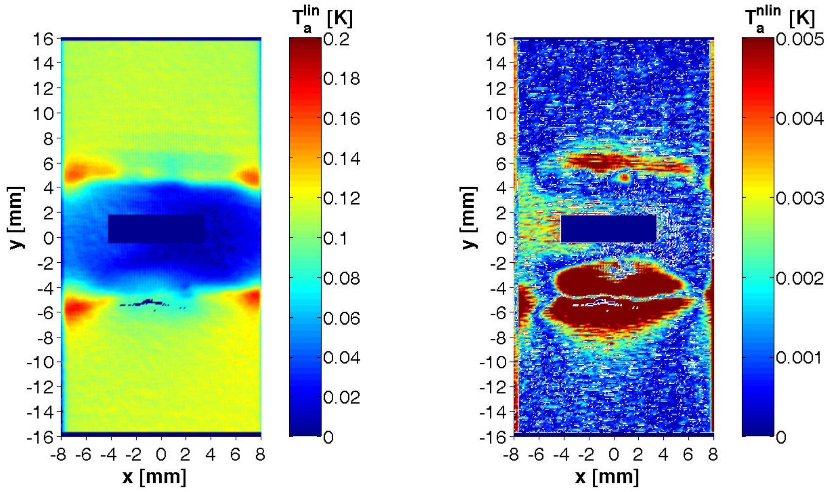

$N = 180000$; $N/N_f = 0.71$

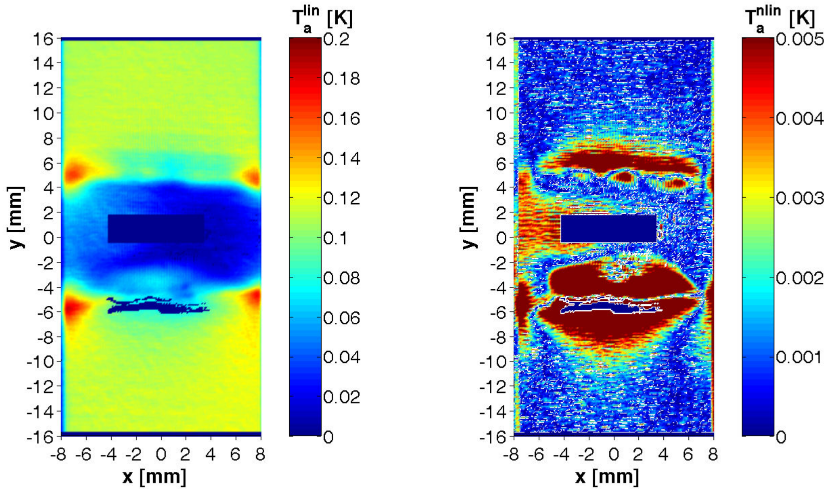

$N = 210000$; $N/N_f = 0.83$

Figure 104-3: Welded specimen SK0611; linear and nonlinear temperature amplitudes

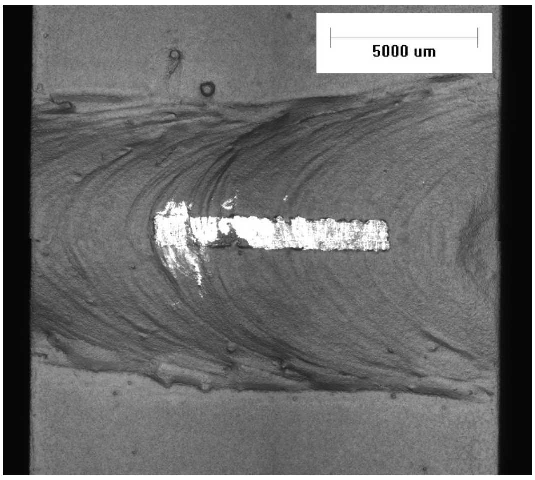

surface detail

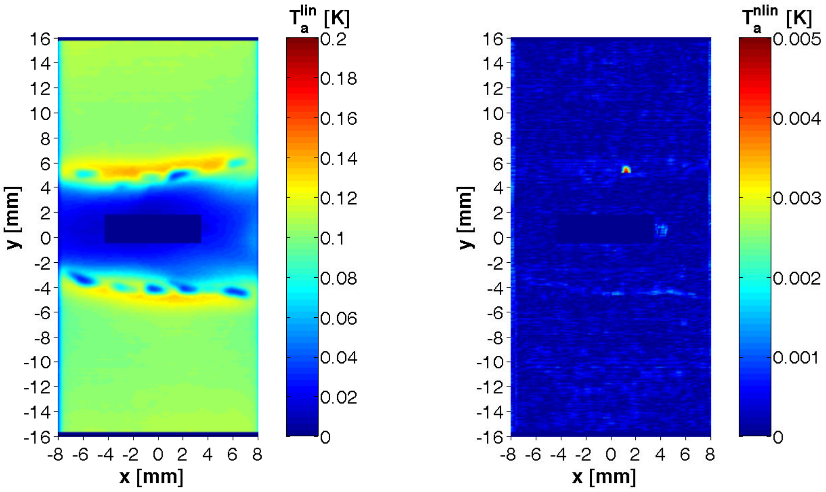

$N = 15000$; $N/N_f = 0.01$

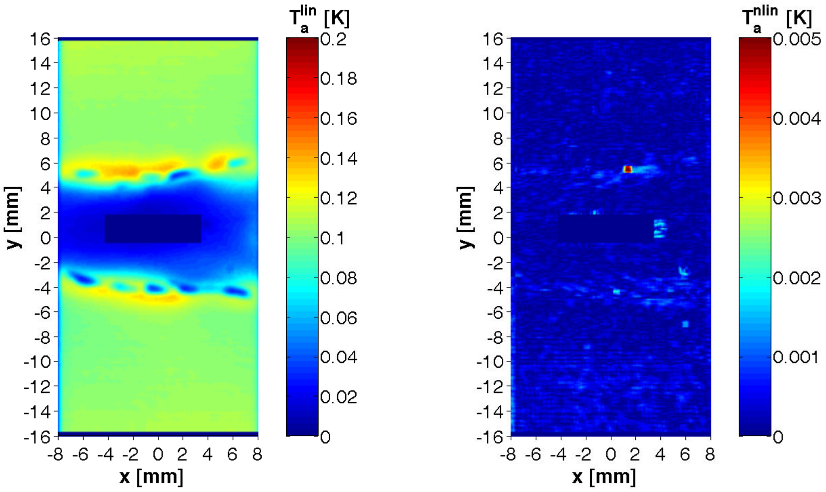

$N = 105000$; $N/N_f = 0.10$

Figure 105-1: Welded specimen SK0612; linear and nonlinear temperature amplitudes

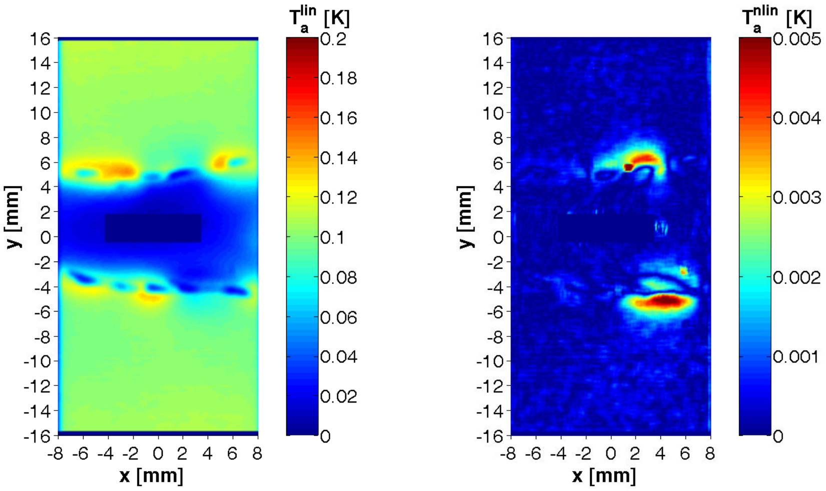

$N = 210000;\ N/N_f = 0.20$

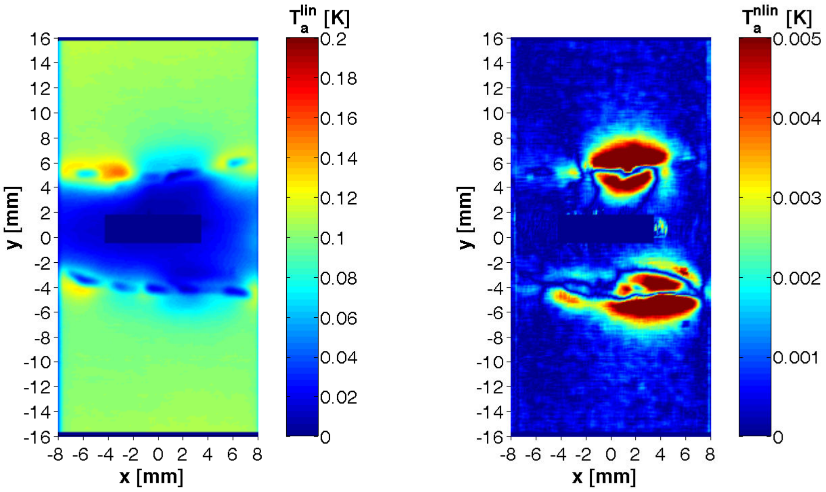

$N = 315000;\ N/N_f = 0.30$

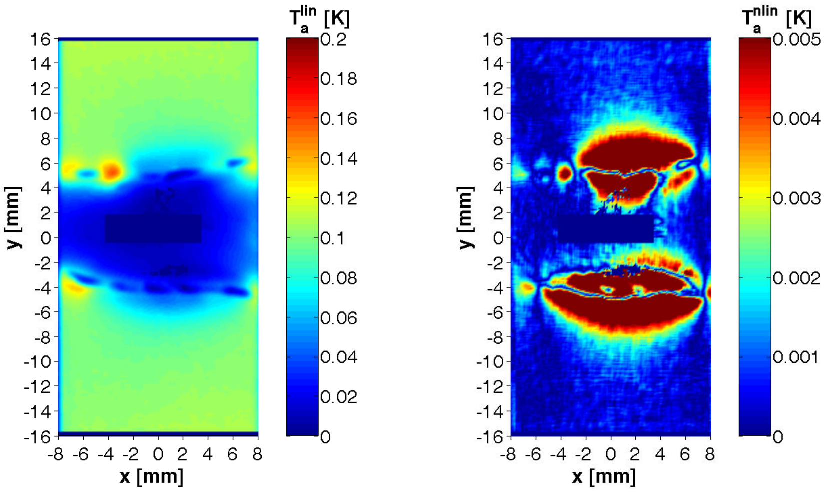

$N = 420000;\ N/N_f = 0.40$

Figure 105-2: Welded specimen SK0612; linear and nonlinear temperature amplitudes

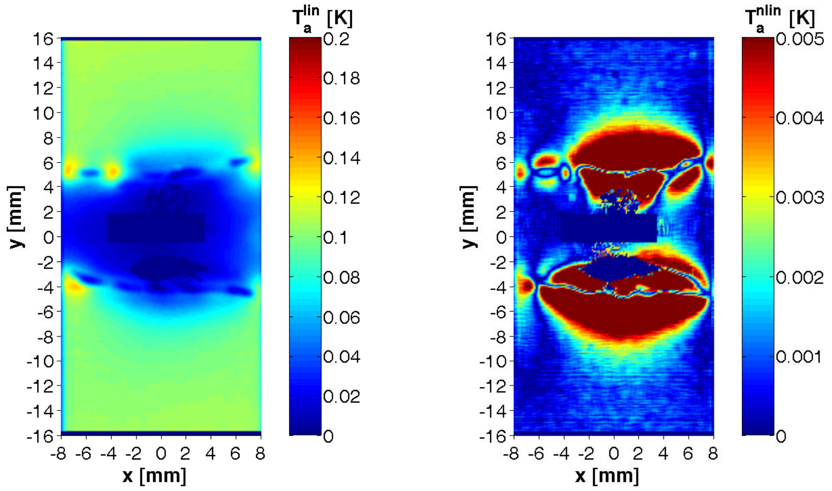

$N = 525000;\ N/N_f = 0.50$

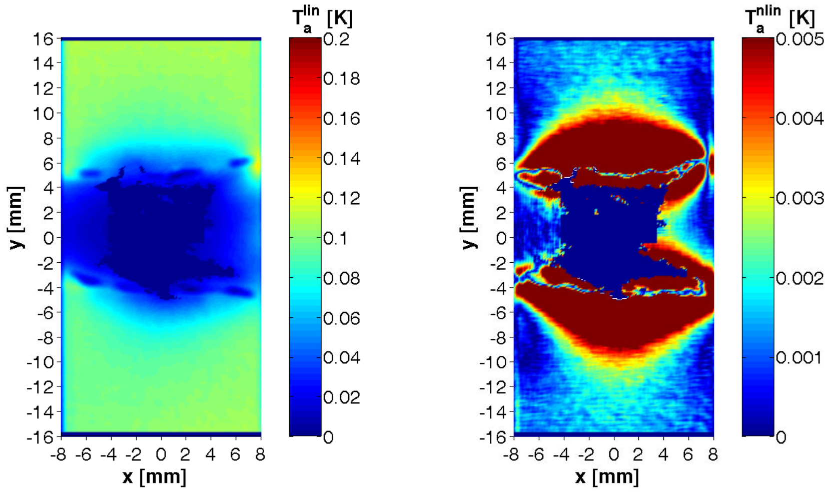

$N = 735000;\ N/N_f = 0.70$

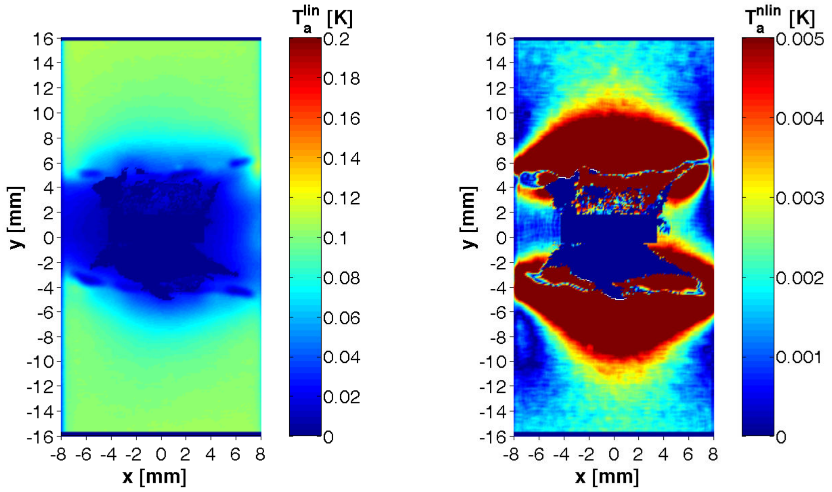

$N = 840000;\ N/N_f = 0.80$

Figure 105-3: Welded specimen SK0612; linear and nonlinear temperature amplitudes

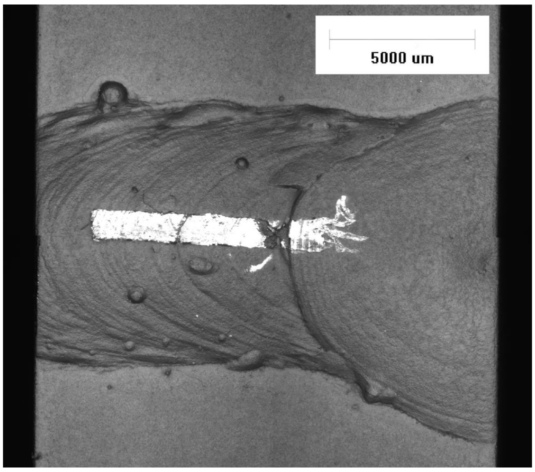

surface detail

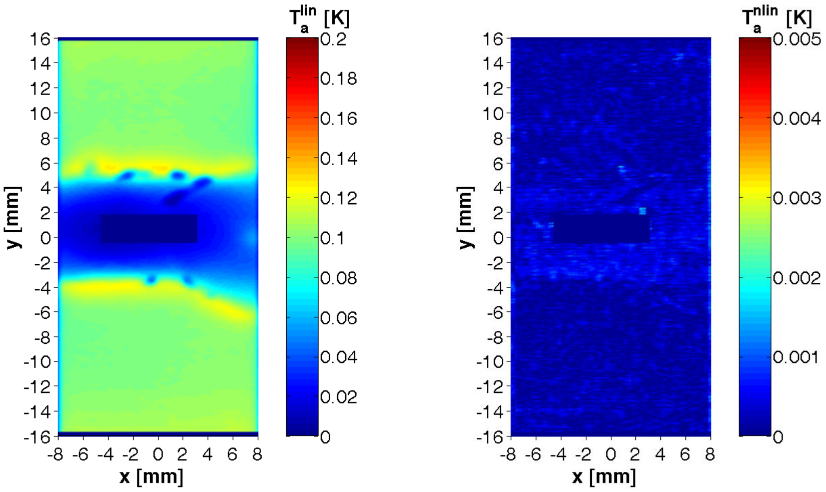

$N = 15000;\ N/N_f = 0.03$

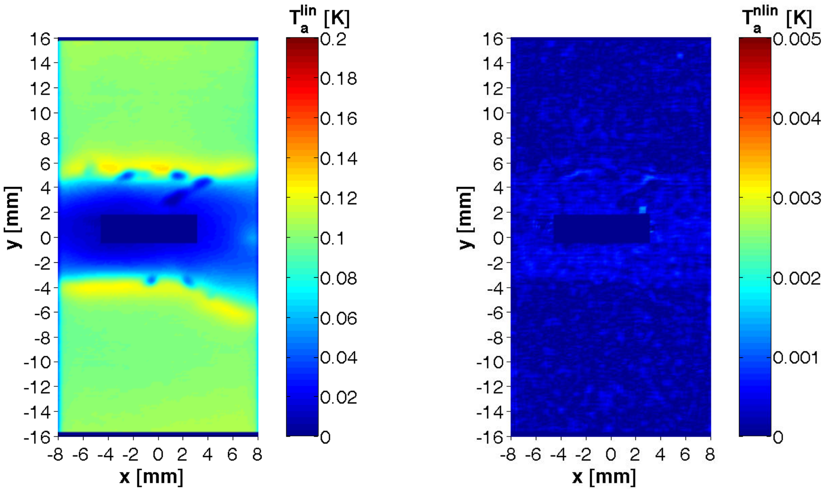

$N = 60000;\ N/N_f = 0.10$

Figure 106-1: Welded specimen SK0613; linear and nonlinear temperature amplitudes

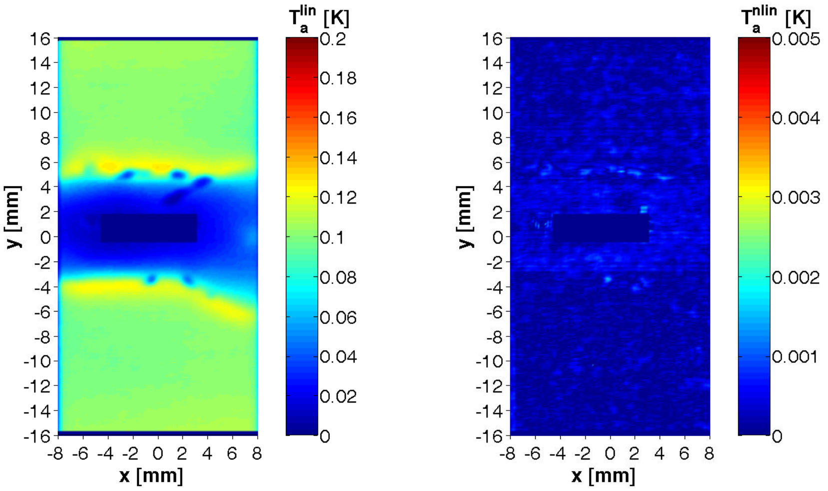

$N = 120000;\ N/N_f = 0.21$

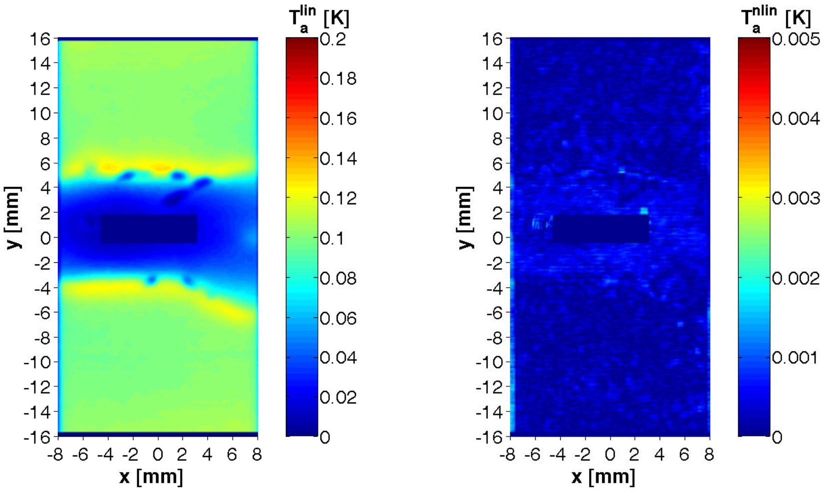

$N = 180000;\ N/N_f = 0.31$

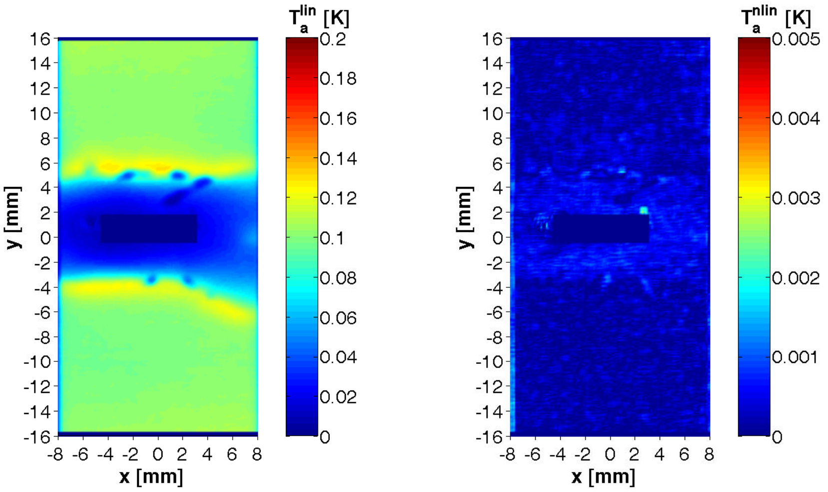

$N = 225000;\ N/N_f = 0.39$

Figure 106-2: Welded specimen SK0613; linear and nonlinear temperature amplitudes

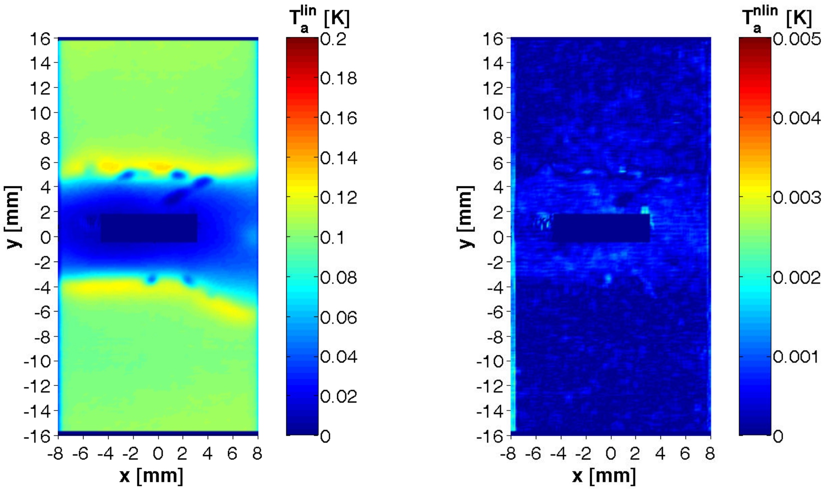

$N = 285000$; $N/N_f = 0.49$

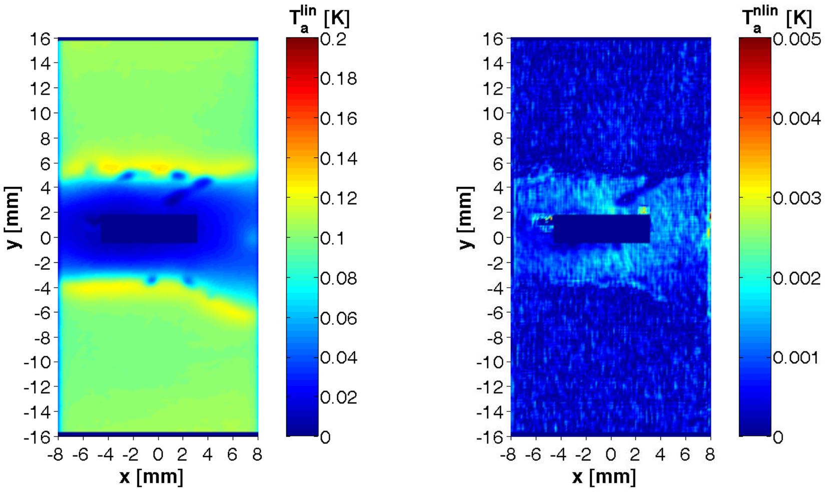

$N = 405000$; $N/N_f = 0.70$

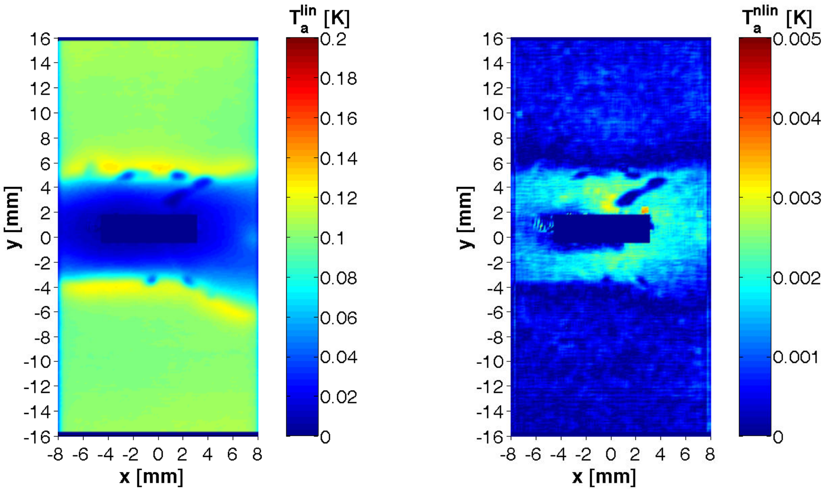

$N = 465000$; $N/N_f = 0.80$

Figure 106-3: Welded specimen SK0613; linear and nonlinear temperature amplitudes

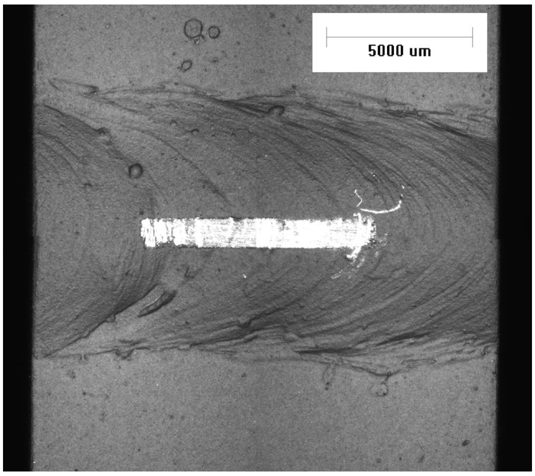

surface detail

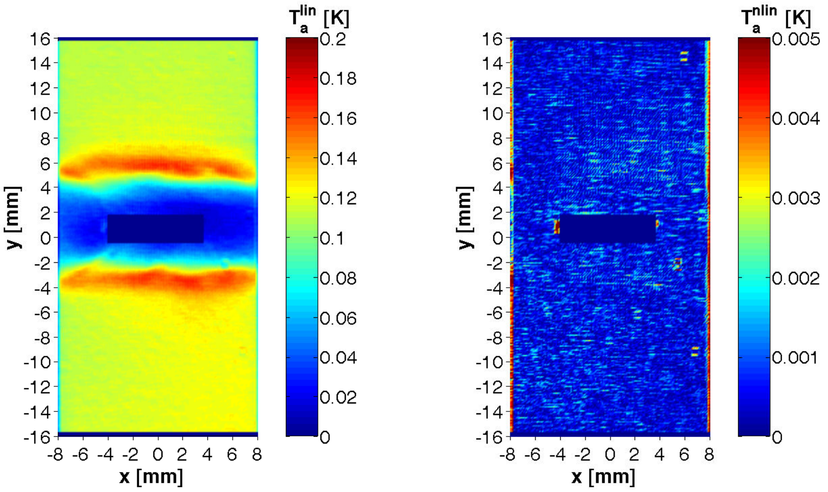

$N = 15000;\ N/N_f = 0.01$

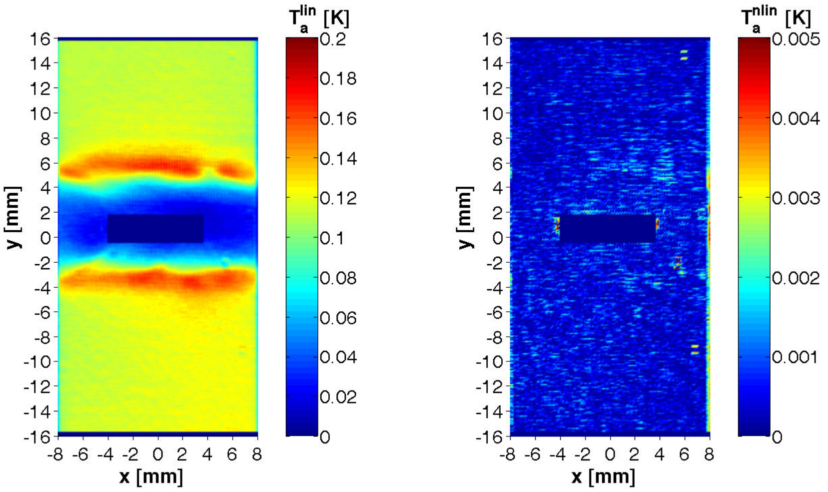

$N = 150000;\ N/N_f = 0.10$

Figure 107-1: Welded specimen SK0615; linear and nonlinear temperature amplitudes

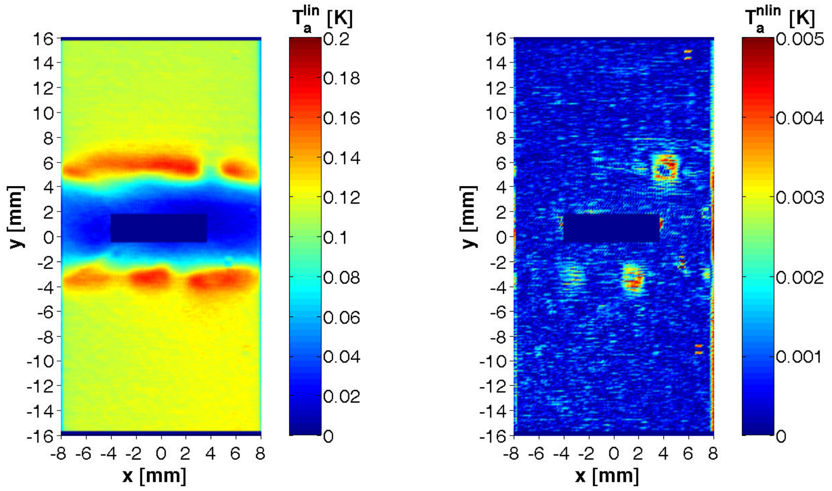

$N = 300000$; $N/N_f = 0.20$

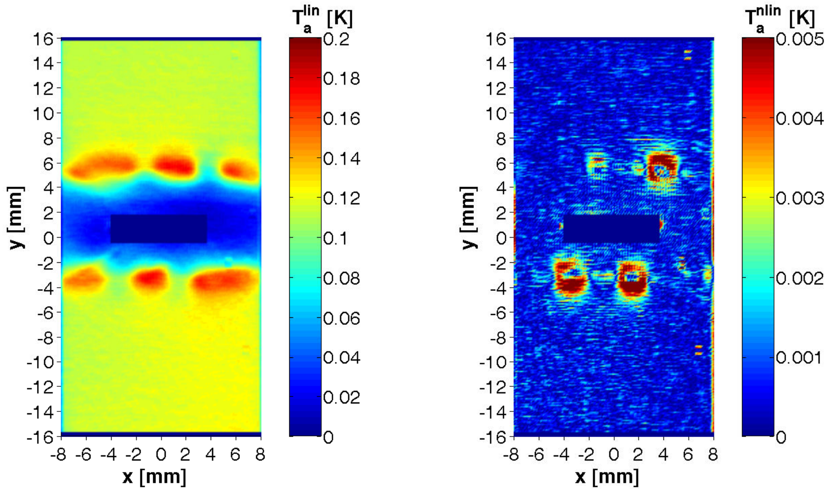

$N = 450000$; $N/N_f = 0.30$

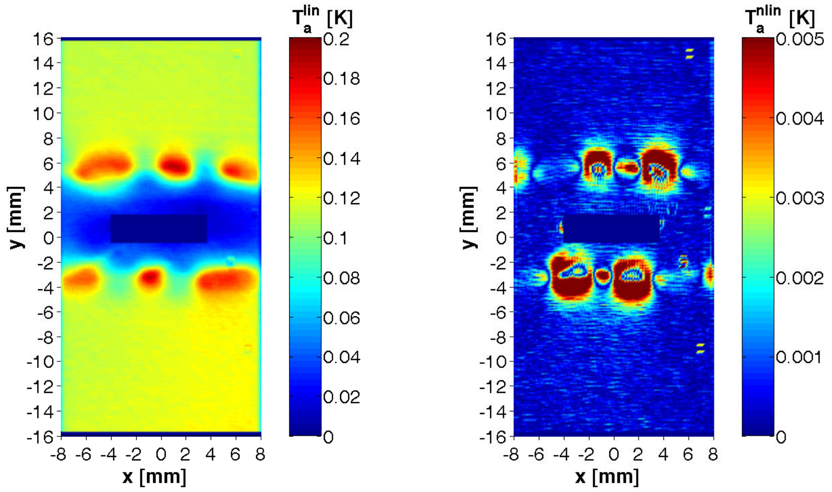

$N = 600000$; $N/N_f = 0.40$

Figure 107-2: Welded specimen SK0615; linear and nonlinear temperature amplitudes

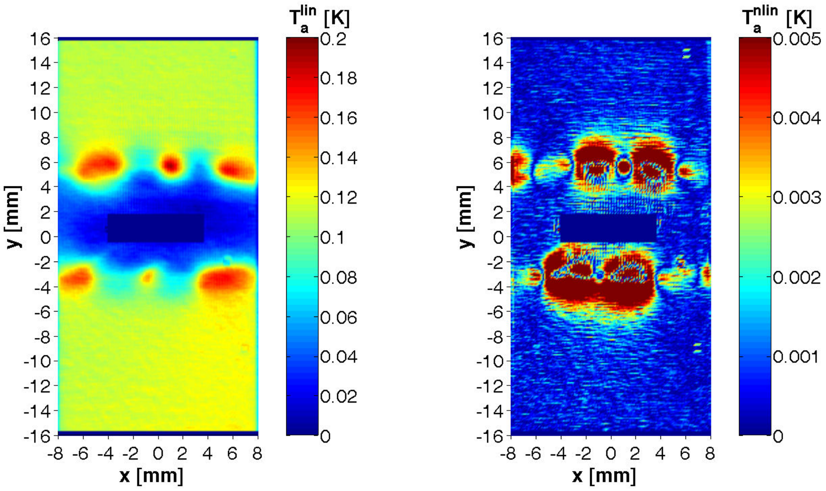

$N = 750000$; $N/N_f = 0.50$

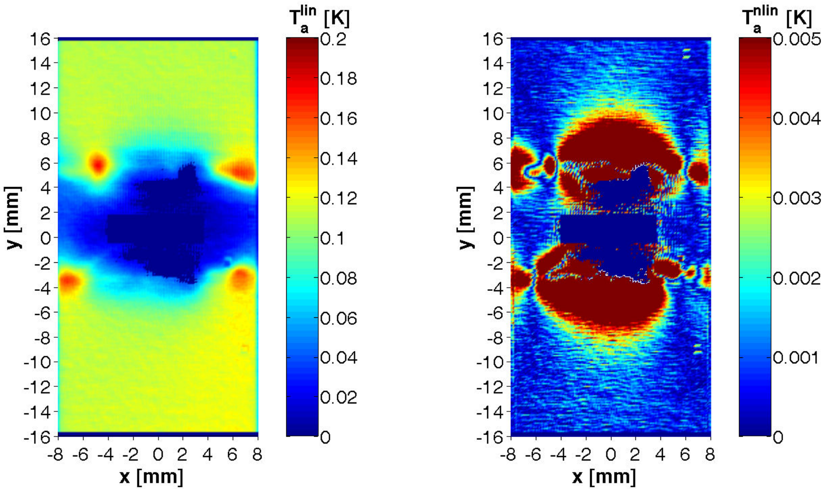

$N = 1050000$; $N/N_f = 0.70$

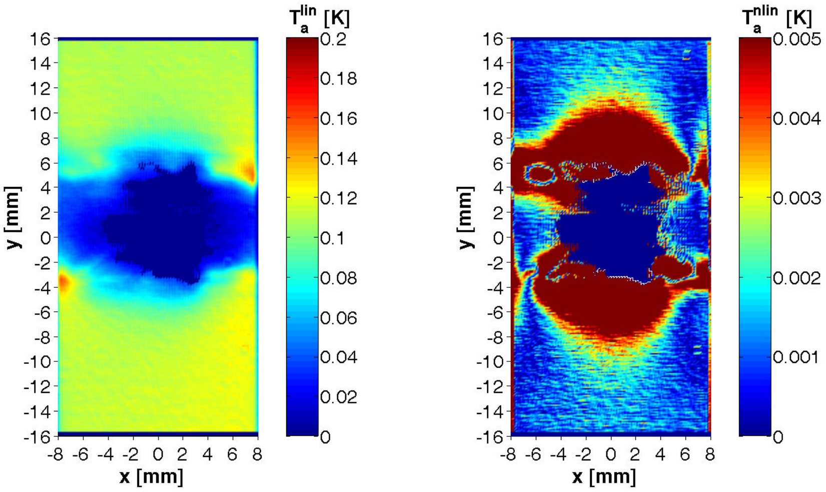

$N = 1200000$; $N/N_f = 0.80$

Figure 107-3: Welded specimen SK0615; linear and nonlinear temperature amplitudes

Lebenslauf / Curriculum vitae

Zur Person

Justus Medgenberg
geboren am 04.07.1976 in Annweiler a.Tr. / Rheinland-Pfalz
ledig

Werdegang

Aug. 1983 - Juli 1987	Grundschule in Steinweiler / Rheinland-Pfalz
Aug. 1987 - Juli 1996	Gymnasium Bad Bergzabern / Rheinland-Pfalz
Juli 1996	Abitur
Aug. 1996 - Okt. 1997	Zivildienst im Ev. Mütter-Kind-Kurheim Bad Bergzabern
Okt. 1997 - Okt. 2002	Studium des Bauingenieurwesens an der Technischen Universität Karlsruhe Vertiefungsrichtung Wasserbau/Hydraulik
Aug. 2000 - Juli 2001	Auslandsstudium an der University of Arizona, Tucson / USA
Apr. 2002 - Okt. 2002	Diplomarbeit an der Universidad de Granada / Spanien
Okt. 2002	Abschluss als Diplom-Ingenieur
Dez. 2002 - Juni 2003	Wissenschaftliche Hilfskraft am Institut für Hydromechanik der Technischen Universität Karlsruhe zur Bearbeitung und Abschluss eines Forschungsprojekts
Juni 2003 - Dez. 2007	Wissenschaftlicher Mitarbeiter am Institut für Bauwerkserhaltung und Tragwerk der Technischen Universität Braunschweig
seit Jan. 2008	Anstellung bei der Bilfinger Berger AG / Mannheim